Waste heat-driven adsorption cooling systems for vehicle air conditioning applications

by

Amirhossein Sharafianardakani

M.Sc., Shiraz University, 2010
B.Sc., Shiraz University, 2007

Dissertation Submitted in Partial Fulfillment of the
Requirements for the Degree of
Doctor of Philosophy

in the
School of Mechatronic Systems Engineering
Faculty of Applied Sciences

SIMON FRASER UNIVERSITY

Fall 2015

Approval

Name:	**Amirhossein Sharafianardakani**
Degree:	**Doctor of Philosophy**
Title:	***Waste heat-driven adsorption cooling systems for vehicle air conditioning applications***
Examining Committee:	**Chair:** Kevin Oldknow Lecturer

Majid Bahrami
Senior Supervisor
Associate Professor _____

Woo Soo Kim
Supervisor
Assistant Professor _____

Krishna Vijayaraghavan
Supervisor
Assistant Professor _____

Michael Eikerling
Internal Examiner
Professor
Department of Chemistry _____

Abdulmajeed Mohamad
External Examiner
Professor
Department of Mechanical and
Manufacturing Engineering
University of Calgary _____

Date Defended/Approved: October 1, 2015

Abstract

Waste heat-driven adsorption cooling systems (ACS) are potential replacements for vapor compression refrigeration cycles in vehicle air conditioning (A/C) applications. Working pairs in an ACS are a combination of an adsorbent material (e.g., zeolite and silica gel), and an adsorbate (e.g., water and methanol). Most of these materials are non-toxic, non-corrosive, non-ozone depleting, and inexpensive. Besides, an ACS operates quietly and valves are its only moving parts. However, the bulkiness and heavy weight of ACS are major challenges facing commercialization of these environmentally friendly systems.

The focus of this research is to develop a proof-of-concept ACS with high specific cooling power for vehicle A/C applications. As such, this Ph.D. dissertation is divided into three main parts: (i) adsorbent material characterization, (ii) adsorber bed design, and (iii) ACS design. In-depth analytical and thermodynamic cycle models are developed to understand the phenomena in adsorption process, adsorber bed and ACS. Also, a modular two-adsorber bed ACS equipped with thermocouples, pressure transducers and flow meters is designed and built for the first time at the Laboratory for Alternative Energy Conversion (LAEC) to test different adsorbent materials, adsorber beds, condensers, and evaporators under different operating conditions. A low-operating pressure evaporator with capillary-assisted tubes is designed and installed on the testbed to improve the performance of ACS. In addition, a novel expansion valve and control valves are proposed to simplify the control system and reduce the complexity of ACS for vehicle A/C applications. Using this ACS testbed with enhanced performance, a specific cooling power of 150 W/kg of dry adsorbent is achieved.

Keywords: Adsorption cooling system; Adsorber bed; Adsorbent; Vehicle air conditioning; capillary-assisted evaporator; Control valves.

To my beloved parents, brothers, and Zohreh for their unconditional support and encouragement

Acknowledgements

I would like to thank my senior supervisor, Dr. Majid Bahrami, for his support and guidance throughout my Ph.D. studies. It has been a privilege to work with him and learn from his experience.

I am also thankful to my supervisory committee members, Dr. Woo Soo Kim and Dr. Krishna Vijayaraghavan, for their discussions and comments on my research project. I am also thankful to Dr. Michael Eikerling and Dr. Abdulmajeed Mohamad for their time reading this thesis and comments. Also, I am grateful to Dr. Kelvin Oldknow to being the defense committee chairman.

I would also like to thank my colleagues at Laboratory for Alternative Energy Conversion at Simon Fraser University for their support and contributions. I thank specially the adsorption group members, Claire McCague, Khorshid Fayazmanesh, Poovanna Cheppudira, Mahdi Nemati Mehr, Mina Rouhani, and Behzad Baghapour. Your support and help made this research possible. Also, I would like to thank our lab engineers, Marius Haiducu and Wendell Huttema, who supported this research project.

I would like to thank the Natural Sciences and Engineering Research Council of Canada (NSERC) for the financial support through the Automotive Partnership Canada Grant. Also, I thank our industrial partner, Cool-It Highway Services, for the financial support of this project.

Finally, I would like to express my gratitude to my parents and brothers for their endless support and encouragement during my life. My special thanks go to my beautiful wife, Zohreh, for her patience, support, and encouragement throughout my professional career.

Table of Contents

List of Figures

List of Acronyms

AAMR	Adsorber Bed to Adsorbent Mass Ratio
A/C	Air Conditioning
ACS	Adsorption Cooling System
ADTR	Adsorption to Desorption Time Ratio
COP	Coefficient of Performance
HVAC	Heating, Ventilation, and Air Conditioning
ICE	Internal Combustion Engine
RSC	Reversed Stirling Cycle
SCP	Specific Cooling Power
TCR	Thermal Contact Resistance
TCS	Temperature Control System
TGA	Thermogravimetric Analysis
VCRC	Vapor Compression Refrigeration Cycle

Glossary

Adsorber Bed to Adsorbent Mass Ratio	Ratio of metal mass of adsorber bed to dry mass of adsorbent material, i.e., dead to active mass ratio
Coefficient of Performance	Ratio of evaporative cooling energy to the waste heat energy supplied to the adsorber beds
Specific Cooling Power	Ratio of evaporative cooling energy to dry mass of adsorbent multiplied by the cycle time

Executive Summary

Motivation

Conventional vapor compression refrigeration cycles (VCRCs) in vehicle air conditioning (A/C) systems can add up to 5-6 kW peak power draw on the internal combustion engine (ICE) of a vehicle; equivalent to the power used to drive a 1200-kg sedan at 56 km/h. Moreover, almost 70% of the total fuel energy released in an ICE is dissipated through the engine coolant and exhaust gas in the form of waste heat. A promising replacement for conventional VCRCs is an adsorption cooling system (ACS) in which adsorber beds replace the compressor and the waste heat of an ICE is utilized to regenerate the adsorber beds and produce cooling power.

Working pairs in an ACS are a combination of an adsorbent material (e.g., zeolite and silica gel), and an adsorbate (e.g., water and methanol). Most of these materials are non-toxic, non-corrosive, non-ozone depleting, and inexpensive. Furthermore, ACS is quiet and valves are its only moving parts. However, the bulkiness and heavy weight of ACS presently limit the commercial viability of this environmentally friendly technology for vehicle A/C applications. The origins of these limitations are low heat and mass transfer inside the adsorber bed. In this Ph.D. dissertation, analytical and thermodynamic cycle modeling as well as experimentations are performed to develop an in-depth understanding of the adsorption phenomenon in adsorbent particles, adsorber beds and ACS. Also, a modular two-adsorber bed ACS equipped with thermocouples, pressure transducers and flow meters is designed and built for the first time at the *Laboratory for Alternative Energy Conversion* (LAEC), at Simon Fraser University to test different adsorbent materials, adsorber beds, condensers, and evaporators under different operating conditions. In addition, innovative ideas for the evaporator, expansion valve and control valves are proposed to improve the evaporation process, simplify the control system, and reduce the complexity and mass of the system for vehicle A/C applications.

Objectives

The objectives of this research project are to understand the heat and mass transfer in an adsorber bed and build a waste heat-driven ACS with specific cooling power

(SCP) of 150 W/kg of dry adsorbent as a proof-of-concept demonstration for vehicle A/C applications.

Methodology

A systematic approach is adopted to understand different aspects of the processes in an ACS; the scope of the research is shown in Figure 1. This project is divided into three parts as follows:

- Understanding of the adsorbate uptake rate and thermal conductivity of adsorbent materials,
- Development of thermodynamic cycle models to predict the ACS performance under different operating conditions, and
- Building a waste heat-driven ACS as a proof-of-concept demonstration for vehicle A/C applications.

Contributions

The contributions of this research program include sets of analytical and thermodynamic cycle models, and design/building a modular ACS proof-of-concept demonstration testbed with enhanced performance. The followings are the main outcomes of this study:

- Development of a new analytical model for calculating adsorbate uptake rate by adsorbent materials and mass diffusivity of working pairs under different mass transfer Biot numbers using a resistance-capacitance model (published in the International Journal of Heat and Mass Transfer, 2013),
- Measurements of the thermal conductivity of mesoporous silica gel adsorbents bound with polyvinylpyrrolidone and its thermal contact resistance with a metallic substrate for thermal design of adsorber beds (published in the International Journal of Heat and Mass Transfer, 2014),
- Assessment of different adsorber bed designs for waste heat-driven ACS for vehicle A/C applications (published in the Renewable and Sustainable Energy Reviews, 2014),

- Experimental investigation of the impact of fin spacing on temperature distribution in a finned tube adsorber bed of an ACS (published in the International Journal of Refrigeration, 2015),
- Studied the effects of different adsorber bed designs on the in-situ water uptake rate of AQSOA FAM-Z02 (under review in the Applied Thermal Engineering Journal),
- Critical analysis of thermodynamic cycle modeling of ACS for light-duty vehicle A/C applications (published in the Renewable and Sustainable Energy Reviews, 2015),
- Performance analysis of a novel expansion valve and control valves designed for a waste heat-driven two-adsorber bed ACS (submitted to the Applied Thermal Engineering Journal),
- Studied the effects of capillary-assisted tubes with different fin geometries on the performance of a low-operating pressure evaporator for ACS (under review in the Applied Energy Journal),
- Investigated the effects of adsorbent mass and number of adsorber beds on the performance of a waste-heat driven ACS for vehicle A/C applications (submitted to the Energy Journal), and
- Practical design considerations in ACS with different composite adsorbents.

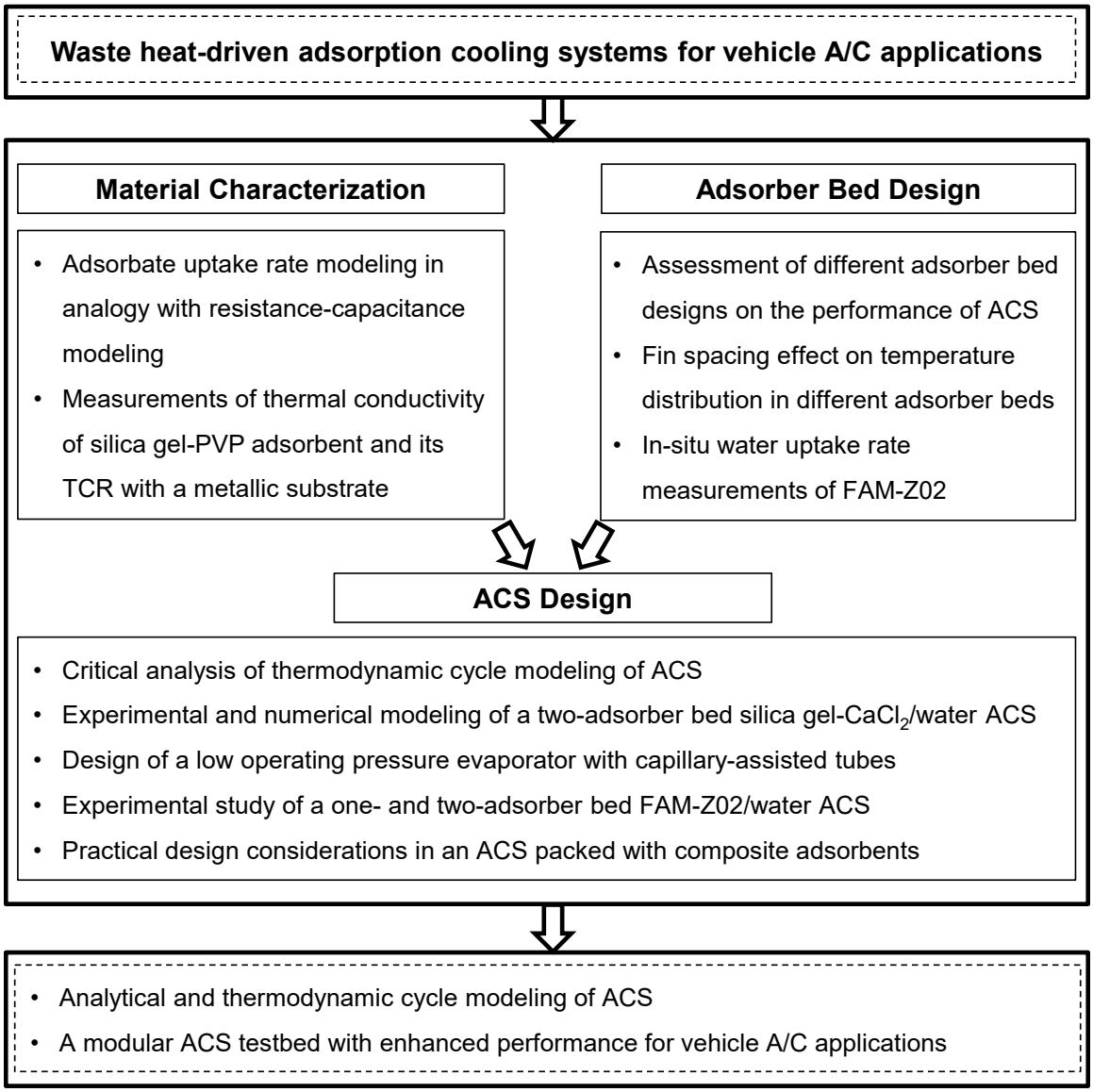

Figure 1. Scope of the present research project and deliverables.

Chapter 1.

Introduction

Air conditioning and refrigeration systems (A/C-R) consume a considerable amount of energy to produce cooling effects in domestic and industrial applications such as ice-making industries [1–3], food industries [4–6], vaccine protection [7–9], and building and vehicle A/C applications [10–13]. Vapor compression refrigeration cycles (VCRCs) are the most popular type of refrigeration systems in which different refrigerants, such as chlorofluoro-carbons (CFCs), hydrochlorofluorocarbons (HCFCs), and hydrofluorocarbons (HFCs) are used [14]. However, these refrigerants cause significant ozone depletion and global warming. An ideal refrigerant should have favorable thermodynamic properties and should be noncorrosive, nontoxic, non-flammable, and environmentally benign [15]. Therefore, development of green, sustainable refrigeration systems, which utilize environmentally friendly refrigerants, is of great importance.

The negative environmental impacts of VCRCs increase in automotive and transportation applications in which a compressor of a VCRC is powered by the mechanical energy drawn from an internal combustion engine (ICE). A compressor of a VCRC can add up to 5-6 kW peak power draw on a vehicle's engine; the equivalent power required for a 1200-kg sedan cruising at 56 km/h [16]. The COP of VCRCs for light-duty vehicles is about 1.0-1.6 because of the compactness of the system [17–19].

The U.S. annually consumes about 40 billion liters of fuel for A/C systems of light duty vehicles [16]. In an ICE vehicle, almost 70% of the total fuel energy is dissipated through the engine coolant and exhaust gas in the form of waste heat [16]. There are several heat-driven systems that can use the waste heat to generate cooling power and reduce the negative impacts of VCRCs. The following is a brief overview of available systems.

1.1. Thermoelectric Cooling

To produce cooling for vehicle A/C applications, a combination of a thermoelectric cooling system and a thermoelectric generator is needed. A thermoelectric generator converts directly the heat into electricity. This process is known as the Seebeck effect [20]. A thermoelectric generator is comprised of two different semiconductor materials such as bismuth telluride and antimony telluride alloys [21]. By heating and cooling the two sides of a thermoelectric generator using the exhaust gas of an ICE and ambient air, respectively, it generates electricity. Thermoelectric generators have no moving part with high longevity. Currently, the efficiency of a thermoelectric generator is less than 9% [22]. Consequently, integration of these systems with the ICE of a light-duty vehicle generates only 450 W of electricity [22] which does not meet the A/C requirements of a vehicle.

The electricity generated by a thermoelectric generator can be transferred to a thermoelectric cooling system (Peltier cooler) to generate cooling. The COP of thermoelectric cooling systems is about 0.3 to 0.6 [21,23]. As a result, the overall efficiency of a combination of a thermoelectric generator and thermoelectric cooling system is about 2.7% to 5.4% (=9% × 0.3 to 0.6). It can be concluded that a thermoelectric cooling is not a viable solution for vehicle A/C applications with the current technology.

1.2. Reversed Stirling Cycle

Reversed Stirling cycle (RSC) is comprised of two isothermal and two constant volume processes. This system is internally reversible and thus its ideal COP is similar to that of a Carnot refrigeration cycle working with the same source temperatures [20]. The main components of a RSC are two pistons located in a cylinder and a regenerator located between the two pistons. However, this cycle has many practical difficulties and its COP varies significantly with the temperature lift [21]. The COP of a 100 W RSC operating at the ambient temperature of 23-28°C decreases from 1.6 to 0.8 by increasing the temperature lift from 13 to 33°C [24]. The power density of SRCs also is less than 1 W/kg [25] which results in a heavy system.

A motor has to mechanically drive the pistons to generate cooling effect. In the case of using the waste heat of an ICE, a thermoelectric generator should be integrated with the RSC to generate required electricity to run the motor. As such the overall efficiency of the RSC integrated with an electric motor with efficiency of 80% is about 5.8% to 11.5% (=9% × 80% × 0.8 to 1.6) making this system impractical for vehicle A/C applications.

1.3. Absorption Cooling System

An absorption cooling system has no compressor. Instead, a pump is used to circulate the refrigerant inside the system. The vaporous refrigerant, such as NH_3, leaves the evaporator and enters an absorber where it is dissolved in a solution, such as water. Due to the absorption of NH_3 in water, heat is generated and to increase the solubility of NH_3 in water, the solution should be cooled down. The cold solution is pumped from the absorber toward a generator and its pressure increases. The pressurized solution is heated up using a waste heat or solar thermal energy and NH_3 is evaporated and flows to the condenser where it is condensed. The weak NH_3–water solution again returns to the absorber and the cycle is repeated. Replacing the compressor with a pump reduces the power consumption of the system dramatically.

The COP of an absorption refrigeration system is about 0.65-0.7 [20]. The two main drawbacks of absorption cooling systems in vehicle A/C application are: i) NH_3 is highly corrosive and is a high health hazard, and ii) its separation from water in the generator is significantly affected by the vehicle vibration [26,27]. Replacing NH_3 with LiBr can reduce the toxicity of the refrigerant used in an absorption cooling system. However, separation of LiBr form water is again affected by the vehicle vibration. As a result, absorption cooling systems cannot be a good candidate for vehicle A/C applications.

1.4. Adsorption Cooling System

In an adsorption cooling system (ACS), adsorber beds replace the compressor and a portion of engine waste heat is sufficient to regenerate the adsorber beds to meet the

A/C needs of a vehicle [28]. ACS works based on the adsorption phenomenon in which a gaseous adsorbate is adsorbed at the surface of a solid adsorbent material. Popular working pairs used in ACS applications include zeolite-water, silica gel-water and activated carbon-methanol. Most of these materials are environmentally friendly, non-toxic, non-corrosive, and inexpensive [29]. Moreover, an ACS is quiet and easy to maintain [30] as its only moving parts are valves. Thus, ACS is an ideal candidate for a variety of applications especially where waste-heat or low-grade thermal energy (temperatures below 100°C) is available. However, commercialization of ACS faces major challenges due to its heavy weight and bulkiness which cause low specific cooling power (SCP) and low coefficient of performance (COP) [31]. As such, proper implementation of ACS in vehicles has the potential to significantly reduce their fuel consumption and carbon footprint.

The SCP is defined as the ratio of evaporative cooling energy to the mass of dry adsorbent multiplied by the cycle time. Therefore, the SCP can be maximized by increasing the evaporative cooling energy and/or reducing the cycle time. The origins of the low performance of ACS are the low thermal conductivity of adsorbent particles (~ 0.1 to 0.4 W/m.K) [32–34] and the low mass diffusivity of adsorbent-adsorbate pairs (~ 10^{-8} to 10^{-14} m^2/s) [33,35]. As a result, heating and cooling of adsorber beds are time consuming. As such, design and optimization of an adsorber bed with improved heat and mass transfer characteristics, and low adsorber bed to adsorbent mass ratio (AAMR) can effectively increase the SCP and COP of ACS [36–38].

1.4.1. Adsorption versus Absorption

Adsorption phenomenon is an exothermic process in which molecules of a liquid or gas, called adsorbate, accumulate on a solid surface, called adsorbent [39–41]. Adsorbents are porous materials with the ability to take up several times of their volume of gases or liquids. The terms “adsorption” and “absorption” are usually assumed to be the same, but they are, in essence, completely different physical phenomena. In an adsorption process, molecules of a gas or liquid adhere on the surface of a solid, whereas in an absorption process, molecules of a gas or liquid penetrate in a solid or liquid phase.

1.4.2. Thermodynamic Processes in an Adsorption Cooling System (ACS)

An ACS works based on two main steps: heating-desorption-condensation and cooling-adsorption-evaporation. Following these steps, the ACS produces evaporative cooling power intermittently. To produce continuous cooling power, the solution is to use more than one adsorber bed. Figure 2a depicts a typical two-adsorber bed ACS. The main components of an ACS consist of adsorber beds, a condenser, an expansion valve, and an evaporator. Therefore, an ACS is similar to a VCRC, except that the adsorber beds replace the compressor.

Figure 2b shows the thermodynamic processes in an ACS which is divided into two subcycles: (i) an adsorbent cycle (on the right side), and (ii) an adsorbate cycle (on the left side). As shown in Figure 2b, the adsorbent cycle includes four steps: (1) isosteric heating (ih); process 1-2, (2) isobaric desorption (ibd); process 2-3', (3) isosteric cooling (ic); process 3'-4', and (4) isobaric adsorption (iba); process 4'-1. Isosteric processes occur at constant specific volume and isobaric processes occur at constant pressure. The adsorbate cycle shown in Figure 2b includes three steps: (1) isobaric condensation in the condenser; process 2-3, (2) isenthalpic process in the expansion valve; process 3-4, and (3) isobaric evaporation in the evaporator; process 4-1. Isenthalpic processes occur at constant enthalpy.

During step 1-2, the adsorbent-adsorbate pair absorbs the heat of Q_{ih} from an external heat source during an isosteric process. In this step, the pressure of the adsorber bed increases due to the adsorbate desorption from the adsorbent particles. This process is continued until the pressure of the adsorber bed reaches the pressure of the condenser and then the inlet valve to the condenser is opened. During step 2-3', the external heat source continuously heats the adsorber bed (Q_{ibd}) in an isobaric desorption process, the adsorbate leaves the adsorber bed, and is condensed inside the condenser through an isobaric condensation process (step 2-3). The total heat transfer to the adsorber bed, $Q_{total\ heating}$, during a desorption process is the sum of Q_{ih} and Q_{ibd}.

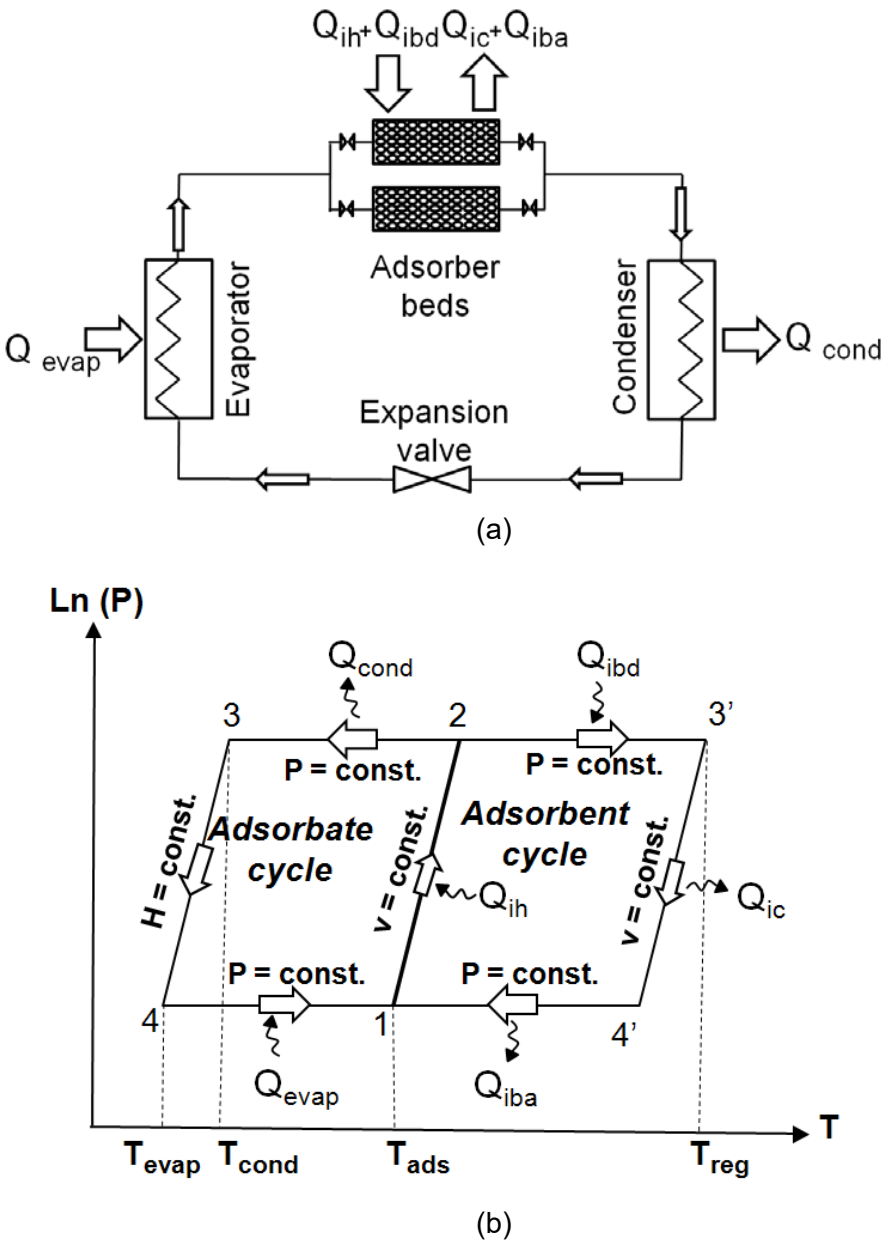

Figure 2. **(a) Main components and (b) thermodynamic processes in a two-adsorber bed ACS** [42]**.**

Upon reaching point 3', the maximum temperature of the system at the end of desorption time, the valve between the adsorber bed and the condenser is closed and during an isosteric cooling process (step 3'-4'), the temperature of the adsorbent is reduced by dissipating the heat of Q_{ic} to a heat sink. In step 3-4, the adsorbate inside the condenser passes through the expansion valve and enters the evaporator. During step 4-

1, the adsorbate absorbs the heat of Q_{evap} from the environment of interest and evaporates. At the same time, the valve between the evaporator and the adsorber bed is opened and the adsorbent adsorbs the vaporous adsorbate in an isobaric adsorption process (step 4'-1) and releases the heat of Q_{iba}. This process continues until reaching the end of adsorption time. The total heat removed from the adsorber bed, $Q_{total\ cooling}$, during an adsorption process is the sum of Q_{ic} and Q_{iba}. The cycle time is the sum of desorption and adsorption times.

The waste heat of an ICE or solar thermal energy can be utilized for desorption process. Waste heat- and solar-driven ACS for ice making and building A/C applications have been discussed at length in the literature [37,43–46]. Although many attempts carried out to improve the performance of ACS, these systems are still bulky thus not practical for vehicle A/C applications. As a result, the effective factors on the performance of the system, namely, adsorbent-adsorbate pair, adsorber bed design, and ACS design should be studied.

1.5. Motivations

A noiseless, environmentally friendly ACS is the outcome of this research program. The performance of the lab-scale ACS designed, constructed, and tested as a part of this research supports the proposition that effectively implemented ACS can reduce the fuel consumption of vehicles and greenhouse gas emissions. Cool-It Highway Services, an automotive A/C manufacturer, is the industrial partner of this Ph.D. research project. The Natural Sciences and Engineering Research Council of Canada (NSERC) financially supports this research project through the Automotive Partnership Canada Grant No. APCPJ 401826-10. The objectives of this research project are to understand the heat and mass transfers in an adsorber bed and ultimately build a waste heat-driven ACS with a SCP of 150 W/kg of dry adsorbent as a proof-of-concept demonstration for vehicle A/C applications. To meet the requirements of an ACS suitable for vehicle A/C applications, the following should be achieved:

- Understanding of the adsorbate uptake rate by adsorbent materials and the thermal conductivity of adsorbent materials,

- Development of accurate analytical and thermodynamic cycle models to predict the ACS performance under various operating conditions, and
- Building a waste heat-driven ACS as a proof-of-concept demonstration for vehicle A/C applications.

1.6. Organization of the Dissertation

This Ph.D. dissertation is comprised of three chapters organized as follows:

Chapter 1 provides an introduction to adsorption phenomenon and ACS including potential opportunities and challenges, thermodynamic processes in an ACS and how the system operates followed by motivations.

Chapter 2 provides a summary of the contributions of this Ph.D. research project. This chapter is comprised of nine sections dedicated to the summaries of peer-reviewed journal papers (published, in press, or currently under review) provided in Appendix A-I.

Chapter 3 provides a brief summary of the achievements and conclusions followed by future work suggested to improve the performance of ACS.

Chapter 2.

Summary of Contributions

The main contributions of this Ph.D. dissertation are published in nine peer-reviewed journal papers presented in Appendix A-I. In this chapter, a summary of each paper is provided followed by the connections between the papers.

2.1. Material Characterization

2.1.1. Adsorbate uptake and mass diffusivity of working pairs in adsorption cooling systems

The ability of porous materials to adsorb gases has been known for more than two centuries. Fontana [47] and Scheele [48] found that charcoal has ability to expel and absorb air when heated or cooled. Further investigations showed that the pore size and surface area of porous materials significantly affected their capacity for adsorption [40,49]. Several experimental techniques are available to measure the adsorbate uptake rate and the mass diffusivity of adsorbent-adsorbate pairs such as infrared spectroscopy, chromatography, nuclear magnetic resonance (NMR) and gravimetric methods [50]. The thermogravimetric analysis (TGA) is convenient for measuring adsorbate uptake rate and the mass diffusivity of adsorbent-adsorbate pairs in ACS applications. However, the measurements do not directly yield the mass diffusivity coefficient. To obtain the value of mass diffusivity, an appropriate model is needed for the analysis.

The adsorbate uptake includes a number of physical processes: (i) adsorbate transfer from the bulk gas to the adsorbent exterior surface, called gas-side resistance, (ii) diffusion of the adsorbate molecules to the pore surface of an adsorbent particle, called solid-side resistance, and (iii) a resistance associated with the adsorption process itself. Often the latter two resistances are more important than the first one [51–55]. Therefore, different mathematical models have been developed for the adsorption kinetics under different boundary conditions.

In this study, a new compact closed-form relationship in analogy with the resistance-capacitance (RC) model was developed. The proposed relationship was compared against the available analytical solutions and applied to the experimental data reported in the literature to find the adsorbate uptake rate and the mass diffusivity of silica gel-water pair under various operating temperatures. The proposed model was general and could be implemented to other adsorbent-adsorbate pairs such as activated carbon-methanol and zeolite-water. Implementation of this relationship in the thermodynamic cycle modeling of ACS can increase the accuracy of the adsorbate uptake rate modeling.

For further information, the reader is referred to Appendix A.

2.1.2. Thermal conductivity and contact resistance of mesoporous silica gel adsorbents bound with polyvinylpyrrolidone in contact with a metallic substrate for adsorption cooling system applications

Low thermal conductivity and high porosity are inherent properties of adsorbent materials. Recently, a new mesoporous silica gel adsorbent mixed with polyvinylpyrrolidone (PVP) binder was prepared and characterized in the LAEC. The adsorbent showed a high water uptake capacity under different operating temperatures and pressures. Binding the silica gel particles with PVP increased the contact between the silica gel particles. Also, PVP helped the silica gel particles adhere to the metallic substrate, and consequently, increased the heat transfer rate. This study shed light on the importance of thermal contact resistance (TCR) at the interface between the adsorbent and substrate, which has been overlooked in most studies reported in the literature. To show the impact of the TCR, several silica gel-PVP adsorbent samples with the bulk density of 450-520 kg/m^3 were prepared and coated on a metallic substrate.

In this study, the thermal conductivity of silica gel-PVP and its TCR with a metallic substrate were measured by using the two-thickness method. A guarded-hot plate apparatus housed under a glass vacuum chamber was used for the measurements. The results showed that due to the low thermal conductivity and high porosity of adsorbent materials, the TCR could not be neglected in the measurements and its effect should be de-convoluted from the bulk thermal resistance of adsorbent. These results can be applied

in the thermal design of adsorber beds to improve the accuracy of analytical and numerical models.

For further information, the reader is referred to Appendix B.

2.2. Adsorber Bed Design

2.2.1. Assessment of adsorber bed designs in waste-heat driven adsorption cooling systems for vehicle air conditioning and refrigeration

Adsorber beds create a pressure difference between the condenser and evaporator to drive the adsorbate (refrigerant) through the system. Adsorber beds should be heated and cooled by the heat transfer fluids to desorb and adsorb the adsorbate, respectively. Adsorber bed design studies in the literature have sought to improve the heat and mass transfer rates. However, the types of adsorber beds best suited to vehicle applications have not been conclusively identified.

In this study, important factors for evaluating the performance of an ACS were introduced and a comprehensive assessment was provided on the adsorber bed design of waste heat-driven ACS for vehicle A/C applications. Pertinent literature was reviewed and studies classified based on the type of adsorber bed, working pair, cooling capacity, cycle time, COP, SCP, and AAMR. The effects of adsorber bed design on the SCP, AAMR and COP were investigated to identify the best adsorber bed designs for vehicle A/C applications. The results showed that finned tube adsorber beds provided a better performance than other types of adsorber beds.

For further information, the reader is referred to Appendix C.

2.2.2. Impact of fin spacing on temperature distribution in adsorption cooling system for vehicle A/C applications

Finned tube adsorber beds showed the best performance compared to other types of adsorber beds. One way of establishing efficient heat transfer from a heat transfer fluid

to adsorbent particles is to experimentally measure the temperature distribution inside an adsorber bed. To our best knowledge, there was no experimental study available that showed the temperature distribution inside a finned tube adsorber bed to investigate the mechanisms of heat transfer to the adsorbent particles to establish optimum fin spacing.

In this study, the effects of fin spacing on the temperature distribution inside two finned tubed adsorber beds and a condenser/evaporator chamber were investigated experimentally. The AAMR was one of the main factors in the ACS for vehicle A/C applications that should be minimized. The main goal of this study was to select a finned tube adsorber bed with proper fin spacing and acceptable AAMR by measuring the temperature inside the adsorber bed. The results showed that proper fin spacing should not be more than twice the adsorbent particle diameter.

For further information, the reader is referred to Appendix D.

2.2.3. Effects of different adsorber bed designs on in-situ water uptake rate measurements of AQSOA FAM-Z02 for vehicle air conditioning applications

Beside heat transfer in an adsorber bed, mass transfer also has a key role on the performance of an ACS. Mass transfer in an adsorber bed is a function of adsorbent material, adsorber bed design, and operating conditions. The TGA is a well-known technique in which changes in mass of few milligrams of an adsorbent due to adsorption or desorption of adsorbate are measured over time at controlled temperatures and adsorbate pressures. In ACS applications, however, adsorption and desorption occur under large pressure jumps and non-isothermal conditions, making the operating conditions far from the ideal found in a TGA. Also, the effects of adsorber bed geometry, interparticle mass transfer resistances, and pressure drop do not present in a TGA. Due to these geometrical and operational constraints, the adsorbate uptake capability of an adsorbent material is reduced in ACS applications.

In this study, an experimental setup was designed and built to measure the adsorbate uptake rate of different adsorbent materials under typical operating conditions. AQSOA FAM-Z02 is an adsorbent material with high water uptake rate and low

regeneration temperature designed by Mitsubishi Chemical Ltd. To investigate the effects of different adsorber bed designs on the in-situ water uptake rate of AQSOA FAM-Z02, the adsorbent material was packed in two adsorber beds with different fin spacing and heat transfer surface areas. Using in-situ water uptake rate measurements, the maximum achievable SCP and COP delivered by an adsorber bed can be calculated before installation in an ACS testbed.

For further information, the reader is referred to Appendix E.

2.3. Adsorption Cooling System Design

2.3.1. Critical analysis of thermodynamic cycle modeling of adsorption cooling systems for light-duty vehicle air conditioning applications

In 1929, Hulse [56] built a commercial silica gel-sulphur dioxide ACS and installed it in a freight car refrigeration system to carry fish and meat all over the U.S. With the advent of compressors and emergence of VCRCs, ACS were forgotten for several decades. However, ACS have been reconsidered from 1990s due to VCRCs' high energy consumption, negative environmental impacts and stringent government emission regulations. Several types of large-scale ACS have been designed and built for commercial buildings where the weight and footprint of ACS were not the first priority. For light-duty vehicles, however, the ACS is still bulky and heavy.

To resolve these limitations, developing an accurate thermodynamic cycle model, that includes the heat and mass transfer phenomena in adsorber beds, and heat transfer inside an evaporator and a condenser, is the first step toward designing an ACS with optimum footprint and weight. Using such a thermodynamic model, the behavior of an ACS can be accurately predicted under various operating conditions. In this study, different thermodynamic models were compared and information about different working pairs was summarized. The nominated thermodynamic model was verified against two sets of experimental data available in the literature and, finally, effects of different parameters were studied on the SCP and COP of ACS. This thermodynamic model gives

the opportunity to study important design factors in ACS and properly size the main components of the system.

For further information, the reader is referred to Appendix F.

2.3.2. Performance analysis of a novel expansion valve and control valves designed for a waste heat-driven two-adsorber bed adsorption cooling system

The heat source and the heat sink connected to the adsorber beds continuously pump the heating and cooling fluids, and control valves direct them to the adsorber beds for adsorption and desorption. In a two-adsorber bed ACS, also, four more valves are required to direct the adsorbate (refrigerant) from the evaporator to the adsorber beds during adsorption and from the adsorber beds to the condenser during desorption. These control valves should automatically operate to generate continuous cooling inside the evaporator and also they should be light enough for vehicle A/C applications.

An ACS which uses water as the refrigerant operates under vacuum pressure. The expansion valve of such systems is different from what is available for conventional refrigeration cycles. There are different solutions for the expansion valve of an ACS. However, for vehicle A/C applications, this valve should have small footprint and be reliable.

In this study, two ideas were proposed for the expansion valve and control valves of an ACS for vehicle A/C applications to simplify the control system, and reduce the parasitic power consumption and the total mass of the valves. As a proof-of-concept demonstration, a two-adsorber bed silica gel/$CaCl_2$ ACS was built and equipped with these expansion and control valves. Parametric studies were performed to evaluate the functionality of the valves under different operating conditions. Also, the numerical results extracted from the thermodynamic cycle modeling developed in Section 2.3.1 were compared against the experimental data. Using the verified model, further modifications to improve the ACS performance were proposed.

For further information, the reader is referred to Appendix G.

2.3.3. Effects of capillary-assisted tubes with different fin geometries on the performance of a low-operating pressure evaporator for adsorption cooling systems

An ACS, which uses water as the refrigerant, operates at low pressure. Accumulation of liquid water in a low-operating pressure evaporator creates a water column which results in a static pressure difference between the liquid water-vapor interface and the bottom of the evaporator chamber. This static pressure changes the saturation pressure, and consequently, saturation temperature of water along the water column. As a result of water saturation temperature variations in the low-operating pressure evaporator, the cooling power generation of ACS reduces drastically. To have a uniform water saturation temperature, the static pressure of water in a low-operating pressure evaporator should be minimized. The performance of the ACS presented in Section 2.3.2 was limited by the evaporator design.

The proposed solution explored in this study was to use capillary-assisted tubes inside a flat evaporator. Five types of enhanced tubes with different fin geometries and a plain tube as a benchmark were tested under different operating conditions. The water column height was kept less than the tube diameter. Due to the capillary effect, a thin-film layer of water covered the whole surface of the tubes. As a result of thin-film evaporation, high heat transfer coefficients were achieved and the heat transfer from the chilled water circulated inside the tubes to the refrigerant was improved. By comparing the overall heat transfer coefficient of different capillary-assisted tubes, the best tube was selected to be installed in the evaporator.

For further information, the reader is referred to Appendix H.

2.3.4. Effects of adsorbent mass and number of adsorber beds on the performance of a waste-heat driven adsorption cooling system for vehicle air conditioning application

The last ACS setup was built based on the thermodynamic cycle modeling of ACS developed in Section 2.3.1, the adsorber bed selected from the in-situ mass measurements in Section 2.2.3, the control valves designed in Section 2.3.2, and the low-operating pressure evaporator with capillary-assisted tubes designed in Section 2.3.3. To

increase the SCP and COP of an ACS, the amount of adsorbent material should be properly selected. In this study, the effects of adsorbent mass and the number of adsorber beds on the SCP and COP of ACS were studied experimentally under different cycle times and operating conditions. The results showed that reducing the mass of adsorbent from 1.9 to 0.5 kg improved the SCP of one-adsorber bed ACS by 81%. Also, addition of a second adsorber bed to the one-adsorber bed ACS testbed showed that the SCP reached 150 W/kg of dry adsorbent and the COP improved by 47% at the baseline operating conditions. The results of this study shed light on the proper sizing of the ACS components and adsorbent mass to reach high SCP and COP, and reduce the overall mass of the system specifically for vehicle A/C applications.

For further information, the reader is referred to Appendix I. Also, practical design considerations in the ACS design packed with composite adsorbents are provided in Appendix K.

Chapter 3.

Conclusions and Future Work

In this Ph.D. program, the research began with adsorbate uptake rate modeling and thermal conductivity measurements of adsorbent materials. Adsorber beds with different geometries were designed and built, and the heat and mass transfer inside the adsorber beds was studied experimentally. Using the knowledge developed during this research program, different adsorption cooling systems were designed and built with successive improvements to the adsorber beds, evaporator, expansion valve, and control valves as described in this dissertation to achieve the target SCP of 150 W/kg of dry adsorbent.

3.1. Conclusions

The followings are the conclusions of this research:

- Development of an analytical model for the adsorbate uptake rate and mass diffusivity calculations
    - An analogy between the mass transfer and electrical circuits was introduced and developed based on a resistance-capacitance model for the adsorbate uptake rate of a spherical adsorbent material.
    - The analytical model was applicable for the entire range of mass transfer Biot numbers and could be used for non-equilibrium adsorbate uptake rate prediction in adsorption and desorption processes in an ACS.
    - Using the isothermal water uptake rate measured by a TGA under small pressure jumps and the model, the mass diffusivity of spherical silica gel particles was calculated.
- Measurements of the thermal conductivity of silica gel bound with PVP and its thermal contact resistance (TCR) with a metallic substrate
    - The TCR between silica gel-PVP and a copper plate and bulk thermal resistance of silica gel-PVP were measured.

- The two-thickness method was adopted to de-convolute the TCR between the silica gel-PVP and the copper plate from the bulk thermal resistance of the samples.

- The thermal conductivity of silica gel bound with PVP increased by 79% in comparison with that of loose silica gel particles.

- The TCR between the silica gel-PVP and a metallic substrate was up to 26% of the bulk resistance of the samples.

- Investigation of the effects of different adsorber bed designs on the performance of a waste heat-driven ACS

    - The SCP, AAMR, and COP were introduced as the main parameters to compare the performance of different ACS.

    - The ideal SCP of 350 W/kg of dry adsorbent and AAMR of less than one were considered as desired values for an ACS for vehicle A/C applications.

    - A comprehensive literature review was conducted on the performance of ACS with respect to their adsorber beds.

    - Finned tube adsorber bed design provided the best performance among the adsorber beds reported in the literature.

- Study of the effects of fin spacing on the temperature distribution in finned tube adsorber beds packed with 2-4 mm loose silica gel particles

    - For the adsorbent particles located at the center of the fins, the only route of heat transfer was through the fins, whereas for those located at the edges of the fins, the heat transfer was happened by the adsorbate and the fins.

    - The temperature gradient between the surface of a fin and the adsorbent particles was higher during the desorption process than that during the adsorption process.

    - The effects of fin spacing on temperature gradient between adsorbent particles were more significant under short cycle times (10 min) rather than long cycle times (25 min).

    - The analysis showed that the fin spacing had to be less than twice the adsorbent particle diameter to achieve an acceptable range for the temperature gradient between a fin and silica gel particles, and AAMR.

- Measurement of the in-situ water uptake rate of 2 mm AQSOA FAM-Z02 adsorbent packed in two different finned tube adsorber beds

    - Analyzing the pertinent literature showed that the in-situ adsorbate uptake rate mass measurements resulted in closer performance prediction for an ACS than those measured by a TGA.

    - Accurate in-situ water uptake rate measurements during adsorption-desorption cycles required the deconvolution of weight changes due to changes in the density of heat transfer fluids and the stiffness of the flexible hosing connected to the adsorber bed.

    - The results showed that the key features for an adsorber bed packed with 2 mm AQSOA FAM-Z02 particles were high heat transfer surface area and small fin spacing (2.5 mm).

    - An ideal SCP and COP of 112.9 W/kg of dry adsorbent and 0.34 were achieved at cycle time of 10 min, respectively.

- Critical analysis of different thermodynamic cycle modeling of ACS, the development of a fully-dynamic model and its validation with the experimental data reported in the literature

    - Different thermodynamic cycle models with respect to their accuracy, complexity and computation time were compared.

    - A fully-dynamic thermodynamic cycle model was developed and compared to two sets of experimental data reported in the literature.

    - A comprehensive parametric study was conducted on the SCP and COP of a 2-kW waste heat-driven ACS for light-duty vehicle A/C applications and results supported the following conclusions:

        - The SCP and COP of the ACS were maximized for the cycle times between 10-15 min and the adsorption to desorption time ratio of one.

        - The overall heat transfer conductance (UA) of the adsorber bed had the highest effect on the SCP, whereas the metal mass of the adsorber bed had the lowest effect on the SCP.

        - The results showed that the mass flow rates of heat transfer fluids had not considerable effects on the SCP and COP after some values.

        - To achieve the required cooling power, heat from both the engine coolant and exhaust gas were required for the regeneration of the adsorber beds.

- Novel designs for the expansion valve and control valves of a two-adsorber bed ACS

    - The replacement of electrically-actuated ball valves with four check valves and eight solenoid valves with an innovative configuration reduced the total mass of ACS by 10.5 kg and the power consumption of the control valves by 50%.

    - A check valve with cracking pressure of 3.5-7 kPa was proposed for the expansion valve.

    - The experimental results showed that the expansion valve and control valves operated effectively under different operating conditions.

    - The fully-dynamic thermodynamic cycle model was compared with the experimental data. The numerical model showed that increasing the adsorber bed overall heat transfer coefficient and heat transfer surface area could improve the SCP up to six times.

- Design and assembly of a low-operating pressure evaporator, and analysis of the effects of different types of capillary-assisted tubes on the evaporator performance

    - The TURBO-Chil® tube with continuous parallel fins, high fin height, and high number of fins (40 fins per inch) showed the best performance among five types of capillary-assisted tubes with high internal and external heat transfer surface areas, and a range of fin spacing (26 and 40 fins per inch).

    - The heat transfer conductance of the chilled water flowing inside the tubes limited the evaporator performance.

    - Increasing the chilled water mass flow rate from 2.5 to 15.3 kg/min (a 6.1 times increase) increased the total evaporation heat transfer rate and evaporator heat transfer coefficient by 20% and 110%, respectively.

- Study of the effects of adsorbent mass and the number of adsorber beds on the performance of a waste heat-driven ACS

    - With 1.9 kg FAM-Z02 in the adsorber bed, the evaporator limited the SCP of the one-adsorber bed ACS. Reducing the mass of adsorbent

to 0.5 kg increased the SCP by 82% and decreased the COP of the one-adsorber bed ACS by 38%.

- The thermal mass of evaporator reduced the SCP and COP of the one-adsorber bed ACS under short cycle times (8-20 min). Thus, a second adsorber bed was added to the one-adsorber bed ACS.

- The SCP and COP of the two-adsorbed bed ACS were always higher than those of the one-adsorber bed ACS. The SCP and COP of the two-adsorber bed ACS increased by 28% and 47% in comparison with those of one-adsorber bed ACS at cycle time of 20 min.

The last two-adsorber bed ACS experimental setup with enhanced performance was equipped with a finned tube adsorber bed with 2.5 mm fin spacing and 2.8 m^2 heat transfer surface area, a shell and tube condenser, and a low-operating pressure evaporator with capillary-assisted tubes. However, the SCP and COP of this system can be improved further.

3.2. Future Work

In the future, additional steps should be taken to increase the ACS performance including:

- Increasing the effectiveness of evaporator; potential solutions include the reduction of the diameter of capillary-assisted tubes from 19.05 mm (3/4”) to 12.7 mm (1/2”) and increasing the tube length from 1.5 m to 3.5 m,

- Elimination of the piping between different components of ACS to compact the system and minimize the pressure drop, and

- Reduction of the AQSOA FAM-Z02 particles diameter from 2 mm to 0.5-1 mm to enhance the adsorbent contact surface area with the adsorbate and increase the adsorbate uptake rate within short cycle times (8-20 min).

It is expected that these modifications significantly increase the SCP of the current ACS.

The adsorber beds in this Ph.D. research program were packed with loose adsorbent grains. Packing of adsorbent particles was a quick process with almost no difficulty. However, loose packing resulted in low contact area between the adsorbent

particles, and between the adsorbent particles and the metallic substrate. As a result, the rate of heat transfer from the heat transfer fluids to the adsorbent materials was limited. One method of increasing the heat transfer rate is to coat the adsorbent particles on the surface. Adsorbent coating process with enough durability under thermal stress and vibration is an active field of research in adsorber bed design.

When a compact ACS with high SCP is ready, it should be installed on a light-duty vehicle for further experiments. Interactions of the ACS with other vehicle components, such as the engine and radiator, under different driving cycles will be a rich, untouched field of research.

References

[1] Oliveira RG, Silveira V, Wang RZ. Experimental study of mass recovery adsorption cycles for ice making at low generation temperature. Appl Therm Eng 2006;26:303–11.

[2] Li TX, Wang RZ, Wang LW, Lu ZS, Chen CJ. Performance study of a high efficient multifunction heat pipe type adsorption ice making system with novel mass and heat recovery processes. Int J Therm Sci 2007;46:1267–74.

[3] Tamainot-Telto Z, Metcalf SJ, Critoph RE, Zhong Y, Thorpe R. Carbon–ammonia pairs for adsorption refrigeration applications: ice making, air conditioning and heat pumping. Int J Refrig 2009;32:1212–29.

[4] James SJ. Food refrigeration and thermal processing at Langford, UK: 32 years of research. Food Bioprod Process 1999;77.

[5] Smale NJ, Moureh J, Cortella G. A review of numerical models of airflow in refrigerated food applications. Int J Refrig 2006;29:911–30.

[6] Aneke M, Agnew B, Underwood C, Menkiti M. Thermodynamic analysis of alternative refrigeration cycles driven from waste heat in a food processing application. Int J Refrig 2012;35:1349–58.

[7] Critoph RE. An ammonia carbon solar refrigerator for vaccine cooling. Renew Energy 1994;5:502–8.

[8] Hammad M, Habali S. Design and performance study of a solar energy powered vaccine cabinet. Appl Therm Eng 2000;20:1785–98.

[9] Dawoud B. A hybrid solar-assisted adsorption cooling unit for vaccine storage. Renew Energy 2007;32:947–64.

[10] Restuccia G, Freni A, Maggio G. A zeolite-coated bed for air conditioning adsorption systems: parametric study of heat and mass transfer by dynamic simulation. Appl Therm Eng 2002;22:619–30.

[11] Jiangzhou S, Wang RZ, Lu YZ, Xu YX, Wu JY. Experimental investigations on adsorption air-conditioner used in internal-combustion locomotive driver-cabin. Appl Therm Eng 2002;22:1153–62.

[12] Tamainot-Telto Z, Metcalf SJ, Critoph RE. Novel compact sorption generators for car air conditioning. Int J Refrig 2009;32:727–33.

[13] Uçkan İ, Yılmaz T, Hürdoğan E, Büyükalaca O. Experimental investigation of a novel configuration of desiccant based evaporative air conditioning system. Energy Convers Manag 2013;65:606–15.

[14] Haaf S, Henrici H. Refrigeration Technology. Ullmann's Encycl. Ind. Chem., Wiley-VCH; 2002.

[15] Wang S. Handbook of Air Conditioning and Refrigeration. 2 edition. McGraw-Hill Professional; 2000.

[16] Farrington R, Rugh J. Impact of vehicle air-conditioning on fuel economy, tailpipe emissions, and electric vehicle range. Proceeding Earth Technol. Forum, Washington, D.C.: 2000.

[17] Hendricks TJ. Vehicle transient air conditioning analysis: Model development & system optimization investigations. National Renewable Energy Laboratory, NREL/TP-540-30715: 2001.

[18] Hendricks TJ. Optimization of vehicle air conditioning systems using transient air conditioning performance analysis. SAE Conf. Proc. P, 2001.

[19] Hendricks TJ. Multi-variable optimization of electrically-driven vehicle air conditioning systems using transient performance analysis. Proc. SAE Veh. Therm. Manag. Syst., 2003.

[20] Cengel YA, Boles MA. Thermodynamcis: An Engineering Approach. New York: McGraw-Hill; 2006.

[21] Kim DS, Infante Ferreira C a. Solar refrigeration options – a state-of-the-art review. Int J Refrig 2008;31:3–15.

[22] Karri M a., Thacher EF, Helenbrook BT. Exhaust energy conversion by thermoelectric generator: Two case studies. Energy Convers Manag 2011;52:1596–611.

[23] Meng JH, Wang XD, Zhang XX. Transient modeling and dynamic characteristics of thermoelectric cooler. Appl Energy 2013;108:340–8.

[24] Ewert MK, Agrella M, DeMonbrun D, Frahm J, Bergeron D., Berchowitz D. Experimental evaluation of a solar PV refrigerator with thermoelectric, Stirling, and vapour compression heat pumps. Proc. ASES Sol. 98 Conf., Albuquerque, USA: 1998.

[25] Global Cooling Inc. 2015. http://www.stirlingultracold.com/ (accessed January 1, 2015).

[26] Boatto P, Boccaletti C, Cerri G, Malvicino C. Internal combustion engine waste heat potential for an automotive absorption system of air conditioning Part 1: tests on the exhaust system of a spark-ignition engine. Proc I MECH E Part D J Automob Eng 2000;214:979–82.

[27] Boatto P, Boccaletti C, Cerri G, Malvicino C. Internal combustion engine waste heat potential for an automotive absorption system of air conditioning Part 2: The automotive absorption system. Proc Inst Mech Eng Part D J Automob Eng 2000;214:983–9.

[28] Christy C, Toossi R. Adsorption air-conditioning for containerships and vehicles. 2004.

[29] Abdullah MO, Tan IAW, Lim LS. Automobile adsorption air-conditioning system using oil palm biomass-based activated carbon: A review. Renew Sustain Energy Rev 2011;15:2061–72.

[30] Demir H, Mobedi M, Ülkü S. A review on adsorption heat pump: Problems and solutions. Renew Sustain Energy Rev 2008;12:2381–403.

[31] Wang RZ, Wu JY, Xu YX, Wang W. Performance researches and improvements on heat regenerative adsorption refrigerator and heat pump. Energy Convers Manag 2001;42:233–49.

[32] Poyelle F, Guilleminot JJ, Meunier F. Experimental tests and predictive model of an adsorptive air conditioning unit. Ind Eng Chem Res 1999;38:298–309.

[33] Tamainot-Telto Z, Critoph RE. Monolithic carbon for sorption refrigeration and heat pump applications. Appl Therm Eng 2001;21:37–52.

[34] Freni A, Tokarev MM, Restuccia G, Okunev AG, Aristov YI. Thermal conductivity of selective water sorbents under the working conditions of a sorption chiller. Appl Therm Eng 2002;22:1631–42.

[35] Sharafian A, Bahrami M. Adsorbate uptake and mass diffusivity of working pairs in adsorption cooling systems. Int J Heat Mass Transf 2013;59:262–71.

[36] Wojcik a. MW, Jansen JC, Maschmeyer T. Regarding pressure in the adsorber of an adsorption heat pump with thin synthesized zeolite layers on heat exchangers. Microporous Mesoporous Mater 2001;43:313–7.

[37] Saha BB, Akisawa A, Kashiwagi T. Solar/waste heat driven two-stage adsorption chiller : the prototype. Renew Energy 2001;23:93–101.

[38] De Boer R, Smeding SF, Grisel RJH. Development and testing of a sorbent filled heat exchanger for use in compact solid sorption cooling systems. Proceeding Int. sorption heat pump Conf., Denver, USA: 2005.

[39] Gregg SJ, Sing KSW. Adsorption, surface area, and porosity. 2 edition. Academic Press; 1982.

[40] De Saussure NT. No Title. NT Gilbert's Annu 1814;47:113–8.

[41] Favre PA. No Title. Comptes Rendus l'Académie Des Sci 1854;39:16.

[42] Sharafian A, Bahrami M. A quasi steady state model for adsorption cooling systems: Automotive applications. ASME 2012 6th Int. Conf. Energy Sustain. 10th Fuel Cell Sci. Eng. Technol. Conf., San Diego, CA, USA: 2012.

[43] Wang LW, Wang RZ, Lu ZS, Chen CJ, Wang K, Wu JY. The performance of two adsorption ice making test units using activated carbon and a carbon composite as adsorbents. Carbon N Y 2006;44:2671–80.

[44] Lu ZS, Wang RZ, Li TX, Wang LW, Chen CJ. Experimental investigation of a novel multifunction heat pipe solid sorption icemaker for fishing boats using CaCl2/activated carbon compound–ammonia. Int J Refrig 2007;30:76–85.

[45] Wang LW, Wang RZ, Xia ZZ, Wu JY. Studies on heat pipe type adsorption ice maker for fishing boats. Int J Refrig 2008;31:989–97.

[46] Askalany A a., Saha BB, Kariya K, Ismail IM, Salem M, Ali AHH, et al. Hybrid adsorption cooling systems–An overview. Renew Sustain Energy Rev 2012;16:5787–801.

[47] Fontana F. No Title. Mem Di Mat E Fis Della Soc Ital 1777;1:679.

[48] Scheele CW. No Title. Chem Obs Air Fire 1780:182.

[49] Mitscherlich E. No Title. Poggendorffs Ann 1843;59:94.

[50] Conner WC, Fraissard J. Fluid Transport in Nanoporous Materials. vol. 219. La Colle Sur Loup, France: Kluwer Academic Publishers; 2006.

[51] Bullock CE. Dehumidification of moist air by adiabatic adsorption. University of Minnesota, 1965.

[52] Nienberg JW. Modeling of desiccant performance for solar-desiccant-evaporative cooling. University of California, Los Angeles, USA, 1977.

[53] Pla-Barby FE, Vliet GC. Rotary bed solid desiccant drying: An analytical and experimental investigation. ASME/AIChE 18th Natinal Heat Transf. Conf., San Diego, CA, USA: 1979.

[54] Pesaran A a., Mills AF. Moisture transport in silica gel packed beds—I.Theoretical study. Int J Heat Mass Transf 1987;30:1037–49.

[55] Pesaran A a., Mills AF. Moisture transport in silica gel packed beds—II. Experimental study. Int J Heat Mass Transf 1987;30:1051–60.

[56] Hulse GE. Freight car refrigeration by an adsorption system employing silica gel. Refrig Eng 1929;17:41–54.

Appendix A.

Adsorbate uptake and mass diffusivity of working pairs in adsorption cooling systems

International Journal of Heat and Mass Transfer 59 (2013) 262–271

Contents lists available at SciVerse ScienceDirect

International Journal of Heat and Mass Transfer

journal homepage: www.elsevier.com/locate/ijhmt

Adsorbate uptake and mass diffusivity of working pairs in adsorption cooling systems

Amir Sharafian, Majid Bahrami *

Laboratory for Alternative Energy Conversion (LAEC), Mechatronic Systems Engineering, Simon Fraser University, BC, Canada V3T 0A3

ARTICLE INFO

Article history:
Received 11 October 2012
Received in revised form 8 December 2012
Accepted 8 December 2012
Available online 12 January 2013

Keywords:
Adsorbate uptake rate
Mass diffusivity
RC model
Solid-side resistance

ABSTRACT

A new closed-form model is proposed to determine the adsorbate uptake rate and the mass diffusivity of adsorbent–adsorbate pairs using experimental data of the gravimetric method based on the concept of Resistance–Capacitance (RC) analogy. The present model is verified against the available analytical solution for the adsorbate uptake for spherical micropore adsorbent particles with solid-side resistance on the surface of adsorbent. Furthermore, a new closed-form relationship for adsorbate uptake rate during the adsorption/desorption processes in adsorption cooling systems (ACS) is developed based on the linear driving force (LDF) model. The proposed adsorbate uptake rate relationship is applicable to the entire range of mass transfer Biot numbers and is as convenient-to-use as the LDF adsorbate uptake rate model. Moreover, the present model can be used to determine the mass diffusivity of spherical micropore adsorbent–adsorbate pairs with less computational time than that of the analytical series solution.

1. Introduction

Diffusion in micropore and mesopore materials is a dominant process in a wide range of applications such as gas separation and purification [1,2], petrochemical processes [3,4], industrial air pollution control [5], air dehumidification in air conditioning systems [6,7], food industries [8–10] and biomechanics [11,12]. An emerging application of micropore and mesopore materials is in adsorption cooling systems (ACS) for air conditioning in buildings and automotive industries which have received an immense attention in the recent years mainly due to higher fuel prices, energy shortages, and stringent governmental environmental/emission regulations [13–15]. Conventional vapor compression refrigeration cycle (VCRC), used in automotive air conditioning systems, consumes a considerable power of the engine [16] to derive the compressor, which significantly increases fuel consumption. A VCRC compressor can add up to 5–6 kW peak power draw on a vehicle's engine that is equivalent to the power required for a 1200-kg sedan cruising at 60 km/h [16]. In a conventional internal combustion engine (ICE), almost 40% of the total fuel energy is dissipated through the exhaust gas of the engine [16] in the form of waste heat. A portion of this waste heat is sufficient to run an ACS to meet the air-conditioning of a vehicle. Proper implementation of ACS in automobiles can significantly reduce the fuel consumption and minimize the carbon footprint of vehicles.

Working pairs in ACS are a combination of a sorbent material, called adsorbent, such as zeolite, silica gel and activated carbon; and a refrigerant, called adsorbate, such as water and methanol. These materials are environmentally friendly, non-toxic, non-corrosive, and inexpensive. Moreover, ACS are quiet and easy to maintain. As such, ACS are ideal candidates for conventional VCRC. However, commercialization of ACS faces major challenges; namely: (i) low specific cooling power (SCP) and (ii) poor coefficient of performance (COP) that result in heavy and bulky air-conditioning systems, which are not practical for automotive applications. Specific cooling power is the ratio of cooling power to the mass of dry adsorbent times the cycle time. Thus, SCP can be maximized by decreasing the adsorbent mass and/or reducing the cycle time. The origins of these limitations are low mass diffusivity and thermal conductivity of the adsorbent–adsorbate pairs. To improve SCP, the following approaches can be adopted:

- Improving thermal conductivity of working pairs by using new synthetic materials such as carbon nanotubes (CNT) embedded in zeolite [17].
- Increasing effective surface area of adsorber bed to increase the heat transfer rate between the exhaust gas (waste heat) and the adsorbent particles.
- Reducing cycle time by increasing adsorbate diffusion rate within the adsorbent particles during the adsorption/desorption processes.

* Corresponding author. Address: Mechatronic Systems Engineering, Simon Fraser University, #4300, 250-13450 102nd Avenue, Surrey, BC, Canada V3T0A3. Tel.: +1 (778) 782 8538; fax: +1 (778) 782 7514.
E-mail address: mbahrami@sfu.ca (M. Bahrami).

0017-9310/$ - see front matter © 2012 Elsevier Ltd. All rights reserved.
http://dx.doi.org/10.1016/j.ijheatmasstransfer.2012.12.019

Nomenclature

a	radius of adsorbent particle (m)
Bi_m	mass transfer Biot number, $h_m a/D$
c	adsorbate concentration (mol/m^3)
$\bar{c}$	total amount of adsorbate within the adsorbent particle (mol/m^3)
c^*	non-dimensional adsorbate concentration distribution
c_0	initial adsorbate concentration (mol/m^3)
c_∞	equilibrium adsorbate concentration, bulk concentration (mol/m^3)
C	electrical capacitance (F)
D	mass diffusivity (m^2/s)
D_{ij}	binary mass diffusion (m^2/s)
Fo	mass Fourier number, tD/a^2
h_m	mass transfer coefficient (m/s)
i	electric current (A)
m_t/m_∞	non-dimensional total amount of adsorbate within the adsorbent particle
r	radial coordinate
R	electrical resistance (Ω)
t	time (s)
V	electric potential (V)
$\forall$	volume (m^3)

Greek symbols

β_n	roots of characteristic equation, Eq. (13)
ε	porosity
η	non-dimensional coordinate, r/a
ω	adsorbate uptake, (kg adsorbate/kg dry adsorbent)
ω_{eq}	equilibrium adsorbate uptake, (kg adsorbate/kg dry adsorbent)

The main objective of this study, as a fundamental block to resolve the issues currently facing ACS, is to develop an in-depth understanding of adsorbate diffusion phenomenon within the adsorbent beds. To this end, a new compact closed-form relationship is developed to determine both adsorbate uptake rate and the mass diffusivity coefficient of adsorbent–adsorbate pairs. The proposed model is verified with experimental data collected from other sources.

2. Pertinent literature

There are several experimental techniques to measure the adsorbate uptake rate and the mass diffusivity reported in the literature, including, infrared spectroscopy, chromatography, nuclear magnetic resonance (NMR) and gravimetric methods, to name a few. More detail on measurement techniques are available elsewhere, e.g. [18]. A commonly used method is thermal gravimetric technique [18]. A thermogravimetric apparatus consists of an electrical furnace, crucible, and microbalance. The dried adsorbent particles are placed in the crucible which is located at the center of the furnace; it is also connected to the microbalance. To run a test, the furnace is set at a specific temperature and the adsorbate flows inside the furnace chamber. Simultaneously, the dried adsorbent particles start to adsorb adsorbate under the adsorption isotherm process and the microbalance measures the variation of the adsorbent mass over time. This method is a time-consuming method but there is almost no technical difficulty [19]. However, the measurement does not directly yield the mass diffusivity coefficient. To obtain the value of the mass diffusivity, an appropriate analytical adsorption model is needed for the analysis. By assuming a value for the mass diffusivity, a corresponding adsorbate uptake curve can be found using the analytical model. Then, it is compared to the experimental adsorbate uptake curve. The value of the mass diffusivity in the analytical model which provides the best match with the experimental result is taken as the true value of the mass diffusivity of the adsorbent–adsorbate pair at a specific pressure and temperature [19,20]. Accuracy of this method increases by developing a proper analytical model that can predict the mass diffusivity of adsorbent–adsorbate pairs under different operating conditions.

In general, the adsorbate uptake includes a number of physical processes, adsorbate transfer from the bulk gas to the adsorbent exterior surface, called gas-side resistance, diffusion of the adsorbate molecules to the pore surface of adsorbent particle, called solid-side resistance, and a resistance associated with the adsorption process itself. Often the last two resistances are more important than the first one [20–24]. Due to these factors, different mathematical models for the adsorption kinetics under different boundary conditions have been developed. Crank [25], and Karger and Ruthven [26] developed two different models for the concentration distribution of adsorbate within a spherical micropore adsorbent particle based on:

- Isothermal adsorption with constant concentration on the surface of adsorbent.
- Isothermal adsorption with solid-side resistance on the surface of adsorbent.

Later, Lee and Ruthven [27] developed a non-isothermal adsorption model with solid-side mass resistance for highly diffusive and/or reactive adsorbent–adsorbate pairs. Ni et al. [19] measured the water uptake rate of silica gel under different operating temperatures using thermogravimetric measurements. Then, they calculated the mass diffusivity of silica gel–water using two series-based models, namely the isothermal model with solid-side mass transfer resistance and the non-isothermal model with solid-side heat and mass transfer resistances. Their curve-fitted to the experimental data indicated that both models yield the same results because the tests were conducted under the adsorption isotherm process. Furthermore, Gurgel et al. [28] studied the water uptake rate of silica gel particles with three different diameters under the adsorption isotherm process. They used the isothermal model with no solid-side mass transfer resistance on the surface of adsorbent to predict the mass diffusivity of silica gel–water pair; however, their model failed to accurately predict the experimental data.

In many applications, adsorbate concentration boundary layer on the surface of adsorbent particle cannot be neglected and the solid-side resistance should be considered. For such problems, the solution of an isothermal process with the solid-side resistance is available in [26,27,29]. In case of negligible solid-side resistance, the solution converges to the isothermal adsorption with constant concentration on the surface of adsorbent.

Besides, several numerical simulations have been conducted by different researchers. Pesaran et al. [20] and San et al. [30,31] numerically investigated the effects of solid-side mass transfer resistance on the adsorption of water vapor by a packed bed of silica gel adsorbent. The challenges associated with the numerical simulation of adsorption phenomenon are its unsteady nature, time-consuming procedure, and iterative method to find the

accurate mass diffusivity of adsorbent–adsorbate pairs. Therefore, using an analytical model that can provide the mass diffusivity of adsorbent–adsorbate pairs in less time is preferred.

Most of the available analytical solutions in the open literature are based on series-solutions with non-linear characteristic equations to find both the adsorbate uptake rate by spherical micropore adsorbent particle and the mass diffusivity of adsorbent–adsorbate pairs. In the following sections, a new compact closed-form relationship has been developed based on the concept of resistance–capacitance (RC) model. The proposed relationship is compared with the available analytical solution, and later on, is applied to the experimental data reported by Ni et al. [19] and Gurgel et al. [28] to find the adsorbate uptake rate and the mass diffusivity of silica gel–water pair under various operating temperatures and silica gel sizes. The proposed model is general and can be applied to other adsorbent–adsorbate pairs such as activated carbon–methanol and zeolite–water.

3. Problem definition

In this study, a unit cell approach is adopted by considering a single spherical micropore adsorbent particle as the representative of the whole packed bed of adsorbent particles. The unit cell (or basic cell) is the smallest volume, which can represent characteristics of the entire microstructure [32]. Fig. 1 shows a schematic of a spherical micropore adsorbent particle with the solid-side resistance on the surface of the adsorbent.

To simplify the analysis, it is assumed that the initial adsorbate concentration distribution within the adsorbent particle is uniform, c_0, and is in equilibrium with the gaseous phase adsorbate. A sudden change in the concentration of gaseous adsorbate leads to adsorbate diffusion through/from the adsorbent particle vs. time. In this study, it is assumed that:

- Adsorbate uptake rate is controlled by the diffusion mass transfer.
- Constant temperature (isothermal) process during the adsorption/desorption time.
- Constant mass diffusivity [33].
- Solid-side resistance on the surface of spherical adsorbent.
- Radial diffusion of adsorbate within the adsorbent.

4. Mathematical model

Based on the assumptions made in Section 3, the mass balance for a single spherical adsorbent particle in spherical coordinate system can be expressed as follows [25,34]:

$$\frac{\partial c}{\partial t} = \frac{D}{r^2}\frac{\partial}{\partial r}\left(r^2\frac{\partial c}{\partial r}\right) \tag{1}$$

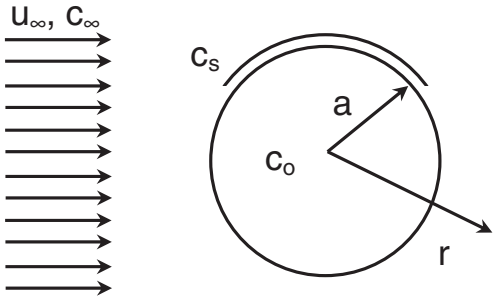

Fig. 1. A schematic of micropore adsorbent particle with solid-side resistance.

For a sudden change in the adsorbate concentration around the adsorbent particle, initial and boundary conditions are:

$$t = 0, \quad c = c_0 \tag{2}$$

$$r = 0, \quad \left.\frac{\partial c}{\partial r}\right|_{r=0} = 0 \tag{3}$$

$$r = a, \quad h_m(c_\infty - c_s) = D\left.\frac{\partial c}{\partial r}\right|_{r=a} \tag{4}$$

The total amount of adsorbate uptake by the spherical adsorbent particle is:

$$\bar{c}(t) = \frac{3}{a^3}\int_0^a cr^2 dr \tag{5}$$

Using the following variables Eqs. (1)–(5) can be non-dimensionalized.

$$c^* = \frac{c - c_0}{c_\infty - c_0}, \quad \eta = \frac{r}{a}, \quad Fo = \frac{tD}{a^2}, \quad Bi_m = \frac{h_m a}{D} \tag{6}$$

where Fo and Bi_m are the mass Fourier number and the mass transfer Biot number, respectively. Note that Fo is the ratio of the diffusion mass transfer to the rate of mass storage, and Bi_m is the ratio of the convective to the diffusive mass transfer within the solid body. Bi_m is generally defined for the transient mass transfer. Eqs. (7)–(10) show the non-dimensional governing equation as well as initial and boundary conditions.

$$\frac{\partial c^*}{\partial Fo} = \frac{1}{\eta^2}\frac{\partial}{\partial \eta}\left(\eta^2\frac{\partial c^*}{\partial \eta}\right) \tag{7}$$

$$Fo = 0, \quad c^* = 0 \tag{8}$$

$$\eta = 0, \quad \left.\frac{\partial c^*}{\partial \eta}\right|_{\eta=0} = 0 \tag{9}$$

$$\eta = 1, \quad Bi_m(1 - c_s^*) = \left.\frac{\partial c^*}{\partial \eta}\right|_{\eta=1} \tag{10}$$

The non-dimensional total amount of adsorbate uptake by the adsorbent particle is:

$$\frac{m_t}{m_\infty} = \frac{\bar{c} - c_0}{c_\infty - c_0} = 3\int_0^1 c^*\eta^2 d\eta \tag{11}$$

where m_t and m_∞ are the adsorbed mass of adsorbate at time t and $t \to \infty$, respectively.

Crank [25] and Ruthven et al. [26,29] solved Eq. (7) by method of separation of variables under the same initial and boundary conditions defined in Eqs. (8)–(10). Eq. (12) gives the concentration distribution within the spherical adsorbent particle [25–27,29].

$$c^* = \frac{2Bi_m}{\eta}\sum_{n=1}^{\infty}\frac{\exp(-\beta_n^2 Fo)}{\beta_n^2 + Bi_m(Bi_m - 1)}\frac{\sin(\beta_n\eta)}{\sin(\beta_n)} \tag{12}$$

where β_n is the roots of Eq. (13).

$$\beta_n\cot(\beta_n) + Bi_m - 1 = 0 \tag{13}$$

The total amount of adsorbate uptake by the spherical adsorbent particle is calculated as follows:

$$\frac{m_t}{m_\infty} = 1 - \sum_{n=1}^{\infty}\frac{6Bi_m^2\exp(-\beta_n^2 Fo)}{\beta_n^2(\beta_n^2 + Bi_m(Bi_m - 1))} \tag{14}$$

The series solution in Eq. (12) has two asymptotes,

- $Bi_m \to 0$ (no diffusive resistance inside the adsorbent, i.e., lumped capacitance),
- $Bi_m \to \infty$ (no solid-side resistance on the surface of adsorbent).

Table 1
Roots of Eq. (13) for different mass transfer Biot numbers.

Roots of Eq. (13)	Mass transfer Biot number, Bi_m							
	0	0.1	0.5	1	2	5	10	∞
β_1	0	0.5423	1.1656	$\pi/2$	2.0287	2.5704	2.8363	π
β_2	4.4934	4.5157	4.6042	$3\pi/2$	4.9132	5.3540	5.7172	2π
β_3	7.7253	7.7382	7.7899	$5\pi/2$	7.9786	8.3029	8.6587	3π
β_4	10.9041	10.9133	10.9499	$7\pi/2$	11.0855	11.3348	11.6532	4π
β_5	14.0662	14.0733	14.1017	$9\pi/2$	14.2074	14.4079	14.6869	5π
β_6	17.2208	17.2266	17.2498	$11\pi/2$	17.3364	17.5034	17.7480	6π
β_7	20.3713	20.3762	20.3958	$13\pi/2$	20.4692	20.6120	20.8282	7π
β_8	23.5195	23.5237	23.5407	$15\pi/2$	23.6043	23.7289	23.9218	8π
β_9	26.6661	26.6698	26.6848	$17\pi/2$	26.7409	26.8514	27.0250	9π
β_{10}	29.8116	29.8149	29.8284	$19\pi/2$	29.8786	29.9778	30.1353	10π

In the limiting case of $Bi_m \to 0$ (lumped capacitance model), the resistance to diffusion within the solid is much less than the resistance to convective mass transfer from the solid-side resistance. Therefore, the assumption of a uniform concentration distribution within the spherical adsorbent particle is reasonable [35]. In this case, β_n is small and the first term in the series solution, Eq. (12), would suffice for calculations [26,29]. Eqs. (15)–(18) show the solution, where $Bi_m \to 0$:

$$\cot(\beta_1) \approx \frac{1}{\beta_1} - \frac{\beta_1}{3} - \frac{\beta_1^3}{45} - \dots \tag{15}$$

$$\beta_1 \cot(\beta_1) - 1 \approx -\frac{\beta_1^2}{3} = -Bi_m \quad \Rightarrow \quad \beta_1^2 = 3Bi_m \tag{16}$$

$$c^* = \exp(-3Bi_m Fo) \tag{17}$$

$$\frac{m_t}{m_\infty} = 1 - \exp(-3Bi_m Fo) \tag{18}$$

In the limiting case of $Bi_m \to \infty$ (no solid-side resistance on the surface of adsorbent), the solution yields to the solution of isothermal adsorption with constant concentration on the surface of the adsorbent particle. Eq. (19) gives the adsorbate concentration distribution within the spherical adsorbent particle at the limit, where $Bi_m \to \infty$:

$$c^* = 1 + \frac{2}{\pi\eta}\sum_{n=1}^{\infty}\frac{(-1)^n}{n}\exp(-n^2\pi^2 Fo)\sin(n\pi\eta) \tag{19}$$

and the total amount of adsorbate uptake by the spherical adsorbent particle for $Bi_m \to \infty$ is:

$$\frac{m_t}{m_\infty} = 1 - \frac{6}{\pi^2}\sum_{n=1}^{\infty}\frac{\exp(-n^2\pi^2 Fo)}{n^2} \tag{20}$$

Roots of Eq. (13) for the first 10 terms of the series solution, Eq. (12), are tabulated in Table 1 for different mass transfer Biot numbers.

The total amount of adsorbate uptake by the spherical adsorbent particle, Eq. (14), vs. Fo number is shown in Fig. 2. As shown in Fig. 2, the adsorbate uptake rate increases by increasing Bi_m at constant Fo.

In addition, Fig. 2 indicates the effects of the solid-side resistance on the amount of adsorbate uptake. In case of no solid-side resistance on the surface of adsorbent, $Bi_m \to \infty$, amount of adsorbate uptake is much higher than that of the high solid-side resistance cases, $Bi_m \to 0$.

The shown values in Fig. 2 are calculated using the first 10 terms of the series solution, Eq. (14). As mentioned in Section 2, finding the mass diffusivity of adsorbent–adsorbate pair by the gravimetric method is an iterative and time consuming procedure. One way to simplify this procedure is to truncate the series solution, Eq. (14). Fig. 3 shows the effect of truncating the series solution, Eq. (14), on the adsorbate uptake curve for different Bi_m.

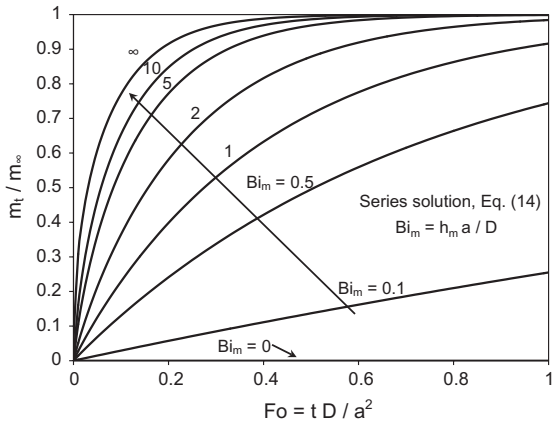

Fig. 2. Total amount of adsorbate uptake vs. mass Fourier number, Eq. (14).

Fig. 3 clearly indicates that by increasing Bi_m, the effect of number of terms in the series solution, Eq. (14), on the calculated adsorbate uptake becomes more important. The maximum relative difference between the adsorbate uptake curves calculated by the limited number of terms in the series solution, Eq. (14), with respect to the first 10 terms of the series solution is summarized in Table 2.

As shown in Table 2, having a closed-form solution for different Bi_m with only the first few terms of the series solution is not accurate; the first 10 terms of series solution is considered in all calculations.

5. Proposed compact closed-form relationship

As discussed in Section 4, the analytical adsorbate uptake calculated by the series solution, Eq. (14), cannot be easily used for the entire range of Bi_m, see Fig. 3. Eq. (21) shows the classical linear driving force (LDF) solution proposed by Glueckauf [36] which is one of the classical solutions used in adsorbate uptake modeling.

$$\frac{m_t}{m_\infty} = 1 - \exp(-15Fo) \tag{21}$$

Eq. (21) corresponds to Eq. (20) which is derived for $Bi_m \to \infty$ with an average relative difference of 1.34%. Eq. (21) is widely used in prediction of both adsorbate uptake rate by the adsorbent

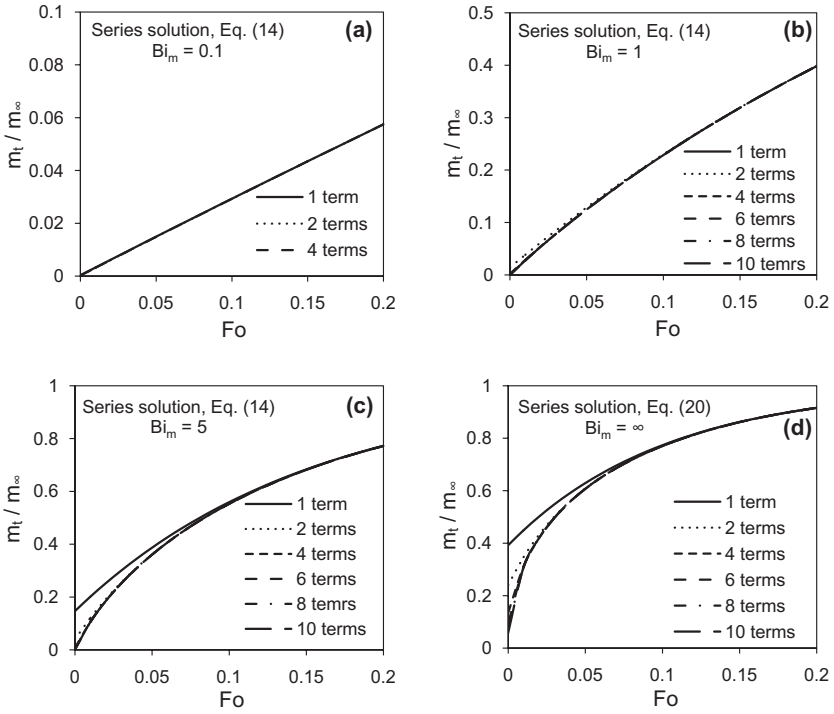

Fig. 3. Effect of truncating the series solution on the adsorbate uptake curve for different Bi_m.

Table 2
Maximum relative difference between the adsorbate uptake curves calculated by finite number of terms of the series solution, Eq. (14), compared with the first 10 terms.

No. of terms in Eq. (14)	Mass transfer Biot number, Bi_m			
	0.1	1	5	∞
1	4.1%	38.7%	90.6%	45.6%
2	0.36%	3.6%	14.14%	12.4%
4	2.5×10^{-3}%	0.09%	0.46%	0.86%
6	2.0×10^{-4}%	2.2×10^{-3}%	0.01%	0.04%
8	3.4×10^{-6}%	3.8×10^{-5}%	2.2×10^{-4}%	9.2×10^{-4}%

particle and the mass diffusivity of adsorbent–adsorbate pairs [15,37–39]. However, its application range is limited to $Bi_m \to \infty$. Moreover, it is not valid for small mass transfer Biot numbers [20].

A careful observation of the adsorbate uptake in spherical adsorbent particle, shown in Fig. 2, reveals similarities with charging of an electrical capacitor. Therefore, we propose a solution for the mass transfer using the solution of the corresponding electrical circuit. The analogous parameters between the heat/mass transfer and the electrical circuit are summarized in Table 3.

Diffusion in micropore materials can be assumed as a quasi-steady state process. As a result, one can use a resistance–capacitance (RC) model to simulate the charging of a spherical micropore adsorbent particle. Shown in Fig. 4 is a simple charging circuit of a capacitor and an equivalent electrical circuit for the adsorbate uptake by the spherical adsorbent particle based on the analogy between the mass transfer and the electrical circuit.

The charging behavior of the capacitor shown in Fig. 4a is [40]:

$$\frac{V_{\text{capacitor}}(t)}{V_0} = 1 - \exp\left(-\frac{t}{\text{RC}}\right) \tag{22}$$

Table 3
Analogous parameters between heat/mass transfer and electrical circuit.

	Mass transfer	Heat transfer	Electrical circuit
Potential	Δc (mol/m^3)	ΔT (K)	V (V)
Flux	J'' (mol/m^{2}s)	q'' (W/m^2)	i (A)
Resistance	$\frac{1}{h_m \varepsilon A}, \frac{a}{D \varepsilon A}$ (s/m^3)	$\frac{1}{hA}, \frac{a}{kA}$ (K/W)	R (Ω)
Capacitance	$\varepsilon \forall$(m^3)	mc_p (J/K)	C (F)

In the same way, the adsorbate uptake by the spherical micropore adsorbent particle corresponding to the electrical circuit is shown in Fig. 4b, where C is the mass capacitance, R_1 is the solid-side resistance, and R_2 is the diffusive resistance within the spherical micropore adsorbent particle, respectively.

With reference to Table 3, the mass capacitance of a spherical micropore adsorbent particle is:

$$C = \frac{4}{3}\pi \varepsilon a^3 \tag{23}$$

where, ε and a are the porosity and the radius of the micropore adsorbent particle, respectively. Moreover, the solid-side resistance, R_1, and the diffusive resistance within the spherical micropore adsorbent particle, R_2, are shown in Table 4.

α in the diffusive resistance, Table 4, is a constant and will be calculated by using the linear driving force (LDF) model. The total resistance can be found by summation of the resistances, see Eq. (24).

$$R = R_1 + R_2 \tag{24}$$

Eq. (25) shows the simplified multiplication of the mass capacitance, Eq. (23), and the total resistance, Eq. (24).

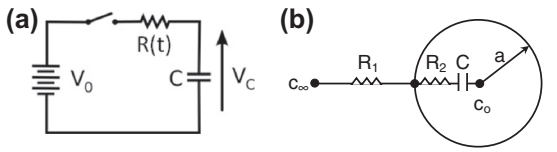

Fig. 4. (a) A simple resistor–capacitor circuit to charge a capacitor [40] (b) Equivalent electrical circuit for the adsorbate uptake by the spherical adsorbent particle.

Table 4
Analogy between mass transfer resistance and electrical resistance.

Resistance	Mass transfer (s/m^3)	Electrical circuit
Solid-side resistance	$1/(4\pi\varepsilon a^2 h_m)$	R
Diffusive resistance	$1/(4\pi\varepsilon\alpha a D)$	R_2

$$RC = \frac{1.0 + \frac{h_m a}{\alpha D}}{3\frac{h_m}{a}} \tag{25}$$

By substituting Eq. (25) in Eq. (22) and using the analogy between the mass transfer and the electrical circuit, the final RC model solution for charging a spherical adsorbent particle becomes:

$$\frac{m_t}{m_\infty} = 1 - \exp\left(-\frac{3\frac{h_m t}{a}}{1.0 + \frac{h_m a}{\alpha D}}\right) \tag{26}$$

Eq. (26) can be further simplified by substituting the non-dimensional parameters defined in Eq. (6). Thus, the total amount of adsorbate uptake by a spherical adsorbent particle becomes:

$$\frac{m_t}{m_\infty} = 1 - \exp\left(-\frac{3Bi_m Fo}{1.0 + \frac{Bi_m}{\alpha}}\right) \tag{27}$$

Eq. (27) has two asymptotes quite similar to those of Eq. (14). In the limiting case of $Bi_m \to 0$ (lumped capacitance model), Eq. (27) yields the exact same result of Eq. (18). In the limiting case of

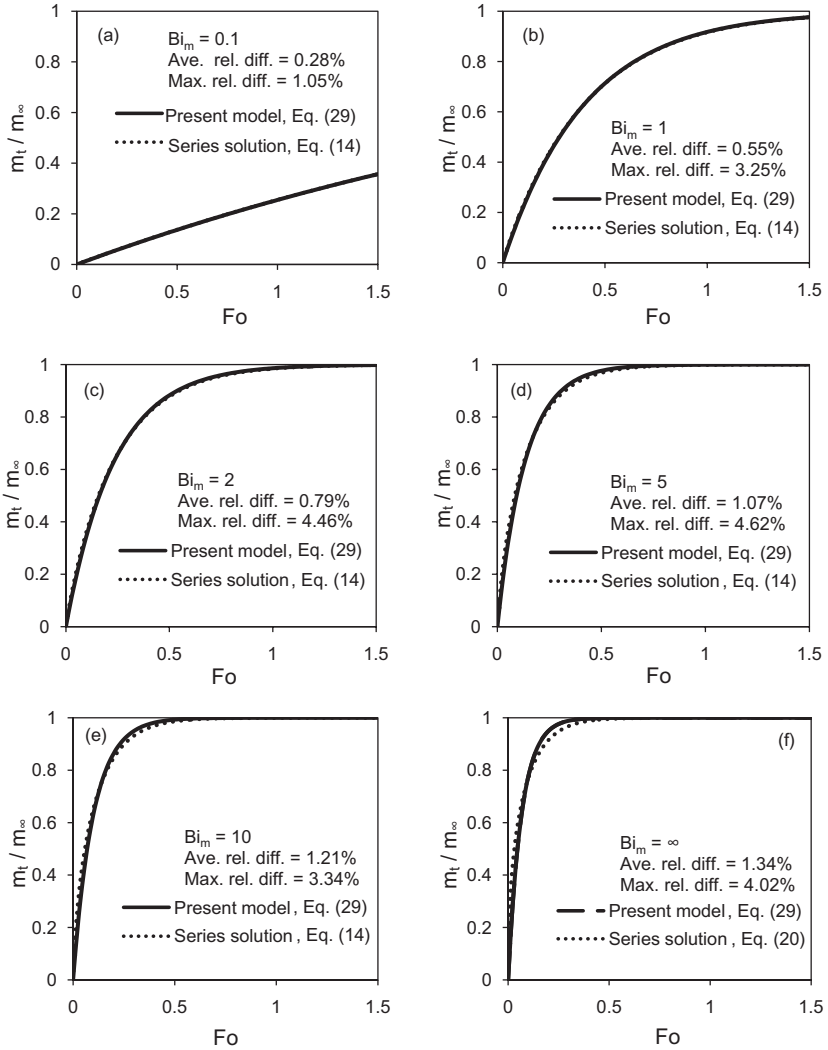

Fig. 5. Comparison between the present compact model and the series solution for (a) $Bi_m = 0.1$, (b) $Bi_m = 1$, (c) $Bi_m = 2$, (d) $Bi_m = 5$, (e) $Bi_m = 10$, and (f) $Bi_m \to \infty$.

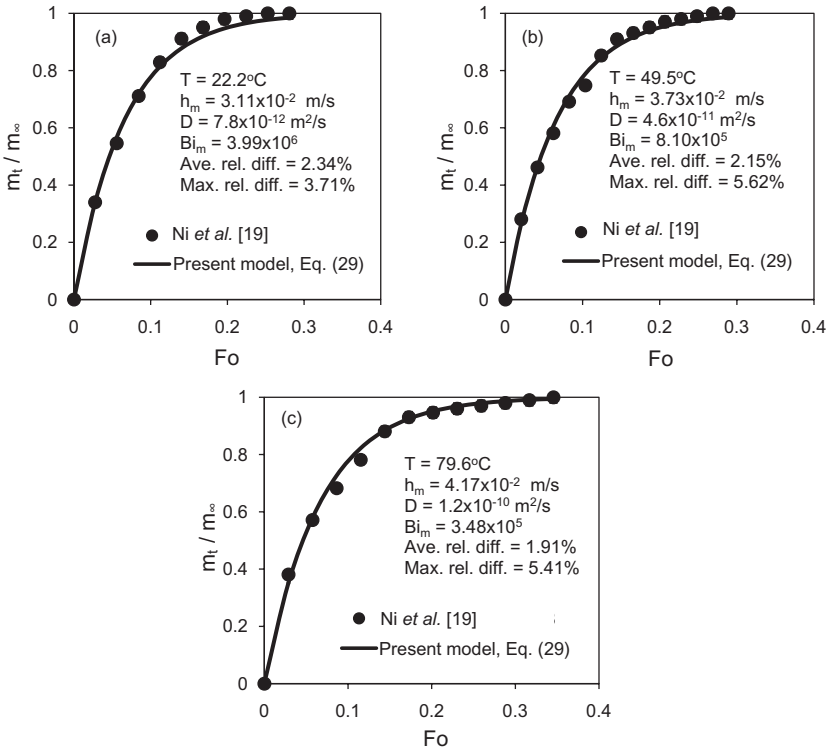

Fig. 6. Total amount of water uptake by 2 mm silica gel adsorbent particles at temperatures of 22.2, 49.5 and 79.6 °C.

$Bi_m \to \infty$ (no solid-side resistance on the surface of adsorbent), Eq. (27) yields Eq. (28) which should be equivalent to the linear driving force (LDF) model, i.e., Eq. (21).

$$\frac{m_t}{m_\infty} = 1 - \exp(-3\alpha Fo) \tag{28}$$

As a result, α in Eq. (28) should be equal to five. Hence, the final closed-form relationship for the adsorbate uptake by the spherical micropore adsorbent particle for the entire range of mass transfer Biot numbers is:

$$\frac{m_t}{m_\infty} = 1 - \exp\left(-\frac{3Bi_m Fo}{1.0 + 0.2Bi_m}\right) \tag{29}$$

A comparison between the present model, Eq. (29), and the analytical series solution for different values of Bi_m are presented in Fig. 5. It can be seen that the present model has a good agreement with the analytical series solution for the entire range of mass transfer Biot numbers. The average relative difference between the present model and the analytical series solution varies between 0% and 1.34% for different Bi_m. It should be mentioned that the maximum relative difference in all cases are reported for $Fo > 0.1$.

To find the mass diffusivity of the adsorbent–adsorbate pairs by using experimental data of the gravimetric method, the mass transfer coefficient, h_m, should be known. To this end, an analogy between heat and mass transfer can be established under specific conditions, commonly referred to as Chilton–Colburn J-factor analogy [41]. To establish a valid heat–mass convection analogy, the mass flux should be low such that the mass transfer between the fluid and the surface does not affect the flow velocity [33]. In case of diffusion within the micropore materials, the low mass flux process assumption is valid and, as a result, the analogy between the convective heat and mass transfer is reasonable. Thus, Eq. (30) developed for the convective heat transfer around a spherical particle, can be applied to convective mass transfer around a spherical micropore particle, Eq. (31) [42].

$$Nu = \frac{h(2a)}{k} = 2.0 + 0.6\mathrm{Re}^{\frac{1}{2}}\mathrm{Pr}^{\frac{1}{3}} \quad 0 \leqslant \mathrm{Re} < 200, \quad 0 \leqslant \mathrm{Pr} < 250 \tag{30}$$

$$Sh = \frac{h_m(2a)}{D_{ij}} = 2.0 + 0.6\mathrm{Re}^{\frac{1}{2}}Sc^{\frac{1}{3}} \quad 0 \leqslant \mathrm{Re} < 200, \quad 0 \leqslant Sc < 250 \tag{31}$$

where Sh is the Sherwood number, Re is the Reynolds number based on the particle diameter and Sc is the Schmidt number which is given by Eq. (32), respectively.

$$Sc = \frac{v}{D_{ij}} \tag{32}$$

where D_{ij} is the binary mass diffusivity of ideal gas mixture. Eq. (33) gives the binary mass diffusivity of water vapor in the air [43].

$$D_{\mathrm{H_2O-air}}(T,P) = 1.87 \times 10^{-10}\frac{T^{2.072}}{P} \quad \left(\frac{m^2}{s}\right) \quad 280K \leqslant T < 450K \tag{33}$$

where P is the total pressure in atmosphere and T is the mixture temperature in K, respectively. The Schmidt number for diffusion of water vapor in the air is about 0.6 [35]. At the end, the mass transfer coefficient, h_m, is given by Eq. (34).

$$h_m = D_{ij}(2.0 + 0.6\mathrm{Re}^{\frac{1}{2}}Sc^{\frac{1}{3}})/(2a) \quad (34)$$

There is no relationship to calculate the mass transfer Biot number directly. Hence, a value for the mass diffusivity should be found based on the experimental data. Accordingly, the mass transfer Biot number can be found using Eqs. (6) and (34).

$$Bi_m = D_{ij}(2.0 + 0.6\mathrm{Re}^{\frac{1}{2}}Sc^{\frac{1}{3}})/(2D) \quad (35)$$

6. Results and discussion

The proposed closed-form relationship is a general transient mass diffusion model applicable to the entire range of Bi_m and can be used in a wide range of applications to predict the transient adsorption/desorption processes in adsorption cooling systems (ACS) and to calculate the mass diffusivity of micropore adsorbent–adsorbate pairs.

6.1. Non-equilibrium adsorbate uptake in ACS

One of the applications of the present model, Eq. (29), is to predict the total amount of adsorbate uptake during the adsorption/desorption processes. The non-equilibrium amount of adsorbate uptake during the adsorption/desorption processes is mainly expressed by ω which is the ratio of mass of adsorbate to the mass of dry adsorbent [15,37–39]. To make the present model, Eq. (29), compatible to this definition, Eq. (36) is introduced.

$$\frac{m_t}{m_\infty} = \frac{m_t/m_{\text{dry adsorbent}}}{m_\infty/m_{\text{dry adsorbent}}} = \frac{\omega}{\omega_{eq}} = 1 - \exp\left(-\frac{3Bi_mFo}{1.0 + 0.2Bi_m}\right) \quad (36)$$

where ω_{eq} is the equilibrium adsorbate uptake at specific temperature and pressure. To implement Eq. (36) in the dynamic modeling of ACS thermodynamic cycle, adsorbate uptake rate is required. Eq. (37) gives the adsorption uptake rate by differentiating Eq. (36) with respect to time.

$$\frac{d\omega}{dt} = \frac{3Bi_m}{1.0 + 0.2Bi_m}\frac{D}{a^2}(\omega_{eq} - \omega) \quad (37)$$

Similarly, the adsorbate uptake rate based on the LDF model, Eq. (21), is given by Eq. (38) that is commonly used in dynamic modeling of ACS thermodynamic cycles and is valid for $Bi_m \to \infty$ (no solid-side resistance on the surface of adsorbent) [15,37–39].

$$\frac{d\omega}{dt} = \frac{15D}{a^2}(\omega_{eq} - \omega) \quad (38)$$

It is noteworthy that the proposed adsorbate uptake rate, Eq. (37), is as convenient-to-use as the LDF adsorbate uptake rate, Eq. (38); also it is applicable to the entire range of mass transfer Biot numbers. Eq. (37) can be easily applied to dynamic modeling of ACS thermodynamic cycles for different mass transfer Biot numbers.

6.2. Calculation of mass diffusivity of spherical micropore adsorbent–adsorbate pair

The other application of the present model, Eq. (29), is to find the mass diffusivity of adsorbent–adsorbate pairs in ACS applications. In this study, the experimental data of water uptake by silica gel particles reported by Ni et al. [19] and Gurgel et al. [28] are used to find the mass diffusivity of silica gel–water pair by the present model, Eq. (29).

Ni et al. [19], used a thermal gravimetrical apparatus to measure the total water uptake (adsorbate) in a 2 mm silica gel

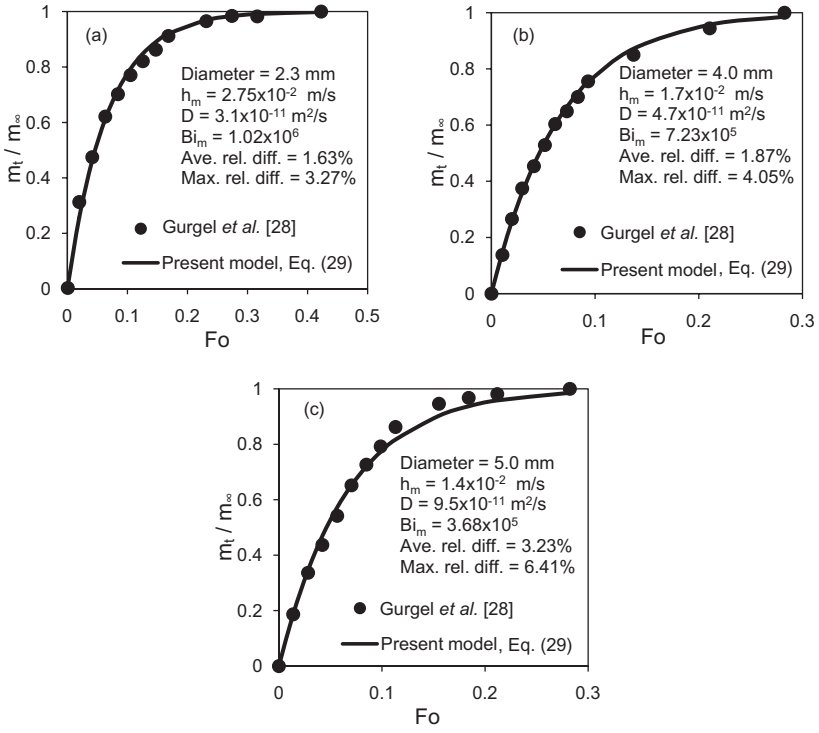

Fig. 7. Total amount of water uptake by silica gel adsorbent particles with diameter of (a) 2.3 mm, (b) 4.0 mm, and (c) 5.0 mm.

adsorbent particles under atmospheric pressure and different operating temperatures. The silica gel particles were placed far from the others with enough spacing to minimize effects of the interaction among them. The moist air average velocity in the experimental work of [19] was 9.3×10^{-3} m/s and the maximum uncertainty for the mass diffusivity was 25%.

Shown in Fig. 6 is the total amount of water uptake by the silica gel adsorbent particles in operating temperatures of 22.2, 49.5 and 79.6 °C.

Fig. 6 shows that the water uptake curve calculated by the present model is in excellent agreement with the experimental data of [19] under the assumption of constant specific mass diffusivity. As it can be seen in Fig. 6, by increasing the operating temperature, the mass transfer coefficient, h_m, and the mass diffusivity, D, of silica gel–water pair increases while the mass transfer Biot number decreases, which is mainly due to a higher increase in the mass diffusivity than the mass transfer coefficient.

The present model, also, is applied to determine the mass diffusivity of the working pair in the experimental data of Gurgel et al. [28] for three different sizes of silica gel–water pairs at a constant temperature of 22 °C and atmospheric pressure. The uncertainty analysis and the moist air average velocity in the experimental work of Gurgel et al. [28] were not reported. To perform the analysis, the same average velocity of 9.3×10^{-3} m/s reported by Ni et al. [19] is used in the calculations. Gurgel et al. [28] used the model of adsorbate uptake with constant concentration on the surface of adsorbent. Fig. 7 shows the water uptake curves produced by the present model, Eq. (29), for spherical silica gel adsorbent particles with diameters of 2.3, 4.0 and 5.0 mm at temperature of 22 °C [28].

As shown in Fig. 7, the water uptake curves calculated by the present model under the constant mass diffusivity have a good agreement with the experimental data reported by Gurgel et al. [28]. The maximum and average relative difference between the present model and the experimental data are 3.3% and 1.6% for 2.3 mm silica gel particle, 4.0% and 1.9% for 4.0 mm silica gel particle and 7.2% and 3.0% for 5.0 mm silica gel particle.

7. Summary and conclusions

In this study the adsorbate diffusion within the spherical micropore adsorbent particle with the solid-side resistance on the surface of adsorbent was investigated. Using an analogy between the mass transfer and electrical circuits, a resistance–capacitance (RC) compact model has been introduced to simulate behavior of adsorbate uptake by spherical micropore adsorbent particles. Calculated adsorbate uptake curves by the proposed model, Eq. (29), and the series solution, Eq. (14), showed a good agreement. The proposed model was also used to determine both adsorbate uptake rate and the mass diffusivity coefficient of adsorbent–adsorbate pairs based on the measured adsorbate uptake curves by Ni et al. [19] and Gurgel et al. [28].

The following are the highlights of the present study:

- The proposed new model has a good agreement with the analytical series solution with an average relative difference of 1.34% for the entire range of mass transfer Biot numbers.
- Non-equilibrium adsorbate uptake rate was proposed for calculation of uptake rate during the adsorption/desorption processes in ACS for different values of mass transfer Biot numbers.
- The proposed RC-based model is able to determine the mass diffusivity of spherical micropore adsorbent–adsorbate pairs using a compact relationship compared to the existing analytical series solution.

Acknowledgments

The authors gratefully acknowledge the financial support of the Natural Sciences and Engineering Research Council of Canada (NSERC) through the Automotive Partnership Canada Grant No. APCPJ 401826-10.

References

[1] J. Caro, Diffusion in porous functional materials: Zeolite gas separation membranes, proton exchange membrane fuel cells, dye sensitized solar cells, Micropor. Mesopor. Mat. 125 (2009) 79–84.
[2] X. Yin, J. Wang, N. Chu, J. Yang, J. Lu, Y. Zhang, D. Yin, Zeolite L/carbon nanocomposite membranes on the porous alumina tubes and their gas separation properties, J. Membrane Sci. 348 (2010) 181–189.
[3] S.S. Kapdi, V.K. Vijay, S.K. Rajesh, R. Prasad, Biogas scrubbing, compression and storage: perspective and prospectus in Indian context, Renew. Energy 30 (8) (2005) 1195–1202.
[4] J.A. Ritter, A.D. Ebner, State-of-the-art adsorption and membrane separation processes for hydrogen production in the chemical and petrochemical industries, Separ. Sci. Technol. 42 (6) (2007) 1123–1193.
[5] S. Aguado, A.C. Polo, M.P. Bernal, J. Coronas, J. Santamaria, Removal of pollutants from indoor air using Zeolite membranes, J. Membrane Sci. 240 (2004) 159–166.
[6] S. Bhatia, A.Z. Abdullah, C.T. Wong, Adsorption of butyl acetate in air over silver-loaded Y and ZSM-5 zeolites: experimental and modeling studies, J. Hazard. Mater. 163 (2009) 73–81.
[7] M. Urbiztondo, I. Pellejero, A. Rodriguez, M.P. Pina, J. Santamaria, Zeolite-coated interdigital capacitors for humidity sensing, Sensor. Actuat. B-Chem. 157 (2011) 450–459.
[8] I. Sjoholm, V. Gekas, Apple shrinkage upon drying, J. Food Eng. 25 (1) (1995) 123–130.
[9] Z. Yusheng, K.P. Poulsen, Diffusion in potato drying, J. Food Eng. 7 (4) (1988) 249–262.
[10] A. Lopez, A. Iguaz, A. Esnoz, P. Virseda, Thin-layer drying behavior of vegetable wastes from wholesale market, Dry. Technol. 18 (4–5) (2000) 995–1006.
[11] R. Langer, New methods of drug delivery, Science (1990) 1527–1533.
[12] K.S. Soppimath, T.M. Aminabhavi, A.R. Kulkarni, W.E. Rudzinski, Biodegradable polymeric nanoparticles as drugdelivery devices, J. Control. Release 70 (1–2) (2001) 1–20.
[13] L.Z. Zhang, L. Wang, Performance estimation of an adsorption cooling system for automotive waste heat recovery, Appl. Therm. Eng. 17 (12) (1997) 1127–1139.
[14] Y.Z. Lu, R.Z. Wang, S. Jianzhou, M. Zhang, Y.X. Xu, J.Y. Wu, Performance of a diesel locomotive waste-heat-powered adsorption air conditioning system, Adsorption 10 (2004) 57–68.
[15] M. Verde, L. Cortes, J.M. Corberan, A. Sapienza, S. Vasta, G. Restuccia, Modeling of an adsorption system driven by engine waste heat for truck cabin A/C. Performance estimation for a standard driving cycle, Appl. Therm. Eng. 30 (2010) 1511–1522.
[16] R. Farrington, J. Rugh, Impact of vehicle air-conditioning on fuel economy, tailpipe emissions, and electric vehicle range, in: Proceeding of the Earth Technologies Forum, Washington, D.C., October 3, 2000.
[17] Z. Han, A. Fina, Thermal conductivity of carbon nanotubes and their polymer nanocomposites: a review, Prog. Polym. Sci. 36 (2011) 914–944.
[18] D.M. Ruthven, in: W.C. Conner, J. Fraissard (Eds.), Fluid Transport in Nanoporous Materials, Springer, Dordrecht, 2006, pp. 151–186.
[19] C.C. Ni, J.Y. San, Measurement of apparent solid-side mass diffusivity of a water vapor–silica gel system, Int. J. Heat Mass Transfer 45 (2002) 1839–1847.
[20] A.A. Pesaran, A.F. Mills, Moisture transport in silica gel packed beds-I theoretical study, Int. J. Heat Mass Transfer 30 (6) (1987) 1037–1049.
[21] J.W. Nienberg, Modeling of desiccant performance for solar-desiccant-evaporative cooling systems, M.S. Thesis, School of Engineering and Applied Science, University of California, Los Angeles, 1977.
[22] J.W. Clark, A.F. Mills, H. Buchberg, Design and testing of thin adiabatic desiccant beds for solar air conditioning applications, J. Sol. Energy Eng. 103 (1981) 89–91.
[23] C.E. Bullock, J.L. Threlkeld, Dehumidification of moist air by adiabatic adsorption, Trans. ASHRAE 72 (1966). Part I 301–313.
[24] F.E. Pla-Barby, G.C. Vliet, Rotary bed solid desiccant drying: An analytical and experimental investigation, in: ASME/AIChE 18th Natinal Heat Transfer Conference, San Diego, CA, 1979.
[25] J. Crank, The Mathematics of Diffusion, Oxford University Press, 1967.
[26] J. Karger, D.M. Ruthven, Diffusion in Zeolites and Other Microporous Solids, Wiley & Sons, Inc., 1992.
[27] L.K. Lee, D.M. Ruthven, Analysis of thermal effects in adsorption rate measurement, J. Chem. Soc. Faraday Trans. 75 (11) (1979) 2406–2422.
[28] J.M. Gurgel, L.S. Andrade, P.P.S. Couto, Apparent diffusivity of water in silica gel and NaX zeolite pellets, High Temp. High Press. 33 (2001) 435–439.
[29] D.M. Ruthven, Principles of Adsorption and Desorption Processes, John Wiley &Sons, Inc., 1984.

[30] J.Y. San, G.D. Jiang, Modeling and testing of a silica gel packed-bed system, Int. J. Heat Mass Transfer 37 (8) (1994) 1173–1179.
[31] J.Y. San, Y.C. Hsu, Adsorption of toluene on activated carbon in a packed bed, Int. J. Heat Mass Transfer 41 (21) (1998) 3229–3238.
[32] A. Tamayol, M. Bahrami, Parallel flow through ordered fibers: an analytical approach, ASME J. Fluid Eng. 132 (2010) 114502.
[33] Y. Cengel, Heat and Mass Transfer: A Practical Approach, third ed., McGraw-Hill Science, 2006.
[34] H.s. Carslaw, J.C. Jaeger, Conduction of Heat in Solids, Oxford University Press, 1947.
[35] F.P. Incropera, D.P. DeWitt, T.L. Bergman, A.S. Lavine, Fundamentals of Heat and Mass Transfer, sixth ed., Wiley, 2006.
[36] E. Glueckauf, Theory of chromatography: 10. Formulate for diffusion into spheres and their application to chromatography, J. Chem. Soc. Faraday Trans. 51 (1955) 1540.
[37] A. Sakoda, M. Suzuki, Fundamental study on solar powered adsorption cooling system, J. Chem. Eng. Jpn. 17 (1984) 52–57.
[38] L.Z. Zhang, L. Wang, Effects of coupled heat and mass transfers in adsorbent on the performance of a waste heat adsorption cooling unit, Appl. Therm. Eng. 19 (1999) 195–215.
[39] K.C. Chan, C.Y.H. Chao, G.N. Sze-To, K.S. Hui, Performance predictions for a new zeolite 13X/CaCl2 composite adsorbent for adsorption cooling systems, Int. J. Heat Mass Transfer 55 (2012) 3214–3224.
[40] T.L. Floyd, Electric Circuits Fundamentals, sixth ed., Prentice Hall, 2003.
[41] B.M. Suryavanshi, L.R. Dongre, Transport Phenomena, first ed., Nirali Prakashan, 2006. section: 15.1.3.
[42] W.E. Ranz, W.R. Marshall, Evaporation from drops, Chem. Eng. Prog. 48 (3) (1952) 141–146. 48(4), 173–180.
[43] M.W. DennyNi, J.Y. San, Air and Water: The Biology and Physics of Life's Media, Princeton University Press, 1993.

Appendix B.

Thermal conductivity and contact resistance of mesoporous silica gel adsorbents bound with polyvinylpyrrolidone in contact with a metallic substrate for adsorption cooling system applications

International Journal of Heat and Mass Transfer 79 (2014) 64–71

Contents lists available at ScienceDirect

International Journal of Heat and Mass Transfer

journal homepage: www.elsevier.com/locate/ijhmt

Thermal conductivity and contact resistance of mesoporous silica gel adsorbents bound with polyvinylpyrrolidone in contact with a metallic substrate for adsorption cooling system applications

Amir Sharafian, Khorshid Fayazmanesh, Claire McCague, Majid Bahrami *

Laboratory for Alternative Energy Conversion (LAEC), School of Mechatronic Systems Engineering, Simon Fraser University, BC V3T 0A3, Canada

ARTICLE INFO

Article history:
Received 26 June 2014
Received in revised form 19 July 2014
Accepted 27 July 2014
Available online 20 August 2014

Keywords:
Adsorption cooling systems
Thermal conductivity
Thermal contact resistance
Silica gel
Polyvinylpyrrolidone

ABSTRACT

Silica gel bound with polyvinylpyrrolidone (PVP) is a new composite adsorbent with promising uptake rate designed for adsorption cooling systems. In this study, the thermal conductivity of silica gel-PVP and its thermal contact resistance (TCR) with a metallic substrate are measured using the guarded-hot plate apparatus under vacuum pressure. This study sheds light on the importance of TCR at the interface between the adsorbent and substrate, which has been overlooked in most studies in the literature. The measurements show that the thermal conductivity of silica gel-PVP adsorbent is 0.26 W/m/K which is 78.6% higher than that of dry silica gel packed bed. Also, the analysis indicates that the TCR between the adsorbent and metallic substrate is between 1.29–3.80 K/W which is equivalent to 0.20–0.69 mm of adsorbent thickness. Finally, the results indicate that the ratio of total TCR between the adsorbent and metallic substrate is up to 26% of the adsorbent-metallic substrate bulk resistance.

1. Introduction

Since 1960s, motor vehicles' fuel consumption in the U.S. has steadily increased by 4.2 times [1] contributing to air pollution, ozone depletion, and global warming. The main auxiliary load in light-duty vehicles comes from air conditioning (A/C) system in which a compressor draws power from the vehicle's internal combustion engine (ICE). During the SFTP-SC03 [2] driving cycle, which represents the engine load and gas emissions due to the use of A/C systems in light-duty vehicles, using a vapor compression refrigeration cycle (VCRC) increases fuel consumption by 28%, and CO_2 and NOx emissions by 71% and 81%, respectively. A VCRC compressor can add up to 5–6 kW peak power draw on a vehicle's ICE [3]. This auxiliary power consumption is equivalent to the power required for a 1200-kg sedan cruising at 56 km/h [3]. Moreover, in a typical ICE, almost 70% of the total fuel energy is dissipated through the engine coolant and the ICE exhaust gas in the form of waste heat. A promising alternative of conventional VCRCs could be adsorption cooling systems (ACS), which have received attention in the recent years motivated by higher fuel prices, energy shortages, and government environmental/emission regulations [4–6]. Therefore, proper implementation of the ACS in vehicles can significantly reduce fuel consumption and minimize carbon footprint of vehicles.

Working pairs in ACS are a combination of an adsorbent, e.g. zeolite, silica gel, and activated carbon, and an adsorbate, e.g. water, methanol, and ammonia. Most of these working pairs, such as zeolite-water, silica gel-water and activated carbon-methanol, are environmentally friendly, non-toxic, non-corrosive, non-ozone depleting, and inexpensive compared to conventional refrigerants, such as chlorofluorocarbons (CFCs), hydrochlorofluorocarbons (HCFCs), and hydrofluorocarbons (HFCs) [7]. Also, ACS is quiet and has no-moving parts except the valves. Thus, ACS is ideal candidates for vehicle A/C systems. However, commercialization of ACS faces major challenges because of (i) low specific cooling power (SCP), which is defined as the ratio of cooling load to the mass of dry adsorbent multiplied by the cycle time; and (ii) poor coefficient of performance (COP).

The low thermal conductivity of the adsorbent particles (~0.1–0.4 W/m/K) [8–10] and low mass diffusivity of adsorbent-adsorbate pairs (~10^{-8}–10^{-14} m^2/s) [9,11] result in a heavy and bulky ACS. The thermal conductivity of dry silica gel packed bed is summarized in Table 1. The experimental data in Table 1 show that

* Corresponding author. Address: School of Mechatronic Systems Engineering, Simon Fraser University, # 4300, 250-13450 102nd Avenue, Surrey, BC V3T 0A3 Canada. Tel.: +1 (778) 782 8538; fax: +1 (778) 782 7514.
E-mail addresses: asharafi@sfu.ca (A. Sharafian), kfayazma@sfu.ca (K. Fayazmanesh), clairem@sfu.ca (C. McCague), mbahrami@sfu.ca (M. Bahrami).

http://dx.doi.org/10.1016/j.ijheatmasstransfer.2014.07.086
0017-9310/

Nomenclature

A	cross-sectional surface area (m^2)
A/C	air conditioning
ACS	adsorption cooling system
COP	coefficient of performance
ΔT	temperature difference (K)
ICE	internal combustion engine
k	thermal conductivity (W/m/K)
L	length (m)
PVP	polyvinylpyrrolidone
$\dot{Q}$	heat flow (W)
R	thermal resistance (K/W)
SCP	specific cooling power (W/kg)
t	thickness (m)
TCR	thermal contact resistance (K/W)
THS	transient hot-strip
THW	transient hot-wire
VCRC	vapor compression refrigeration cycle
W	width (m)

Subscripts

ads	adsorbent layer
ads-metal	adsorbent layer and metallic substrate
flux	fluxmeter
flux-metal	fluxmeter and metallic substrate
metal	metallic substrate
sample	prepared sample

the thermal conductivity of dry silica gel is low and varies with bed density.

To increase the heat transfer rate to adsorbent particles, several solutions were proposed in the literature such as mixing and consolidating adsorbent particles with expanded graphite, carbon fiber, metal foam and aluminum hydroxide [20]. However, consolidation of adsorbent particles results in decreasing permeability of adsorbate through the adsorbent particles. As such, finding alternative solutions to enhance both heat and mass transfer rates are preferred.

Recently, a new mesoporous silica gel adsorbent with polyvinylpyrrolidone (PVP) binder was prepared and characterized in our group, Laboratory for Alternative Energy Conversion (LAEC), with high water uptake capacity. Instead of consolidating the silica gel which reduces the permeability of adsorbate or adding metal foam which increases the weight of adsorbent, the silica gel particles bound with PVP. This polymeric binder improves the contact between the silica gel particles and increases water uptake capacity of adsorbent due to its hydrophilic nature. Also, PVP helps the silica gel particles to adhere to the metallic substrate and increases heat transfer rate. This study will shed light on the importance of thermal contact resistance (TCR) at the interface between the adsorbent and substrate, which has been overlooked in most studies in the literature. TCR is an interfacial phenomenon and is fundamentally different from thermal conductivity, which is a bulk property and thus should be treated separately. To show the impact of the TCR, several silica gel-PVP adsorbent samples with the bulk density of 450–520 kg/m^3 were prepared and coated on a metallic substrate and its thermal conductivity and TCR are measured. It is observed through experiments that the TCR forms up to 13% of the total thermal resistance, and therefore, should be included in the design and analysis of adsorber beds.

2. Pertinent literature

Several methods were used in the literature to find the thermal conductivity of adsorbent materials. Gustafsson et al. [21] developed a transient hot-strip (THS) method to measure the thermal conductivity and the thermal diffusivity of solids and fluids with low electrical conductivity. In this method, the metal strip, which functions as a heat source, is placed between two slabs of the solid material. The THS method has better accuracy than the transient hot-wire (THW) method because for many solid materials, such as porous materials, the metal strip has better contact for transferring heat to the material than the wire [21]. The THS method was used to measure the thermal conductivity of moist silica gel by Bjurström et al. [12]. They measured the thermal conductivity of moist silica gel under different porosity, water content, water vapor pressure and silica gel temperature. Bjurström et al. [12] indicated that the thermal conductivity of the moist silica gel bed increased from 0.147 to 0.265 W/m/k by increasing the water content from 0 to 0.329 kg/kg, respectively.

Sarwar and Majumdar [22] developed an analytical model to predict the effective thermal conductivity of wet composite porous media as a function of porosity and water content. They added the effects of water content to the unit cell model proposed by Dul'Nev [23] and Luikov et al. [24]. Sarwar and Majumdar [22] showed that their model can predict the experimental data reported by Bjurström et al. [12] with maximum relative difference of 21%.

The thermal conductivity of composite silica gel and $CaCl_2$ was measured by Tanashev and Aristov [25,26] using the THW method at 20°C. Their results indicated that the effective thermal conductivity of silica gel and $CaCl_2$ increased from 0.112 to 0.153 W/m/K by increasing the water content of the composite adsorbent from 0.01 to 0.34 kg/kg [25]. They concluded that

Table 1
Thermal conductivity packed bed of dry silica gel reported in the literature [12].

Ref.	Particle density (kg/m^3)	Bed density (kg/m^3)	Effective thermal conductivity (W/m/K)	Mean temperature (°C)
Mantell [13]	1201	720	0.144	–
Nienergall [14]	–	–	0.198	–
Vasilev et al. [15]	–	850	0.153	20
	–	998	0.182	20
	–	865	0.160	20
Sharma et al. [16]	891	452–750	0.128–0.168	20–135
Sharma and Hughes [17]	–	428–690	0.116–0.148	48.7
Blasinski and Heim [18]	870	461–609	0.106–0.135	140
Simonova [19]	–	634	0.151	20
	–	838	0.179	20

changes in the effective thermal conductivity of composite silica gel and $CaCl_2$ at water contents less than 0.4 kg/kg were negligible. In a real ACS, the water content of silica gel is less than 0.4 kg/kg because silica gel cannot uptake water beyond 0.4 kg/kg during short cycle times (~10–20 min) [27,28]. Thus, the assumption of constant thermal conductivity for composite silica gel and $CaCl_2$ in an ACS can be a good approximation.

Tamainot-Telto and Critoph [9] measured the effective thermal conductivity of monolithic carbon by using the guarded-hot plate device which is a standard method for determining the steady state thermal conductivity of materials [9]. The effective thermal conductivity of monolithic carbon was reported between 0.349–0.4455 W/m/k. However, the monolithic carbon had permeability of 10^{-14} m^2/s [9] which significantly reduces the adsorbate penetration depth through the monolithic carbon. The other point, which was neglected in Tamainot-Telto's and Critoph's [9] measurements, was the TCRs between the heat source and sink, and the sample.

Freni et al. [10] measured the thermal conductivity of composite silica gel and $CaCl_2$ bound with aluminum hydroxide by using the THW method under different water vapor pressure and temperature, and water content. Their results showed that the effects of vapor pressure and temperature were negligible on the thermal conductivity of the composite adsorbent. However, the effective thermal conductivity of silica gel and $CaCl_2$ increased from 0.12 to 0.227 W/m/K by increasing the water content from 0.05 to 0.28 kg/kg dry adsorbent, respectively. Critoph and Zhong [29] summarized the thermal conductivity of a wide range of adsorbents reported in the literature, Table 2.

It can be seen in Table 2 that the composite adsorbents with expanded graphite [30,31,34–36] resulted in higher thermal conductivities. These experiments were performed under atmospheric pressure and unsteady thermal conductivity measurement methods, e.g. THW or THS methods. Adsorption process is an exothermic process and adsorbent particles adsorb the air humidity and generate heat. Therefore, the measured temperature difference in the unsteady thermal conductivity measurement methods is less than that of with no adsorption [37]. To reduce this misleading error, Wang et al. [37,38] measured the thermal conductivity of the consolidated expanded natural graphite slab using the guarded-hot plate apparatus. Their measurements indicated that the thermal conductivity of the consolidated adsorbent increased from 1.4 to 1.7 W/m/K by increasing its density from 200 to 500 kg/m^3, respectively. However, Wang et al. [37,38] did not excluded the effects of TCR in their calculations.

In all above mentioned studies, two main parameters were neglected which can considerably affect the results: (i) thermal conductivity measurement under atmospheric pressure, and (ii) including TCR in the thermal conductivity calculations. It should be noted that TCR is an interfacial phenomena and is a function of compression (pressure), surface characteristics (e.g. roughness, out-of-flatness) and bonding of the adsorbent with the substrate whereas conductivity is a bulk property and depends on the material microstructure and composition. Due to the low thermal conductivity and high porosity of adsorbent materials, the TCR cannot be neglected in the measurements and it should be excluded from the thermal resistance of adsorbent. Also, adsorbents adsorb air humidity and generate heat. As a result, the measured temperature difference is smaller than where there is no adsorption process. To cancel these errors, the thermal conductivity of adsorbent materials should be measured under vacuum pressure and the TCR effect should be treated separately and de-convoluted from the conductivity measurements.

Table 2
Thermal conductivity of different adsorbents reported in literature [29].

Adsorbent material	Thermal conductivity (W/m/K)	Density (kg/m^3)	Ref.
Expanded graphite–metal chloride	10–40	–	[30]
Expanded graphite–zeolite 13×	5–15	–	[31]
Consolidated zeolite 4A	0.3	960	[32]
Consolidated zeolite 4A+ adhesive bond to the wall	0.3	960	[32]
Consolidated zeolite 13×	0.58	–	[33]
Expanded graphite (20–30%) – silica gel	10–20	–	[34,35]
Silica gel – $CaCl_2$	0.12–0.22	–	[10]
Monolithic carbon	0.35–0.44	750	[9]
Expanded natural graphite – silica gel	3.7–19.1	38–286	[36]

3. Sample preparation

Silica gel bound with PVP sample was prepared utilizing chromatography-grade commercial silica gel with irregular-shaped grains (0.2–0.5 mm) and average pore diameter of 9 nm supplied from Silicycle, Inc (Quebec, Canada). In batches of 100 g, the dry mesoporous silica gel was mixed with PVP. The mixture was baked at 200°C until judged dry by consistent weight measurements.

4. Thermal conductivity measurement

4.1. Test bed

A custom-built thermal conductivity measurement test bed was used to measure the thermal conductivity of the prepared samples. The test bed and schematic of sample location between two fluxmeters are shown in Fig. 1. The test bed is designed based on the guarded-hot plate apparatus recommended by ASTM standard C177-13 [39]. The test column is housed under a glass vacuum chamber which is connected to a vacuum pump to evacuate the chamber during the experiments. Further details of the test bed are explained elsewhere [40,41].

The two-thickness method is used to measure the sample thermal conductivity and de-convolute the effect of TCR between the fluxmeters and sample. This method is a precise method to exclude the TCR from the thermal conductivity of the sample.

4.2. Test procedure

To measure the thermal conductivity of silica gel-PVP adsorbent, two experiments were designed as shown in Fig. 2.

Fig. 2a shows the first method to find the thermal conductivity of the composite adsorbent and TCR between the adsorbent and metallic substrate. The thermal resistance network of this sample is shown in Fig. 2a. Heat, $\dot{Q}$, passes through the top fluxmeter, different thermal resistances and the bottom fluxmeter. To find the thermal resistances, the thermal conductivity of a bare metallic substrate, copper was used in our experiments, should be measured separately to find the metallic substrate resistance, R_{metal}, and the TCR between the fluxmeter and metallic substrate, $TCR_{flux\text{-}metal}$. The next step is to measure the thermal conductivity of an adsorbent layer, R_{ads}, and the TCR between the adsorbent and metallic substrate, $TCR_{ads-metal}$, by using the two-thickness method. To find the last unknown, $TCR_{ads-metal}$, the whole sample including the adsorbent and metallic substrate should be placed in the thermal conductivity measurement test bed. However, during the preparation of the samples, we noticed that the surface of the prepared samples were not identical and smooth, and as a result, the $TCR_{flux-ads}$ for different samples were not the same. To solve this problem, the silica gel-PVP adsorbent was sandwiched

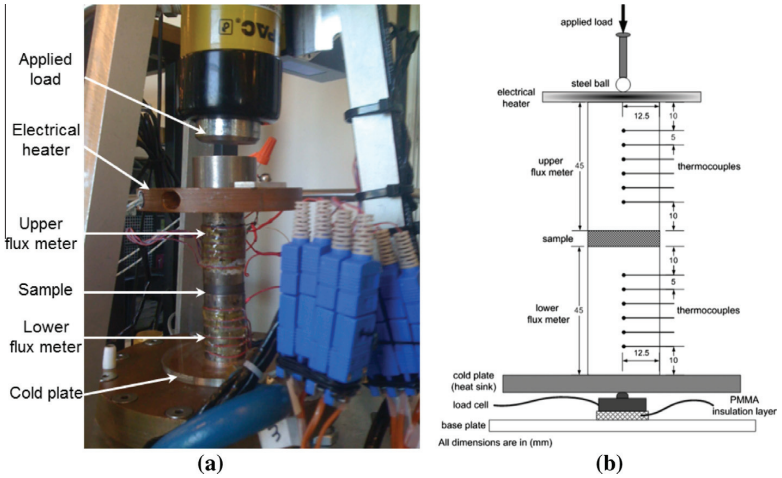

Fig. 1. (a) Thermal conductivity and TCR measurement testbed, and (b) schematic of sample location, fluxmeters and thermocouples in the testbed [40,41].

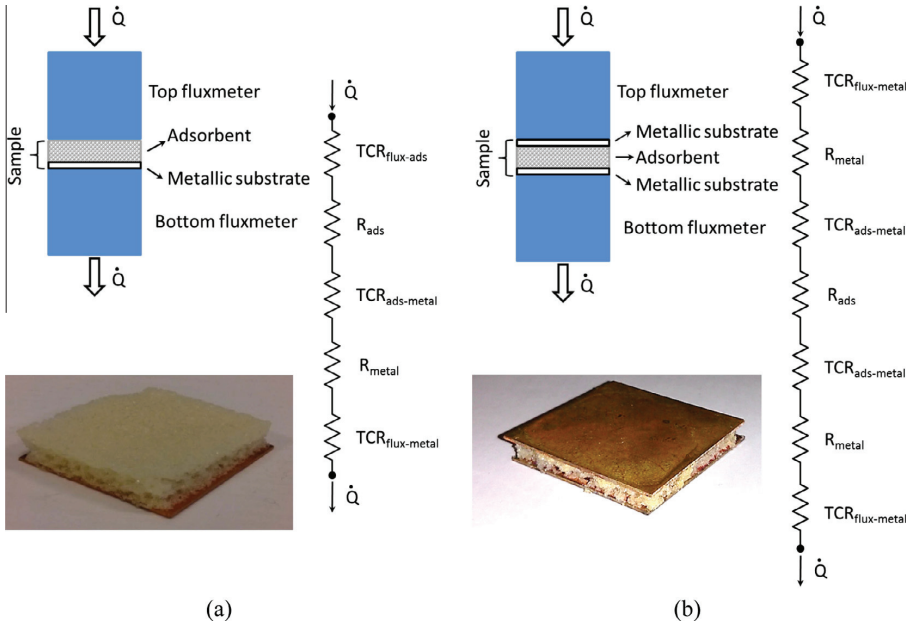

Fig. 2. Prepared samples and resistance network to measure the thermal conductivity of silica gel bound with PVP and TCR between the sample and metallic substrate: (a) adsorbent on a metallic substrate (copper plate), and (b) adsorbent sandwiched between two copper plates.

between two metallic substrates, as shown in Fig. 2b. Similar to the previous procedure, R_{metal} and $TCR_{flux-metal}$ should be measured separately by using a bare metallic substrate. Then, the two-thickness method can be used to find the R_{ads} and $TCR_{ads-metal}$. Eqs (1)–(6) show the mathematical calculations to find the R_{ads} and $TCR_{ads-metal}$. Eqs (1) and (2) give the bulk resistances of two samples with different thicknesses which were prepared based on Fig. 2b.

$$R_{sample\,1} = 2TCR_{flux-metal} + 2R_{metal} + 2TCR_{ads-metal} + R_{ads,1} \quad (1)$$

$$R_{sample\,2} = 2TCR_{flux-metal} + 2R_{metal} + 2TCR_{ads-metal} + R_{ads,2} \quad (2)$$

By subtracting Eq. (1) from Eq. (2),

$$R_{sample\,2} - R_{sample\,1} = R_{ads,2} - R_{ads,1} \quad (3)$$

where, $R_{ads,1}$ and $R_{ads,1}$ are the adsorbent resistance with different thicknesses and are equal to $\frac{t_{ads,1}}{k_{ads}A}$, $\frac{t_{ads,2}}{k_{ads}A}$, respectively. t_{ads}, k_{ads} and A refer to the adsorbent thickness, thermal conductivity, and cross-sectional surface area, respectively. $R_{sample\,1}$ and $R_{sample\,2}$ are calculated from Eqs. (4) and (5):

$$R_{sample\,1} = \frac{\Delta T_1}{\dot{Q}_1} \quad (4)$$

$$R_{sample\,2} = \frac{\Delta T_2}{\dot{Q}_2} \quad (5)$$

where, $\dot{Q}$ and ΔT are the heat transfer rate that passes through the fluxmeters and temperature difference between two sides of the

sample, respectively. By substituting Eqs. (4) and (5) in Eq. (3), the thermal conductivity of composite adsorbent can be determined.

$$k_{ads} = \frac{t_{ads,2} - t_{ads,1}}{A(R_{sample\,2} - R_{sample\,1})} \quad (6)$$

Table 3
Uncertainty of relevant parameters in the thermal conductivity and TCR measurements.

$\frac{\delta\dot{Q}}{\dot{Q}}$	$\frac{\delta\Delta T}{\Delta T}$	$\frac{\delta t}{t}$	$\frac{\delta A}{A}$	$\frac{\delta k_{flux}}{k_{flux}}$
0.15–0.29	0.018	0.0019	0.00056	0.00139

Table 4
Dimensions of prepared samples.

Sample No.	Thickness (mm)			Heat transfer surface area (m^2)
	Copper plate	Adsorbent	Total	
1	0.762	3.75	5.27	6.45×10^{-4}
2	0.762	6.6	8.12	6.45×10^{-4}

As shown in Eq. (6), the thermal conductivity of adsorbent can be calculated by using the two-thickness method and de-convoluting the TCR between different layers. The TCR between the adsorbent and metallic substrate, $TCR_{ads-metal}$, is determined by replacing the measured values in Eqs. (1) or (2).

4.3. Uncertainty analysis

To find the uncertainty during the thermal conductivity and TCR measurements, the relevant parameters to the bulk thermal resistance or thermal conductivity of adsorbent are shown in Eq. (7):

$$k_{ads} = f(\dot{Q}, \Delta T, t, A, k_{flux}) \quad (7)$$

The uncertainty in the thermal conductivity measurements can be calculated similar to the procedure explained by Unsworth et al. [42]. The main uncertainty in the calculations is due to the heat flow that passes through the fluxmeters. The maximum errors in the temperature and length measurements are ±1°C and 0.01 mm, respectively. The fluxmeters have been made out of Armco iron with tolerance in thermal conductivity of ±0.1 W/m/K. Eq (8) gives the total uncertainty in measurements [42].

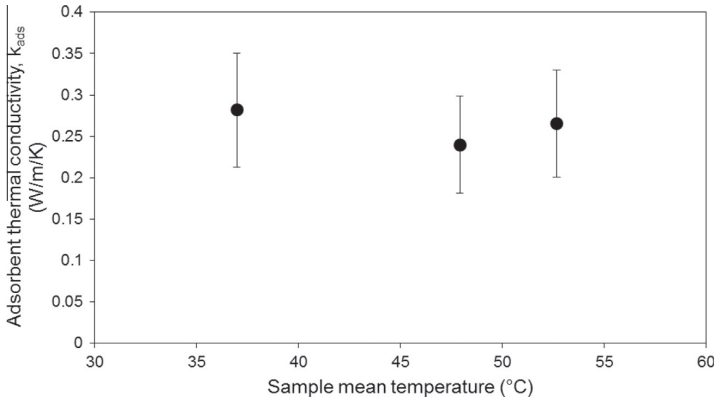

Fig. 3. Thermal conductivity of silica gel bound with PVP vs. sample mean temperature.

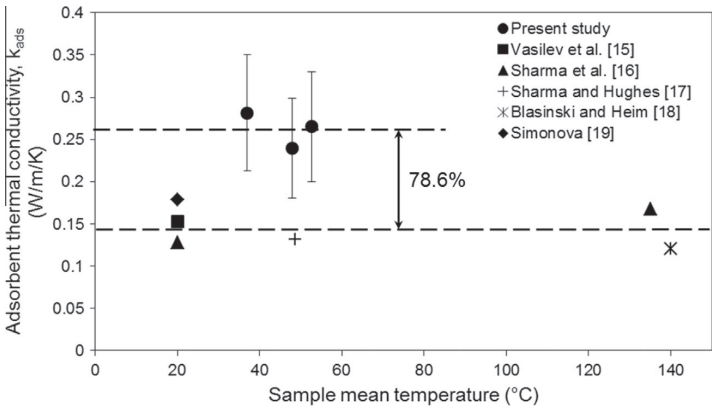

Fig. 4. Comparison between thermal conductivity of silica gel bound with PVP in the present study with those reported for dry silica gel packed bed.

$$\frac{\delta k_{ads}}{k_{ads}} = \sqrt{\left(\frac{\delta \dot{Q}}{\dot{Q}}\right)^2 + \left(\frac{\delta \Delta T}{\Delta T}\right)^2 + \left(\frac{\delta t}{t}\right)^2 + \left(\frac{\delta A}{A}\right)^2 + \left(\frac{\delta k_{flux}}{k_{flux}}\right)^2} \quad (8)$$

where $\frac{\delta \dot{Q}}{\dot{Q}}$ and $\frac{\delta A}{A}$ are calculated as follows [42]:

$$\frac{\delta \dot{Q}}{\dot{Q}} = \frac{1}{2}\frac{\dot{Q}_{top\,flux} - \dot{Q}_{bottom\,flux}}{\dot{Q}_{ave}} \quad (9)$$

$$\frac{\delta A}{A} = \sqrt{\left(\frac{\delta L}{L}\right)^2 + \left(\frac{\delta W}{W}\right)^2} \quad (10)$$

In Eq. (10), L and W are the length and width of the sample, which are equal to 25.4 mm. The uncertainty associated with the adsorbent thermal conductivity and TCR measurements are summarized in Table 3.

By substituting the calculated uncertainties tabulated in Table 3 in Eq. (8), the experiment uncertainty is estimated to be between 15–29% with average uncertainty of 24.5%.

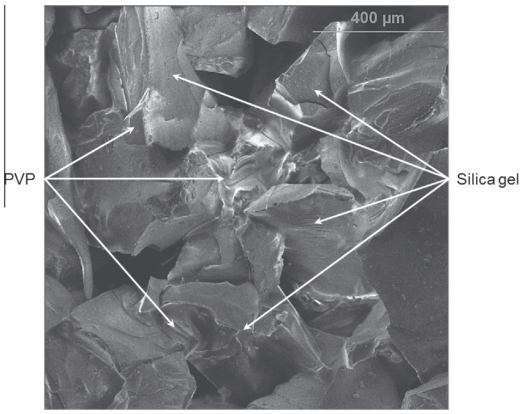

Fig. 5. SEM image of silica gel-PVP adsorbent.

5. Results and discussion

To measure the thermal conductivity of silica gel bound with PVP based on the designed experiment shown in Fig. 2b, two samples were prepared. The dimensions of the prepared samples are summarized in Table 4. The composite adsorbent was placed between two copper plates with 0.762 mm in thickness and baked at 200°C until judged dry by consistent weight measurements.

After running the experiments at different heat transfer rates (thus various temperatures), the thermal conductivity of composite adsorbent were determined by using Eq. (6). Fig. 3 shows the thermal conductivity of composite silica gel vs. sample mean temperature.

As shown in Fig. 3, the thermal conductivity of composite adsorbent varies between 0.24–0.28 W/m/K. The comparison between the measured thermal conductivity in this study and those of reported for the packed bed of dry silica gel is shown in Fig. 4. The experimental data in the literature indicates that the sample mean temperature does not significantly affect the thermal conductivity of silica gel packed bed. Also, the comparison indicates that the average measured thermal conductivity of silica gel bound with PVP is 78.6% higher than those reported in the literature for the packed bed of dry silica gel [15–19].

The reason for the present higher thermal conductivity of silica gel-PVP adsorbent is that the mesoporous silica gel grains are bound with PVP and, as a result, the grains have better connection together. Fig. 5 shows the scanning electron microscope (SEM) image of silica gel-PVP adsorbent. Also, the thermal conductivity measured by Ref. [15–19] did not de-convolute the TCR from the

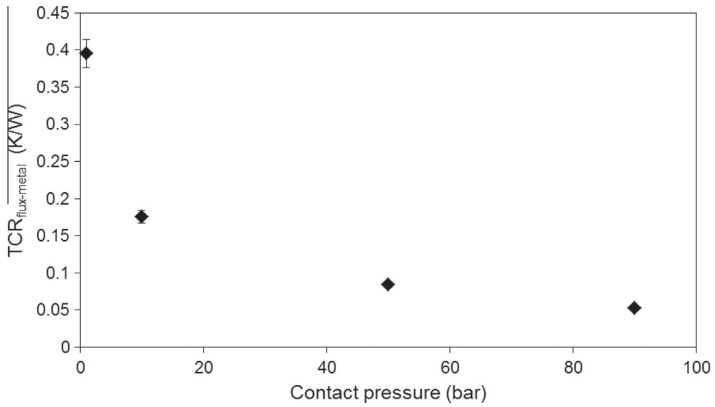

Fig. 6. Thermal contact resistance between fluxmeters and copper plate.

Table 5
Thermal resistance and TCR between different layers of adsorbent layer sandwiched between two metallic substrates, Fig. 2b.

Sample mean temperature (°C)	k_{ads} (W/m/K)	R_{metal} (K/W)	$TCR_{flux\text{-}metal}$ (K/W)	$TCR_{ads\text{-}metal}$ (K/W)	Equivalent adsorbent thickness due to $TCR_{ads\text{-}metal}$ (= $TCR_{ads\text{-}metal} \times k_{ads} \times A$) (mm)
36.98	0.282	0.003	0.395	3.80	0.69
47.93	0.240	0.003	0.395	1.29	0.20
52.68	0.265	0.003	0.395	2.46	0.42

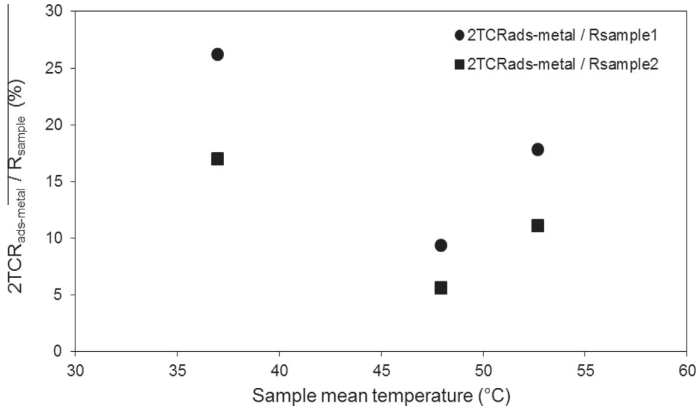

Fig. 7. Ratio of $2TCR_{ads\text{-}metal}$ to the bulk resistances, $R_{sample\,1}$ and $R_{sample\,2}$ vs. sample mean temperature.

total resistance which results in lower thermal conductivity measurement.

To find the $TCR_{flux-metal}$, a copper (alloy 110) plate with thermal conductivity of 388 W/m/K were selected as the metallic substrate. The TCR between the fluxmeters and copper plate, $TCR_{flux-metal}$, was measured under different contact pressures, Fig. 6.

The maximum uncertainty in the $TCR_{flux-metal}$ measurement was 4.8%. As shown in Fig. 6, the $TCR_{flux-metal}$ reduces by increasing the contact pressure. However, due to the brittle nature of silica gel-PVP adsorbent, it is not possible to increase the contact pressure up to 90 bars. As such, the $TCR_{flux-metal}$ of 0.395 K/W at the contact pressure of 1.3 bar was used in the calculations, the same contact pressure which was applied on the samples during the tests. By substituting the calculated values in Eqs. (1) or (2), the TCR between the adsorbent layer and metallic substrate, $TCR_{ads-metal}$, is calculated. The calculated thermal resistances and TCR in this study are summarized in Table 5.

It can be seen in Table 5 that the $TCR_{ads-metal}$ varies from 1.29–3.80 K/W which is equivalent to 0.2–0.69 mm of the silica gel-PVP thickness. These results indicate that the effects of $TCR_{ads-metal}$ becomes important where the adsorbent thickness is small, e.g., adsorbent coating. The ratio of $2TCR_{ads-metal}$ (there are two TCRs of the adsorbent and metallic substrate in the bulk resistance) to the bulk resistances, $R_{sample\,1}$ and $R_{sample\,2}$, are shown in Fig. 7.

Fig. 7 shows that the effect of two TCRs between the adsorbent layer and substrate to the bulk resistance, $2TCR_{ads-metal}/R_{sample\,1}$, can be as high as 26%. This clearly shows that TCR is significant and cannot be neglected; and should be considered in thermal design and analysis of adsorber beds.

6. Conclusions and final remarks

In this study, the effect of TCR on the overall heat resistance of an adsorbent layer on a metallic substrate was studied experimentally. To demonstrate the impact of TCR, silica gel bound with PVP samples were coated on copper plates and their thermal conductivity and TCR were measured using a custom-built guarded-hot plate apparatus under vacuum conditions. The two-thickness method was used to de-convolute the TCR between the adsorbent layer and the copper plate from the thermal conductivity measurements. The experimental data showed that the thermal conductivity of silica gel-PVP adsorbent was 0.26 W/m/K, i.e., 78.6% higher than that of packed bed of dry silica gel. Also, the results indicated that the $TCR_{ads-metal}$ varied between 1.29–3.80 K/W which is equal to silica gel-PVP adsorbent with 0.2–0.69 mm in thickness. Besides, our measurements showed that the two TCRs between the adsorbent and metallic substrate, $TCR_{ads-metal}$, can be up to 26% of the bulk resistance of the adsorbent-metallic composite.

Acknowledgement

The authors gratefully acknowledge the financial support of the Natural Sciences and Engineering Research Council of Canada (NSERC) through the Automotive Partnership Canada Grant No. APCPJ 401826-10.

References

[1] Motor vehicle fuel consumption and travel in the U.S., 1960–2006, U.S. Dep. Transp., 2006.
[2] T.J. Hendricks, Optimization of vehicle air conditioning systems using transient air conditioning performance analysis, in: SAE Conf. Proc. P, 2001.
[3] R. Farrington, J. Rugh, Impact of vehicle air-conditioning on fuel economy, tailpipe emissions, and electric vehicle range, in: Proceeding Earth Technol. Forum, Washington, D.C., 2000.
[4] L.Z. Zhang, L. Wang, Performance estimation of an adsorption cooling system for automobile waste heat recovery, Appl. Therm. Eng. 17 (1997) 1127–1139.
[5] Y.Z. Lu, R.Z. Wang, S. Jianzhou, M. Zhang, Y. Xu, J. Wu, Performance of a diesel locomotive waste-heat-powered adsorption air conditioning system, Adsorption 10 (2004) 57–68.
[6] M. Verde, L. Cortés, J.M. Corberán, A. Sapienza, S. Vasta, G. Restuccia, Modelling of an adsorption system driven by engine waste heat for truck cabin A/C. Performance estimation for a standard driving cycle, Appl. Therm. Eng. 30 (2010) 1511–1522.
[7] H. Demir, M. Mobedi, S. Ülkü, A review on adsorption heat pump: Problems and solutions, Renew. Sustain. Energy Rev. 12 (2008) 2381–2403.
[8] F. Poyelle, J.J. Guilleminot, F. Meunier, Experimental tests and predictive model of an adsorptive air conditioning unit, Ind. Eng. Chem. Res. 38 (1999) 298–309.
[9] Z. Tamainot-Telto, R.E. Critoph, Monolithic carbon for sorption refrigeration and heat pump applications, Appl. Therm. Eng. 21 (2001) 37–52.
[10] A. Freni, M.M. Tokarev, G. Restuccia, A.G. Okunev, Y.I. Aristov, Thermal conductivity of selective water sorbents under the working conditions of a sorption chiller, Appl. Therm. Eng. 22 (2002) 1631–1642.
[11] A. Sharafian, M. Bahrami, Adsorbate uptake and mass diffusivity of working pairs in adsorption cooling systems, Int. J. Heat Mass Transfer 59 (2013) 262–271.
[12] H. Bjurström, E. Karawacki, B. Carlsson, Thermal conductivity of a microporous particulate medium: moist silica gel, Int. J. Heat Mass Transfer 27 (1984) 2025–2036.
[13] C.L. Mantell, Adsorption, 2nd ed., McGraw-Hill, New York, 1951.
[14] W. Niebergall, Arbeitsstoffpaare für Sorptions-Kältemaschinen, Sorptions-Kältemaschinen. 7 (1959) 119–164.
[15] S.Z. Vasil'ev, V.I. Letichevskii, V.L. Mal'ter, M.Y. Solntsev, G.M. Yusova, O.M. Kostenok, et al., The effective thermal conductivity of zeolite and silica gel layers, Chem. Pet. Eng. 15 (1979) 33–35.
[16] C.S. Sharma, P. Harriott, R. Hughes, Thermal conductivity of catalyst pellets and other porous particles: Part II: Experimental measurements, Chem. Eng. J. 10 (1975) 73–80.
[17] C.S. Sharma, R. Hughes, The thermal conductivity of porous catalyst compacts, Can. J. Chem. Eng. 54 (1976) 358–363.

[18] H. Blasinski, A. Heim, The influence of porosity on the thermal conductivity of granular layers, Zesz. Nauk. Politech. Łódzkiej – Chem. 24 (1973) 91–106.
[19] L.K. Simonova, Determination of thermal constants of samples of activated carbon and silica gels, Zhurnal Prikl. Khimii. 16 (1943) 87–94.
[20] K. Fujioka, K. Hatanaka, Y. Hirata, Composite reactants of calcium chloride combined with functional carbon materials for chemical heat pumps, Appl. Therm. Eng. 28 (2008) 304–310.
[21] S.E. Gustafsson, E. Karawacki, M.N. Khan, Transient hot-strip method for simultaneously measuring thermal conductivity and thermal diffusivity of solids and fluids, J. Phys. D. Appl. Phys. 12 (1979) 1411–1421.
[22] M. Sarwar, P. Majumdar, Thermal conductivity of wet composite porous media, Heat Recover. Syst. CHP. 15 (1995) 369–381.
[23] G. Dul'Nev, Heat transfer through solid disperse systems, J. Eng. Phys. Thermophys. 9 (1965) 399–404.
[24] A.V. Luikov, A.G. Shashkov, L.L. Vasiliev, Y.E. Fraiman, Thermal conductivity of porous systems, Int. J. Heat Mass Transfer 11 (1968) 117–140.
[25] Y.Y. Tanashev, Y.I. Aristov, Thermal conductivity of a silica gel+ calcium chloride system: the effect of adsorbed water, J. Eng. Phys. Thermophys. 73 (2000) 876–883.
[26] Y.Y. Tanashev, A.V. Krainov, Y.I. Aristov, Thermal conductivity of composite sorbents "salt in porous matrix" for heat storage and transformation, Appl. Therm. Eng. 61 (2013) 401–407.
[27] H.T. Chua, K.C. Ng, A. Chakraborty, N.M. Oo, M.A. Othman, Adsorption characteristics of silica gel + water systems, J. Chem. Eng. Data. 47 (2002) 1177–1181.
[28] B.B. Saha, A. Chakraborty, S. Koyama, Y.I. Aristov, A new generation cooling device employing CaCl2-in-silica gel–water system, Int. J. Heat Mass Transfer 52 (2009) 516–524.
[29] R.E. Critoph, Y. Zhong, Review of trends in solid sorption refrigeration and heat pumping technology, Proc. Inst. Mech. Eng. Part E J. Process Mech. Eng. 219 (2005) 285–300.
[30] S. Mauran, P. Prades, F. L'Haridon, Heat and mass transfer in consolidated reacting beds for thermochemical systems, Heat Recover. Syst. CHP. 13 (1993) 315–319.
[31] M. Pons, D. Laurent, F. Meunier, Experimental temperature fronts for adsorptive heat pump applications, Appl. Therm. Eng. 16 (1996).
[32] L. Marletta, G. Maggio, A. Freni, M. Ingrasciotta, G. Restuccia, A non-uniform temperature non-uniform pressure dynamic model of heat and mass transfer in compact adsorbent beds, Int. J. Heat Mass Transfer 45 (2002) 3321–3330.
[33] T. Miltkau, B. Dawoud, Dynamic modeling of the combined heat and mass transfer during the adsorption/desorption of water vapor into/from a zeolite layer of an adsorption heat pump, Int. J. Therm. Sci. 41 (2002) 753–762.
[34] T. Eun, H. Song, J. Hun, K. Lee, J. Kim, Enhancement of heat and mass transfer in silica-expanded graphite composite blocks for adsorption heat pumps: Part I. Characterization of the composite blocks, Int. J. Refrig. 23 (2000) 64–73.
[35] T. Eun, H. Song, J. Hun, K. Lee, J. Kim, Enhancement of heat and mass transfer in silica-expanded graphite composite blocks for adsorption heat pumps. Part II. Cooling system using the composite blocks, Int. J. Refrig. 23 (2000) 74–81.
[36] X. Zheng, L.W. Wang, R.Z. Wang, T.S. Ge, T.F. Ishugah, Thermal conductivity, pore structure and adsorption performance of compact composite silica gel, Int. J. Heat Mass Transfer 68 (2014) 435–443.
[37] L.W. Wang, Z. Tamainot-Telto, S.J. Metcalf, R.E. Critoph, R.Z. Wang, Anisotropic thermal conductivity and permeability of compacted expanded natural graphite, Appl. Therm. Eng. 30 (2010) 1805–1811.
[38] L.W. Wang, Z. Tamainot-Telto, R. Thorpe, R.E. Critoph, S.J. Metcalf, R.Z. Wang, Study of thermal conductivity, permeability, and adsorption performance of consolidated composite activated carbon adsorbent for refrigeration, Renew. Energy 36 (2011) 2062–2066.
[39] ASTM C177-13, Standard Test Method for Steady-State Heat Flux Measurements and Thermal Transmission Properties by Means of the Guarded-Hot-Plate Apparatus, ASTM Int., 2004.
[40] E. Sadeghi, S. Hsieh, M. Bahrami, Thermal conductivity and contact resistance of metal foams, J. Phys. D. Appl. Phys. 44 (2011) 125406.
[41] E. Sadeghi, N. Djilali, M. Bahrami, Effective thermal conductivity and thermal contact resistance of gas diffusion layers in proton exchange membrane fuel cells. Part 1: Effect of compressive load, J. Power Sources 196 (2011) 246–254.
[42] G. Unsworth, N. Zamel, X. Li, Through-plane thermal conductivity of the microporous layer in a polymer electrolyte membrane fuel cell, Int. J. Hydrogen Energy 37 (2012) 5161–5169.

Appendix C.

Assessment of adsorber bed designs in waste-heat driven adsorption cooling systems for vehicle air conditioning and refrigeration

Renewable and Sustainable Energy Reviews 30 (2014) 440–451

Contents lists available at ScienceDirect

Renewable and Sustainable Energy Reviews

journal homepage: www.elsevier.com/locate/rser

Assessment of adsorber bed designs in waste-heat driven adsorption cooling systems for vehicle air conditioning and refrigeration

Amir Sharafian, Majid Bahrami *

Laboratory for Alternative Energy Conversion (LAEC), School of Mechatronic Systems Engineering, Simon Fraser University, BC, Canada V3T 0A3

ARTICLE INFO

Article history:
Received 18 July 2013
Received in revised form
17 October 2013
Accepted 22 October 2013
Available online 14 November 2013

Keywords:
Adsorption cooling system
Vehicle air conditioning
Finned tube adsorber bed
Specific cooling power
Adsorber bed to adsorbent mass ratio

ABSTRACT

Adsorber bed design strongly affects the performance of waste-heat driven adsorption cooling systems (ACS) for vehicle air conditioning and refrigeration (A/C–R) applications. Adsorber beds should be specifically sized for vehicle A/C–R considering the limitations of mobile applications. However, there is no conclusive evidence on what type of adsober bed is proper for vehicle applications. To evaluate the performance of ACS, specific cooling power (SCP), adsorber bed to adsorbent mass ratio, and coefficient of performance (COP) are introduced and their order of importance are assessed. To investigate the available studies in the open literature, desired SCP of 350 W/kg dry adsorbent and adsorber bed to adsorbent mass ratio of less than one are calculated for a 1-ton-of-refrigeration, 2-adsorber bed, silica gel–water ACS. According to these criteria, previous studies are summarized into nine groups with respect to their adsober beds and consequently, finned tube adsorber bed design is selected among the existing designs. Finally, optimization of fin spacing and fin height, and enhancing thermal conductivity of adsorbent material by adding metal wool inside the finned tube adsorber bed are proposed as the practical solutions to increase heat and mass transfer rates within the adsorber bed.

Contents

1. Introduction

Refrigeration systems consume a considerable amount of energy to produce cooling power in domestic and industrial applications such as ice-making [1–3] and food industries [4–6], vaccine protection [7–9], and air conditioning applications [10–13]. Vapor compression refrigeration cycles (VCRCs) are the most popular type of refrigeration systems in which different refrigerants such as chlorofluorocarbons (CFCs), hydrochlorofluorocarbons (HCFCs), and hydrofluorocarbons (HFCs) [14] are used. Ozone depletion and global warming resulting from such refrigerants are direct environmental impacts of VCRCs. An ideal refrigeration system should use a refrigerant which has favorable thermodynamic properties and be noncorrosive, nontoxic,

* Corresponding author. Tel.: +1 778 782 8538; fax: +1 778 782 7514.
E-mail addresses: asharafi@sfu.ca (A. Sharafian), mbahrami@sfu.ca (M. Bahrami).

1364-0321/$ - see front matter © 2013 Elsevier Ltd. All rights reserved.
http://dx.doi.org/10.1016/j.rser.2013.10.031

Nomenclature

COP	coefficient of performance
c_p	specific heat capacity at constant pressure, (J/kg/K)
Δh_{ads}	enthalpy of adsorption, (J/kg)
HEX	heat exchanger
h	enthalpy, (J/kg)
m	mass, (kg)
Q	total heat transfer, (J)
SCP	specific cooling power, (W/kg dry adsorbent)
SS	stainless steel
T	temperature, (K)
t	time, (s)
VSCP	volumetric specific cooling power, (W/m^3 adsorber bed)

Greek symbols

τ_{cycle}	cycle time, (s)
ω	adsorbate uptake, (kg adsorbate/kg dry adsorbent)

Subscripts

bed	adsorber bed
cond	condenser
evap	evaporator
iba	isobaric adsorption
ibd	isobaric desorption
ic	isosteric cooling
ih	isosteric heating
sat	saturation
sorbent	adsorbent

non-flammable, and environmentally benign [15]. Therefore, development of green, sustainable refrigeration systems which utilize environmentally friendly refrigerants is of great importance.

The negative impacts of air conditioning and refrigeration (A/C–R) systems become more pronounce in automotive and transportation applications where a VCRC compressor is powered by mechanical energy from the internal combustion engine (ICE). Current A/C–R systems significantly increase fuel consumption and greenhouse gas production. The U.S. annually consumes about 40 billion liters of fuel for heating, ventilation, and air conditioning (HVAC) systems of light duty vehicles [16]. A VCRC compressor can add up to 5–6 kW peak power draw on a vehicle's engine, the equivalent power required for a 1200-kg sedan cruising at 56 km/h [16].

In an ICE vehicle, almost 70% of total fuel energy is dissipated through the ICE coolant and exhaust gas in the form of waste heat [16]. To retrieve the waste heat and reduce the negative impacts of VCRCs, an alternative solution is adsorption cooling systems (ACS) in which adsorber beds replace the compressor. A portion of ICE waste heat is sufficient to run an ACS to meet the A/C–R needs of a vehicle [17]. ACS, also, can be applied in natural gas vehicles (NGVs) similarly to the gasoline-powered vehicles because the exhaust gas of the engine is available. However, in hybrid electric vehicles (HEVs) and plug-in hybrid electric vehicles (PHEVs) the exhaust gas of the engine is not available continuously. The required heat to regenerate the adsorber beds can be supplied from a heat storage tank and/or the electric motor and battery cooling systems. In the case of electric vehicles (EVs), similarly, the waste heat energy can be supplied from the electric motor and battery cooling systems. As such, proper implementation of ACS in vehicles has the potential to significantly reduce fuel consumption and minimize the carbon footprint of vehicles.

ACS work based on the sorption phenomenon in which a fluid (adsorbate) is adsorbed at the surface of a solid material (adsorbent). Most popular working pairs used in ACS include zeolite–water, silica gel–water and activated carbon–methanol. These materials are environmentally friendly, non-toxic, non-corrosive, and inexpensive [18]. Moreover, ACS are quiet and easy to maintain [19] as there is no moving part, except valves, in these systems. Thus, ACS are ideal candidates for a variety of applications especially where waste-heat or low-grade thermal energy is available. However, commercialization of ACS faces major challenges; namely: (i) low specific cooling power (SCP) and (ii) low coefficient of performance (COP) that result in heavy and bulky A/C–R systems which make them impractical for vehicle A/C–R applications [20]. The origin of the ACS low performance is low thermal conductivity of adsorbent materials due to high porosity and thermal contact resistance between the adsorbent particles, for example, thermal conductivity of zeolite 13X, silica gel–$CaCl_2$ and activated carbon are 0.1, 0.12 and 0.3 W/m/K, respectively [21–23]. As a result, heating and cooling of ACS adsorber beds are time consuming processes. As such, design and optimization of an adsorber bed with improved heat and mass transfer characteristics, and low adsorber bed to adsorbent mass ratio can effectively increase the SCP and COP of ACS [24–26].

In this paper, an in-depth assessment of available adsorber bed design of waste-heat driven ACS is presented with a focus on vehicle A/C–R applications. The previous studies are classified based on the ACS working pairs, cooling capacity, cycle time, COP, SCP, and adsorber bed to adsorbent mass ratio. Based on these data, the effects of different adsorber bed designs are investigated on the SCP, adsorber bed to adsorbent mass ratio and COP to identify the best adsorber bed designs suitable for vehicle A/C–R applications. Finally, several practical solutions and remedies are proposed to improve the performance of ACS.

2. Adsorption versus absorption

Adsorption is, in general, the adhesion of ions or molecules of gases, liquids or dissolved solids to a solid surface [27]. Adsorption phenomenon is an exothermic process in which molecules of a liquid or gas, called adsorbate, accumulate on a solid surface, called adsorbent [28,29]. Adsorbents are porous materials with ability to take up several times of their volume of gases or liquids. The terms “adsorption” and “absorption” are usually assumed to be the same, but they are, in essence, completely different physical phenomena. In the adsorption process, molecules of gas or liquid adhere on the surface of the solid, whereas in the absorption process, molecules of gas or liquid penetrate into the solid or liquid phase.

3. Thermodynamic cycle of ACS

ACS work based on two main steps: heating–desorption–condensation and cooling–adsorption–evaporation. Using these steps, the ACS produces evaporative cooling power intermittently. To produce continuous cooling power, the solution is to use more than one adsober bed. Fig. 1a depicts the schematic of a 2-adsorber bed ACS. The main components of an ACS consist of adsorber beds, condenser, expansion valve, and evaporator. Therefore, the ACS is similar to the VCRC, except that the adsorber beds replace the compressor.

Thermodynamic cycle of an ACS, Fig. 1b, includes four processes: (1) Isosteric heating (ih), process 1–2; (2) Isobaric desorption (ibd), process 2–3′; (3) Isosteric cooling (ic), process 3′–4′; and (4) Isobaric adsorption (iba), process 4′-1. During step 1–2, adsorbent-adsorbate pair through an isosteric process, absorbs heat in amount of Q_{ih} from an external heat source. In this step, temperature and pressure of the adsorber bed increase due to the adsorbate desorption from the adsorbent particles. This process is continued until the pressure of adsorber bed reaches the pressure of condenser. At this time, the entrance valve to the condenser is opened [19].

In step 2–3′, the external heat source continuously heats the adsorber bed (Q_{ibd}) during an isobaric desorption process and the adsorbate leaves the adsorber bed and is condensed inside the condenser during an isobaric cooling process (step 2–3) [19]. After heating the adsorber bed up to the point 3′ which is the maximum temperature of the cycle, the valve between the adsorber bed and the condenser is closed and during an isosteric cooling process (step 3′–4′), the adsorbent loses its heat (Q_{ic}) in contact with a heat sink [19]. In step 3–4, the adsorbate inside the condenser passes through the expansion valve and enters to the evaporator. During step 4–1, the adsorbate absorbs heat in amount of Q_{evap} from the environment of interest and converts to the vapor. At the same time, the entrance valve to the adsorber bed is opened and the adsorbent adsorbs the vapor adsorbate during an isobaric adsorption process (step 4′–1) and releases its heat (Q_{ibd}) [19].

Waste-heat of engine and solar energy can be utilized to desorb adsorbate from adsorbent during the desorption process. Waste-heat and solar driven ACS for ice making and building A/C applications have been discussed at length in literature [25,31–34]. Although many attempts carried out to improve the performance of ACS, the available systems are still bulky thus not suitable for vehicle A/C–R applications. Adsorbent–adsorbate pair, thermodynamic cycle, and adsorber bed are effective factors on the performance of ACS.

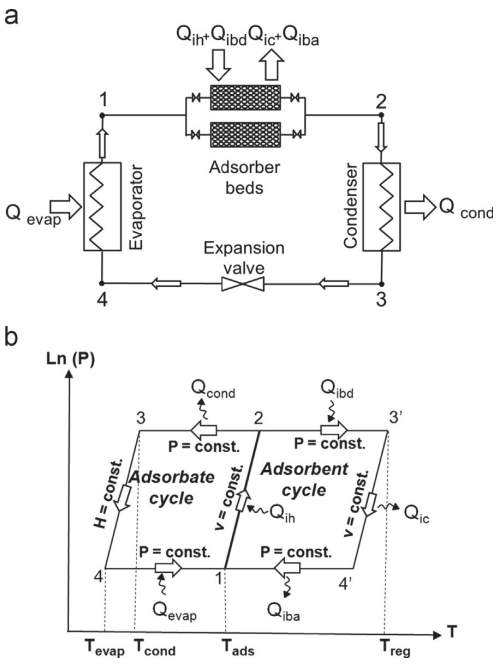

Fig. 1. (a) Schematic, and (b) Thermodynamic cycle of a 2-adsorber bed ACS [30].

3.1. Adsorbent materials

Zeolite, silica gel and activated carbon are common materials applied in ACS. Recently, new composite adsorbent materials have been designed with higher sorption rate such as zeolite–$CaCl_2$ and silica gel–$CaCl_2$. More information about adsorption working pairs was reported by Wang et al. [35]. Adsorbent materials are porous particles with low thermal conductivity. Also, thermal contact resistance between the adsorbent particles reduces the overall thermal conductivity of the adsorber beds [10,36–38]. Beside, adsorbate diffusion coefficient through the solid adsorbent particles is small. For instance, water vapor diffusion coefficient in a 2-mm silica gel bead is in the order of 10^{-10}–10^{-12} m^2/s [39].

3.2. Different ACS thermodynamic cycles

Different adsorption cycles were designed for proof-of-concept demonstrations. The simplest cycle is single-bed ACS which work intermittently such as solar driven ACS. To produce continuous cooling power, two- to six-bed ACS have been designed [40–45]. Although multi-bed ACS provide continuous cooling, they are more complex, heavier and bulkier than the single-bed ACS. Fig. 2 shows a six-bed, silica gel–water ACS which works with 40–90 °C heat sources to produce evaporative cooling power of 1.14–4.0 kW [43]. Unfortunately, the cost of these systems has not been reported in the literature; however, according to the

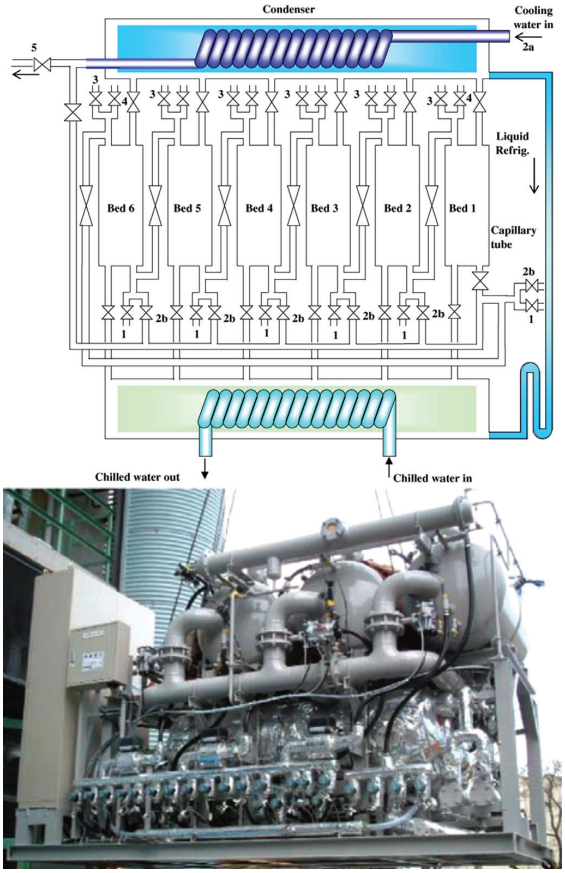

Fig. 2. A six-bed, silica gel–water, waste-heat driven ACS for building A/C applications designed by Saha et al. [43].

information prepared by SorTech AG Company who builds 8-kW adsorption cooling systems for building air conditioning applications, the cost of this system is about $27,000.

To improve the performance of ACS, some modifications are proposed such as adding heat recovery cycle [46], heat and mass recovery cycles [47], thermal wave cycle [48], forced convective thermal wave cycle [49], and cascade cycle [50,51]. In an ACS with heat recovery cycle, heat is transferred to the heat transfer fluid from a hot bed at the end of the desorption process to a cold bed at the start of the desorption process to recover heat between two or more adsober beds. In heat and mass recovery cycles, which borrow the same concept as the heat recovery cycle, heat is transferred to the heat transfer fluid from the hot bed to the cold bed, and adsorber beds are, also, directly connected to each other. In the mass recovery cycle, a hot bed with high pressure at the end of desorption process is connected to a cold bed with low pressure at the start of desorption process. Due to the pressure gradient between the beds, the remainder of the adsorbate inside the hot bed with high pressure is transferred to the cold bed which is at low pressure. The advantage of heat and mass recovery cycles is that they do not add more complexity to the system while significantly increase the performance of ACS. Adding heat and mass recovery cycles to a 2-adsorber bed ACS can increase the COP up to 30% [52,53]. Also, Qu et al. experimentally showed that adding only mass recovery cycle to the ACS can increase the cooling capacity by 20% [52]. The other modifications have some limitations and complexities; more detailed information is available elsewhere, e.g. [54]. Heat and mass recovery cycles are mainly of interest for building A/C applications where the amount of waste heat is limited and the COP is a major concern. In vehicles, however, waste-heat is abundant and added weight, cost and complexity due to the heat recovery cycle are problematic. As such, ACS with only mass recovery cycle suffices for vehicle A/C–R applications.

4. Important parameters to evaluate the performance of ACS

The SCP, adsorber bed to adsorbent mass ratio, and COP are the three main parameters used to evaluate the overall performance of ACS in this study.

4.1. Specific cooling power (SCP)

It is defined as the ratio of evaporative cooling energy to the mass of dry adsorbent multiplied by the cycle time, Eq. (1). The SCP represents the amount of cooling power produced per unit mass of dry adsorbent.

$$\mathrm{SCP} = \frac{Q_{evap}}{m_{sorbent}\tau_{cycle}} \left(W/\mathrm{kg\ dry\ adsorbent}\right) \tag{1}$$

where Q_{evap} is the evaporative cooling energy (J), $m_{sorbent}$ is the mass of dry adsorbent (kg) and τ_{cycle} is the cycle time (s), respectively. Eq. (2) defines Q_{evap}:

$$Q_{evap} = m_{sorbent}\int_{time}^{adsorption}\left(h_{sat,\ vapor@T_{evap}} - h_{sat,\ liquid@T_{cond}}\right)\frac{d\omega}{dt}dt\ (J) \tag{2}$$

where ω is the adsorbate to dry adsorbent mass ratio (kg/kg dry adsorbent), $d\omega/dt$ is the adsorbate sorption rate by adsorbent particles, and h_{sat} is the adsorbate saturation enthalpy (J/kg), respectively. Adsorbate sorption rate represents the amount of adsorbate uptake by the adsorbent particles as a function of time. By substituting Eq. (2) in Eq. (1), the SCP is expressed as follows:

$$SCP = \frac{1}{\tau_{cycle}}\int_{time}^{adsorption}\left(h_{sat,\ vapor@T_{evap}} - h_{sat,\ liquid@T_{cond}}\right)\frac{d\omega}{dt}dt\ \left(W/\mathrm{kg\ dry\ adsorbent}\right) \tag{3}$$

Eq. (3) shows that the SCP increases by increasing adsorbate sorption rate and enthalpy difference, and decreasing the cycle time. Adsorbate sorption rate increases by decreasing heat and mass transfer resistances within the adsober bed as well as designing new adsorbents with higher sorption rate. To increase the enthalpy difference inside the evaporator, a practical solution is to install a receiver tank between the condenser and the expansion valve. The receiver tank helps to accumulate sub-cooled liquid adsorbate at the outlet of condenser. Sub-cooling is a process by which a saturated liquid adsorbate is cooled below the saturation temperature of condenser.

The SCP of ACS for vehicle A/C–R applications should be maximized since the foot-print and weight of A/C–R system are of great importance. A typical value for the SCP of waste-heat driven ACS reported in open literature is 80–150 W/kg dry adsorbent. However, the current SCP definition, Eq. (3), does not show all aspects of ACS performance. The deadweight and volume of the adsorber beds are not included in the above SCP definition. For example, consider a thin layer of adsorbent that is coated on the surface of an adsorber bed; The resulting SCP value becomes large due to small heat and mass transfer resistances inside the bed which result in high adsorbate sorption rate and, consequently, short cycle time. However, the weight and volume of the adsorber bed create an excessively large and bulky system. Such very high SCP values were reported by Critoph et al. [23,55–58]. Besides, the adsorbent mass does not directly affect the SCP value, as shown in Eq. (3); this can be misinterpreted by the unit of SCP (W/kg dry adsorbent). The term that affects the SCP value is the adsorbate sorption rate, $d\omega/dt$. To overcome this issue and describe accurately the compactness of ACS, the following parameters are recommended for the evaluation of ACS performance:

- Volumetric specific cooling power (VSCP) which shows the effects of adsorber beds volume:

$$\mathrm{VSCP} = \frac{Q_{evap}}{V_{bed}\tau_{cycle}} \left(W/m^3\ \mathrm{adsorber\ bed}\right) \tag{4}$$

  where V_{bed} is the adsorber beds total volume (m^3).
- Adsorber bed to adsorbent mass ratio which represents the ratio of dead to live masses. When heating or cooling the adsorbent particles, the adsorber bed metal is, also, heated up or cooled down. Therefore, lower metal mass results in faster heating and cooling of adsorbent particles in a shorter cycle time, and consequently, higher SCP.

4.2. Coefficient of performance (COP)

To evaluate the efficiency of refrigeration cycles, a dimensionless parameter called COP is used. In ACS, the COP is defined as the ratio of evaporative cooling energy to the amount of supplied heat, Eq. (5).

$$\mathrm{COP} = \frac{Q_{evap}}{Q_{waste\ heat}} \tag{5}$$

where Q_{evap} and $Q_{waste\ heat}$ are the evaporative cooling energy (J) and the amount of waste heat energy supplied during the

desorption process (J), respectively. Eq. (6) defines $Q_{waste\ heat}$:

$$Q_{waste\ heat} = m_{sorbent} \int_{desorption\ time} \left[(c_{sorbent} + c_{p,\ liquid\ adsorbate}\ \omega + \frac{m_{bed}}{m_{sorbent}} c_{bed}) \frac{dT}{dt} - \Delta h_{ads} \frac{d\omega}{dt} \right] dt\ (J) \quad (6)$$

where $m_{bed}/m_{sorbent}$ is the adsober bed to adsorbent mass ratio, c_p is the specific heat capacity at constant pressure (J/kg/K) and Δh_{ads} is the enthalpy of adsorption (J/kg), respectively. As shown in Eqs. (2) and (6), to increase the COP under constant evaporation and condensation temperatures, the adsorbate sorption rate, $d\omega/dt$, should be increased and the adsorber bed to adsorbent mass ratio, $m_{bed}/m_{sorbent}$, should be decreased. The COP is important where the supplied energy is costly and limited, such as hot water in buildings.

4.3. Desired range for the performance of ACS

The cooling power required for A/C of a subcompact vehicle is approximately 1 t of refrigeration (TR) [17,42], which is equal to 3.517 kW. Lambert and Jones [41] showed that the total daily commute time in the U.S. is about 40 min, ≈20 min to work and ≈20 min returning home. A properly sized A/C of a light-duty vehicle should be able to cool down the cabin temperature within 10 min after start-up [59,60]. As a result, adsorption and desorption times in a 2-adsorber bed ACS with 10 min cycle time is 5 min (300 s). For example, the amount of water, which should be circulated through a 2-adsorber bed, silica gel–water ACS, to supply 1-TR cooling power is equal to:

$$m_{adsorbate} = \frac{\dot{Q}_{evap}(\mathrm{kW}) \times \Delta t_{adsorption}(\mathrm{s})}{h_{sat,\ water\ vapor@T_{evap}=10\ ^\circ C} - h_{sat,\ liquid\ water@T_{cond}=45\ ^\circ C}(\mathrm{kJ/kg})} = \frac{3.517 \times 300}{2519.2 - 188.44} = 0.453\ \mathrm{kg} \quad (7)$$

It should be noted that the amount of discharged adsorbate depends on the adsorbent particles filled inside the adsorber bed; here, silica gel is used for the calculation as it can work with low temperature heat sources ($<90\ ^\circ C$) such as engine coolant. The amount of equilibrium water uptake of silica gel particles is about $\omega = 0.185$ kg/kg dry silica gel at 35 °C and 1.2 kPa, which is equal to the evaporator saturation pressure at 10 °C, and $\omega = 0.05$ kg/kg dry silica gel at 90 °C and 9.6 kPa, which is equal to the condenser saturation pressure at 45 °C [61,62]. However, in a real adsorption cycle, adsorbent does not fully saturated with adsorbate during the adsorption process and it does not completely dry out during the desorption process. It has been shown that a typical water uptake and discharge difference for silica gel particles, $\Delta\omega$, is approximately 0.09–0.1 kg/kg dry silica gel [62]. Therefore, the amount of silica gel per adsorber bed is calculated as follows:

$$m_{sorbent} = \frac{m_{adsorbate}}{\Delta\omega} = \frac{0.453}{0.09} = 5\ \mathrm{kg\ dry\ silica\ gel/bed} \quad (8)$$

By substituting the calculated parameters in Eq. (1), the maximum SCP of a 2-adsorber bed, silica gel–water ACS can be estimated as follows:

$$SCP_{max} = \frac{\dot{Q}_{evap} \times \Delta t_{adsorption}}{m_{sorbent}\tau_{cycle}} = \frac{3.517 \times 10^3 \times 300}{5 \times 600} \approx 350\ W/\mathrm{kg\ dry\ adsorbent} \quad (9)$$

To reach the maximum SCP, an adsorber bed with the following characteristics is required: (i) high heat transfer surface area to increase heat transfer rate, and (ii) low adsorbent thickness to increase mass transfer rate. To design an adsorber bed with such characteristics, the amount of utilized metal (dead mass) increases significantly. A critical factor for auxiliary systems designed for vehicle applications is dead mass which should be minimized. Therefore, the adsorber bed to adsorbent mass ratio in an ACS should be reduced. Here, the goal is to reach the ideal adsorber bed to adsorbent mass ratio of less than one.

The COP of waste-heat driven ACS is less than that of VCRCs. Meunier [63] theoretically showed that the COP of an ACS with an infinite number of cascades reaches 1.8; however, the practical COP of ACS is about 0.3–0.4. In vehicle A/C–R applications, the COP of ACS is not as important as the SCP and adsorber bed to adsorbent mass ratio because the supplied heat comes from the ICE coolant and/or the exhaust gas. However, ACS with higher COP are preferred. In brief, the order of importance to evaluate suitability of a waste-heat driven ACS for vehicle A/C–R applications are: (i) high SCP; (ii) low adsorber bed to adsorbent mass ratio; and (iii) high COP.

5. Comparison of existing ACS adsorber bed designs

A number of literature reviews have been published on waste-heat driven ACS with a focus on challenges and opportunities facing ACS development; however, they lack practical solutions toward design of efficient adsorber beds for waste-heat driven ACS; for more information refer to Ref. [19,34,35,54,64–78].

To increase heat and mass transfer within an adsorber bed, different heat exchangers are used in previous studies. Fig. 3 shows nine different types of adsorber beds used in different experiments/studies of waste-heat driven ACS.

The main goals of using heat exchangers in adsorber beds are to increase heat transfer surface area between the heat transfer fluids and adsorbent particles during adsorption and desorption processes, and to decrease mass transfer resistance between adsorbate and adsorbent particles. However, there is no conclusive evidence on which types of adsorber bed are suitable for vehicle A/C–R applications. To find proper adsorber bed types, the data reported in the literature is summarized in Table 1 based on working pairs, cooling capacity, COP, SCP, cycle time, and adsorber bed to adsorbent mass ratio. To compare the data tabulated in Table 1, we tried to extract the reported cooling capacity, SCP and COP of ACS at evaporation and condensation temperatures of 10 and 45 °C, respectively; these temperatures are in agreement with those of required for vehicle A/C purposes. Also, minimum and maximum temperatures of the adsorber beds are set at an adsorption temperature of 45 °C, and a regeneration temperature of 90 °C for silica gel and activated carbon, and 180 °C for zeolite; however, in some studies, the performance of ACS was not available in the operating temperatures mentioned above.

As shown in Table 1, different working pairs are utilized in waste-heat driven ACS. Silica gel desorbs water using low temperature heat sources ($<90\ ^\circ C$) which is appropriate for A/C applications. Activated carbon is another adsorbent material which works with higher temperature heat sources ($<130\ ^\circ C$) and adsorbs different adsorbates such as ethanol, methanol and ammonia. Beyond 140 °C, methanol is dissociated at the presence of activated carbon as it acts as a catalyst for methanol [46]. The condenser and evaporator pressures in the ACS are fixed by the adsorbate saturation pressures at condensation and evaporation temperatures, respectively. As a result, ACS, which work using water, methanol, or ethanol as an adsorbate, operate under vacuum pressures, while activated carbon–ammonia ACS work above atmospheric pressures. Lambert and Jones [41,42], and Critoph et al. [12,70,93,94] designed activated carbon–ammonia ACS for vehicle A/C–R applications; however, we do not

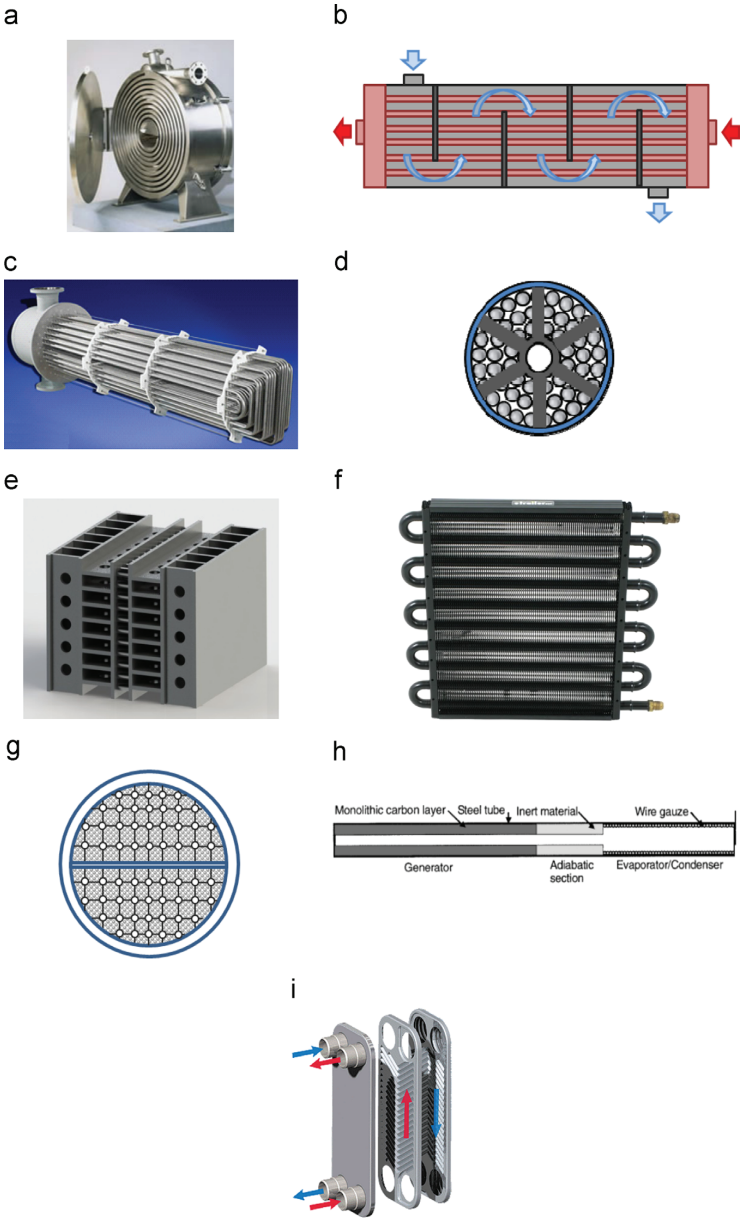

Fig. 3. Various heat exchanger types used as adsorber bed of waste-heat driven ACS. (a) Spiral plate [20,79], (b) Shell and tube [80,81], (c) Hairpin [51], (d) Annulus tube [82], (e) Plate fin [83–85], (f) Finned tube [86–88], (g) Plate-tube [52,53,67,89–91], (h) Simple tube [23,55–58], (i) Plate [92].

recommend them for vehicle A/C–R applications because of the poisonous nature of ammonia.

Zeolite can work with high temperature heat sources ($>180\ ^{\circ}C$) such as exhaust gas of engine which is at least 400 °C at the idle condition [120,121]. Zeolite is more durable than silica gel and activated carbon [122]. For instance, water uptake capacity of zeolite Na-13X reduces by 20% after 3500 cycles of adsorption and desorption, whereas adsorbate uptake capacity of silica gel and activated carbon reduces by 35% after 1600 cycles [122]. Moreover, adsorbate uptake capacity of zeolite is more than that of activated carbon and silica gel. In other words, to uptake a specific amount of adsorbate, less amount of zeolite is required compared with activated carbon and silica gel. The other important factor for vehicle A/C–R systems is adsorbent density which affects the bulkiness of adsorber bed. Density of zeolite and silica gel beads are about 800 [10] and 700–750 kg/m^3 [123], respectively, whereas density of activated carbon pellets is between 400–500 kg/m^3 [23]. Therefore, volume of adsorber beds filled

Table 1
Summary of existing studies on waste-heat driven ACS for A/C–R application. Summary of existing studies on waste-heat driven ACS for A/C–R application.

Reference no.	Working pairs	Cooling capacity	Cycle time (min)	COP	SCP (W/kg)	Adsorber bed info.	Adsorbent mass	Adsorber bed to adsorbent mass ratio
[51]	Zeolite/water, Act. carbon/methanol	1.44 kW[a], (14351 kJ)	164	0.65[a]	23[a]	3 Copper hairpin HEX, 3 × 118 kg	12.5+23.5+27.5=63.5 kg, 1.5 mm in dia.	9.4, 5, 4.3, Average: 6.3
[86–88]	Consolidated act. carbon/ammonia	52.8 W[a]	20	0.061[a]	33[a]	Aluminum finned tube HEX, 4.6 kg[a]	0.8 kg	5.75[a]
[95]	Silica gel/methanol	23 W[a] (70 kJ)[a]	65	–	30[a]	SS[b] Finned tube HEX[c]	0.6 kg	–
[96–98]	Zeolite 13X/water	242.6 W (1114 kJ)	131.5	0.38	22.8[a]	SS cylindrical finned tube HEX, 31 kg	6.2 kg, 2–3 mm in dia.	5
[11,99]	Zeolite 13X/water	6 kW[a]	180, Ads./Des.: 2/1	0.25	28.5	Finned tube HEX, 260 kg	140 kg, 3 mm in dia.	1.86
[100]	Silica gel+$CaCl_2$(SWS-1L)/water	60 W[a]	167, Ads./Des.: 3/4	0.43[a]	23.5[a]	SS finned tube HEX, 3.3 kg[a]	1.1 kg, 0.8–1.6 mm in dia.	3
[101]	AQSOA-FAM-Z02/water	1 kW[a]	8.6[a]	0.27[a]	131.5[a]	2 Aluminum finned tube HEX, 15 kg/bed	1.9 kg/bed	7.9
[102–104]	Silica gel/water	9.6 kW	34	0.43	48[a]	2 Finned tube HEX, 32.7 kg/bed	50 kg/bed, 0.5–1 mm in dia.	0.654
[105]	Coated hydrophobic Y zeolite (CBV-901)/methanol	–	18[a]	0.11[a]	25[a]	SS Finned tube HEX	Coated zeolite thickness: 10 mm	3
[106]	Silica gel/water	700 W[a]	37	0.29[a]	35[a]	2 Finned tube HEX	5 kg/bed	–
[31,107–109]	Act. carbon+$CaCl_2$ (1:4)/ammonia	680 W[a]	40[a]	0.19[a]	70.8[a]	2 Finned tube HEX	2.4 kg/bed	–
[110]	Silica gel+$CaCl_2$(SWS-1L)/water	480 W[a]	10	0.15	137[a]	Aluminum finned tube HEX, 6.08 kg	1.75 kg	3.47
[111]	Silica gel+$CaCl_2$/water	103 W[a]	100	0.23	43	Finned tube HEX	1.2 kg	–
[112]	Silica gel/water	1.9 kW	6	0.29	158[a]	2 Aluminum finned tube HEX, 13.6 kg/bed[a]	3 kg/bed	4.53
[113,114]	$LiNO_3$–Silica KSK/water	155 W[a] (42.9 kJ)[a]	6.4 Ads./Des.: 5/2	0.176[a]	318[a]	Aluminum finned tube HEX, 0.636 kg	0.350 kg, 0.25–0.5 mm in dia.	1.82
[82]	Consolidated graphite+zeolite 13X/water	213 W[a]	72[a]	0.28[a]	38[a]	SS 304 annulus tube HEX, 5.18 kg[a]	2.8 kg	1.85[a]
[21]	Consolidated zeolite/water	3.14 kW[a], (5657 kJ)	60	0.41	97	2 Annulus tube HEX	8.1 kg/bed	–
[20,79]	Act. carbon/methanol	31.5 kg ice/day	100	0.2	2.63 kg ice/kg adsorbent per day	2 SS spiral plate HEX, 80 kg/bed	6 kg/bed	13.3
[52,53,67,89–91]	Act. carbon/ammonia	15.8 kW[a] (19 MJ)[a]	40[a]	0.37[a]	152[a]	2 Plate-tube HEX, 90 kg[a]/bed	26 kg/bed	3.46[a]
[80,81]	Act. carbon/methanol	1.7 kW	50[a]	0.08[a]	7.6[a]	2 Shell and tube HEX, 184.8 kg/bed	56 kg/bed	3.3
[1]	Act. carbon/ammonia	500 kJ[a]	–	0.06[a]	–	4 Shell and tube HEX, 73 kg/bed[a]	8 kg/bed	9.1[a]
[23,55–58]	Consolidated act. carbon/ammonia	16 W	10	0.22	200	78.11 g/tube	38.78 g/tube	2.0
		42 W	3.3	0.19	550	609.97 g/tube	77.19 g	7.9
		27 W	5	0.18	350	770.66 g/tube	77.91 g	9.89
[12,70,93,94]	Consolidated act. carbon/ammonia	1.6 kW	1	0.22	800[a]	Plate HEX, 9 kg	1 kg	9
[92]	Silica gel/water	2336 kJ[a]	4.6	0.33[a]	118[a]	2 Plate HEX	36 kg/bed	–
[115,116]	Silica gel/water	21.4 kW[a]	20	0.51[a]	57[a]	4 Plate fin HEX, 115 kg/bed	47 kg/bed	2.45
[83–85]	Silica gel/water	2.8 kW[a]	17.66	0.21[a]	26.5[a]	2 Plate fin HEX, 180 kg/bed	26.4 kg/bed, 0.5–1 mm in dia.	6.8
[117]	Silica gel/water	8.5 kW[a]	17	0.36[a]	132[a]	2 Plate fin HEX, 115 kg/bed	16 kg/bed, 0.6 mm in dia.	7.2
[118]	Silica gel/water	4.3 kW	12	0.45	87.8[a]	Flat tube HEX with corrugated fins,	24.5 kg, 0.5–1.5 mm in dia.	–
[119]	Silica gel/water	3.7 kW	45	0.5	26[a]	2 HEX, 129 kg/bed	35 kg/bed	3.7

[a] We extracted these parameters based on the reported experimental data at T_{evap}=10 °C, T_{cond}=45 °C, T_{ads}=45 °C, and T_{reg}=90 °C (for silica gel and activated carbon) and T_{reg}=180 °C (for zeolite).
[b] SS: Stainless steel.
[c] HEX: Heat exchanger.

with the same amount of zeolite and silica gel are 1.4–2 times smaller than those of filled with activated carbon.

Although zeolite has shown better performance than activated carbon and silica gel, it starts to desorb adsorbate at temperatures higher than 110 °C [46]. As a result, zeolite–water ACS are costly because their valves, fittings, sensors, etc. should be rated for high temperatures. To reduce the maximum temperature of ACS and increase the adsorbate uptake capacity of adsorbents, new composite adsorbent materials have been introduced, see Table 1. The composite adsorbents are usually a mixture of an inorganic salt,

such as $CaCl_2$, LiBr and $MgCl_2$, which is impregnated in an adsorbent, such as silica gel, zeolite and activated carbon. Water uptake capacity of silica gel–$CaCl_2$,called selective water sorbent (SWS), is about 0.8 kg/kg dry adsorbent [62]. More detailed information on composite adsorbents is available elsewhere, see e.g. [35,62].

6. Results and discussions

The main functions of ACS adsorber beds are to provide proper heat and mass distribution within the adsorbent particles. The proposed method to select a proper adsorber bed designs for vehicle A/C–R applications is to compare the effects of various adsorber bed types on the SCP, adsorber bed to adsorbent mass ratio, and the COP. Fig. 4 shows the effects of different adsober beds on the performance of waste-heat driven ACS according to the tabulated data in Table 1. These adsorber beds are classified into nine groups: (1) Spiral plate (2 experiments), (2) Shell and tube (3 experiments), (3) Hairpin (1 experiments), (4) Annulus tube (2 experiments), (5) Plate fin (6 experiments), (6) Finned tube (25 experiments), (7) Plate-tube (7 experiments), (8) Simple tube (5 experiments), and (9) Plate (5 experiments). In Fig. 4, to compare the performance of different ACS, averaged values of SCPs, adsorber bed to adsorbent mass ratios and COPs are calculated due to a large number of experimental data for each adsorber bed type. For convenience, the data shown in Fig. 4 are sorted according to the ascending SCP.

As mentioned in Section 4.3, the maximum SCP of 350 W/kg dry adsorbent, adsorber bed to adsorbent mass ratio of less than one and high COP are the desired values for 1-TR ACS. To this end, adsorber bed types with higher SCPs located at the right-hand side of Fig. 4 is preferred. The second criterion is the adsorber bed to adsorbent mass ratio which is equal to 6.6 and 9 for simple tube and plate adsorber beds (adsorber bed No. 8 and 9 in Fig. 4a), respectively. Therefore, these adsorber beds are not recommended for vehicle applications as the dead mass is considerable. Our analyses based on the aforementioned criteria show that annulus tube, plate fin, finned tube, and plate-tube adsorber beds result in better performance than the other adsorber beds, demarcated gray region in Fig. 4.

Among the considered bed designs, annulus tube is suitable for small cooling capacity ACS as the amount of adsorbent filled inside the bed is limited to the volume between the two tubes, see Fig. 3d. As a result, the number of adsorber beds increases significantly to supply 1TR. In addition, by increasing the space between the two tubes, the adsorbent thickness increases which results in higher heat and mass transfer resistances inside the bed, and consequently, lower SCP and COP. Plate fin adsorber bed, shown in Fig. 3e, is a compact heat exchanger which results in an average SCP of 72 W/kg dry adsorbent, average adsorber bed to adsorbent mass ratio of 5.5, and average COP of 0.36, respectively; however, vacuum sealing of this type of adsober beds may be difficult due to its geometry, a large number of units stack over each other and vehicle's vibration.

Fig. 4 also shows that finned tube and plate-tube adsorber beds can supply an average SCP of 80–150 W/kg, average adsorber bed to adsorbent mass ratio of 3.45–3.6, and average COP of 0.25–0.37, respectively. The plate-tube adsorber beds are more compact than the finned tube adsorber beds; however, adsorbate should be able to penetrate into the center of plate-tube adsorber bed, see Fig. 3g. As such, mass transfer resistance within the adsorber bed increases. To this end, these adsober beds are mainly applicable for activated carbon–ammonia ACS in which typical operating pressures of evaporator and condenser are 3 and 30 bars, respectively, and adsorbate can easily penetrate into the center of adsorber bed; whereas the operating pressure of ACS, which work with water, ethanol and methanol as an adsorbent, is

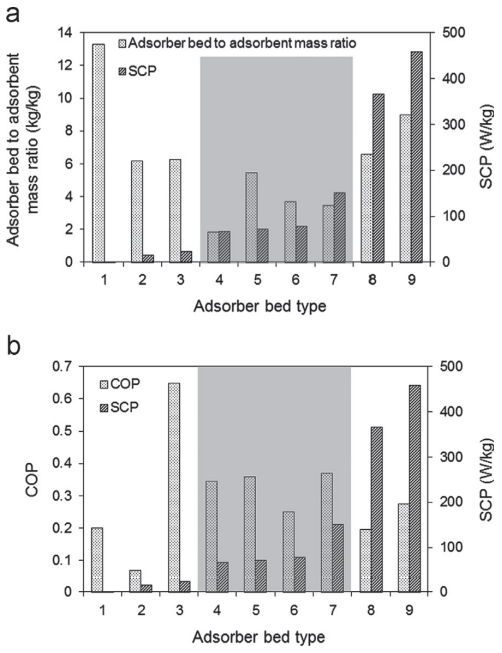

Fig. 4. Effects of different adsorber bed designs on: (a) adsorber bed to adsorbent mass ratio and SCP, and (b) COP and SCP. Adsorber bed type: (1) Spiral plate, (2) Shell and tube, (3) Hairpin, (4) Annulus tube, (5) Plate fin, (6) Finned tube, (7) Plate-tube, (8) Simple tube, and (9) Plate.

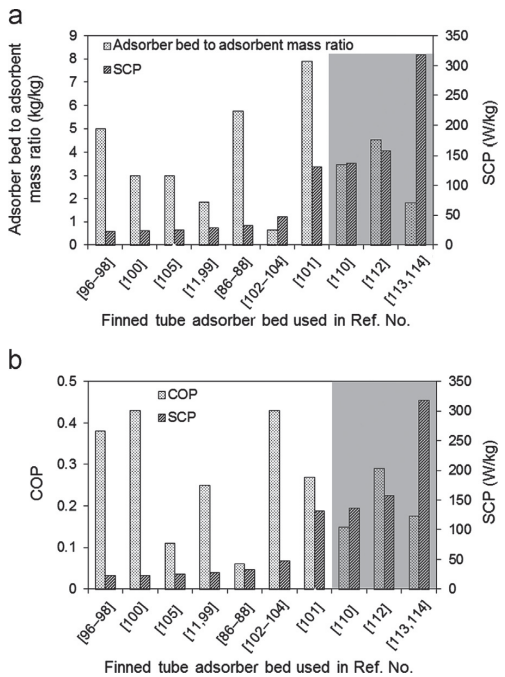

Fig. 5. Effects of different finned tube adsorber bed designs on: (a) adsorber bed to adsorbent mass ratio and SCP, and (b) COP and SCP.

below atmospheric pressure. For instance, the operating pressure of evaporator and condenser in an activated carbon–methanol ACS are 5 and 30 kPa (absolute pressure), respectively [20,79]. As a result, selecting an adsorber bed with small adsorbate penetration depth and ability to work with a variety of working pairs is preferred. To this end, finned tube adsorber bed design seems to be a better candidate among the existing designs.

As shown in Table 1, the studies conducted with finned tube adsorber beds show a variety of SCPs, adsorber bed to adsorbent mass ratios and COPs. To make the analysis easier, the effects of different finned tube adsorber bed designs are illustrated on the performance of waste-heat driven ACS in Fig. 5. The data shown in Fig. 5 are sorted based on the ascending SCP.

The gray region demarcated in Fig. 5 is selected based on the desired values for the ACS performance mentioned in Section 4.3. The finned tube adsorber beds used by Freni et al. [110], Verde et al. [112], and Sapienza et al. [113] and Aristov et al. [114] reported to achieve SCP of 137–318 W/kg dry adsorbent, adsorber bed to adsorbent mass ratio of 1.8–4.5, and COP of 0.15–0.29. The common features of these adsorber beds, depicted in Fig. 6, are a large number of fins to increase heat transfer surface area and small fin spacing to decrease adsorbent thickness. However, none of these heat exchangers are specifically designed for an ACS adsorber bed. For example, the heat exchanger used by Sapienza et al. and Aristov et al. is an off-the-shelf air-cooled heat exchanger manufactured by Valeo Thermique [113,114].

Although adsorber beds shown in Fig. 6 result in better performance, the cooling capacity of ACS designed by Freni et al. [110], Verde et al. [112], and Sapienza et al. [113] and Aristov et al. [114] are 480 W, 1.9 kW and 155 W with adsorbent mass of 1.75, 3 and 0.35 kg/bed, respectively. The calculation in Section 4.3 shows that to build a 1-TR (3.517 kW) ACS, 5 kg adsorbent per bed is required. As such, using off-the-shelf finned tube heat exchangers increase the volume and mass of the adsorber bed. As a consequence, a new finned tube adsorber bed, which is specifically sized and optimized for waste-heat driven ACS, should be designed and to improve its performance, the following suggestions should be considered:

- Optimization of fin spacing vs. the weight and volume of the finned tube adsorber bed.
- Calculation of proper fin height in the finned tube adsorber bed to have an effective heat transfer and, also, appropriate adsorbent thickness.
- Enhancing thermal conductivity of adsorbent materials, e.g. by adding metallic wire mesh and wire wool between adsorbent particles [124].

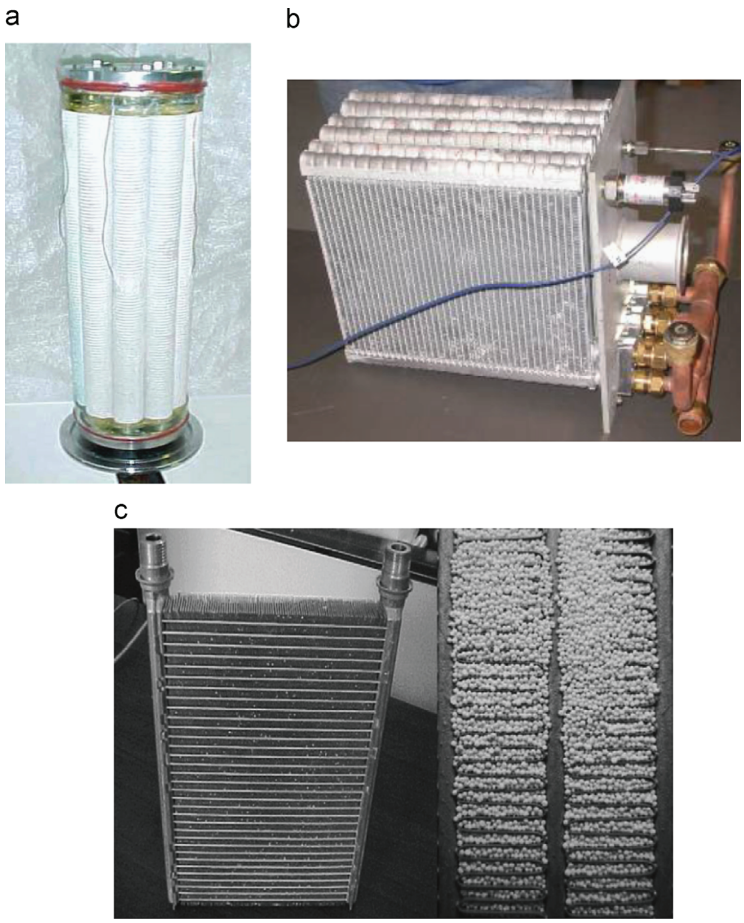

Fig. 6. The finned tube adsorber beds used in waste-heat driven ACS reported with high SCP. (a) Freni et al. [110], (b) Verde et al. [112], (c) Sapienza et al. [113] and Aristov et al. [114].

7. Conclusion

In this study, the effects of different available adsorber bed types were studied on the performance of waste-heat driven ACS for vehicle A/C–R applications. To assess the performance of ACS, the SCP, adsorber bed to adsorbent mass ratio and COP were used and their importance were explained. The SCP of 350 W/kg dry adsorbent, adsorber bed to adsorbent mass ratio of less than one were estimated as desired values for a 1-TR ACS. To this end, previous studies available in the literature were categorized based on their working pair, cooling capacity, COP, SCP, cycle time, and adsorber bed to adsorbent mass ratio. Based on the tabulated data, the adsorber beds were classified into nine types: (1) Spiral plate, (2) Shell and tube, (3) Hairpin, (4) Annulus tube, (5) Plate fin, (6) Finned tube, (7) Plate-tube, (8) Simple tube, and (9) Plate. Based on the estimated desired values for the 1-TR ACS, finned tube adsorber bed design was observed to have a better performance among the existing adsorber beds. Finally, prominent finned tube adsorber bed designs, based on the reported data, were selected for vehicle A/C–R applications and practical solutions, namely, optimization of fin spacing and fin height in finned tube adsorber beds, and increasing thermal conductivity of adsorbent materials, were proposed to increase heat and mass transfer rates inside the adsorber beds.

Acknowledgment

The authors gratefully acknowledge the financial support of the Natural Sciences and Engineering Research Council of Canada (NSERC) through the Automotive Partnership Canada Grant No. APCPJ 401826-10.

References

[1] RG Oliveira, Silveira V, Wang RZ. Experimental study of mass recovery adsorption cycles for ice making at low generation temperature. Appl Therm Eng 2006;26:303–11.
[2] TX Li, RZ Wang, LW Wang, ZS Lu, Chen CJ. Performance study of a high efficient multifunction heat pipe type adsorption ice making system with novel mass and heat recovery processes. Int J Therm Sci 2007;46:1267–74.
[3] Tamainot-Telto Z, SJ Metcalf, RE Critoph, Zhong Y, Thorpe R. Carbon–ammonia pairs for adsorption refrigeration applications: ice making, air conditioning and heat pumping. Int J Refrig 2009;32:1212–29.
[4] James SJ. Food refrigeration and thermal processing at Langford, UK: 32 years of research. Food Bioprod Process 1999:77.
[5] NJ Smale, Moureh J, Cortella G. A review of numerical models of airflow in refrigerated food applications. Int J Refrig 2006;29:911–30.
[6] Aneke M, Agnew B, Underwood C, Menkiti M. Thermodynamic analysis of alternative refrigeration cycles driven from waste heat in a food processing application. Int J Refrig 2012;35:1349–58.
[7] Critoph RE. An ammonia carbon solar refrigerator for vaccine cooling. Renewable Energy 1994;5:502–8.
[8] Hammad M, Habali S. Design and performance study of a solar energy powered vaccine cabinet. Appl Therm Eng 2000;20:1785–98.
[9] Dawoud B. A hybrid solar-assisted adsorption cooling unit for vaccine storage. Renewable Energy 2007;32:947–64.
[10] Restuccia G, Freni A, Maggio G. A zeolite-coated bed for air conditioning adsorption systems: parametric study of heat and mass transfer by dynamic simulation. Appl Therm Eng 2002;22:619–30.
[11] Jiangzhou S, RZ Wang, YZ Lu, YX Xu, Wu JY. Experimental investigations on adsorption air-conditioner used in internal-combustion locomotive driver-cabin. Appl Therm Eng 2002;22:1153–62.
[12] Tamainot-Telto Z, SJ Metcalf, Critoph RE. Novel compact sorption generators for car air conditioning. Int J Refrig 2009;32:727–33.
[13] Uçkan İ, Yılmaz T, Hürdoğan E, Büyükalaca O. Experimental investigation of a novel configuration of desiccant based evaporative air conditioning system. Energy Convers Manage 2013;65:606–15.
[14] Haaf S, Henrici H. Refrigeration technology. Ullmann's encyclopedia of industrial chemistry. Wiley-VCH; 2002.
[15] Wang S. Handbook of air conditioning and refrigeration. 2nd ed.McGraw-Hill Professional; 2000.
[16] Farrington R, Rugh J. Impact of vehicle air-conditioning on fuel economy, tailpipe emissions, and electric vehicle range. In: Proceeding of the Earth Technologies Forum, Washington, D.C.; 2000.
[17] Christy C, Toossi R. Adsorption air-conditioning for containerships and vehicles; 2004.
[18] MO Abdullah, IAW Tan, Lim LS. Automobile adsorption air-conditioning system using oil palm biomass-based activated carbon: a review. Renewable Sustainable Energy Rev 2011;15:2061–72.
[19] Demir H, Mobedi M, Ülkü S. A review on adsorption heat pump: problems and solutions. Renewable Sustainable Energy Rev 2008;12:2381–403.
[20] RZ Wang, JY Wu, YX Xu, Wang W. Performance researches and improvements on heat regenerative adsorption refrigerator and heat pump. Energy Convers Manage 2001;42:233–49.
[21] Poyelle F, JJ Guilleminot, Meunier F. Experimental tests and predictive model of an adsorptive air conditioning unit. Ind Eng Chem Res 1999;38:298–309.
[22] Freni A, MM Tokarev, Restuccia G, AG Okunev, Aristov YI. Thermal conductivity of selective water sorbents under the working conditions of a sorption chiller. Appl Therm Eng 2002;22:1631–42.
[23] Tamainot-Telto Z, Critoph RE. Monolithic carbon for sorption refrigeration and heat pump applications. Appl Therm Eng 2001;21:37–52.
[24] Wojcik a. MW, Jansen JC, Maschmeyer T. Regarding pressure in the adsorber of an adsorption heat pump with thin synthesized zeolite layers on heat exchangers. Microporous Mesoporous Mater 2001;43:313–7.
[25] BB Saha, Akisawa A, Kashiwagi T. Solar/waste heat driven two-stage adsorption chiller : the prototype. Renewable Energy 2001;23:93–101.
[26] De Boer R, Smeding SF, Grisel RJH. Development and testing of a sorbent filled heat exchanger for use in compact solid sorption cooling systems. In: Proceeding of international sorption heat pump conference, Denver, USA; 2005.
[27] SJ Gregg, Sing KSW. Adsorption, surface area, and porosity. 2nd ed. Academic Press; 1982.
[28] De Saussure NT. No Title. NT Gilbert's Annual; 1814 47:113–8.
[29] Favre PA. No Title. Comptes Rendus de l'Académie Des Sciences ; 1854. 39:16.
[30] Sharafian A, Bahrami M. A quasi steady state model for adsorption cooling systems: automotive applications. In: ASME 2012 sixth international conference on energy sustainability & 10th fuel cell science, engineering and technology conference, San Diego, CA, USA; 2012.
[31] LW Wang, RZ Wang, ZS Lu, CJ Chen, Wang K, Wu JY. The performance of two adsorption ice making test units using activated carbon and a carbon composite as adsorbents. Carbon 2006;44:2671–80.
[32] ZS Lu, RZ Wang, TX Li, LW Wang, Chen CJ. Experimental investigation of a novel multifunction heat pipe solid sorption icemaker for fishing boats using $CaCl_2$/activated carbon compound–ammonia. Int J Refrig 2007;30:76–85.
[33] LW Wang, RZ Wang, ZZ Xia, Wu JY. Studies on heat pipe type adsorption ice maker for fishing boats. Int J Refrig 2008;31:989–97.
[34] Askalany A a, BB Saha, Kariya K, IM Ismail, Salem M, AHH Ali, et al. Hybrid adsorption cooling systems—an overview. Renewable Sustainable Energy Rev 2012;16:5787–801.
[35] LW Wang, RZ Wang, Oliveira RG. A review on adsorption working pairs for refrigeration. Renewable Sustainable Energy Rev 2009;13:518–34.
[36] Eun T, Song H, Hun J, Lee K, Kim J. Enhancement of heat and mass transfer in silica-expanded graphite composite blocks for adsorption heat pumps : Part I. Characterization of the composite blocks. Int J Refrig 2000;23:64–73.
[37] Zhu D, Wang S. Experimental investifation of contact resistance in adsorber of solar adsorption refrigeration. Solar Energy 2002;73:177–85.
[38] Rezk A, RK Al-Dadah, Mahmoud S, Elsayed A. Effects of contact resistance and metal additives in finned-tube adsorbent beds on the performance of silica gel/water adsorption chiller. Appl Therm Eng 2013;53:278–84.
[39] Sharafian A, Bahrami M. Adsorbate uptake and mass diffusivity of working pairs in adsorption cooling systems. Int J Heat Mass Transfer 2013;59:262–71.
[40] KCA Alam, Akahira A, Hamamoto Y, Akisawa A, Kashiwagi T. A four-bed mass recovery adsorption refrigeration cycle driven by low temperature waste/renewable heat source. Renewable Energy 2004;29:1461–75.
[41] MA Lambert, Jones BJ. Automotive adsorption air conditioner powered by exhaust heat. Part 1: Conceptual and embodiment design. Proc Inst Mech Eng Part D: J Automob Eng 2006;220:959–72.
[42] MA Lambert, Jones BJ. Automotive adsorption air conditioner powered by exhaust heat. Part 2: Detailed design and analysis. Proc Inst Mech Eng Part D: J Automob Eng 2006;220:973–89.
[43] BB Saha, Koyama S, Choon Ng K, Hamamoto Y, Akisawa A, Kashiwagi T. Study on a dual-mode, multi-stage, multi-bed regenerative adsorption chiller. Renewable Energy 2006;31:2076–90.
[44] Verde M, Cortés L, JM Corberán, Sapienza A, Vasta S, Restuccia G. Modelling of an adsorption system driven by engine waste heat for truck cabin A/C. Performance estimation for a standard driving cycle. Appl Therm Eng 2010;30:1511–22.
[45] Freni A, Sapienza A, IS Glaznev, YI Aristov, Restuccia G. Experimental testing of a lab-scale adsorption chiller using a novel selective water sorbent "silica modified by calcium nitrate." Int J Refrig 2012;35:518–24.
[46] Cacciola G, Restuccia G. Reversible adsorption heat pump: a thermodynamic model. Int J Refrig 1995;18:100–6.
[47] Akahira A, Alam KC a, Hamamoto Y, Akisawa A, Kashiwagi T. Mass recovery adsorption refrigeration cycle—improving cooling capacity. Int J Refrig 2004;27:225–34.
[48] SV Shelton, DJ Miles, Wepfer WJ. Ramp wave analysis of the solid/vapor heat pump. J Energy Res Technol 1990;112:69–78.

[49] Critoph RE. Forced convection enhancement of adsorption cycles. Heat Recovery Syst CHP 1994;14:343–50.
[50] Douss N, Meunier F, Sun LM. Predictive model and experimental results for a two-adsorber solid adsorption heat pump. Ind Eng Chem Res 1988;27:310–6.
[51] Douss N, Meunier F. Experimental study of cascading adsorption cycles. Chem Eng Sci 1989;44:225–35.
[52] TF Qu, RZ Wang, Wang W. Study on heat and mass recovery in adsorption refrigeration cycles. Appl Therm Eng 2001;21:439–52.
[53] Wang RZ. Performance improvement of adsorption cooling by heat and mass recovery operation. Int J Refrig 2001;24:602–11.
[54] DC Wang, YH Li, Li D, YZ Xia, Zhang JP. A review on adsorption refrigeration technology and adsorption deterioration in physical adsorption systems. Renewable Sustainable Energy Rev 2010;14:344–53.
[55] Critoph RE. Simulation of a continuous multiple-bed regenerative adsorption cycle. Int J Refrig 2001;24:428–37.
[56] Critoph RE. Multiple bed regenerative adsorption cycle using the monolithic carbon–ammonia pair. Appl Therm Eng 2002;22:667–77.
[57] Tamainot-Telto Z, Critoph RE. Advanced solid sorption air conditioning modules using monolithic carbon–ammonia pair. Appl Therm Eng 2003;23:659–74.
[58] Critoph RE. Adsorption refrigeration research at Warwick. 1st TECCS meeting; 2007.
[59] Boatto P, Boccaletti C, Cerri G, Malvicino C. Internal combustion engine waste heat potential for an automotive absorption system of air conditioning Part 1: Tests on the exhaust system of a spark-ignition engine. Proc Inst Mech Eng Part D: J Automob Eng 2000;214:979–82.
[60] Boatto P, Boccaletti C, Cerri G, Malvicino C. Internal combustion engine waste heat potential for an automotive absorption system of air conditioning Part 2: The automotive absorption system. Proc Inst Mech Eng Part D: J Automob Eng 2000;214:983–9.
[61] HT Chua, KC Ng, Chakraborty A, NM Oo, Othman MA. Adsorption characteristics of silica gel+water systems. J Chem Eng Data 2002;47:1177–81.
[62] BB Saha, Chakraborty A, Koyama S, Aristov YI. A new generation cooling device employing $CaCl_2$-in-silica gel–water system. Int J Heat Mass Transfer 2009;52:516–24.
[63] Meunier F, Poyelle F, LeVan MD. Second-law analysis of adsorptive refrigeration cycles: the role of thermal coupling entropy production. Appl Therm Eng 1997;17:43–55.
[64] Critoph RE. Forced convection adsorption cycles. Appl Therm Eng 1998;18:799–807.
[65] NC Srivastava, Eames IW. A review of adsorbents and adsorbates in solid–vapour adsorption heat pump systems. Appl Therm Eng 1998;18:707–14.
[66] Meunier F. Solid sorption heat powered cycles for cooling and heat pumping applications. Appl Therm Eng 1998;18:715–29.
[67] Wang RZ. Adsorption refrigeration research in Shanghai Jiao Tong University. Renewable Sustainable Energy Rev 2001;5:1–37.
[68] Yong L, Sumathy K. Review of mathematical investigation on the closed adsorption heat pump and cooling systems. Renewable Sustainable Energy Rev 2002;6:305–38.
[69] Lambert M a, Jones BJ. Review of regenerative adsorption heat pumps. J Thermophys Heat Transfer 2005;19:471–85.
[70] RE Critoph, Zhong Y. Review of trends in solid sorption refrigeration and heat pumping technology. Proc Inst Mech Eng Part D J Automob Eng 2005;219:285–300.
[71] SG Wang, RZ Wang, Li XR. Research and development of consolidated adsorbent for adsorption systems. Renewable Energy 2005;30:1425–41.
[72] RZ Wang, Oliveira RG. Adsorption refrigeration—an efficient way to make good use of waste heat and solar energy. Prog Energy Combust Sci 2006;32:424–58.
[73] Fan Y, Luo L, Souyri B. Review of solar sorption refrigeration technologies: development and applications. Renewable Sustainable Energy Rev 2007;11:1758–75.
[74] Attan D, Alghoul M a, BB Saha, Assadeq J, Sopian K. The role of activated carbon fiber in adsorption cooling cycles. Renewable Sustainable Energy Rev 2011;15:1708–21.
[75] Askalany A a, Salem M, IM Ismail, AHH Ali, Morsy MG. A review on adsorption cooling systems with adsorbent carbon. Renewable Sustainable Energy Rev 2012;16:493–500.
[76] THC Yeo, Tan I aW, Abdullah MO. Development of adsorption air-conditioning technology using modified activated carbon—a review. Renewable Sustainable Energy Rev 2012;16:3355–63.
[77] Kalkan N, Young E a, Celiktas A. Solar thermal air conditioning technology reducing the footprint of solar thermal air conditioning. Renewable Sustainable Energy Rev 2012;16:6352–83.
[78] Askalany A a, Salem M, IM Ismael, AHH Ali, MG Morsy, Saha BB. An overview on adsorption pairs for cooling. Renewable Sustainable Energy Rev 2013;19:565–72.
[79] RZ Wang, JY Wu, YX Xu, Teng Y, Shi W. Experimental on a continuous heat regenerative adsorption refrigerator using spiral plate heat exchanger as adsorbers. Appl Therm Eng 1998;18:13–23.
[80] Wang D, Wu J, Shan H, Wang R. Experimental study on the dynamic characteristics of adsorption heat pumps driven by intermittent heat source at heating mode. Appl Therm Eng 2005;25:927–40.
[81] Wang D, Wu J. Influence of intermittent heat source on adsorption ice maker using waste heat. Energy Convers Manage 2005;46:985–98.
[82] Pons M, Laurent D, Meunier F. Experimental temperature fronts for adsorptive heat pump applications. Appl Therm Eng 1996:16.
[83] YL Liu, RZ Wang, Xia ZZ. Experimental performance of a silica gel–water adsorption chiller. Appl Therm Eng 2005;25:359–75.
[84] YL Liu, RZ Wang, Xia ZZ. Experimental study on a continuous adsorption water chiller with novel design. Int J Refrig 2005;28:218–30.
[85] DC Wang, ZZ Xia, Wu JY. Design and performance prediction of a novel zeolite–water adsorption air conditioner. Energy Convers Manage 2006;47:590–610.
[86] Critoph RE. Towards a one tonne per day solar ice maker. Renewable Energy 1996;9:626–31.
[87] Tamainot-Telto Z, Critoph RE. Adsorption refrigerator using monolithic carbon–ammonia pair. Int J Refrig 1997;20:146–55.
[88] Critoph RE. Rapid cycling solar/biomass powered adsorption refrigeration system. Renewable Energy 1999;16:673–8.
[89] JY Wu, RZ Wang, Xu YX. Dynamic simulation and experiments of a heat regenerative adsorption heat pump. Energy Convers Manage 2000;41:1007–18.
[90] JY Wu, RZ Wang, Xu YX. Experimental results on operating parameters influence for an adsorption refrigerator. Int J Therm Sci 2002;41:137–45.
[91] YB Gui, RZ Wang, Wang W, JY Wu, Xu YX. Performance modeling and testing on a heat-regenerative adsorptive reversible heat pump. Appl Therm Eng 2002;22:309–20.
[92] Wang X, HT Chua, Ng KC. Experimental investigation of silica gel–water adsorption chillers with and without a passive heat recovery scheme. Int J Refrig 2005;28:756–65.
[93] RE Critoph, Metcalf SJ. Specific cooling power intensification limits in ammonia–carbon adsorption refrigeration systems. Appl Therm Eng 2004;24:661–78.
[94] SJ Metcalf, Tamainot-Telto Z, Critoph RE. Application of a compact sorption generator to solar refrigeration: case study of Dakar (Senegal). Appl Therm Eng 2011;31:2197–204.
[95] Oertel K, Fischer M. Adsorption cooling system for cold storage using methanol/silicagel. Appl Therm Eng 1998;18:773–86.
[96] LZ Zhang, Wang L. Momentum and heat transfer in the adsorbent of a waste-heat adsorption cooling system. Energy 1999;24:605–24.
[97] LZ Zhang, Wang L. Effects of coupled heat and mass transfers in adsorbent on the performance of a waste heat adsorption cooling unit. Appl Therm Eng 1999;19:195–215.
[98] Zhang LZ. Design and testing of an automobile waste heat adsorption cooling system. Appl Therm Eng 2000;20:103–14.
[99] YZ Lu, RZ Wang, Jianzhou S, Zhang M, Xu Y, Wu J. Performance of a diesel locomotive waste-heat-powered adsorption air conditioning system. Adsorption 2004;10:57–68.
[100] Restuccia G, Freni A, Vasta S, Aristov YI. Selective water sorbent for solid sorption chiller: experimental results and modelling. Int J Refrig 2004;27:284–93.
[101] Magnetto D. Thermally Operated Mobile Air Conditioning Systems, 1–53, 2005.
[102] DC Wang, ZZ Xia, JY Wu, RZ Wang, Zhai H, Dou WD. Study of a novel silica gel–water adsorption chiller. Part I. Design and performance prediction. Int J Refrig 2005;28:1073–83.
[103] DC Wang, JY Wu, ZZ Xia, Zhai H, RZ Wang, Dou WD. Study of a novel silica gel–water adsorption chiller. Part II. Experimental study. Int J Refrig 2005;28:1084–91.
[104] DC Wang, ZX Shi, QR Yang, XL Tian, JC Zhang, Wu JY. Experimental research on novel adsorption chiller driven by low grade heat source. Energy Convers Manage 2007;48:2375–81.
[105] Restuccia G, Freni A, Russo F, Vasta S. Experimental investigation of a solid adsorption chiller based on a heat exchanger coated with hydrophobic zeolite. Appl Therm Eng 2005;25:1419–28.
[106] GZ Yang, ZZ Xia, RZ Wang, Keletigui D, DC Wang, ZH Dong, et al. Research on a compact adsorption room air conditioner. Energy Convers Manage 2006;47:2167–77.
[107] LW Wang, RZ Wang, ZS Lu, CJ Chen, Wu JY. Comparison of the adsorption performance of compound adsorbent in a refrigeration cycle with and without mass recovery. Chem Eng Sci 2006;61:3761–70.
[108] ZS Lu, RZ Wang, LW Wang, Chen CJ. Performance analysis of an adsorption refrigerator using activated carbon in a compound adsorbent. Carbon 2006;44:747–52.
[109] CJ Chen, RZ Wang, LW Wang, Lu ZS. Studies on cycle characteristics and application of split heat pipe adsorption ice maker. Energy Convers Manage 2007;48:1106–12.
[110] Freni A, Russo F, Vasta S, Tokarev M, YI Aristov, Restuccia G. An advanced solid sorption chiller using SWS-1L. Appl Therm Eng 2007;27:2200–4.
[111] Daou K, RZ Wang, ZZ Xia, Yang GZ. Experimental comparison of the sorption and refrigerating performances of a $CaCl_2$ impregnated composite adsorbent and those of the host silica gel. Int J Refrig 2007;30:68–75.
[112] Verde M, Corberan JM, de Boer R, Smeding S. Modelling of a waste heat driven silica gel/water adsorption cooling system comparison with experimental results. In: ISHPC conference, Padua, Italy; 2011, p. 7–8.
[113] Sapienza A, Santamaria S, Frazzica A, Freni A. Influence of the management strategy and operating conditions on the performance of an adsorption chiller. Energy 2011;36:5532–8.
[114] YI Aristov, Sapienza a, Ovoshchnikov DS, Freni a, Restuccia G. Reallocation of adsorption and desorption times for optimisation of cooling cycles. Int J Refrig 2012;35:525–31.

[115] Akahira A, KCA Alam, Hamamoto Y, Akisawa A, Kashiwagi T. Mass recovery four-bed adsorption refrigeration cycle with energy cascading. Appl Therm Eng 2005;25:1764–78.
[116] Alam KC a, MZI Khan, AS Uyun, Hamamoto Y, Akisawa A, Kashiwagi T. Experimental study of a low temperature heat driven re-heat two-stage adsorption chiller. Appl Therm Eng 2007;27:1686–92.
[117] Akahira A, KCA Alam, Hamamoto Y, Akisawa A, Kashiwagi T. Experimental investigation of mass recovery adsorption refrigeration cycle. Int J Refrig 2005;28:565–72.
[118] WS Chang, C-C Wang, Shieh C-C. Experimental study of a solid adsorption cooling system using flat-tube heat exchangers as adsorption bed. Appl Therm Eng 2007;27:2195–9.
[119] Núñez T, Mittelbach W, Henning H-M. Development of an adsorption chiller and heat pump for domestic heating and air-conditioning applications. Appl Therm Eng 2007;27:2205–12.
[120] Heywood J. Internal combustion engine fundamentals. 1st ed.. 1988.
[121] Pulkrabek WW. Engineering fundamental of the internal combustion engine. 2nd ed.Prentice Hall; 2003.
[122] Storch G, Reichenauer G, Scheffler F, Hauer a. Hydrothermal stability of pelletized zeolite 13X for energy storage applications. Adsorption 2008;14:275–81.
[123] WS Loh, El-Sharkawy II, Ng KC, Saha BB. Adsorption cooling cycles for alternative adsorbent/adsorbate pairs working at partial vacuum and pressurized conditions. Appl Therm Eng 2009;29:793–8.
[124] Demir H, Mobedi M, Ülkü S. The use of metal piece additives to enhance heat transfer rate through an unconsolidated adsorbent bed. Int J Refrig 2010;33:714–20.

Appendix D.

Impact of fin spacing on temperature distribution in adsorption cooling system for vehicle A/C applications

INTERNATIONAL JOURNAL OF REFRIGERATION 51 (2015) 135–143

Available online at www.sciencedirect.com

ScienceDirect

journal homepage: www.elsevier.com/locate/ijrefrig

Impact of fin spacing on temperature distribution in adsorption cooling system for vehicle A/C applications

*Amir Sharafian, Claire McCague, Majid Bahrami**

Laboratory for Alternative Energy Conversion (LAEC), School of Mechatronic Systems Engineering, Simon Fraser University, # 4300, 250-13450 102nd Avenue, Surrey, BC V3T 0A3, Canada

ARTICLE INFO

Article history:
Received 29 June 2014
Received in revised form
26 September 2014
Accepted 4 December 2014
Available online 12 December 2014

Keywords:
Fin spacing
Finned tube heat exchanger
Adsorption cooling system
Adsorption to desorption time ratio
Adsorber bed to adsorbent mass ratio

ABSTRACT

Effects of fin spacing on the temperature distribution in a finned tube adsorber bed are studied to decrease the temperature gradient inside the adsorber bed and minimize the adsorber bed to adsorbent mass ratio (AAMR) for vehicle air conditioning applications. Finned tube adsorber beds have shown higher specific cooling power and coefficient of performance, and low AAMR among the existing adsorber beds. A single-adsorber bed ACS with interchangeable heat exchangers is built and equipped with hermetic type T thermocouples. Two copper heat exchangers with 6.35 mm (1/4″) and 9.5 mm (3/8″) fin spacing are custom-built and packed with 2–4 mm silica gel beads. The experimental results show that by decreasing the fin spacing from 9.5 mm to 6.35 mm, the temperature difference between the fin and adsorbent reduces by 4.6 °C under the cycle time of 600 s and an adsorption to desorption time ratio (ADTR) of one. A greater reduction in the temperature gradient inside the adsorber bed with smaller fin spacing is observed for short cycle time operation, e.g. 600 s, compared to long cycle time operation, e.g. 1400 s. Finally, simultaneous comparison of the temperature gradient between the fins and AAMR against fin spacing indicates that the optimum fin spacing for a finned tube heat exchanger packed with 2–4 mm silica gel beads is about 6 mm.

Impact de l'espacement des ailettes sur la distribution des températures dans un système de froid à adsorption pour des applications de conditionnement d'air automobile

Mots clés : Espacement des ailettes ; Echangeur de chaleur à tubes à ailettes ; Système de froid à adsorption ; Vitesse du passage de l'adsorption à la désorption ; Rapport du lit adsorbeur et de la masse de l'adsorbant

* *Corresponding author*. Tel.: +1 778 782 8538; fax: +1 778 782 7514.
E-mail addresses: asharafi@sfu.ca (A. Sharafian), clairem@sfu.ca (C. McCague), mbahrami@sfu.ca (M. Bahrami).
http://dx.doi.org/10.1016/j.ijrefrig.2014.12.003

Nomenclature

AAMR	adsorber bed to adsorbent mass ratio (kg_{metal} $kg^{-1}_{dry\ adsorbent}$)
ACS	adsorption cooling system
A/C	air conditioning
ADTR	adsorption to desorption time ratio
Ads.	adsorption
COP	coefficient of performance
Des.	desorption
FS	fin spacing
ICE	internal combustion engine
SCP	specific cooling power (W kg^{-1})
T	temperature (°C)

Subscript

ambient	ambient
bed	adsorber bed
cond	condenser
evap	evaporator

1. Introduction

Adsorption cooling systems (ACS) produce cooling power through utilization of low grade thermal energy, e.g. waste heat from an engine, and have received significant attention during the last decade mainly due to higher fuel prices, energy shortages, and stringent government environmental/emission regulations (Zhang and Wang, 1997; Lu et al., 2004; Verde et al., 2010). In a typical internal combustion engine (ICE), almost 70% of the total fuel energy is dissipated through the engine coolant and the exhaust gas in the form of waste heat (Farrington and Rugh, 2000). Also, auxiliary loads such as air conditioning (A/C) in light-duty vehicles increase the fuel consumption. The SFTP-SC03 driving cycle showed that a vapor compression refrigeration cycle (VCRC) in light-duty vehicles increases the fuel consumption by 28%, and CO_2 and NOx emissions by 71% and 81%, respectively (Hendricks, 2001). ACS is a promising alternative to VCRC for air conditioning that can reduce the fuel consumption and gas emissions, and increase the overall efficiency of vehicles. A working pair in ACS is a combination of an adsorbent (e.g., zeolite, silica gel, and activated carbon) and an adsorbate (e.g., water and methanol). These materials are environmentally friendly, non-toxic, non-corrosive, non-ozone depleting, and inexpensive (Demir et al., 2008).

A single-adsorber bed ACS consists of an adsorber bed packed with an adsorbent, and an adsorbate container. To produce cooling power, ACS cycle undergoes two main processes: heating-desorption-condensation and cooling-adsorption-evaporation. During the first process, the adsorber bed is heated up to desorb the adsorbate and pressure of the adsorber bed increases. Due to higher pressure of the adsorber bed than the adsorbate container, the vaporous adsorbate flows through the adsorbate container and is condensed inside the container. In the next process, the adsober bed is cooled down and the adsorbent adsorbs the adsorbate and pressure of the adsorber bed reduces. When pressure of the adsober bed drops below the adsorbate container, liquid adsorbate inside the adsorbate container is evaporated due to the suction of the adsorber bed and cooling effect happens inside the adsorbate container. Following these processes, the single-adsorber bed ACS produces evaporative cooling power intermittently. However, commercialization of ACS faces major challenges because of (i) low specific cooling power (SCP), which is defined as the ratio of the cooling load to the mass of dry adsorbent multiplied by the cycle time; and (ii) poor coefficient of performance (COP).

The low thermal conductivity of the adsorbent particles (~0.1–0.4 W m^{-1} K^{-1}) (Poyelle et al., 1999; Tamainot-Telto and Critoph, 2001; Freni et al., 2002) and low mass diffusivity of adsorbent–adsorbate pairs (~10^{-8} to 10^{-14} m^2 s^{-1}) (Sharafian and Bahrami, 2013) result in low heat and mass transfer rate inside the adsorber bed, and consequently, heavy and bulky ACS. Fins inside the adsorber bed decrease the heat transfer resistance caused by the adsorbent particles and increase the heat transfer surface area leading to improved adsorption and

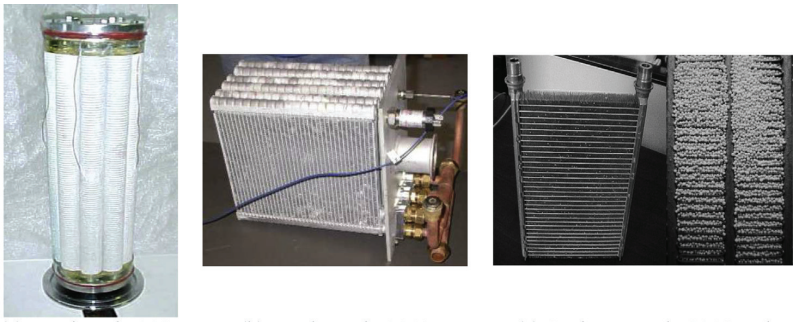

(a) Freni et al., 2007 (b) Verde et al., 2011 (c) Sapienza et al., 2011 and Aristov et al., 2012

Fig. 1 – Finned tube adsorber beds used in waste-heat driven ACS with high SCP and COP, and low AAMR (Sharafian and Bahrami, 2014).

Table 1 – Temperature measurements in the adsorbent packed bed.

Ref. No.	Working pair	Purpose
Zhang and Wang (1999a, 1999b)	Zeolite 13X-water	Developing a non-equilibrium 3D model for heat and mass transfer in an adsorber bed
Eun et al. (2000a, 2000b)	Silica gel/expanded graphite-water	Measuring temperature in an adsorbent composite block and pure silica gel packed bed, and comparing their differences
Pentchev et al. (2002)	Zeolite 4A-water	Measuring the axial and radial temperature distributions inside the adsorbent packed bed under adiabatic, near adiabatic and non-adiabatic boundary conditions and developing a 2D numerical model
El-Sharkawy et al. (2006)	Activated carbon fiber-ethanol	Activated carbon fiber characterization and measuring its temperature variation during the adsorption process vs. time
Wu et al. (2009)	Zeolite 13X-water	Measuring the wall temperature of adsorbent packed bed to verify a numerical model
Zhao et al. (2012)	Activated carbon-methanol	Measuring temperature distribution in an adsorbent packed bed to verify a numerical model
Mahdavikhah and Niazmand (2013)	SWS 1L-water	Developing a numerical model to study the effects of fin height and spacing on the performance of ACS
White (2012)	Silica gel-water	Measuring temperature in a finned tube adsober bed to verify a numerical model

desorption processes for a shorter cycle time. However, adding fins increases the total mass of the adsorber bed which is not desirable especially for vehicle A/C applications that require light-weight systems. Recently, Sharafian and Bahrami (2014) critically reviewed the SCP, adsorber bed to adsorbent mass ratio (AAMR), and COP of more than 50 studies/experiments reported in the literature with a focus on adsorber beds to establish the state-of-the-art adsorber bed design. They categorized the available adsorber beds into nine types, namely, (1) spiral plate, (2) shell and tube, (3) hairpin, (4) annulus tube, (5) plate fin, (6) finned tube, (7) plate-tube, (8) simple tube, and (9) plate. Among the existing adsorber bed designs, finned tube adsorber beds are more desirable by showing higher SCP and COP, and lower AAMR. The common features of these adsorber beds, depicted in Fig. 1, are a large number of fins to increase the heat transfer surface area and small fin spacing to decrease the heat transfer resistance inside the adsorber bed. However, none of the reported adsorber beds in the literature were specifically designed for the ACS applications.

One way of establishing efficient heat transfer from a heat transfer fluid (HTF) to the adsorbent particles is to experimentally measure the temperature distribution inside the adsorber bed. In several studies and experiments, the temperature distribution inside packed beds of adsorbent particles has been measured (Zhang and Wang, 1999a, 1999b; Eun et al., 2000a; Eun et al., 2000b; Pentchev et al., 2002; El-Sharkawy et al., 2006; Wu et al., 2009; Zhao et al., 2012; Mahdavikhah and Niazmand, 2013; White, 2012). The highlights of these studies are summarized in Table 1.

As shown in Table 1, two main purposes of the temperature measurements in the adsorbent packed beds are to verify the accuracy of numerical models (Zhang and Wang, 1999a, 1999b; Pentchev et al., 2002; Wu et al., 2009; Zhao et al., 2012; Mahdavikhah and Niazmand, 2013; White, 2012) and compare loose grain adsorbent against the consolidated adsorbent (Eun et al., 2000a, 2000b). To our best knowledge, there is no experimental study available that shows the temperature distribution inside a finned tube adsorber bed to investigate the effectiveness of heat transferred to and from the adsorbent particles and to establish optimum fin spacing. In this study, the effects of fin spacing on temperature distribution inside a finned tubed adsober bed and condenser/evaporator are investigated experimentally. The AAMR is one of the main factors in the ACS for vehicle applications. A lower AAMR means less 'dead' to 'live' mass ratio. As such, in the next step, the goal is to select a finned tube adsorber bed with proper fin spacing and acceptable AAMR through measuring the temperature inside the adsorber bed.

2. Experimental apparatus

ACS cycle works based on two main processes: heating-desorption-condensation and cooling-adsorption-evaporation. Following these steps, an ACS intermittently produces cooling power, such as data reported in Refs. (Boelman et al., 1995; Chua et al., 1999; Alam et al., 2000; Saha et al., 2009). In this study, a single-adsorber bed ACS was built to test different finned tube heat exchangers with different fin spacing. As shown in Fig. 2a, a vacuum chamber equipped with hermetic thermocouples was used as an adsorber bed

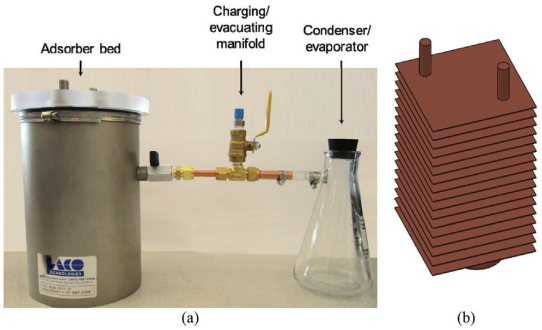

Fig. 2 – (a) Single-adsorber bed ACS experimental setup, and (b) schematic of finned tube heat exchanger located inside the adsorber bed.

and, a Buchner flask was used as a condenser/evaporator to visually monitor the condensation and evaporation processes. Silica gel beads with 2–4 mm diameters (3.2 mm average diameter) and water were selected as the working pair because the low regeneration temperature of silica gel (<95 °C) is similar to that of the engine coolant in ICE. This is ideal, especially when compared to activated carbon and zeolite with higher regeneration temperatures, 130 °C and 180 °C, respectively.

Two finned tube adsober beds with 6.35 mm (1/4″) and 9.5 mm (3/8″) fin spacing were built to study the effects of fin spacing on the temperature distribution inside the adsorber bed and condenser/evaporator under different cycle times and adsorption/desorption time ratios (ADTRs). The finned tube heat exchanger, shown in Fig. 2b, was made from copper plates and tubes and the fins were soldered to the tubes to minimize the thermal contact resistance between the heat exchanger parts. The finned section of the heat exchangers had 11.4–11.45 cm height to fit inside the adsorber bed.

Reducing the fin spacing can lead to an increase in the number of fins, heat transfer surface area and metal mass of the heat exchanger. It also decreases the amount of silica gel packed inside the heat exchanger, and, consequently, results in a higher AAMR. For instance, in the case where 2 mm silica gel beads are used, the minimum possible fin spacing for the heat exchanger would ideally be 2 mm. Our calculations showed that a finned tube heat exchanger with 9 × 9 × 0.0762 cm (length × width × thickness) fins, 2 mm fin spacing and 11.4 cm finned section would have 42 fins, a total heat transfer surface area of 0.68 m^2 (= 42 × 0.09 × 0.09 × 2) and a metal mass of 2307 g (= 42 × 9 × 9 × 0.0762 × 8.9 g cm^{-3}). This heat exchanger would hold only 531 g (= 41 × 9 × 9 × 0.2 × 0.8 g cm^{-3}) of silica gel. Thus, the AAMR becomes 4.34 (= 2307 g/531 g). To reduce this ratio, the only solution is to increase the fin spacing. The specifications of our two heat exchangers with 6.35 mm and 9.53 mm fin spacing as well as heating and cooling fluids inlet temperatures and mass flow rates are summarized in Table 2. These fin spacing were selected such that the ratio of fin spacing to the average silica gel particles became approximately 2.0 (≈6.35 mm/3.2 mm) and 3.0 (≈9.53 mm/3.2 mm), respectively.

As shown in Table 2, the heat exchanger with 6.35 mm fin spacing packed with 770 g of silica gel provides an AAMR of 1.27, whereas that of with 9.5 mm fin spacing packed with 820 g of silica gel gives an AAMR of 0.87, respectively.

Fig. 3 shows the location of nine hermetic thermocouples mounted inside the heat exchangers with 6.35 mm and 9.5 mm fin spacing to monitor the temperature distribution during the adsorption and desorption processes. The hermetic thermocouples used inside the adsorber bed were type T with accuracy of ±1.0 °C supplied by PAVE Technology Company. In Fig. 3, thermocouples TC0 and TC8 measure the working fluid inlet and outlet temperatures to the adsorber bed. Thermocouples TC1 and TC2 measure the temperatures on the fin wall and at the center of the first two fins, respectively. Thermocouples TC3 and TC5 also display the temperatures at the center of the fins whereas thermocouples TC4, TC6 and TC7 show the temperatures at the corners of the fins. To measure the condenser/evaporator and ambient temperatures, type T thermocouples with accuracy of ±1.0 °C supplied by Omega were used. A LabVIEW interface was developed to monitor and record the temperatures as a function of time.

Table 2 – Specifications of heat exchangers and heat transfer fluids.

Parameters	Heat exchanger	
	6.35 mm fin spacing	9.53 mm fin spacing
No. of fins	17	12
Mass of heat exchanger	978 g	716 g
Mass of silica gel	770 g	820 g
AAMR	1.27 (978 g/770 g)	0.87 (716 g/820 g)
Heat transfer surface area	0.266 m^2	0.188 m^2
Mass of water in the condenser/evaporator	80 g	
Heating water flow rate to the bed	0.062 kg s^{-1} (3.72 L min^{-1})	
Heating water inlet temperature to the bed	88–93 °C	
Cooling water flow rate to the bed	0.03 kg s^{-1} (1.78 L min^{-1})	
Cooling water inlet temperature to the bed	28–33 °C	
Fin thickness	0.0762 cm (0.03″)	
Fin dimensions	9 × 9 cm	

3. Results and discussion

Fig. 4 shows the temperature distribution and pressure profile in the adsorber bed with 9.5 mm fin spacing and temperature variation in the condenser/evaporator under the cycle time of 1400 s and ADTR of one. It can be seen in Fig. 4 that after the first cycle (time > 1400 s), temperature and pressure profiles in the adsorber bed are replicated. Fig. 4a demonstrates that as the ambient temperature is lower than water vapor temperature during the desorption process, the flask behaves as a condenser and condensation occurs on the walls of the flask. During the adsorption process, the flask serves as an evaporator. When the adsorber bed is cooled down, the pressure inside the adsorber bed reduces, and consequently, the liquid water inside the flask starts evaporating. As a result of evaporation, the liquid water temperature drops and cooling occurs. The adsorption and desorption processes with an ADTR of one (700 s adsorption, 700 s desorption) are demarcated in Fig. 4.

To assure the reproducibility of the measured experimental data, the evaporator temperature was measured on two different days. Fig. 5 shows the temperature of evaporator at the end of adsorption process when it is connected to the adsorber bed with 9.5 mm fin spacing under different cycle times and ADTR of one. It can be seen in Fig. 5 that the measured data on different days under the same operating conditions are the same. Both have a maximum relative difference of 5%; thus it can be concluded that the results are reproducible. Also, Fig. 5 indicates that the evaporator temperature reduces by increasing the cycle time. Longer cycle time permits a greater heat removal from the adsorbent particles, a greater adsorbate uptake by the adsorbent particles and, consequently, reaching to lower evaporation

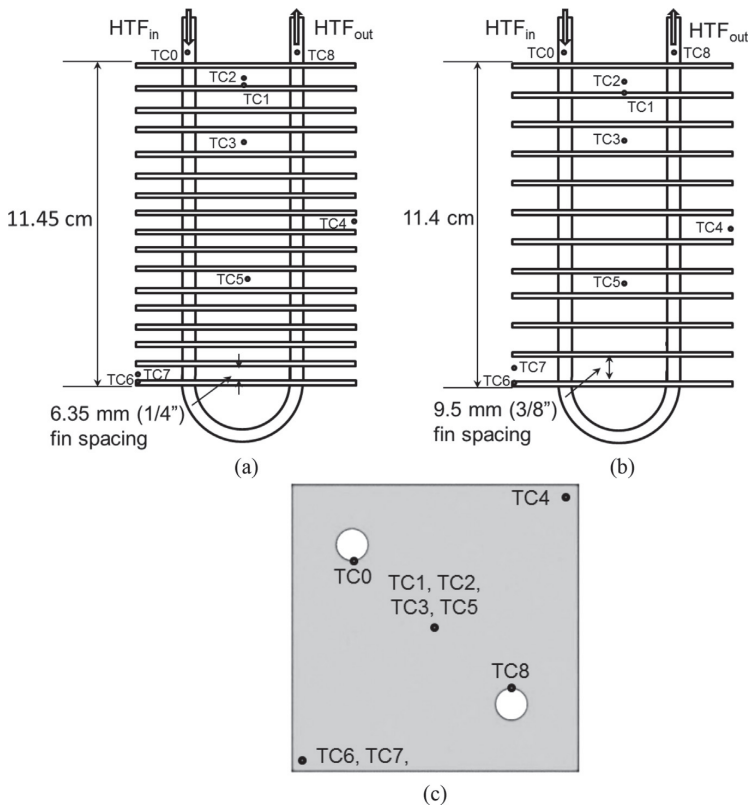

Fig. 3 – Location of thermocouples inside the heat exchanger with (a) 6.35 mm fin spacing and (b) 9.5 mm fin spacing, and (C) top view.

temperature. However, the cycle time also depends on and is limited by the vehicle driving cycle. For example, the total daily commute time in the U.S. is about 40 min, ≈20 min to work and ≈20 min returning home (Lambert and Jones, 2006a, 2006b). To accelerate heat and mass transfer to and from the adsorbent particles, the adsorber bed fin spacing should be reduced to minimize the thermal resistance of adsorbent particles.

Fig. 6 shows the temperature differences between thermocouples TC1 and TC2 at the end of adsorption and desorption processes under different cycle times and ADTRs. Fig. 6 shows that by increasing the cycle time from 600 s to 1400 s, the temperature gradient between TC1 and TC2 gradually reduces as a result of more heat transfer to and from the adsorbent particles. However, Fig. 6 indicates that the temperature differences between TC1 and TC2 in the heat exchanger with 6.35 mm fin spacing are much lower than those in the heat exchanger with 9.53 mm fin spacing, specifically under short cycle times. For example, under the cycle time of 600 s and ADTR of one, Fig. 6a, the temperature differences between TC1 and TC2 at the end of desorption process are 3.1 °C and 7.7 °C for the heat exchangers with 6.35 mm and 9.53 mm fin spacing, respectively.

Fig. 6a indicates that the temperature differences between TC1 and TC2 at the end of desorption process and ADTR of one are always higher than those at the end of the adsorption process. Adsorption is an exothermic process and, therefore, heat generation occurs throughout the adsorber bed and the temperature difference between the adsorbent particles reduces. Whereas desorption is an endothermic process and adsorbent particles gain heat from an internal heat source during which the temperature difference between the adsorbent particles increases. As a result, it can be concluded that the largest temperature gradient inside the adsorber bed, under ADTR of one, happens during the desorption process.

Figs. 6b and c show that by increasing the ADTR from one to three, the temperature difference between TC1 and TC2 does not vary significantly at the end of adsorption process for both heat exchangers. However, the temperature difference between TC1 and TC2 at the end of desorption process increases for the heat exchanger with 9.35 mm fin spacing. For instance, the temperature difference between TC1 and TC2 at the end of desorption process and cycle time of 600 s increases from 7.7 °C to 10.9 °C in the heat exchanger with 9.35 mm fin spacing by increasing the ADTR from one to three, respectively.

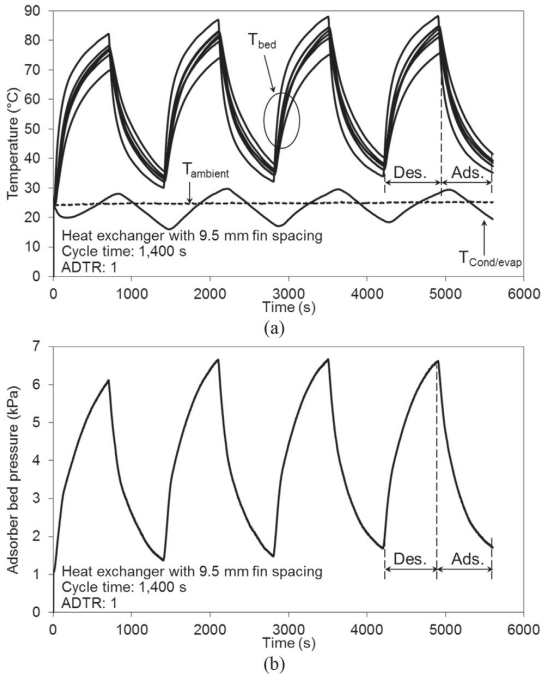

Fig. 4 – (a) Temperature distribution and (b) pressure profile in the single-adsorber bed ACS under the cycle time of 1400 s and ADTR of one.

Fig. 7 shows the temperature differences between TC6 and TC7 at the end of adsorption and desorption processes in the adsorber beds with 6.35 mm and 9.5 mm fin spacing under different cycle times and ADTRs. The location of thermocouples TC6 and TC7 are different from thermocouples TC1 and TC2. Thermocouples TC6 and TC7 are located at the corner of the fins and are in contact with the adsorbate flow which has different temperature than the adsorbent particles. As opposed to thermocouples TC1 and TC2 that are located at the center of the fins and are exposed to the vaporous adsorbate flow with the same temperature as the adsorbent particles. As

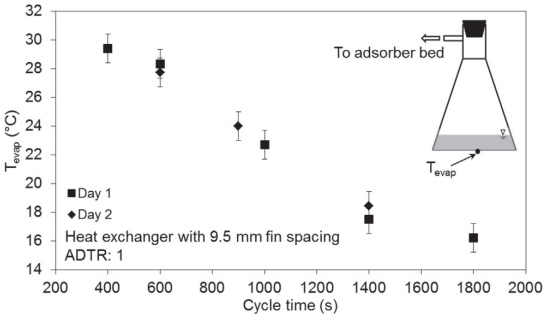

Fig. 5 – Evaporator temperature at the end of adsorption process vs. cycle time.

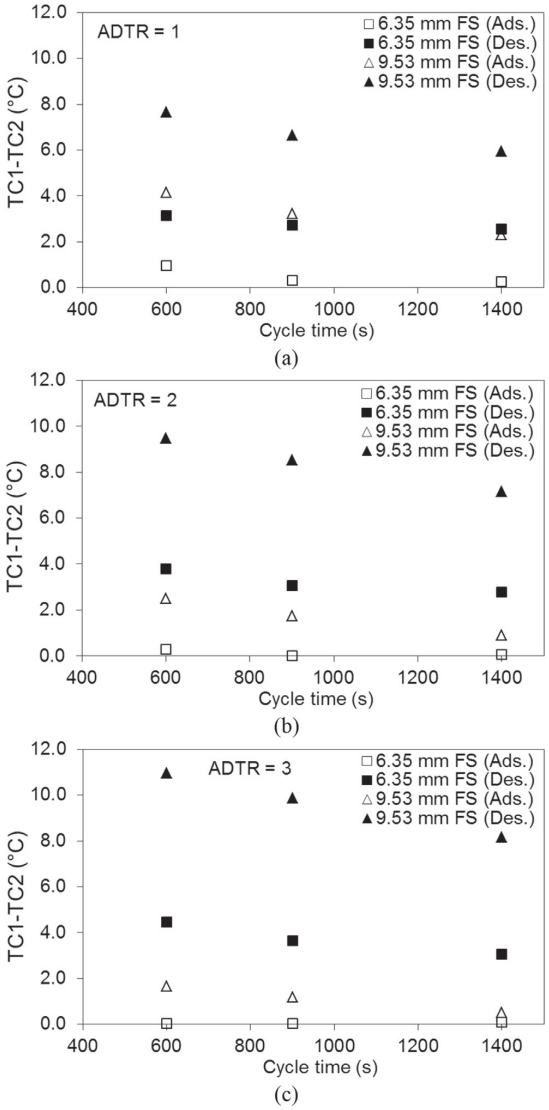

Fig. 6 – Temperature differences between thermocouples TC1 and TC2 at the end of adsorption and desorption processes for adsorber beds with 6.35 mm and 9.5 mm fin spacing under different cycle times and ADTRs.

a result, the temperatures measured by TC6 and TC7 are not merely caused by heating and cooling of the adsorbent particles. For example, during the adsorption process, TC6 and TC7 measure the adsorbent particles temperature and the cold vaporous adsorbate which comes from the evaporator. As such, it can be seen in Fig. 7 that in the heat exchanger with 9.53 mm fin spacing, temperature differences between TC6 and TC7 do not change significantly by increasing the cycle time from 600 s to 1400 s. However, by reducing the fin spacing from 9.53 mm to 6.35 mm, the temperature difference

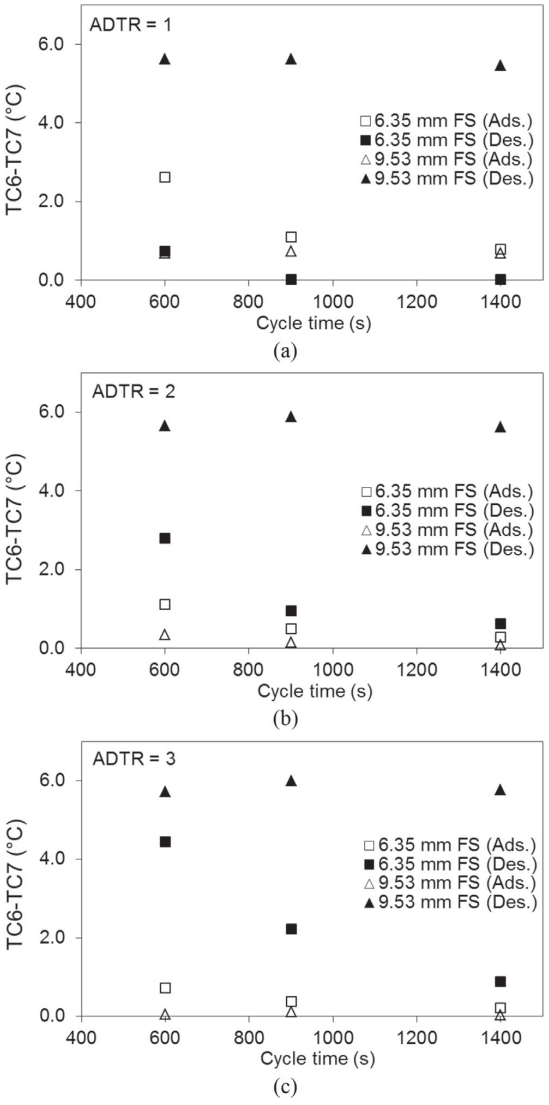

Fig. 7 – Temperature differences between thermocouples TC6 and TC7 at the end of adsorption and desorption processes for adsorber beds with 6.35 mm and 9.5 mm fin spacing under different cycle times and ADTRs.

between TC6 and TC7 changes under different cycle times and ADTRs.

To magnify the effects of fins in heat transfer, Fig. 7 shows that fin spacing needs to be reduced. The heat exchanger with 6.35 mm fin spacing results in reducing the temperature differences between TC6 and TC7, specifically at the end of the desorption process. By comparing Figs. 6 and 7, it can be shown that the adsorbent particles experience different temperatures during the adsorption and desorption

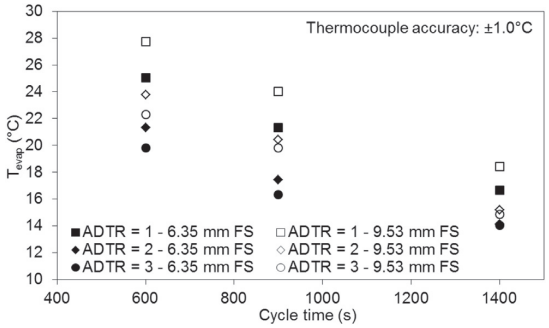

Fig. 8 – Effects of fin spacing on the evaporator temperature under different cycle times and ADTRs.

processes. The adsorbent particles at the center of the fins are only heated up and cooled down by the fins and are affected by their adjacent adsorbent particles. However, the adsorbent particles at the edge of the fins are mainly influenced by the adsorbate temperature unless otherwise fin spacing becomes small.

The effects of fin spacing on the temperature of evaporator at the end of adsorption process are shown in Fig. 8. It can be seen in Fig. 8 that the heat exchanger with 6.35 mm fin spacing produces lower evaporation temperatures than that with 9.53 mm fin spacing, especially at the cycle time of 600 s. Also, Fig. 8 demonstrates that the evaporator temperature highly depends on the ADTR. In A/C systems, the evaporator pressure is lower than the condenser pressure. The low evaporation pressure in ACS results in a slower uptake rate of adsorbate by the adsorbent particles, thus, the adsorption time should be increased to charge the adsorber bed. Fig. 8 depicts the two practical solutions to increase the adsorption uptake of adsorbate by the adsorbent particles. The first solution is to increase ADTR from one to three. However, in order to reach an ADTR of three, four adsorber beds are required (i.e., one adsorber bed desorbs and three adsorber beds adsorb the adsorbate). A four-adsorber bed ACS leads to a heavy and bulky system; which is not practical for vehicle applications. The second solution is to increase the cycle time.

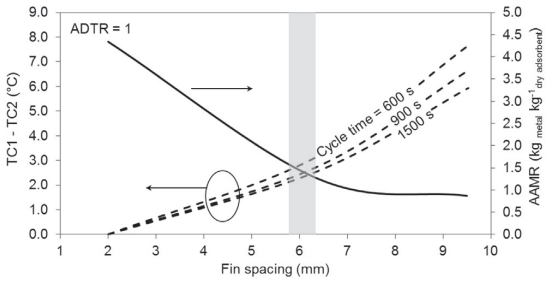

Fig. 9 – Temperature difference between thermocouples TC1 and TC2 at the end of desorption process under different cycle times and AAMR vs. adsorber beds with different fin spacing.

As shown in Fig. 8, the difference between the evaporator temperatures at cycle time of 1400 s is not noticeably affected by ADTR. In the case of using the heat exchanger with 6.35 mm fin spacing under cycle time of 1400 s, the maximum evaporation temperature difference between ADTR of one and three is equal to 2.6 °C.

Based on the measured temperatures inside the single-adsorber bed ACS, one can conclude that to have an adsorber bed with a more uniform temperature distribution between the adsorbent particles and an ACS with smaller foot-print and weight, the fin spacing must be reduced and ADTR should be kept at one. To find the optimum fin spacing based on the experimental data, the temperature differences between thermocouples TC1 and TC2 at the end of desorption process and AAMR are plotted against adsorber beds with different fin spacing in Fig. 9. As mentioned in Section 2, our calculations showed that the AAMR for the heat exchanger with 2 mm fin spacing would be equal to 4.34 and the temperature difference between thermocouples TC1 and TC2 is negligible (~0). The other data to generate Fig. 9 are provided in Table 2 and Fig. 6a.

Fig. 9 shows that by increasing the fin spacing from 2 mm to 9.5 mm, the temperature difference between thermocouples TC1 and TC2 increases from zero to 7.7 °C under the cycle time of 600 s whereas AAMR reduces from 4.34 to 0.87. For vehicle applications, the AAMR should be minimized; however, it should not significantly affect the performance of the ACS. To this end, the intersection of the temperature difference between thermocouples TC1 and TC2 under different cycle times, and AAMR is selected as the optimum fin spacing. The gray region in Fig. 9 demarcates the optimum fin spacing (about 6 mm) for a finned tube adsorber bed packed with 2–4 mm silica gel beads.

4. Conclusion

Effects of fin spacing on the temperature distribution in a finned tube adsorber bed were studied experimentally. Two heat exchangers with 6.35 mm and 9.5 mm fin spacing were custom-built and packed with 2–4 mm silica gel beads. The results showed that the adsorbent particles experience different temperatures at different locations of the adsober bed. For the adsorbent particles at the center of the fins, the only route of heat transfer to and from the adsorbent particles was through the fins. However, for the adsorbent particles at the edges of the fins, the adsorbate temperature also affected the adsorbent particles' temperature. For the adsorbent particles at the center of the fins, the temperature gradient was always higher during the desorption process than the adsorption process. The results also indicated that the effects of fin spacing on the temperature gradient inside the adsorber bed and the evaporator temperature were more significant under short cycle times (600 s) rather than long cycle times (1400 s). Comparing the temperature differences between the fins, and AAMR vs. fin spacing showed that 6 mm fin spacing was an optimum value for the finned tube adsorber bed packed with 2–4 mm silica gel beads.

Acknowledgment

The authors gratefully acknowledge the financial support of the Natural Sciences and Engineering Research Council of Canada (NSERC) through the Automotive Partnership Canada Grant No. APCPJ 401826-10.

REFERENCES

Alam, K.C.A., Saha, B.B., Kang, Y.T., 2000. Heat exchanger design effect on the system performance of silica gel adsorption refrigeration systems. Int. J. Heat Mass Transf. 43, 4419–4431.

Aristov, Y.I., Sapienza, A., Ovoshchnikov, D.S., Freni, A., Restuccia, G., 2012. Reallocation of adsorption and desorption times for optimisation of cooling cycles. Int. J. Refrigeration 35, 525–531.

Boelman, E.C., Saha, B.B., Kashiwagi, T., 1995. Experimental investigation of a silica gel-water adsorption refrigeration cycle- the influence of operating conditions on cooling output and COP. ASHRAE Trans. 101, 358–366.

Chua, H.T., Ng, K.C., Malek, A., Kashiwagi, T., Akisawa, A., Saha, B.B., 1999. Modeling the performance of two-bed, silica gel–water adsorption chillers. Int. J. Refrigeration 22, 194–204.

Demir, H., Mobedi, M., Ülkü, S., 2008. A review on adsorption heat pump: problems and solutions. Renew. Sustain. Energy Rev. 12, 2381–2403.

El-Sharkawy, I.I., Kuwahara, K., Saha, B.B., Koyama, S., Ng, K.C., 2006. Experimental investigation of activated carbon fibers/ethanol pairs for adsorption cooling system application. Appl. Therm. Eng. 26, 859–865.

Eun, T., Song, H., Hun, J., Lee, K., Kim, J., 2000. Enhancement of heat and mass transfer in silica-expanded graphite composite blocks for adsorption heat pumps: Part I. Characterization of the composite blocks. Int. J. Refrigeration 23, 64–73.

Eun, T., Song, H., Hun, J., Lee, K., Kim, J., 2000. Enhancement of heat and mass transfer in silica-expanded graphite composite blocks for adsorption heat pumps. Part II. Cooling system using the composite blocks. Int. J. Refrigeration 23, 74–81.

Farrington, R., Rugh, J., 2000. Impact of vehicle air-conditioning on fuel economy, tailpipe emissions, and electric vehicle range. In: Proceeding Earth Technol. Forum, Washington, D.C.

Freni, A., Tokarev, M.M., Restuccia, G., Okunev, A.G., Aristov, Y.I., 2002. Thermal conductivity of selective water sorbents under the working conditions of a sorption chiller. Appl. Therm. Eng. 22, 1631–1642.

Freni, A., Russo, F., Vasta, S., Tokarev, M., Aristov, Y.I., Restuccia, G., 2007. An advanced solid sorption chiller using SWS-1L. Appl. Therm. Eng. 27, 2200–2204.

Hendricks, T.J., 2001. Optimization of vehicle air conditioning systems using transient air conditioning performance analysis. In: SAE Conf. Proc. P.

Lambert, M.A., Jones, B.J., 2006. Automotive adsorption air conditioner powered by exhaust heat. Part 1: conceptual and embodiment Design. Proc. Inst. Mech. Eng. Part D J. Automob. Eng. 220, 959–972.

Lambert, M.A., Jones, B.J., 2006. Automotive adsorption air conditioner powered by exhaust heat. Part 2: detailed design and analysis. Proc. Inst. Mech. Eng. Part D J. Automob. Eng. 220, 973–989.

Lu, Y.Z., Wang, R.Z., Jianzhou, S., Zhang, M., Xu, Y., Wu, J., 2004. Performance of a diesel locomotive waste-heat-powered adsorption air conditioning system. Adsorption 10, 57–68.

Mahdavikhah, M., Niazmand, H., 2013. Effects of plate finned heat exchanger parameters on the adsorption chiller performance. Appl. Therm. Eng. 50, 939–949.
Pentchev, I., Paev, K., Seikova, I., 2002. Dynamics of non-isothermal adsorption in packed bed of biporous zeolites. Chem. Eng. J. 85, 245–257.
Poyelle, F., Guilleminot, J.J., Meunier, F., 1999. Experimental tests and predictive model of an adsorptive air conditioning unit. Ind. Eng. Chem. Res. 38, 298–309.
Saha, B.B., Chakraborty, A., Koyama, S., Aristov, Y.I., 2009. A new generation cooling device employing $CaCl_2$-in-silica gel–water system. Int. J. Heat Mass Transf. 52, 516–524.
Sapienza, A., Santamaria, S., Frazzica, A., Freni, A., 2011. Influence of the management strategy and operating conditions on the performance of an adsorption chiller. Energy 36, 5532–5538.
Sharafian, A., Bahrami, M., 2013. Adsorbate uptake and mass diffusivity of working pairs in adsorption cooling systems. Int. J. Heat Mass Transf. 59, 262–271.
Sharafian, A., Bahrami, M., 2014. Assessment of adsorber bed designs in waste-heat driven adsorption cooling systems for vehicle air conditioning and refrigeration. Renew. Sustain. Energy Rev. 30, 440–451.
Tamainot-Telto, Z., Critoph, R.E., 2001. Monolithic carbon for sorption refrigeration and heat pump applications. Appl. Therm. Eng. 21, 37–52.
Verde, M., Cortés, L., Corberán, J.M., Sapienza, A., Vasta, S., Restuccia, G., 2010. Modelling of an adsorption system driven by engine waste heat for truck cabin A/C. Performance estimation for a standard driving cycle. Appl. Therm. Eng. 30, 1511–1522.
Verde, M., Corberan, J.M., de Boer, R., Smeding, S., 2011. Modelling of a waste heat driven silica gel/water adsorption cooling system comparison with experimental results. In: ISHPC Conf., Padua, Italy, pp. 7–8.
White, J., 2012. CFD Simulation of Silica Gel and Water Adsorbent Beds Used in Adsorption Cooling System. University of Birmingham.
Wu, W., Zhang, H., Sun, D., 2009. Mathematical simulation and experimental study of a modified zeolite 13X–water adsorption refrigeration module. Appl. Therm. Eng. 29, 653–659.
Zhang, L.Z., Wang, L., 1997. Performance estimation of an adsorption cooling system for automobile waste heat recovery. Appl. Therm. Eng. 17, 1127–1139.
Zhang, L.Z., Wang, L., 1999. Effects of coupled heat and mass transfers in adsorbent on the performance of a waste heat adsorption cooling unit. Appl. Therm. Eng. 19, 195–215.
Zhang, L.Z., Wang, L., 1999. Momentum and heat transfer in the adsorbent of a waste-heat adsorption cooling system. Energy 24, 605–624.
Zhao, Y., Hu, E., Blazewicz, A., 2012. Dynamic modelling of an activated carbon–methanol adsorption refrigeration tube with considerations of interfacial convection and transient pressure process. Appl. Energy 95, 276–284.

Appendix E.

Effects of different adsorber bed designs on in-situ water uptake rate measurements of AQSOA FAM-Z02 for vehicle air conditioning applications

(under review in the Applied Thermal Engineering journal)

Effects of different adsorber bed designs on in-situ water uptake rate measurements of AQSOA FAM-Z02 for vehicle air conditioning applications

Amir Sharafian[*], Seyyed Mahdi Nemati Mehr[*], Wendell Huttema, Majid Bahrami[†]

Laboratory for Alternative Energy Conversion (*LAEC*), School of Mechatronic Systems Engineering, Simon Fraser University, BC, Canada V3T 0A3

Abstract

Adsorption cooling systems (ACS) utilize waste heat or low grade thermal energy to produce the cooling power required for air conditioning (A/C) in vehicles. However, the bulkiness and heavy weight of ACS presently limit their commercialization. In addition to having an adsorbent with high adsorbate uptake rate and thermal conductivity, different adsorber bed designs can significantly affect the performance and footprint of an ACS. In this study, the water uptake rate of AQSOA FAM-Z02 packed in two different adsorber beds is measured in-situ under adsorption and desorption temperatures of 30 and 90°C, and the water source temperature of 20°C. The comprehensive literature review conducted in this study indicates that in-situ adsorbate uptake rate measurement is a precise technique for analyzing the performance of an adsorber bed before installation on an ACS. However, the effects of some parameters, such as changes in the density of heat transfer fluid and stiffness of flexible hosing connected to the adsorber bed, have been overlooked in the literature and they may result in miscalculations of the adsorbate uptake mass. To de-convolute these undesirable effects from the in-situ mass measurements, a two-step mass measurement is performed to precisely measure the adsorbate uptake rate. To verify the developed method, the equilibrium water uptakes of AQSOA FAM-Z02 are measured at 30 and 90°C, and water source temperature of 20°C, and compared against

[*] These authors have been contributed equally to the work.
[†] Corresponding author: School of Mechatronic Systems Engineering, Simon Fraser University, # 4300, 250-13450 102nd Avenue, Surrey, BC, Canada V3T0A3.
Tel.: +1 (778) 782-8538; Fax: +1 (778) 782-7514.
E-mail addresses: snematim@sfu.ca (S. Nemati Mehr), asharafi@sfu.ca (A. Sharafian), mbahrami@sfu.ca (M. Bahrami).

the available data in the literature measured by a thermogravimetric analysis. Next, the water uptake difference of AQSOA FAM-Z02 during adsorption and desorption is measured for different cycle times, following by calculation of specific cooling power (SCP) and coefficient of performance (COP). Comparison of water uptake differences with two different adsorber beds show that high heat transfer surface area and small fin spacing are the main specifications of a well-designed adsorber bed for ACS applications. As a result of using AQSOA FAM-Z02 and a well-designed adsorber bed, a SCP of 112.9 W/kg and a COP of 0.34 are achieved at cycle time of 10 min.

Keywords: AQSOA FAM-Z02, uptake rate, adsorption cooling system, air conditioning.

1. Introduction

Air conditioning and refrigeration (A/C-R) systems are responsible for using about 30% of the total worldwide energy produced [1] and the number of A/C-R units is expected to reach 78.8 million units by 2015. The Supplemental Federate Test Procedure (SFTP) for emission tests of A/C systems (SC03) in vehicles with gross weight of under 2608 kg showed that A/C systems contributed to 37% of the total tailpipe emissions [2]. Furthermore, about 70% of the total fuel energy released in an internal combustion engine (ICE) is wasted as a high temperature heat that is dissipated through the engine coolant and exhaust gas [3]. Waste heat-driven adsorption cooling systems (ACS) are potential energy efficient replacements for vapor compression refrigeration cycles (VCRCs) where low-grade thermal energy is available. ACS can use the waste heat of an ICE to provide cooling in vehicles and drastically reduce the fuel consumption and carbon footprint of vehicles.

A waste heat-driven ACS uses an adsorbate, such as water or methanol, that is adsorbed and desorbed from the surface of a solid adsorbent, such as zeolite, silica gel, or activated carbon.

Most of these materials are non-toxic, non-corrosive, and inexpensive [4] making an ACS a safe and environmentally friendly technology. ACS operate quietly and are easy to maintain because valves are their only moving parts [5]. However, current ACS are limited in their usefulness for commercial vehicle applications, specifically light-duty vehicles, because of their bulkiness and heavy weight. The main challenges facing this technology are low coefficient of performance (COP = cooling energy / input energy) and low specific cooling power (SCP = cooling energy / (adsorbent mass × cycle time)) that originate from the low thermal conductivity of adsorbent particles (~ 0.1 to 0.4 W/mK) [6–8] and the low mass diffusivity of adsorbent-adsorbate pairs (~ 10^{-8} to 10^{-14} m^2/s) [7,9].

To overcome these limitations, different composite adsorbent materials with high thermal conductivity and high adsorbate uptake have been developed such as the ones reported in Refs. [10,11]. AQSOA FAM-Z02 is one of these synthetic materials developed for A/C applications by Mitsubishi Chemical Ltd. [12]. FAM-Z02 showed high durability of 60,000 cycles with no reduction in its uptake capacity and low desorption temperature of 75-95°C [12] making it a good candidate for ACS applications. Thermogravimetric analysis (TGA) is a well-known technique for measuring the adsorbate uptake of an adsorbent material. In a TGA, mass changes of few milligrams of an adsorbent are measured during adsorption or desorption under a controlled temperature and pressure. The water vapor sorption isotherms of FAM-Z02 measured by a TGA can be found in Refs. [13–16]. The nominal adsorption and desorption temperatures of a waste heat-driven FAM-Z02 ACS reported in the open literature were 30°C and 90°C. TGA measurements showed that the equilibrium water uptakes of FAM-Z02 at 30°C and 90°C were 0.33 and 0.023 kg/kg with the water source temperature maintained constant at 20°C [15]. Therefore, the equilibrium water uptake difference of FAM-Z02 under these operating conditions

was 0.307 kg/kg. In a real application, however, adsorption and desorption occur under large pressure jumps and non-isothermal conditions, making the operating conditions far from the ideal found in a TGA.

Adsorbate uptake capability of an adsorbent material packed in an adsorber bed may be further reduced by the adsorber bed design, interparticle mass transfer resistance, and pressure drop within the adsorber bed, as well as effects from other components of the ACS, e.g. condenser and evaporator. A metallic wire mesh or perforated sheet is necessary for holding loose adsorbent grains inside the adsorber bed, which contributes to the pressure drop and mass transfer resistance. More importantly, an ACS is a dynamic system and, as a result of adsorption and desorption within short cycle times (less than 30 min), the adsorbate uptake of an adsorbent material does not reach the equilibrium value measured by a TGA. Due to these geometrical and operational constrains, the adsorbate uptake capability of an adsorbent material reduces in the short periods of adsorption and desorption processes. To quantify these effects and measure the adsorbate uptake rate of adsorbent materials in conditions close to reality than in a TGA, a variety of experiments have been designed, as summarized in Table 1.

Table 1. In-situ adsorbate uptake rate measurements of different adsorbent materials in a large-scale test bed.

Ref.	Adsorbent-adsorbate pair	Adsorbent mass	Purpose
Dawoud and Aristov [17]	Mesoporous silica gel-water Alumina-water Silica gel + $CaCl_2$ (SWS-1L)-water Alumina + $CaCl_2$ (SWS-1A)-water	3 g	Measuring the kinetics of water sorption of loose adsorbent grains under real ACS operating conditions
Aristov et al. [18,19]	Silica gel + $CaCl_2$ (SWS-1L)-water	0.022 - 0.025 g	Effects of grain size (0.7-2.8 mm) and temperature (33-69°C) on the kinetics of water sorption of SWS-1L under real ACS operating conditions
Dawoud [13]	FAM-Z02-water	0.150 g	Effects of grain size (0.7-2.6 mm) on water sorption rate of FAM-Z02 under real ACS operating conditions
Dawoud et al. [20]	Consolidated zeolite-water	3 g	Measuring the kinetics of water sorption of consolidated zeolite layer with 0.7 mm thickness on an aluminum substrate under real ACS operating conditions
Glaznev and Aristov [21–23] Glaznev et al. [24]	Silica gel + $CaCl_2$ (SWS-1L)-water RD silica gel-water FAM-Z02-water	0.420 - 0.425 g	Effects of residual air on water sorption rate of adsorbents under real ACS operating conditions
Storch et al. [25]	Zeolite 13X-water	180 g	Effects of 3500 adsorption/desorption cycles on the equilibrium water uptake of zeolite 13X
Schnabel et al. [26]	Coated zeolite A-water Coated zeolite X-water	0.170 g 1.030 g	Measuring water uptake rate of zeolite coated directly on a metallic substrate
Riffel et al. [27]	Silica gel-water Zeolite water	1.051 kg 1.093 kg	Measuring water uptake rate of two different adsorbent materials packed in a finned tube heat exchanger under real ACS operating conditions
Solmuş et al. [28]	Natural zeolite-water	1.667 g	Measuring equilibrium water uptake of zeolite packed in an adsorber bed
Ovoshchnikov et al. [29]	Silica gel + $CaCl_2$ (SWS-1L)-water	-	Measuring water uptake rate of SWS-1L to find different water diffusion mechanism inside SWS-1L
Askalany et al. [30]	Activated carbon-R134a	-	Measuring equilibrium R134a uptake of granular activated carbon
Aristov et al. [31] Aristov [32] Chakraborty et al. [33]	RD silica gel-water	-	Effects of adsorbent grain size and number of adsorbent layers on its water uptake rate under large temperature jumps
Dawoud [34]	FAM-Z02-water	204 g 1.5-2.53 kg	Calculating the kinetics of water uptake of FAM-Z02 indirectly by using the performance analysis of an adsorption heat pump

Gordeeva et al. [35]	LiBr + silica gel-ethanol	0.300 g 56-76 g	Measuring in-situ ethanol uptake rate of loose LiBr+silica gel grains packed in finned tube heat exchangers with different length/height ratios
Santamaria et al. [36]	FAM-Z02-water	72-90 g	Effect of heat exchanger geometry, adsorbent grain size and heat transfer fluid flow rate on in-situ water uptake rate measurement of FAM-Z02
Frazzica et al. [37]	SAPO 34 + bentonite clay + carbon fiber-water	0.26-0.85 g	Measuring the water uptake rate of the composite adsorbent coated on a metallic plate with different thicknesses
Sapienza et al. [38]	SAPO 34-water	4.49-33.13 g	Effects of adsorbent grain size and number of adsorbent layers on in-situ water uptake rate measurement of SAPO 34 under real ACS operating conditions
Gordeeva and Aristov [39]	Activated carbon ACM-35.4-methanol	0.5 g	Effects of 0.8-4.0 mm adsorbents and number of adsorbent layers on water uptake rate of activated carbon ACM-35.4
Freni et al. [40]	Coated SAPO 34-water	84 g	Measuring in-situ water uptake rate of SAPO 34 with 0.1 mm thickness coated on an aluminum heat exchanger under real ACS operating conditions

The main goal of these studies tabulated in Table 1 was to find the effects of large-scale masses (> 1 mg) of different adsorbent materials with different grain sizes and number of adsorbent layers on their in-situ adsorbate uptake rate. Riffel et al. [27], Dawoud [34], Gordeeva et al. [35] and Santamaria et al. [36] also studied the effects of different adsorber bed designs on the adsorbate uptake rate of adsorbent materials. Riffel et al. [27] measured the water uptake rate of silica gel and zeolite packed in a finned tube heat exchanger for adsorption times of less than 3 min. They have mentioned that the scale had to be calibrated for each set of experiments because of the flexible tubes and different heat exchangers. However, they had not noted the effects of the density change of the heat transfer fluid during adsorption and desorption on the adsorber bed mass measurements. Dawoud [34] measured the water uptake rate of FAM-Z02 indirectly from the performance analysis of an adsorption heat pump. Using this method can be misleading

because of the thermal masses of condenser and evaporator. For example, the thermal mass of an evaporator delays the heat transfer from the chilled water to the adsorbate and calculating the adsorbate uptake of an adsorbent material from the chilled water cooling power results in underestimating the water uptake. To minimize such errors, therefore, in-situ adsorbate uptake rate measurements are preferred. Santamaria et al. [36] calculated the performance of an ACS by measuring the water uptake of FAM-Z02 with 72-90 g mass. Their measurements showed 6-8 times higher values than what they found in their large-scale tests because of mass transfer resistances between particles and the metal mesh wrapped around the adsorber bed, and the designs of the condenser and evaporator of the ACS [36].

Based on the literature review, one can conclude that large-scale adsorbate uptake rate measurements for ACS applications lead to more realistic data than those measured by a TGA, but new parameters affect the measurements and, in some cases, they result in underestimating the adsorbate uptake rate. In this study, we tried to resolve some of these parameters, namely, density change of heat transfer fluid and stiffness change of flexible hosing connected to the adsorber bed. The equilibrium water uptake of FAM-Z02 packed in two different adsorber beds is measured in-situ and compared against the TGA data under the adsorption and desorption temperatures of 30°C and 90°C, respectively, and the water source temperature of 20°C. The effects of different cycle times on the water uptake rate of FAM-Z02 are also studied. The significance of heat transfer fluid density change and flexible hosing stiffness variations are investigated and, finally, the maximum achievable SCP and COP of the designed ACS are calculated.

2. Experimental testbed

To measure the mass exchange of an adsorbent packed in an adsorber bed under adsorption or desorption, an experimental test setup was designed and built as shown in Figure 1. The adsorber bed was placed on a scale (Setra, Supper II) with ±1 g accuracy and connected to cooling and heating fluid temperature control systems, TCS_{CF} and TCS_{HF}, for intermittent adsorption and desorption. A water source at a constant temperature, shown in Figure 1, was connected to the adsorber bed using a vacuum rated flexible hose. This water source served as an evaporator and a condenser during adsorption and desorption, respectively.

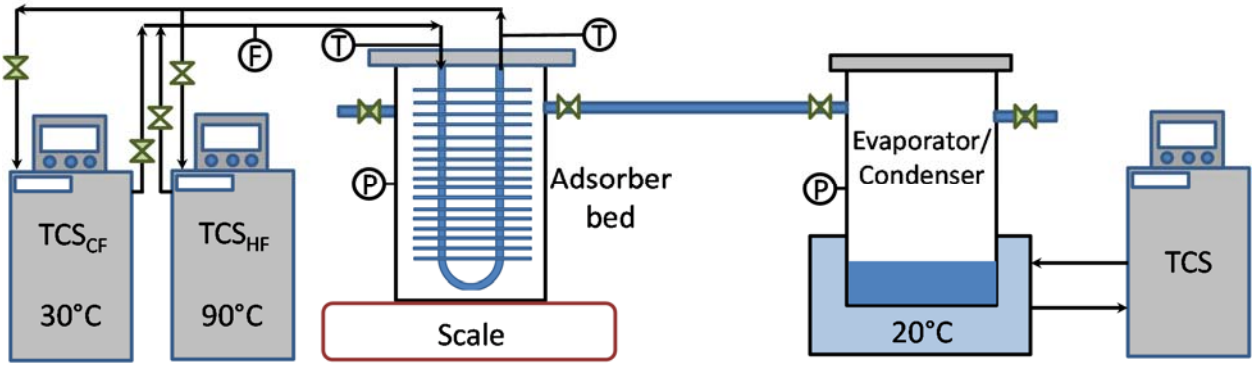

Figure 1. Schematic of the experimental test setup.

To test the effects of different adsorber bed designs, two heat exchangers with different geometries (No. 1 in Figure 2a and Figure 2b) were connected to the evaporator/condenser container (No. 3 in Figure 2a and Figure 2b). The first heat exchanger (called Design I) was built based on the results of Sharafian et al. [41] and was placed inside a vacuum chamber, as shown in Figure 2a. The second adsorber bed (called Design II), which was an engine oil cooler manufactured by Hayden Automotive (model #1268), was placed in a custom-built vacuum chamber, as shown in Figure 2b. The fin spacing and heat transfer surface area of heat exchangers in Designs I and II were 8.47 mm and 0.235 m^2, and 2.54 mm and 2.8 m^2,

respectively. To measure the temperature and pressure of the adsorber beds and evaporator/condenser container, thermocouples type T (Omega, model #5SRTC-TT-T-36-36) with accuracy of 0.75% of reading, and two pressure transducers (Omega, model #PX309-005AI) with 0-34.5 kPa absolute pressure range and ±0.4 kPa accuracy were installed. A positive displacement flow meter (FLOMEC, Model # OM015S001-222) with accuracy of 0.5% of reading was installed on the adsorber bed to measure the heating and cooling fluid flow rates. Table 2 shows further details on the adsorber bed geometries and operating conditions. It can be seen in Table 2 that the amount of adsorbent material inside the adsorber bed of Design II is more than that of Design I. To supply enough water vapor during adsorption process, two evaporators of the same type were connected to the adsorber bed of Design II, as shown in Figure 2b.

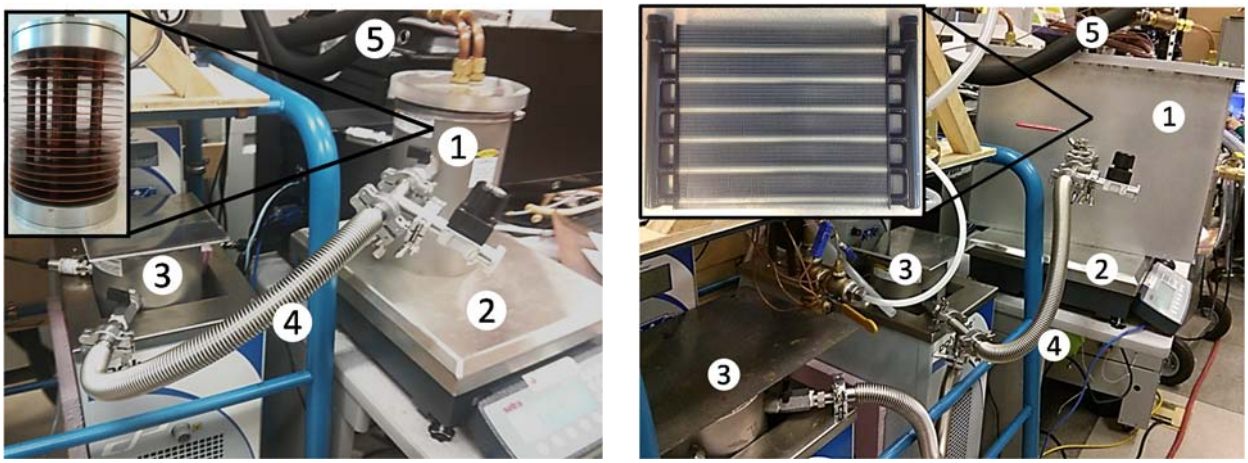

(a) (b)

Figure 2. Details of the experimental setup for (a) Design I and (b) Design II. 1: adsorber bed, 2: scale, 3: evaporator/condenser, 4: flexible hose, and 5: heating/cooling fluid ports.

Table 2. Specifications of adsorber beds and operating conditions.

Parameter	**Design I**	**Design II**
Working pairs	AQSOA FAM-Z02/water	
Adsorbent particles diameter (m)	0.002	
Mass of adsorbent (kg)	0.62	1.50
Metal mass of adsorber bed (kg)	2.80	2.87
Adsorber bed heat transfer surface area, A_{bed}, (m^2)	0.235	2.80
Fin spacing (mm)	8.47 (3 fins per inch)	2.54 (10 fins per inch)
Fin dimensions	12.7 cm (5") diameter	43.18×30.48 cm (17"×12")
Heating fluid mass flow rate to adsorber bed (kg/s)	0.058 (4.1 L/min of silicone oil)	
Cooling fluid mass flow rate to adsorber bed (kg/s)	0.062 (4.1 L/min of silicone oil)	
Heat capacity of silicone oil (kJ/kgK)	1.8	
Heating fluid inlet temperature (°C)	90	
Cooling fluid inlet temperature (°C)	30	
Evaporation/condensation temperature (°C)	20	

The adsorber bed, packed with the FAM-Z02, was heated using a 90°C heating fluid and simultaneously evacuated for 8 hours to be completely dried out. The adsorber bed was then placed on the scale and connected to the evaporator, TCS_{HF}, and TCS_{CF}. For an adsorption process, TCS_{CF} circulated a 30°C cooling fluid to the adsorber bed and once the valve between the adsorber bed and the evaporator was opened the FAM-Z02 adsorbed the water vapor from the evaporator. This adsorption caused the adsorber bed mass to increase over time. For a desorption process, the adsorber bed was heated up with a 90°C heating fluid and the adsorber bed mass reduced due to desorption of water.

3. Data Analysis

The performance of the adsorber beds is evaluated by calculating the COP and SCP of the ACS. Equation (1) gives the ideal evaporation cooling energy, calculated based on the in-situ water uptake rate measurements of FAM-Z02:

$$Q_{evap,ideal}(J) = \Delta\omega_{adsorption}\, m_{adsorbent}\, h_{fg} \tag{1}$$

where $\Delta\omega_{\text{adsorption}}$ is equal to $\Delta m_{\text{adsrobate uptake}}/m_{\text{adsorbent}}$, i.e. the amount of water adsorbed during an adsorption process over the mass of dry adsorbent, and h_{fg} is the enthalpy of evaporation of water at the evaporator temperature. In this study, the ideal evaporation cooling energy refers to an evaporator with the effectiveness of one and thermal mass of zero in which there is no temperature drop between the refrigerant and the chilled water circulated inside the evaporator. This assumption is in agreement with the data measured using a TGA such as the data reported in Ref. [13]. The total heat transfer to the adsorbent material during a desorption process is:

$$Q_{total\ heating}(J) = \int_{desorption} \dot{m}_{hf} c_{p,hf} \left(T_{hf,i} - T_{hf,o}\right) dt \tag{2}$$

where $\dot{m}_{hf}$ is the heating fluid mass flow rate and $T_{hf,i}$ - $T_{hf,o}$ is the temperature difference between the inlet and outlet of the adsorber bed. Using Eqs. (1) and (2), the ideal COP and SCP of the ACS can be calculated:

$$COP_{ideal} = \frac{Q_{evap,ideal}}{Q_{total\ heating}} \tag{3}$$

$$SCP_{ideal}(W/kg) = \frac{Q_{evap,ideal}}{m_{adsorbent}\,\tau_{cycle}} \tag{4}$$

where τ_{cycle} in Eq. (4) is the cycle time.

4. Results and discussion

4.1. Effects of adsorber bed design on the equilibrium water uptake of FAM-Z02

To compare the equilibrium data collected using our experimental setup and the TGA data reported in Ref. [15], two adsorption and desorption isotherm tests were run under the operating conditions summarized in Table 2. To run the equilibrium adsorption test, the dried FAM-Z02 packed in the adsorber beds of Designs I and II was exposed to the water vapor provided by the evaporator at a constant temperature of 20°C. As shown in Figure 3a, the FAM-Z02 adsorbs the water vapor and the adsorber bed mass increases until it reaches a constant value of 30% kg/kg. It can be seen in Figure 3a that the mass of the adsorber bed in Design II increases faster than that in Design I. This is because of the higher heat transfer surface area and faster removal of the heat of adsorption from the adsorber bed. At the adsorption time of 240 min, the equilibrium water uptakes of both adsorber beds reach the same value. Figure 3a also indicates that the equilibrium water uptakes measured using Designs I and II are 3% (= 33% - 30%) less than that measured by the TGA.

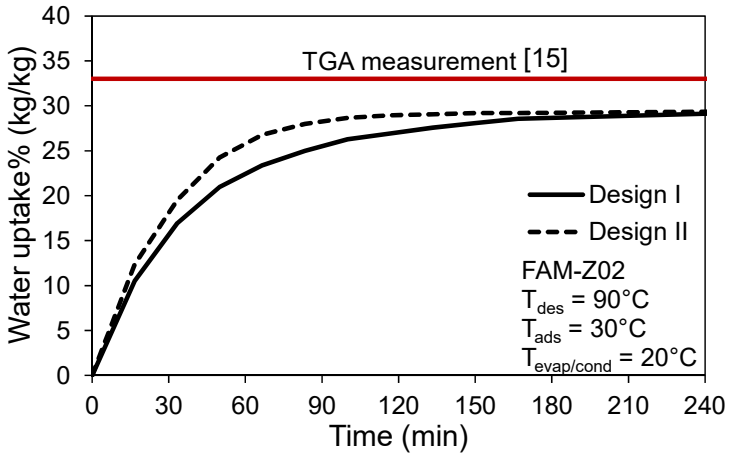

(a)

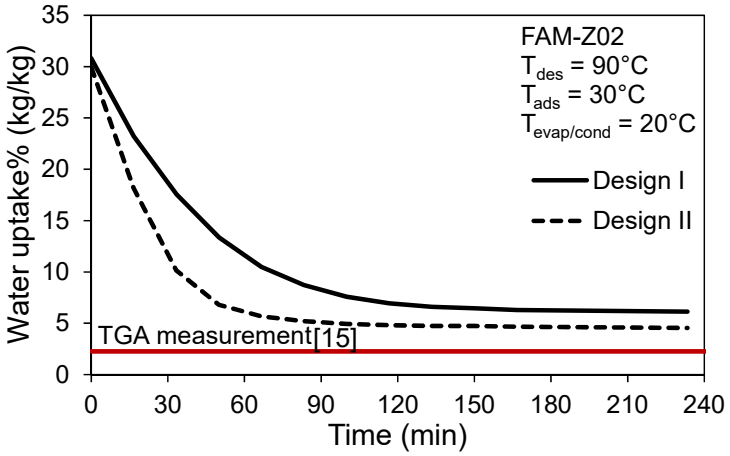

(b)

Figure 3. (a) Adsorption and (b) desorption isotherms measured by using Designs I and II, and compared against the TGA data measurements reported in Ref. [15].

Figure 3b shows the desorption curves for Designs I and II under the operating conditions tabulated in Table 2. Figure 3b demonstrates that the adsorber bed of Design II results in faster water desorption from the FAM-Z02 due to the higher heat transfer rate. Also, at the end of the desorption process the equilibrium water uptake of FAM-Z02 in Design II is 1.6% kg/kg less than that in Design I. The equilibrium water uptakes at the end of the desorption tests of Designs I and II are 3.8% and 2.2% kg/kg more than that of the TGA measurement. Finally, by

comparing the running times of adsorption and desorption processes in Design II, one can conclude that the desorption time of water (120 min) is almost two times shorter than the adsorption time of water (240 min) by FAM-Z02 under the defined operating conditions.

4.2. Effects of adsorber designs on the performance of an ACS

Figure 4 shows the variations in the heating and cooling fluid inlet and outlet temperatures, and the mass changes of the adsorber bed in Design II during adsorption and desorption at cycle time of 60 min. It can be seen in Figure 4 that by cooling the adsorber bed in Design II, adsorption process starts and mass of adsorber bed increases. At the end of adsorption process, the mass of adsorber bed reaches its maximum value. By heating the adsorber bed, the adsorbate is desorbed from the FAM-Z02 and flows to the condenser, and as a result, the mass of adsorber bed starts reducing, as shown in Figure 4b.

The heat transfer fluid used for heating and cooling of the adsorber beds was silicone oil (Julabo, Thermal P60), which had a density change from 909 kg/m^3 at 30°C to 854 kg/m^3 at 90°C. Further, the stiffness of the hosing connected to the adsorber beds changed during heating and cooling processes and affected the mass measurements. To eliminate these undesirable changes in the adsorber bed mass measurements, the adsorber beds were disconnected from the evaporator/condenser container, and heating and cooling processes were performed to measure the adsorber bed mass change caused only by the variations of heat transfer fluid density and the stiffness of the hosing. Figure 4b indicates that these variations can have significant effects on the adsorber bed mass measurement and, consequently, the water uptake rate calculations and should thus be de-convoluted from the measured data.

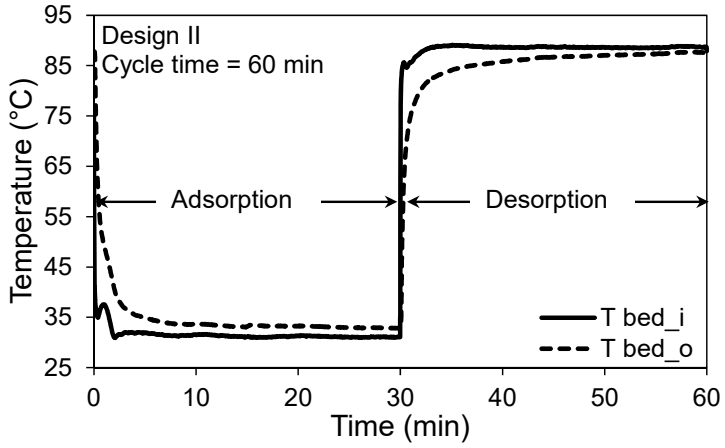

(a)

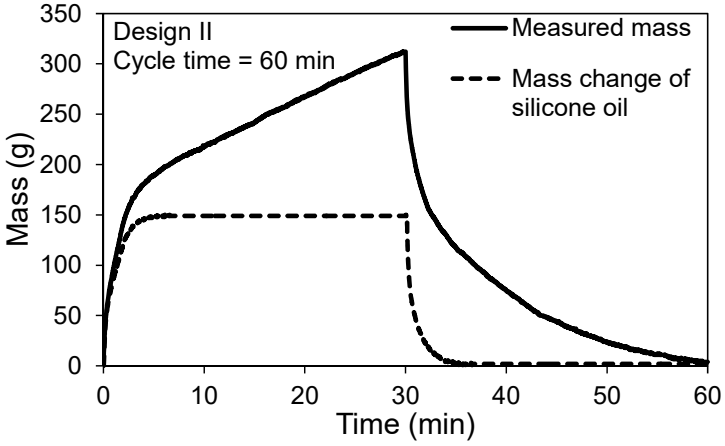

(b)

Figure 4. (a) Heating and cooling fluid inlet and outlet temperatures and (b) mass changes of adsorber bed in Design II and silicone oil during adsorption and desorption under cycle time of 60 min.

Figure 5 shows the variation of evaporator/condenser pressure, $P_{evap/cond}$, for Designs I and II under a cycle time of 60 min. The red line in Figure 5 shows the saturation pressure of water at 20°C. It can be seen in Figure 5 that during the adsorption process, the adsorber beds in Designs I and II create suction, and $P_{evap/cond}$ reduces. This reduction in the evaporator pressure causes water to start evaporating inside the evaporator. Figure 5 also indicates that $P_{evap/cond}$ is lower when the evaporator is connected to the adsorber bed in Design II than when it is connected to

the adsorber bed in Design I, because of higher suction created by the adsorber bed in Design II. Higher suction by the adsorber bed in Design II causes more water evaporation and, as a result, the FAM-Z02 adsorbs more water vapor within a constant adsorption time. By heating the adsorber beds in the desorption process, water is desorbed from the FAM-Z02 and pressures of the adsorber beds increase. Due to the pressure gradient between the adsober bed and the condenser container, water vapor is pushed from the adsorber beds to the condenser.

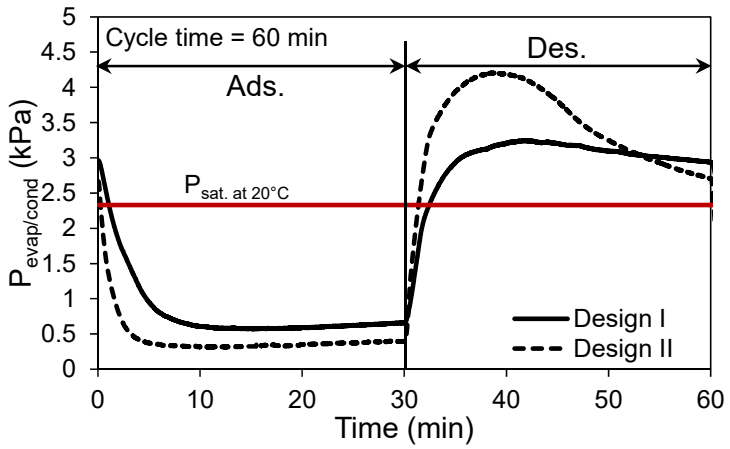

Figure 5. Variations in $P_{evap/cond}$ due to the different adsorber beds in Designs I and II during the adsorption and desorption processes. The red line demarcates the saturation pressure of water at 20°C.

The FAM-Z02 water uptake differences, $\Delta\omega$, between two continuous adsorption and desorption processes were measured in-situ under different cycle times, as shown in Figure 6a. It can be seen in Figure 6a that the adsorber bed in Design II provides higher $\Delta\omega$ than that in Design I for a constant cycle time. For example, under the cycle time of 60 min, the adsorber beds in Designs I and II provide $\Delta\omega$ of 3.5% and 10.8% kg/kg, respectively (a three times higher uptake for Design II). The main reasons for this significant difference between the $\Delta\omega$ of Designs I and II are the high heat transfer surface area and small fin spacing of the adsorber bed in Design II.

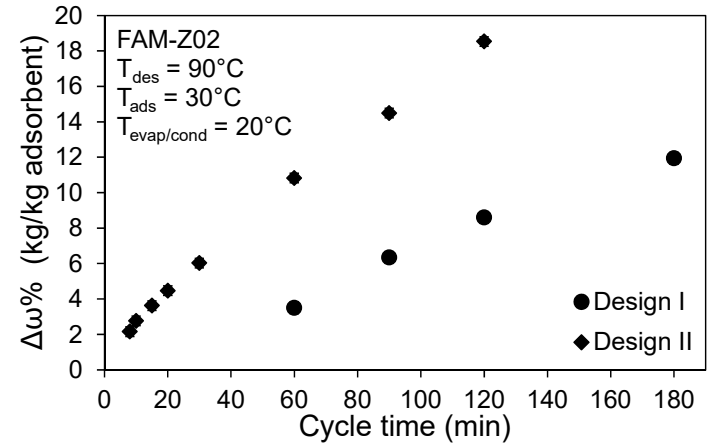

(a)

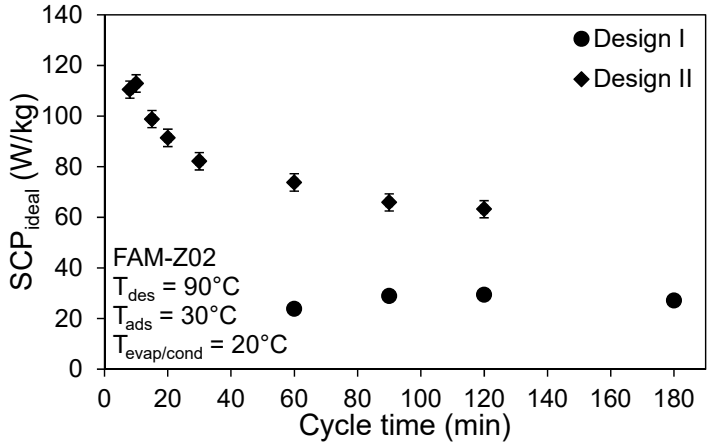

(b)

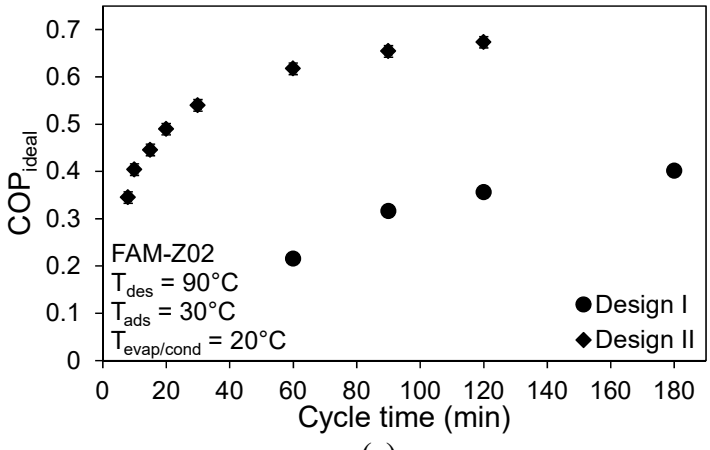

(c)

Figure 6. (a) FAM-Z02 water uptake difference between adsorption and desorption processes, (b) SCP_{ideal} and (c) COP_{ideal} in Designs I and II vs. different cycle times.

These features help the FAM-Z02 adsorb more water vapor during adsorption by more quickly removing the heat of adsorption. Using the measured $\Delta\omega$, the SCP_{ideal} and COP_{ideal} of Designs I and II can be calculated.

Figure 6b shows that the SCP_{ideal} of Design I varies between 23.8-29.3 W/kg for cycle times of 60-180 min. In contrast, the SCP_{ideal} of Design II decreases from 112.9 to 63.2 W/kg by increasing the cycle time from 10 to 120 min. Figure 6c displays that the COP_{ideal} of Design I increases from 0.22 to 0.40 as cycle time is increased from 60 to 180 minutes while the COP_{ideal} of Design II increases from 0.34 to 0.67 as the cycle time is increased from 10 to 120 min. Comparing the SCP_{ideal} and COP_{ideal} of Designs I and II, as shown in Figure 6, indicates that high heat transfer surface area and small fin spacing are two key features of a well-designed adsorber bed for ACS applications and having a proper adsorbent material, such as FAM-Z02, is not necessarily sufficient to reach high ACS performance.

5. Conclusion

The effects of different adsorber bed designs on the performance of an ACS were studied by in-situ water uptake rate measurements of FAM-Z02. The results of a comprehensive literature review showed that large-scale adsorbate uptake rate mass measurements could result in closer performance prediction of an ACS than the adsorbate uptake rate measurements from a TGA. However, other issues affected the mass measurements, such as changes in the density of the heat transfer fluid and variations in the stiffness of the flexible hosing connected to the adsorber beds. In this study, a systematic procedure was introduced to de-convolute these parameters from the in-situ mass measurements to get a precise adsorbate uptake rate and uptake difference measurements. The performance of an ACS was studied under different cycle times and the

results showed that high heat transfer surface area and small fin spacing were key features of a good adsorber bed design for ACS applications. Finally, the results indicated that a combination of high quality adsorbent (FAM-Z02) and a well-designed adsorber bed could produce a SCP_{ideal} of 112.9 W/kg and a COP_{ideal} of 0.34 at cycle time of 10 min.

Acknowledgments

The authors gratefully acknowledge the financial support of the Natural Sciences and Engineering Research Council of Canada (NSERC) through the Automotive Partnership Canada Grant No. APCPJ 401826-10.

Nomenclature

c_p	heat capacity at constant pressure (*J/kg.K*)
COP	coefficient of performance
h_{fg}	enthalpy of evaporation (*J/kg*)
m	mass (*kg*)
$\dot{m}$	mass flow rate (*kg/s*)
P	Pressure (*kPa*)
Q_{total}	total heat transfer (*J*)
SCP	specific cooling power (*W/kg dry adsorbent*)
ω	adsorbate uptake (*kg/kg dry adsorbent*)

T	temperature (K)
t	time (s)
τ_{cycle}	cycle time (s)

Subscripts

adsorbate	adsorbate
adsorbent	adsorbent particles
cf	cooling fluid
cond	condenser
evap	evaporator
hf	heating fluid
i	in
o	out

References

[1] Buzelin LOS, Amico SC, Vargas JVC, Parise JAR. Experimental development of an intelligent refrigeration system. Int J Refrig 2005;28:165–75. doi:10.1016/j.ijrefrig.2004.08.013.

[2] Farrington R, Rugh J. Impact of vehicle air-conditioning on fuel economy, tailpipe emissions, and electric vehicle range. Proceeding Earth Technol. Forum, Washington, D.C.: 2000.

[3] Suzuki M. Application of adsorption cooling systems to automobiles. Heat Recover Syst CHP 1993;13:335–40.

[4] Abdullah MO, Tan IAW, Lim LS. Automobile adsorption air-conditioning system using oil palm biomass-based activated carbon: A review. Renew Sustain Energy Rev 2011;15:2061–72. doi:10.1016/j.rser.2011.01.012.

[5] Demir H, Mobedi M, Ülkü S. A review on adsorption heat pump: Problems and solutions. Renew Sustain Energy Rev 2008;12:2381–403. doi:10.1016/j.rser.2007.06.005.

[6] Poyelle F, Guilleminot JJ, Meunier F. Experimental tests and predictive model of an adsorptive air conditioning unit. Ind Eng Chem Res 1999;38:298–309. doi:10.1021/ie9802008.

[7] Tamainot-Telto Z, Critoph RE. Monolithic carbon for sorption refrigeration and heat pump applications. Appl Therm Eng 2001;21:37–52. doi:10.1016/S1359-4311(00)00030-2.

[8] Freni A, Tokarev MM, Restuccia G, Okunev AG, Aristov YI. Thermal conductivity of selective water sorbents under the working conditions of a sorption chiller. Appl Therm Eng 2002;22:1631–42. doi:10.1016/S1359-4311(02)00076-5.

[9] Sharafian A, Bahrami M. Adsorbate uptake and mass diffusivity of working pairs in adsorption cooling systems. Int J Heat Mass Transf 2013;59:262–71. doi:10.1016/j.ijheatmasstransfer.2012.12.019.

[10] Askalany AA, Salem M, Ismael IM, Ali AHH, Morsy MG, Saha BB. An overview on adsorption pairs for cooling. Renew Sustain Energy Rev 2013;19:565–72. doi:10.1016/j.rser.2012.11.037.

[11] Aristov Y. Concept of adsorbent optimal for adsorptive cooling/heating. Appl Therm Eng 2014;72:166–75. doi:10.1016/j.applthermaleng.2014.04.077.

[12] Himooka SS, Shima KO. The evaluation of direct cooling and heating desiccant device coated with FAM. J Chem Eng Japan 2007;40:1330–4.

[13] Dawoud B. On the Effect of Grain Size on the Kinetics of Water Vapor Adsorption and Desorption into/from Loose Pellets of FAM-Z02 under a Typical Operating Condition of Adsorption Heat Pumps. J Chem Eng Japan 2007;40:1298–306. doi:10.1252/jcej.07WE163.

[14] Henninger SK, Schmidt FP, Henning HM. Water adsorption characteristics of novel materials for heat transformation applications. Appl Therm Eng 2010;30:1692–702. doi:10.1016/j.applthermaleng.2010.03.028.

[15] Okamoto K, Teduka M, Nakano T, Kubokawa S, Kakiuchi H. The development of AQSOA water vapor adsorbent and AQSOA coated heat exchanger. Int. Symp. Innov. Mater. Process. Energy Syst., Singapor: 2010.

[16] Goldsworthy MJ. Measurements of water vapour sorption isotherms for RD silica gel, AQSOA-Z01, AQSOA-Z02, AQSOA-Z05 and CECA zeolite 3A. Microporous Mesoporous Mater 2014;196:59–67. doi:10.1016/j.micromeso.2014.04.046.

[17] Dawoud B, Aristov YI. Experimental study on the kinetics of water vapor sorption on selective water sorbents, silica gel and alumina under typical operating conditions of sorption heat pumps. Int J Heat Mass Transf 2003;46:273–81. doi:10.1016/S0017-9310(02)00288-0.

[18] Aristov YI, Glaznev IS, Freni a., Restuccia G. Kinetics of water sorption on SWS-1L (calcium chloride confined to mesoporous silica gel): Influence of grain size and temperature. Chem Eng Sci 2006;61:1453–8. doi:10.1016/j.ces.2005.08.033.

[19] Aristov YI, Dawoud B, Glaznev IS, Elyas a. A new methodology of studying the dynamics of water sorption/desorption under real operating conditions of adsorption heat pumps: Experiment. Int J Heat Mass Transf 2008;51:4966–72. doi:10.1016/j.ijheatmasstransfer.2007.10.042.

[20] Dawoud B, Vedder U, Amer E-H, Dunne S. Non-isothermal adsorption kinetics of water vapour into a consolidated zeolite layer. Int J Heat Mass Transf 2007;50:2190–9. doi:10.1016/j.ijheatmasstransfer.2006.10.052.

[21] Glaznev IS, Aristov YI. Kinetics of water adsorption on loose grains of SWS-1L under isobaric stages of adsorption heat pumps: The effect of residual air. Int J Heat Mass Transf 2008;51:5823–7. doi:10.1016/j.ijheatmasstransfer.2008.04.061.

[22] Okunev BN, Gromov a. P, Zelenko VL, Glaznev IS, Ovoshchnikov DS, Heifets LI, et al. Effect of residual gas on the dynamics of water adsorption under isobaric stages of adsorption heat pumps: Mathematical modelling. Int J Heat Mass Transf 2010;53:1283–9. doi:10.1016/j.ijheatmasstransfer.2009.12.040.

[23] Glaznev IS, Aristov YI. The effect of cycle boundary conditions and adsorbent grain size on the water sorption dynamics in adsorption chillers. Int J Heat Mass Transf 2010;53:1893–8. doi:10.1016/j.ijheatmasstransfer.2009.12.069.

[24] Glaznev I, Ovoshchnikov D, Aristov YI. Effect of Residual Gas on Water Adsorption Dynamics Under Typical Conditions of an Adsorption Chiller. Heat Transf Eng 2010;31:924–30. doi:10.1080/01457631003604335.

[25] Storch G, Reichenauer G, Scheffler F, Hauer a. Hydrothermal stability of pelletized zeolite 13X for energy storage applications. Adsorption 2008;14:275–81. doi:10.1007/s10450-007-9092-7.

[26] Schnabel L, Tatlier M, Schmidt F, Erdem-Şenatalar A. Adsorption kinetics of zeolite coatings directly crystallized on metal supports for heat pump applications (adsorption

kinetics of zeolite coatings). Appl Therm Eng 2010;30:1409–16. doi:10.1016/j.applthermaleng.2010.02.030.

[27] Riffel DB, Wittstadt U, Schmidt FP, Núñez T, Belo F a., Leite APF, et al. Transient modeling of an adsorber using finned-tube heat exchanger. Int J Heat Mass Transf 2010;53:1473–82. doi:10.1016/j.ijheatmasstransfer.2009.12.001.

[28] Solmuş İ, Yamalı C, Kaftanoğlu B, Baker D, Çağlar A. Adsorption properties of a natural zeolite–water pair for use in adsorption cooling cycles. Appl Energy 2010;87:2062–7. doi:10.1016/j.apenergy.2009.11.027.

[29] Ovoshchnikov DS, Glaznev IS, Aristov YI. Water sorption by the calcium chloride/silica gel composite: The accelerating effect of the salt solution present in the pores. Kinet Catal 2011;52:620–8. doi:10.1134/S0023158411040124.

[30] Askalany A a., Salem M, Ismail IM, Ali AHH, Morsy MG. Experimental study on adsorption–desorption characteristics of granular activated carbon/R134a pair. Int J Refrig 2012;35:494–8. doi:10.1016/j.ijrefrig.2011.04.002.

[31] Aristov YI, Glaznev IS, Girnik IS. Optimization of adsorption dynamics in adsorptive chillers : Loose grains configuration. Energy 2012;46:484–92. doi:10.1016/j.energy.2012.08.001.

[32] Aristov YI. Experimental and numerical study of adsorptive chiller dynamics: Loose grains configuration. Appl Therm Eng 2013;61:841–7. doi:10.1016/j.applthermaleng.2013.04.051.

[33] Chakraborty A, Baran B, Aristov YI. Dynamic behaviors of adsorption chiller : Effects of the silica gel grain size and layers. Energy 2014;78:304–12. doi:10.1016/j.energy.2014.10.015.

[34] Dawoud B. Water vapor adsorption kinetics on small and full scale zeolite coated adsorbers; A comparison. Appl Therm Eng 2013;50:1645–51. doi:10.1016/j.applthermaleng.2011.07.013.

[35] Gordeeva L, Frazzica A, Sapienza A, Aristov YI, Freni A. Adsorption cooling utilizing the “LiBr/silica – ethanol” working pair: Dynamic optimization of the adsorber/heat exchanger unit. Energy 2014;75:390–9. doi:10.1016/j.energy.2014.07.088.

[36] Santamaria S, Sapienza A, Frazzica A, Freni A, Girnik IS, Aristov YI. Water adsorption dynamics on representative pieces of real adsorbers for adsorptive chillers. Appl Energy 2014;134:11–9. doi:10.1016/j.apenergy.2014.07.053.

[37] Frazzica A, Füldner G, Sapienza A, Freni A, Schnabel L. Experimental and theoretical analysis of the kinetic performance of an adsorbent coating composition for use in

adsorption chillers and heat pumps. Appl Therm Eng 2014;73:1020–9. doi:10.1016/j.applthermaleng.2014.09.004.

[38] Sapienza A, Santamaria S, Frazzica A, Freni A, Aristov YI. Dynamic study of adsorbers by a new gravimetric version of the Large Temperature Jump method. Appl Energy 2014;113:1244–51. doi:10.1016/j.apenergy.2013.09.005.

[39] Gordeeva L, Aristov YI. Dynamic study of methanol adsorption on activated carbon ACM-35.4 for enhancing the specific cooling power of adsorptive chillers. Appl Energy 2014;117:127–33. doi:10.1016/j.apenergy.2013.11.073.

[40] Freni A, Bonaccorsi L, Calabrese L, Caprì A, Frazzica A, Sapienza A. SAPO-34 coated adsorbent heat exchanger for adsorption chillers. Appl Therm Eng 2015;82:1–7. doi:10.1016/j.applthermaleng.2015.02.052.

[41] Sharafian A, McCague C, Bahrami M. Impact of fin spacing on temperature distribution in adsorption cooling system for vehicle A/C applications. Int J Refrig 2015;51:135–43.

Appendix F.

Critical analysis of thermodynamic cycle modeling of adsorption cooling systems for light-duty vehicle air conditioning applications

Renewable and Sustainable Energy Reviews 48 (2015) 857–869

Contents lists available at ScienceDirect

Renewable and Sustainable Energy Reviews

journal homepage: www.elsevier.com/locate/rser

Critical analysis of thermodynamic cycle modeling of adsorption cooling systems for light-duty vehicle air conditioning applications

Amir Sharafian, Majid Bahrami *

Laboratory for Alternative Energy Conversion (LAEC), School of Mechatronic Systems Engineering, Simon Fraser University, # 4300, 250-13450 102nd Avenue, Surrey, BC, Canada V3T 0A3

ARTICLE INFO

Article history:
Received 30 November 2013
Received in revised form
1 February 2015
Accepted 19 April 2015
Available online 22 April 2015

Keywords:
Adsorption cooling system
Vehicle air conditioning
Thermodynamic cycle
Fully dynamic modeling

ABSTRACT

Thermodynamic cycle of adsorption cooling systems (ACS) is thoroughly studied under different operating conditions for light-duty vehicles air conditioning applications. Available ACS prototypes installed in vehicles are discussed in detail followed by different ACS thermodynamic cycle modeling. Also, equilibrium uptake and uptake rate of commonly used working pairs in ACS are summarized. The proper ACS thermodynamic cycle with capability of integration with vehicles' Engine Control Unit (ECU) is developed and it is validated against two sets of experimental data reported in the literature. The realistic input data in agreement with light-duty vehicles are introduced to the model as the base-case condition to produce 2 kW cooling power. Sensitivity of ACS specific cooling power (SCP) and coefficient of performance (COP) are studied with respect to the input parameters. According to the results, the SCP and COP of the base-case ACS are maximized at 10–15 min cycle times and adsorption to desorption time ratio (ADTR) of one. In addition, the results indicate that the adsorber bed overall heat transfer conductance and mass have the highest and the lowest effects on the SCP, respectively. Also, the results show that during the operation of ACS, the heating and cooling fluids, coolant fluid and chilled water mass flow rates do not change the SCP and COP after specific values. As a result, variable speed pumps are required to adjust these mass flow rates to reduce feeding pump powers. Finally, the results indicate that the engine coolant cannot provide enough heat for the adsorber bed desorption process under different operating conditions. Therefore, a portion of the exhaust gas of the engine is recommended to be utilized during the desorption process.

Contents

* Corresponding author. Tel.: +1 778 782 8538; fax: +1 778 782 7514.
E-mail addresses: asharafi@sfu.ca (A. Sharafian), mbahrami@sfu.ca (M. Bahrami).

http://dx.doi.org/10.1016/j.rser.2015.04.055
1364-0321/

Nomenclature

A	heat transfer surface area (m^2)
A/C-R	air conditioning and refrigeration
ACS	adsorption cooling system
$ADTR$	adsorption to desorption time ratio
a_i	constants
b_i	constants
c	heat capacity of solid materials (J/kg K)
c_p	heat capacity at constant pressure (J/kg K)
COP	coefficient of performance
D_s	solid-side mass diffusivity (m^2/s)
D_{s0}	pre-exponential constant (m^2/s)
E_a	activation energy (J/mol)
Δh_{ads}	enthalpy of adsorption (J/kg)
ΔT_{LM}	log mean temperature difference (K)
HTS	heat transfer fluid
h_{fg}	enthalpy of vaporization (J/kg)
ICE	internal combustion engine
M	molar mass (kg/mol)
m	mass (kg)
$\dot{m}$	mass flow rate (kg/s)
P	pressure (mbar)
Q_{total}	total heat transfer (J)
$\dot{q}$	heat transfer rate (W)
R_p	average radius of adsorbent particles (m)
R_u	universal gas constant (J/mol K)
SCP	specific cooling power (W/kg dry adsorbent)
ω	adsorbate uptake (kg/kg dry adsorbent)
T	temperature (K)
t	time (s)
τ_{cycle}	cycle time (s)
U	overall heat transfer coefficient (W/m^2 K)
$VCRC$	vapor compression refrigeration cycle

Subscripts

adsorbate	adsorbate
adsorbent	adsorbent particles
bed	adsorber bed
chilled	chilled water
cf	cooling fluid
cond	condenser
coolant	coolant fluid
cooling	cooling process
eq	equilibrium state
evap	evaporator
heating	heating process
hf	heating fluid
i	in
liq.	liquid phase
max	maximum
min	minimum
o	out
sat	saturation
vaporous	vaporous phase

1. Introduction

Vapor compression refrigeration cycles (VCRC) are the most popular air conditioning and refrigeration (A/C-R) systems used in residential and industrial buildings, chemical and process engineering, and the automotive sector. Annually, A/C systems of light duty vehicles in the US consume about 40 billion liters of fuel [1]. To maintain the cabin temperature within the acceptable thermal comfort temperature range, 20–23 °C [2], a compressor of VCRC installed in a typical medium size sedan consumes up to 5–6 kW of the power that the internal combustion engines (ICE) generates. This power is equivalent to the required power for a 1200-kg sedan cruising at 56 km/h [1]. Moreover, approximately 70% of the total fuel energy released in the ICE is wasted through the engine coolant and exhaust gases [3]. A prominent replacement of VCRC is adsorption cooling systems (ACS) in which adsorber beds replace the compressor. ACS take advantage of sorption phenomenon in which a fluid (adsorbate) is adsorbed at the surface of a porous solid material (adsorbent). Common working adsorption pairs used in ACS include: zeolite–water, silica gel–water and activated carbon–methanol. Most of these materials are environmentally friendly, non-toxic, non-corrosive, and inexpensive [4]. Moreover, ACS are quiet and easy to maintain because they do not have any moving parts, except valves [5]. Thus, ACS are ideal candidates for applications where waste-heat or low-grade thermal energy (~100 °C) is available. However, commercialization of ACS faces major challenges; namely: (i) low specific cooling power (SCP), (ii) low coefficient of performance (COP), and (iii) high adsorber bed to adsorbent mass ratio which result in heavy and bulky system. The focus of this study is on light-duty vehicle applications and the following provides the pertinent literature to ACS designed and built for vehicles A/C-R applications.

In 1929, Hulse [6] built the first commercial silica gel–sulphur dioxide ACS and installed it in a freight car refrigeration system to carry fish and meat all over the US. The designed system was able to keep the freezer room temperature as low as −12 °C with minimum moving and control parts, and has the capability of working at car idle time. This ACS consisted of two adsorber beds, an air-cooled condenser and two gas burners to supply high temperature gas for the desorption process. With the advent of compressors and emergence of VCRC, ACS were forgotten for several decades; however, due to VCRC high energy consumption, negative environmental impacts and stringent government emission regulations, ACS have been reconsidered from 1990s. Feasibility of VCRC replacement with ACS in electric vehicles (EVs) was analytically investigated by Aceves [7]. According to his calculations, during a 60 min driving cycle, the A/C system should be able to bring the cabin temperature down from the hot soak (43 °C) to the comfort (25 °C and 60% relative humidity) conditions within the first 15 min. As a result, Aceves' calculations showed that the maximum required cooling power is 2 kW and to keep the cabin temperature constant, the A/C system should continuously supply 1.5 kW cooling power. Finally, Aceves concluded that the mass of VCRC could be up to 20% lighter than that of ACS. It should be noted that, in Aceves' analysis, the COP of 2.2 was assumed for the vehicles' VCRC; however, the COP of vehicles' VCRC is between 1.0–1.6 in real applications [8–10]. Suzuki [3] assessed the possibility of using the ACS for automobile A/C applications and studied the effects of adsorber bed overall heat transfer conductance, UA (W/K), on the SCP of zeolite–water ACS. Suzuki reported that the engine coolant at the inlet of the radiator and the engine exhaust gas at the outlet of the piston compartment were at 95 °C and 400–600 °C, respectively; and these temperatures were enough for regeneration of the adsorber beds. Suzuki, also, mentioned that the power generated in a compact vehicle with a 2000 cc ICE were about 10.8 and 35–50 kW at the idle and city driving (60 km/h) conditions, respectively [3]. As such, one can conclude that the

amount of heat dissipated through the engine coolant and the ICE exhaust gas during the idle and city driving conditions are equal to 7.5 and 24.5–35 kW, which is equivalent to 70% of fuel released energy. Accordingly, the COP of an ACS with 2 kW cooling power should be at least 0.27 (=2 kW (max. cooling load)/7.5 kW (available waste heat at the idle condition)) and 0.057 (=2 kW (max. cooling load)/35 kW (available waste heat at the city driving condition)). Thus, one can conclude that: (i) the COP of ACS is not important in vehicle applications where the ICE waste-heat is utilized, and (ii) a fraction of the ICE waste heat suffices to run an ACS to meet the A/C needs of a vehicle. As such, our focus in this study will be on the SCP and adsorber bed to adsorbent mass ratio of ACS for vehicle applications.

Zhang et al. [11–15] proposed non-equilibrium lumped-body and 3D numerical models for a two-adsorber bed, zeolite–water ACS for automobile waste heat recovery. They studied the effects of different parameters such as heat transfer fluid (HTF) inlet temperature, evaporation and condensation temperatures, cycle time, and overall heat transfer conductance on the SCP and COP of ACS. They concluded that the SCP is more sensitive to the variation of operating conditions, namely, evaporation, condensation and regeneration temperatures, than the COP. In both Suzuki's [3] and Zhang's [11–15] models, the evaporator and condenser physical properties were not included in the modeling and it was assumed that the evaporator and condenser are perfect heat exchangers with infinite overall heat transfer conductance.

Jiangzhou et al. [16] and Lu et al. [17] built a locomotive waste heat driven, single-adsorber bed, zeolite 13X-water ACS to produce 4 kW cooling power with a SCP and COP of 19 W/kg dry adsorbent and 0.25, respectively. In their system, 140 kg of zeolite was packed in a 260-kg steel adsorber bed with 10–12 W/m^2 K overall heat transfer coefficient; the low overall heat transfer coefficient resulted in a low heat transfer rate and, consequently, low SCP of 19 W/kg dry adsorbent. Christy and Toossi [18] studied the feasibility of installing a four-adsorber bed, activated carbon-ammonia ACS on containerships and heavy-duty vehicles. Their analysis showed that to drive a compressor of refrigerated trailers, a 25-kW auxiliary diesel engine annually consumed about 4500–6000 l of diesel fuel and emitted 29 kg of carbon monoxide if the A/C system only worked during 50% of the duty cycle. In their adsorber bed design, they determined that if the waste heat is directly supplied from the exhaust pipe, the maximum allowable backpressure on the exhaust gas along the exhaust line should be less than 10 kPa. To prevent increasing the backpressure, the inner diameter of HTF line inside the adsorber bed should be between 12.7 and 15.24 cm (5–6 in.) [18]. Also, they tried to build a prototype ACS; however, their system failed due to ammonia leakage.

Lambert and Jones [19,20] studied the viability of using ACS for automotive A/C applications and proposed a conceptual design for an activated carbon–ammonia ACS. To reduce the backpressure on the exhaust gas line, they suggested using a phase-change material (PCM) heat storage tank to transfer heat from the exhaust gas to HTF and storing heat for running the ACS after shutting off the engine. Wang et al. [21–25] designed a two-adsorber bed, consolidated activated carbon/$CaCl_2$–ammonia ACS to produce ice in fishing boats. The exhaust gas of the boats' diesel engine was utilized to regenerate the adsorbent particles and to prevent corrosion of the adsorber beds and condenser in contact with the salt water, Wang et al. [21–25] proposed using heat pipes. The added heat pipes increased the ACS performance, however, the overall mass of the system also increased. Therefore, using heat pipes is not recommended for light-duty vehicles' A/C applications. De Boer et al. [2,26] built and installed a two-adsorber bed, silica gel–water ACS with 2-kW cooling power for the first time in a compact car, Fiat Stilo. Their analysis showed that the engine coolant was sufficient to meet the A/C needs of the cabin if the COP of ACS was greater than 0.5. However, in the final product, they added a heat exchanger to use the ICE exhaust gas as well. In their setup, each adsorber bed was filled with about 3 kg of silica gel and the adsorber bed to adsorbent mass ratio was 4.2 which indicated that each adsorber bed was 12.6 kg. The 86 kg total mass of their system greatly exceeded the 35 kg limit set by the car manufacturer [2].

Narayanan et al. [27,28] recently proposed the idea of an adsorption-based thermal battery for EVs' A/C application. The 2-kWh single-adsorber bed thermal battery was regenerated by electric heaters when the EV's batteries were being charged to produce cooling power for the on-duty vehicle. However, Narayanan et al. [27,28] did not discuss about the total weight of the thermal battery and its advantages instead of adding extra Li-ion battery packs for running the conventional VCRC. One can conclude from the literature review that bulkiness and weight of the current designs are the main challenges facing the commercialization of ACS.

Developing an accurate thermodynamic model that includes the heat and mass transfer phenomena in the adsorber bed, evaporator and condenser, and accurately predicts the behavior of ACS under various operating conditions is the first step toward designing a mobile ACS with optimum footprint and weight. The proposed model should provide (i) high convergence rate to find the optimized operating conditions of the system within a short time, and (ii) possibility of integrating with the vehicles' Engine Control Unit (ECU). In this paper, different thermodynamic models are compared against each other and required information about different working pairs is summarized. The nominated thermodynamic model is verified against two sets of experimental data available in the literature and, finally, effects of different parameters are studied on the SCP and COP of silica gel–water ACS for light-duty vehicle A/C applications.

2. Thermodynamic cycle of ACS

An ACS works based on two main processes: heating–desorption–condensation and cooling–adsorption–evaporation. When repeating

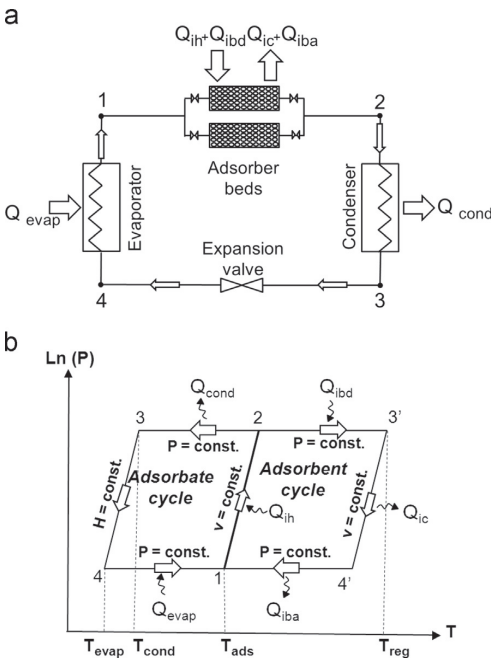

Fig. 1. (a) Schematic of main parts in a waste heat-driven two-adsorber bed ACS, and (b) thermodynamic processes in an ACS [29].

these processes, ACS produces intermittent evaporative cooling power during each cycle. To produce continuous cooling power, more than one adsorber bed can be used. Fig. 1a depicts a typical ACS including adsorber beds, condenser, expansion valve, and evaporator. As shown in Fig. 1a, the ACS is similar to a VCRC, except that the adsorber beds replace the compressor.

Fig. 1b shows the thermodynamic cycle of an ACS which is divided into two subcycles: (i) adsorbent cycle (on the right-side), and (ii) adsorbate cycle (on the left-side). As shown in Fig. 1b, thermodynamic processes in the adsorbent cycle are: (1) isosteric heating (ih); process 1-2, (2) isobaric desorption (ibd); process 2-3′, (3) Isosteric cooling (ic); process 3′-4′, and (4) isobaric adsorption (iba); process 4′-1. Isosteric and isobaric processes refer to constant specific volume and pressure processes, respectively.

During step 1-2, adsorbent–adsorbate pair through an isosteric process absorbs heat in amount of Q_{ih} from an external heat source. In this step, temperature and pressure of the adsorber bed increase due to the adsorbate desorption from the adsorbent particles. This process is continued until the pressure of the adsorber bed reaches the pressure of the condenser. At this time, the inlet valve to the condenser is opened. In step 2-3′, the external heat source continuously heats the adsorber bed (Q_{ibd}) during an isobaric desorption process and the adsorbate leaves the adsorber bed and is condensed inside the condenser during an isobaric cooling process (step 2-3). After heating the adsorber bed up to the point 3′ which is the maximum temperature of the cycle, the valve between the adsorber bed and the condenser is closed and during an isosteric cooling process (step 3′-4′), the adsorbent loses its heat (Q_{ic}) in contact with a heat sink. In step 3-4, the adsorbate inside the condenser passes through the expansion valve and enters to the evaporator. During step 4-1, the adsorbate absorbs heat in amount of Q_{evap} from the environment of interest and converts to the vapor. At the same time, the entrance valve to the adsorber bed is opened and the adsorbent adsorbs the vapor adsorbate during an isobaric adsorption process (step 4′-1) and releases its heat (Q_{ibd}).

To simulate the ACS thermodynamic cycle, different assumptions and simulations have been reported in the literature. Yong and Sumathy [30] reviewed and categorized the available mathematical models in the ACS thermodynamic cycle modeling. However, there is no conclusive evidence on what model is superior. We categorized the mathematical models into three main groups: (i) analytical models, (ii) lumped-body models, and (iii) geometry-dependent models. Analytical models are the simplest and fastest method in design and analysis of ACS performance. In these models, the first law of thermodynamics is used to analytically evaluate the SCP and COP of ACS such as models reported by Aceves [7], Christy and Toossi [18] and Lambert and Jones [19,20]. The analytical models cannot predict the cycle time and the status each process. To solve these limitations, lumped-body models were proposed. These models are a combination of the first law of thermodynamics and mass transfer equations. They consist of ordinary differential equations to increase the accuracy of the model and can predict the cycle time, SCP, and the ACS status during each process. Geometry-dependent models are a combination of heat and mass transfer equations, and spatial parameters. The governing equations are mainly partial differential equations and the finite element, finite volume and finite difference methods are used to discretize and solve the set of equations. Further information about geometry-dependent models can be found elsewhere, e.g. [12,15,31–42]. Although these models are suitable to study the heat and mass transfers through the adsorber bed in detail, the computing time and complexity of analysis do not permit the integration of these models with the on-duty vehicle A/C system. In this study, we focus on lumped-body models to find a reliable model with short computing time. To this end, we classified ACS lumped-body models into three subgroups as summarized in Table 1.

As shown in Table 1, quasi-steady state models have some limitations and cannot predict the cycle time and SCP of ACS. The ACS dynamic modeling with perfect condenser and evaporator are more flexible; however, they cannot estimate the effects of condenser and evaporator on the COP and SCP of ACS. Also, Restuccia et al. [63] experimentally showed that the condenser and evaporator pressures are not constant during the desorption and adsorption processes (processes 2-3′ and 4′-1 in Fig. 1b) because the condenser and evaporator pressures vary with the adsorbate flow rate, for example the condenser pressure is higher at the start of the desorption process than the end of the desorption process. Therefore, the ACS dynamic modeling with perfect condenser and evaporator is not a complete model and should be modified. To

Table 1
Different ACS lumped-body models reported in the literature.

ACS lumped-body models	Governing equations	Advantages	Limitations	Used by
Quasi-steady state	• 1st law of thermodynamics • Equilibrium adsorbate uptake	• Quick method • Estimates maximum evaporative cooling energy and COP	• Time-independent • Cannot predict the cycle time and SCP	• Cacciola and Restuccia [43] • Hajji and Khalloufi [44] • Sharafian and Bahrami [29]
Dynamic modeling with perfect condenser and evaporator	• 1st law of thermodynamics • Equilibrium adsorbate uptake • Adsorbate uptake rate	• Predicts adsorbate uptake rate, cycle time, COP, and SCP • Captures trend of experimental data • High convergence rate	• Perfect condenser and evaporator with infinite heat transfer conductance • Constant condenser and evaporator pressures • Overestimating the results	• Sakoda and Suzuki [45,46] • Tiansuwan et al. [47] • Saha et al. [48,49] • Wu et al. [50]
Fully dynamic modeling	• 1st law of thermodynamics • Equilibrium adsorbate uptake • Adsorbate uptake rate • Condenser and evaporator heat transfer equations	• Predicts adsorbate uptake rate, cycle time, COP, and SCP • Variable condenser and evaporator pressures • High convergence rate • Good accuracy	• Requires a large number of inputs to the model	• Chua et al. [51] • Ref. [52–62]

solve these limitations, ACS fully dynamic thermodynamic cycle is proposed.

3. ACS governing equations

In this section, governing equations for an ACS fully dynamic model are developed. In addition, different working pairs' characteristics were included in this modeling to develop a comprehensive model for the ACS sizing and rating under different operating conditions.

3.1. Mathematical modeling

The governing equations of the ACS fully dynamic thermodynamic cycle are summarized in Table 2.

To find the adsorbent particles temperature, adsorbate uptake rate, and heating fluid and condenser coolant outlet temperatures during the isosteric heating and isobaric desorption processes, Eqs. (1)–(3) and Eqs. (2)–(8) should be solved simultaneously. Similarly, Eqs. (11)–(13), and Eq. (5) and Eqs. (12)–(17) should be solved simultaneously during the isosteric cooling and isobaric adsorption processes. The total amount of heat transfer to/removal from the adsorber beds, condenser and evaporator are calculated from Eqs. (20)–(23), and the COP and SCP of ACS are determined using Eqs. (24) and (25), respectively.

3.2. Working pairs' characteristics

Silica gel–water, activated carbon–methanol, activated carbon–ethanol, and zeolite–water are conventional working pairs in ACS. To increase the adsorbate uptake rate in ACS, a wide range of composite adsorbent materials have been developed recently; however, limited information about the adsorbate uptake rate has been reported in the literature which is an important parameter in ACS thermodynamic cycle modeling. In this section, performance parameters and thermo-physical properties are presented for well-

Table 2
Governing equations on ACS fully dynamic thermodynamic cycle modeling.

Process in Fig. 1b	Governing equation (Eq. no.)
Isosteric heating (Step 1-2)	$m_{adsorbent}\left[c_{adsorbent}+c_{p,liq.\ \ adsorbate}\omega_{max}+c_{bed}\frac{m_{bed}}{m_{adsorbent}}\right]\frac{dT_{adsorbent}}{dt}=U_{bed}A_{bed}\Delta T_{LM,bed}$ (1)
	$\Delta T_{LM,bed}=\frac{T_{hf,i}-T_{hf,o}}{\ln\left(\frac{T_{hf,i}-T_{adsorbent}}{T_{hf,o}-T_{adsorbent}}\right)}$ (2)
	$\dot{m}_{hf}c_{p,hf}\left(T_{hf,i}-T_{hf,o}\right)=U_{bed}A_{bed}\Delta T_{LM,bed}$ (3)
Isobaric desorption (Step 2-3')	$m_{adsorbent}\left[c_{adsorbent}+c_{p,liq.\ \ adsorbate}\omega+c_{bed}\frac{m_{bed}}{m_{adsorbent}}\right]\frac{dT_{adsorbent}}{dt}-m_{adsorbent}\frac{d\omega}{dt}\Delta h_{ads}$ $=U_{bed}A_{bed}\Delta T_{LM,bed}$ (4)
	$\frac{d\omega}{dt}=\frac{15D_s}{R_p^2}(\omega_{eq}-\omega)=\frac{15D_{s0}}{R_p^2}\exp\left(-\frac{E_a}{R_uT_{adsorbent}}\right)(\omega_{eq}-\omega)=k_1\exp(-\frac{k_2}{T_{adsorbent}})(\omega_{eq}-\omega)$ (5)
Condensation (Step 2-3)	$-m_{adsorbent}\frac{d\omega}{dt}[h_{fg,\ adsorbate\ @\ T_{cond}}+c_{p,vaporous\ adsorbate}(T_{adsorbent}-T_{cond})]-U_{cond}A_{cond}\Delta T_{LM,cond}$ $=m_{cond}c_{cond}\frac{dT_{cond}}{dt}$ (6)
	$\Delta T_{LM,cond}=\frac{T_{coolant,i}-T_{coolant,o}}{\ln\left(\frac{T_{cond}-T_{coolant,o}}{T_{cond}-T_{coolant,i}}\right)}$ (7)
	$\dot{m}_{coolant}c_{p,coolant}\left(T_{coolant,o}-T_{coolant,i}\right)=U_{cond}A_{cond}\Delta T_{LM,cond}$ (8)
Heating and condensation heat transfer rates	$\dot{q}_{heating}=\dot{m}_{hf}c_{p,hf}\left(T_{hf,i}-T_{hf,o}\right)$ (9)
	$\dot{q}_{cond}=\dot{m}_{coolant}c_{p,coolant}\left(T_{coolant,i}-T_{coolant,o}\right)$ (10)
Isosteric cooling (Step 3'-4')	$m_{adsorbent}\left[c_{adsorbent}+c_{p,liq.\ \ adsorbate}\omega_{min}+c_{bed}\frac{m_{bed}}{m_{adsorbent}}\right]\frac{dT_{adsorbent}}{dt}=U_{bed}A_{bed}\Delta T_{LM,bed}$ (11)
	$\Delta T_{LM,bed}=\frac{T_{cf,i}-T_{cf,o}}{\ln\left(\frac{T_{cf,i}-T_{adsorbent}}{T_{cf,o}-T_{adsorbent}}\right)}$ (12)
	$\dot{m}_{cf}c_{p,cf}\left(T_{cf,i}-T_{cf,o}\right)=U_{bed}A_{bed}\Delta T_{LM,bed}$ (13)
Isobaric adsorption (Step 4'-1)	$m_{adsorbent}\left[c_{adsorbent}+c_{p,liq.\ \ adsorbate}\omega+c_{bed}\frac{m_{bed}}{m_{adsorbent}}\right]\frac{dT_{adsorbent}}{dt}-$ $m_{adsorbent}\frac{d\omega}{dt}[\Delta h_{ads}-c_{p,vaporous\ adsorbate}\left(T_{adsorbent}-T_{evap}\right)]$ $=U_{bed}A_{bed}\Delta T_{LM,bed}$ (14)
Evaporation (Step 4-1)	$-m_{adsorbent}\frac{d\omega}{dt}\left[h_{fg,\ adsorbate\ @\ T_{evap}}-c_{p,liq.\ adsorbate}\left(T_{cond}-T_{evap}\right)\right]+U_{evap}A_{evap}\Delta T_{LM,evap}$ $=m_{evap}c_{evap}\frac{dT_{evap}}{dt}$ (15)
	$\Delta T_{LM,evap}=\frac{T_{chilled,i}-T_{chilled,o}}{\ln\left(\frac{T_{chilled,i}-T_{evap}}{T_{chilled,o}-T_{evap}}\right)}$ (16)
	$\dot{m}_{chilled}c_{p,chilled}\left(T_{chilled,i}-T_{chilled,o}\right)=U_{evap}A_{evap}\Delta T_{LM,evap}$ (17)
Cooling and evaporation heat transfer rates	$\dot{q}_{cooling}=\dot{m}_{cf}c_{p,cf}\left(T_{cf,i}-T_{cf,o}\right)$ (18)
	$\dot{q}_{evap}=\dot{m}_{chilled}c_{p,chilled}\left(T_{chilled,i}-T_{chilled,o}\right)$ (19)
Total heat transfer to adsorber beds, condenser and evaporator	$Q_{total\ \ heating}=\int_{steps\ (1-2)+(2-3')}\dot{q}_{heating}\ dt(J)$ (20)
	$Q_{total\ \ cooling}=\int_{steps\ (3'-4')+(4'-1)}\dot{q}_{cooling}\ dt(J)$ (21)
	$Q_{cond}=\int_{step\ (2-3)}\dot{q}_{cond}\ dt(J)$ (22)
	$Q_{evap}=\int_{step\ (4-1)}\dot{q}_{evap}\ dt(J)$ (23)
Performance of ACS	$COP=\frac{Q_{evap}}{Q_{total\ \ heating}}$ (24)
	$SCP=\frac{Q_{evap}}{m_{adsorbent}\tau_{cycle}}(W/kg)$ (25)

Table 3
Equilibrium adsorbate uptake and enthalpy of adsorption of different working pairs in ACS.

Working pair	Equilibrium equation	Enthalpy of adsorption (J/kg)	Constant parameters	Ref. no.
Zeolite 4A–water	$\ln(P)=a(\omega)+\frac{b(\omega)}{T_{adsorbent}}$, P in mbar, T in K $a(\omega)=a_0+a_1\omega+a_2\omega^2+a_3\omega^3$ $b(\omega)=b_0+b_1\omega+b_2\omega^2+b_3\omega^3$	$\Delta h_{ads}=\frac{R_u}{M_{adsorbate}}b(\omega)$	$a_0=14.8979$, $b_0=-7698.85$ $a_1=95.408$, $b_1=21498.1$ $a_2=-636.66$, $b_2=-184598.0$ $a_3=1848.8$, $b_3=512605.0$ $R_u=8.314$ J/mol K $M_{adsorbate}=0.018$ kg/mol	[43]
Zeolite 13X–water	$\ln(P)=a(\omega)+\frac{b(\omega)}{T_{adsorbent}}$, P in mbar, T in K $a(\omega)=a_0+a_1\omega+a_2\omega^2+a_3\omega^3$ $b(\omega)=b_0+b_1\omega+b_2\omega^2+b_3\omega^3$	$\Delta h_{ads}=\frac{R_u}{M_{adsorbate}}b(\omega)$	$a_0=13.4244$, $b_0=-7373.78$ $a_1=110.854$, $b_1=6722.92$ $a_2=-731.76$, $b_2=5624.47$ $a_3=1644.8$, $b_3=-3486.7$ $R_u=8.314$ J/mol K $M_{adsorbate}=0.018$ kg/mol	[43]
Act. carbon–methanol	$\ln(P)=a(\omega)+\frac{b(\omega)}{T_{adsorbent}}$, P in mbar, T in K $a(\omega)=a_0+a_1\omega+a_2\omega^2+a_3\omega^3$ $b(\omega)=b_0+b_1\omega+b_2\omega^2+b_3\omega^3$	$\Delta h_{ads}=\frac{R_u}{M_{adsorbate}}b(\omega)$	$a_0=20.3305$, $b_0=-6003.58$ $a_1=6.53035$, $b_1=6315.16$ $a_2=-16.6841$, $b_2=-26058.7$ $a_3=52.3793$, $b_3=40537.9$ $R_u=8.314$ J/mol K $M_{adsorbate}=0.032$ kg/mol	[43]
Act. carbon–ethanol	$\omega_{eq}=\omega_0\exp\left[-A\left[T_{adsorbent}\ln\left(\frac{P_{sat}@T_{adsorbent}}{P_{cond\ or\ evap}}\right)\right]^2\right]$, T in K	$\frac{\Delta h_{ads}-h_{fg}}{E}=\left[\ln\left(\frac{\omega_0}{\omega_{eq}}\right)\right]^{1/n}+a\left[\frac{T_{adsorbent}}{T_c}\right]^b$	$\omega_0=0.797$ kg/kg $A=1.716\times10^{-6}$ K^{-2} $a=6.717$, $b=9.75$ $n=2$, $E=138$ kJ/kg $T_c=789.15$ K	[64]
RD silica gel–water	$\omega_{eq}=\frac{K_0\exp\left(\frac{\Delta h_{ads}M_{adsorbate}}{R_uT_{adsorbent}}\right)P}{\left[1+\left[\frac{K_0}{\omega_m}\exp\left(\frac{\Delta h_{ads}M_{adsorbate}}{R_uT_{adsorbent}}\right)P\right]^n\right]^{1/n}}$, P in *mbar*, T in *K*	$\Delta h_{ads}=2693$ kJ/kg	$K_0=7.3\times10^{-11}$ mbar^{-1} $\omega_m=0.45$ kg/kg $n=12$ $R_u=8.314$ J/mol K $M_{adsorbate}=0.018$ *kg/mol*	[65]
Silica gel/$CaCl_2$–water	$\omega_{eq}=\frac{\omega_mK_0\exp\left(\frac{\Delta h_{ads}M_{adsorbate}}{R_uT_{adsorbent}}\right)P}{\left[1+\left[K_0\exp\left(\frac{\Delta h_{ads}M_{adsorbate}}{R_uT_{adsorbent}}\right)P\right]^n\right]^{1/n}}$, P in mbar, T in K	$\Delta h_{ads}=2760$ *kJ/kg*	$K_0=2.0\times10^{-10}$ mbar$^-$ $\omega_m=0.8$ kg/kg $n=1.1$ $R_u=8.314$ J/mol K $M_{adsorbate}=0.018$ kg/mol	[57,66]

Table 4
Constant parameters in the LDF model (Eq. (5)) for adsorbate uptake rate modeling.

LDF model: $\frac{d\omega}{dt}=\frac{15D_s}{R_p^2}(\omega_{eq}-\omega)=\frac{15D_{s0}}{R_p^2}\exp\left(-\frac{E_a}{R_uT_{adsorbent}}\right)(\omega_{eq}-\omega)=k_1\exp(-\frac{k_2}{T_{adsorbent}})(\omega_{eq}-\omega)$

Working pair	Constant parameters					Ref. no.
	D_{s0} (m^2/s)	R_p (m)	E_a (J/mol)	k_1 (1/s)	k_2 (K)	
Zeolite 4 A–water	1.31×10^{-9}	4.0×10^{-6}	5660	1228.12	680.7	[70,71]
Zeolite 13X–water	–	–	7530	4.004×10^{-2}	905.8	[11]
Act. carbon–methanol	–	–	8131	7.35×10^{-3}	978	[72]
Act. carbon–ethanol	$11/15\times1.8\times10^{-12}$	6.5×10^{-6}	14,100	3.046×10^{-6}	1696	[64]
RD silica gel–water	2.54×10^{-4}	1.7×10^{-4}	42,000	1.318×10^{5}	5051.7	[45,57,73]
Silica gel/$CaCl_2$–water	2.54×10^{-4}	1.74×10^{-4}	42,000	1.258×10^{5}	5051.7	[57,73]

known working pairs, namely, zeolite 4A–water, zeolite 13X–water, activated carbon–methanol, activated carbon fibers–ethanol, silica gel–water, and silica gel/$CaCl_2$ (SWS-1)-water. The equilibrium adsorbate uptake by various adsorbent materials and the enthalpy of adsorption of different working pairs are summarized in Table 3.

The information summarized in Table 3 only provides the equilibrium adsorbate uptake by the adsorbent particles whereas in the ACS thermodynamic cycle modeling, adsorbate uptake rate is required because ACS is a dynamic system in which adsorbent particles cannot be fully saturated or dried out during a cycle. Different models for the adsorbate uptake rate have been reported for various boundary conditions and geometries. Ruthven et al. [67,68] provided analytical solutions for the adsorbate uptake rate by zeolite and other microporous materials which, in some cases, are not easy to use. To this end, Glueckauf [69] proposed a simplified model, called linear driving force (LDF) model, for the adsorbate uptake rate of the adsorbent particles. Table 4 shows a summary of the constant parameters in the LDF model, Eq. (5), to calculate the adsorbate uptake rate of different adsorbent particles.

Further information required for thermo-physical properties of working pairs, such as heat capacity, enthalpy of vaporization and saturation pressure, as a function of temperature are tabulated in Table 5.

3.3. Solution method

To solve the set of differential equations simultaneously, an in-house code is developed using the FORTRAN language. The Runge–

Table 5
Thermo-physical properties of working pairs in ACS modeling.

Material	Thermo-physical properties[a]	Ref. no.
Water	$c_{p,\ liq.\ water} = 5\times10^{-5}T^3 - 0.0465T^2 + 13.476T + 2884.0$ (J/kg K)	Fitted to the data in Ref. [74]
	$c_{p,\ water\ vapor} = 0.0006T^2 - 0.0426T + 1824.1$ (J/kg K)	Fitted to the data in Ref. [74]
	$h_{fg,\ water} = -7.1T^2 + 2620.4T + 2.2866\times10^6$ (J/kg)	Fitted to the data in Ref. [74]
	$P_{sat.,\ water} = \exp(20.5896 - \frac{5098.26}{T})$ (mbar)	[43]
Methanol	$c_{p,\ liq.\ methanol} = 6.3T + 287.8$ (J/kg K)	Fitted to the data in Ref. [75]
	$c_{p,\ methanol\ vapor} = 2.4016T + 657.21$ (J/kg K)	Fitted to the data in Ref. [75]
	$h_{fg,\ methanol} = -10.7T^2 + 5203.4T + 5.5415\times10^5$ (J/kg)	Fitted to the data in Ref. [75]
	$P_{sat.,\ methanol} = \exp(20.84 - \frac{4696.0}{T})$ (mbar)	[43]
Ethanol	$c_{p,\ liq.\ ethanol} = 10.99T - 701.5$ (J/kg K)	Fitted to the data in Ref. [75]
	$c_{p,\ ethanol\ vapor} = 1.635\times10^{-4}T^3 - 0.1391T^2 + 42.3T - 2981.0$ (J/kg K)	Fitted to the data in Ref. [75]
	$h_{fg,\ ethanol} = -6.531T^2 + 2858.0T + 6.526\times10^5$ (J/kg)	Fitted to the data in Ref. [75]
	$P_{sat.,\ ethanol} = \exp(20.272 - \frac{4687.0}{T})$ (mbar)	Fitted to the data in Ref. [75]
Zeolite	$c_{p,\ zeolite} = 836.0$ (J/kg K)	[11]
Activated carbon	$c_{p,\ act.\ carbon} = 920.0$ (J/kg K)	[76]
Silica gel	$c_{p,\ silica\ gel} = 924.0$ (J/kg K)	[57]

[a] Temperature unit in the relationships is in kelvin.

Table 6
Operating conditions in experiments conducted by Grisel et al. [77] and Freni et al. [78].

Reference	Grisel et al. [77]	Freni et al. [78]
System specifications	2-bed silica gel–water ACS	Single-bed silica gel–water ACS
Adsorbent grain size (mm)	0.2–1.0	0.25–0.425
Mass of adsorbent per bed (kg)	8.7	0.437
Metal mass of adsorber bed (kg)	8.4	4.3
Adsorber bed heat transfer surface area, A_{bed}, (m^2)	Not reported	1.66
Adsorber bed heat transfer coefficient, U_{bed}, (W/m^2 K)	Not reported	40.0
Adsorber bed heat transfer conductance, $U_{bed}A_{bed}$, (W/K)	450	66.4
Heating fluid mass flow rate to adsorber bed (kg/s)	0.27 (16.2 L/min water)	0.118 (7.08 L/min water)
Cooling fluid mass flow rate to adsorber bed (kg/s)	0.25 (15.2 L/min water)	0.254 (15.24 L/min water)
Metal mass of condenser (kg)	3.5 (assumed)	3.5
Water mass of condenser (kg)	Not reported	1.5
Condenser heat transfer surface area, A_{cond}, (m^2)	Not reported	0.2719
Condenser heat transfer coefficient, U_{cond}, (W/m^2 K)	Not reported	500.0
Condenser heat transfer conductance, $U_{cond}A_{cond}$, (W/K)	1000	136.0
Coolant water mass flow rate to condenser (kg/s)	0.23 (13.8 L/min water)	0.15 (9.0 L/min water)
Metal mass of evaporator (kg)	3.5 (assumed)	3.5
Water mass of evaporator (kg)	Not reported	1.5
Evaporator heat transfer surface area, A_{evap}, (m^2)	Not reported	0.2719
Evaporator heat transfer coefficient, U_{evap}, (W/m^2 K)	Not reported	500.0
Evaporator heat transfer conductance, $U_{evap}A_{evap}$, (W/K)	1666	136.0
Chilled water mass flow rate to evaporator (kg/s)	0.18 (11.0 L/min water)	0.137 (8.22 L/min water)

Kutta–Fehlberg method (RKF45) is adopted because the differential terms in the governing equations of the ACS fully dynamic modeling are only time-dependent. In the present model, a marching time step of 0.1 s is used and the relative error difference between two consequent iterations at each time step is set at 10^{-9}, respectively. Also, the absolute error difference between the results at the end of two consequent cycles is set at 10^{-3}.

4. Results and discussion

In this section, the accuracy of ACS fully dynamic modeling in prediction of SCP and COP are investigated against the available data in the literature. Next, base-case operating conditions are defined to supply 2 kW of cooling power for a light-duty vehicle under nominal operating conditions. Then, parametric study is conducted to investigate the effects of different parameters on the performance of ACS installed in a light-duty vehicle.

4.1. Comparison of the model against the experimental data

The information required as inputs to the ACS fully dynamic model is summarized in Table 6. These data are extracted from two sets of experimental data reported by Grisel et al. [77] and Freni et al. [78]. It is noteworthy to mention that some of these data have not been reported in Ref. [77,78] and were provided by the corresponding authors in our communications.

Fig. 2 shows the validation of the developed model with the experimental data reported by Grisel et al. [77]. The uncertainty in the data measurements has not been reported by Grisel et al. [77]. Fig. 2a shows the effects of different cycle times on the SCP and COP of ACS. As shown in Fig. 2a, the model followed the same trend as the experimental data with the average relative differences of 10% and 7% for the SCP and COP, respectively. In Fig. 2a, our modeling indicates that the maximum SCP occurs at the cycle time between 10 and 15 min which is in agreement with the experimental data. Fig. 2b and c shows the comparison of the present model with the experimental data for various heating and

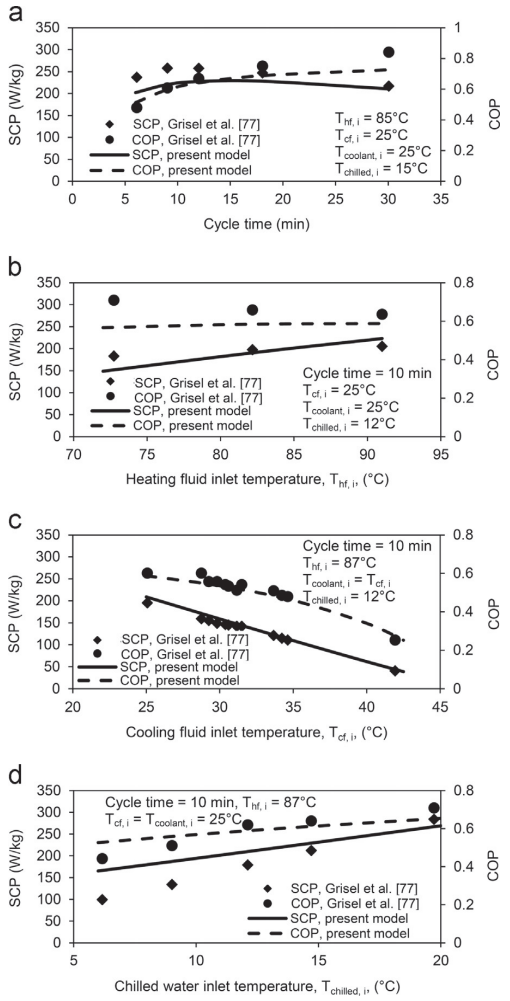

Fig. 2. Comparison between the ACS fully dynamic model and the experimental data reported by Grisel et al. [77]. Variation of SCP and COP vs. (a) cycle time, (b) heating fluid inlet temperature, (c) cooling fluid inlet temperature, and (d) chilled water inlet temperature.

cooling fluids inlet temperatures. The average relative differences for the SCP and COP in Fig. 2b are 10.9% and 12.9%, and for those in Fig. 2c are 6.3% and 5.2%, respectively. Fig. 2d depicts the effects of the chilled water inlet temperature on the SCP and COP of the ACS. It can be seen in Fig. 2d that the model predicts the experimental data with good accuracy.

The comparison between the model and the experimental data reported by Freni et al. [78] is shown in Fig. 3. The uncertainty of 10% was reported in the measurements of the experimental data [78]. In Fig. 3a, the model shows a good agreement with the experimental data. In Fig. 3a, the average relative differences between the predicted SCP and COP with the experimental data are 13% and 3%, respectively. Similar to Fig. 2a, Fig. 3a indicates that the SCP is maximized at the cycle time of 10 min. Fig. 3b and c depicts the variation of SCP and COP for various heating and cooling fluids inlet temperatures. The predicted SCP and COP by the model follow the same trend as the experimental data with a reasonable accuracy.

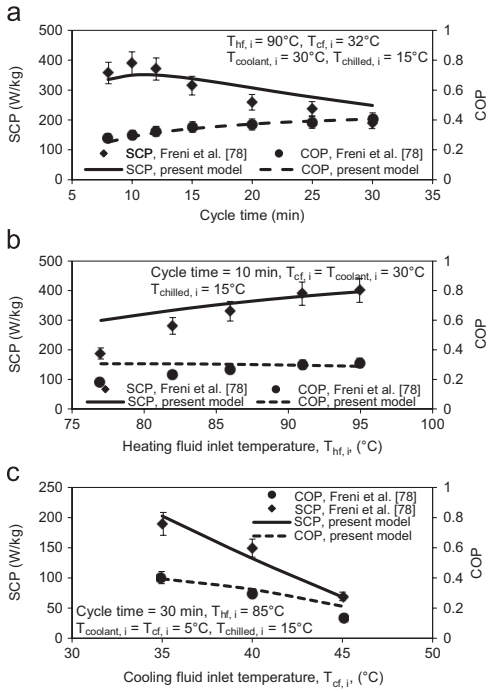

Fig. 3. Comparison between the ACS fully dynamic model and the experimental data reported by Freni et al. [78]. Variation of SCP and COP vs. (a) cycle time, (b) heating fluid inlet temperature, and (c) cooling fluid inlet temperature.

4.2. Base-case model

The ACS designed for a light-duty vehicle A/C system should be able to supply 2 kW of cooling power using the available heat sources in the vehicle, namely, the engine coolant and the exhaust gas of the ICE [2,26]. In the case of using the exhaust gas of the ICE, backpressure along the exhaust line should not increase. For example, the maximum allowable backpressure for diesel engines with powers less than 50, 50–500, and above 500 kW should be 40, 20, and 10 kPa, respectively [79]. To reduce the difficulty of using the exhaust gas of the ICE, the engine coolant is selected as a primary heat source with temperature of 90 °C [26]. The base-case operating conditions as input to our ACS fully dynamic model are summarized in Table 7.

The performance of ACS at the base-case operating conditions is summarized in Table 8. The analysis conducted by De Boer et al. [2] showed that to use solely the engine coolant to regenerate the adsorber beds, the COP of system should be greater than 0.5. As shown in Table 8, the designed ACS for a light-duty vehicle A/C applications has the SCP of 185 W/kg and the COP of 0.55 which is in agreement with De Boer et al. [2] analysis.

4.3. Parametric study

In this section, effects of different salient parameters are investigated on the SCP and COP of ACS. These analyses assist (i) to specify important parameters in the ACS, (ii) to size the system properly, and (iii) to determine the best performance of ACS under different operating conditions.

Fig. 4a shows the effects cycle time on the SCP and COP. It can be seen in Fig. 4 that the SCP is maximized at the cycle time of 10–15 min. By increasing the cycle time from 5 to 10 min, the SCP and

Table 7
Base-case operating conditions applied in the ACS fully dynamic model.

Parameter	Value	Ref. No.
Working pairs	Silica gel–water	–
Mass of adsorbent per bed (kg)	5.0	Calculated
Metal mass of adsorber bed (kg)	5.0	Calculated
Adsorber bed heat transfer surface area, A_{bed}, (m^2)	3.2	Calculated
Adsorber bed heat transfer coefficient, U_{bed}, (W/m^2 K)	100.0	[78]
Heating fluid mass flow rate to adsorber bed (kg/s)	0.2 (12 L/min water)	[26]
Cooling fluid mass flow rate to adsorber bed (kg/s)	0.2 (12 L/min water)	[26]
Metal mass of condenser (kg)	1.5	Calculated
Condenser heat transfer surface area, A_{cond}, (m^2)	0.77	Calculated
Condenser heat transfer coefficient, U_{cond}, (W/m^2 K)	500	[78]
Coolant water mass flow rate to condenser (kg/s)	0.2 (12 L/min water)	[26]
Metal mass of evaporator (kg)	1.5	Calculated
Evaporator heat transfer surface area, A_{evap}, (m^2)	0.77	Calculated
Evaporator heat transfer coefficient, U_{evap}, (W/m^2 K)	1000	[78]
Chilled water mass flow rate to evaporator (kg/s)	0.13 (8 L/min water)	[26]
Heating fluid inlet temperature (°C)	90	[26]
Cooling fluid inlet temperature (°C)	33	[26]
Coolant fluid inlet temperature (°C)	33	[26]
Chilled water inlet temperature (°C)	15	[26]
Cycle time (min)	10	Assumed
Adsorption to desorption time ratio (ADTR)	1.0	Assumed

Table 8
Performance of the proposed ACS for a compact vehicle A/C system under the base-case operating conditions.

Parameter	Value	
Evaporative cooling power, Q_{evap}	2.04 kW	555.16 kJ
Condensation power, Q_{cond}	2.19 kW	588.15 kJ
Total heating power, $Q_{total\ heating}$	10.96 kW	1011.13 kJ
Total cooling power, $Q_{total\ heating}$	10.86 kW	960.35 kJ
COP, Eq. (24)	0.55	
SCP, Eq. (25)	185.0 W/kg	

COP increase by 19% and 42%, respectively. Whereas, by increasing the cycle time from 10 to 30 min, the SCP reduces from 185 to 164 W/kg (11%) and the COP increase from 0.55 to 0.68 (24%). Fig. 4b depicts the effects of different adsorption to desorption time ratios (ADTR) and cycle times on the SCP and COP. Fig. 4b serves as the characteristic curves of the designed ACS. As shown in Fig. 4b, the highest values for the SCP and COP under a constant cycle time are achieved at the ADTR of one. In addition, Fig. 4b indicates that the maximum SCP and COP are obtained at the cycle times more than 10 min. From Fig. 4b, it can be concluded that the highest SCP and COP of the designed ACS can be accomplished by 2-adsorber bed ACS (ADTR of one) and the cycle times between 10 and 20 min. It should be noted that each ACS has its own characteristic curves and its performance may maximize at different ADTRs such as data reported by Sapienza et al. [80].

Fig. 5 shows the effects of normalized adsorber bed mass and overall heat transfer conductance on the SCP and COP. The adsorber bed mass (dead mass) in vehicles is an important parameter that should be minimized. Fig. 5a indicates that by

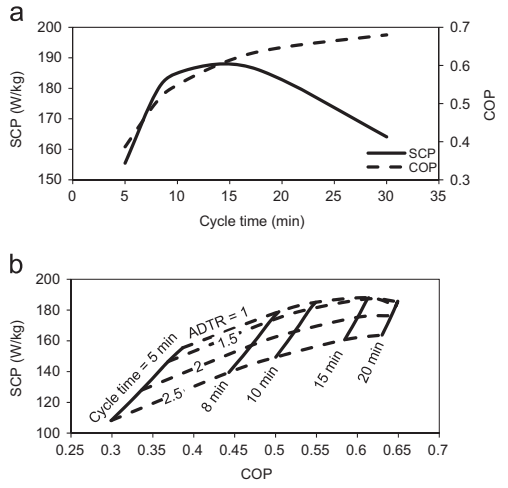

Fig. 4. Variation of SCP and COP as a function of (a) cycle time, and (b) ADTR and cycle time (other parameters are at the base-case operating conditions).

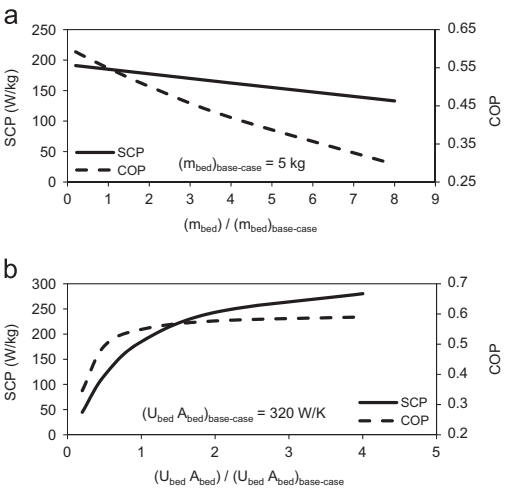

Fig. 5. Variation of SCP and COP as a function of (a) normalized adsorber bed mass, and (b) normalized adsorber bed overall heat transfer conductance (other parameters are at the base-case operating conditions).

increasing the normalized adsorber bed mass from 1 to 8, the SCP and COP reduce from 185 to 133 W/kg (28%) and from 0.55 to 0.3 (46%), respectively.

Fig. 5b shows that the SCP is more sensitive than the COP to the overall heat transfer conductance variations. By increasing the normalized adsorber bed overall heat transfer conductance from 1 to 4, the SCP increases by 51%, whereas the COP increases only 7.5%.

Effects of heating fluid inlet temperature on the variations of SCP and COP are shown in Fig. 6a. Although the engine coolant has high temperature, Fig. 6a depicts that the low engine coolant temperature at the cold start-up results in very low SCP and COP. Fig. 6a also indicates that by increasing the heating fluid inlet temperature from 70 to 95 °C, the SCP linearly increases by 127% and the COP increases by 20%, respectively.

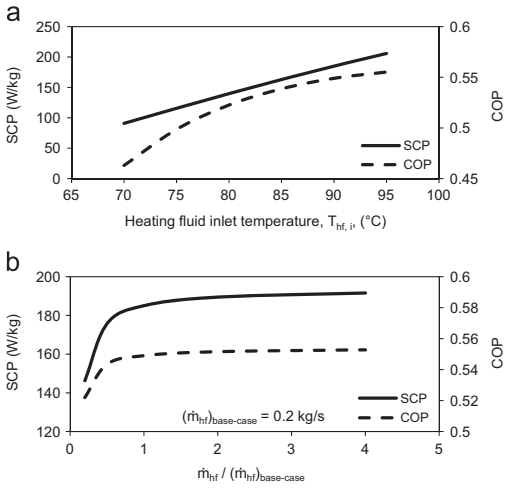

Fig. 6. Variation of SCP and COP as a function of (a) heating fluid inlet temperature, and (b) normalized heating fluid mass flow rate (other parameters are at the base-case operating conditions).

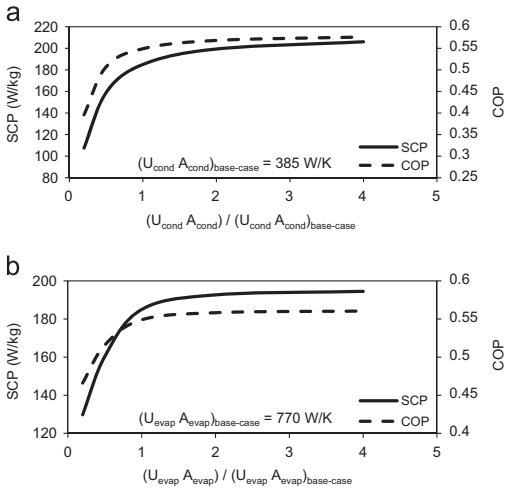

Fig. 8. Variation of SCP and COP as a function of (a) normalized condenser overall heat transfer conductance, and (b) normalized evaporator overall heat transfer conductance (other parameters are at the base-case operating conditions).

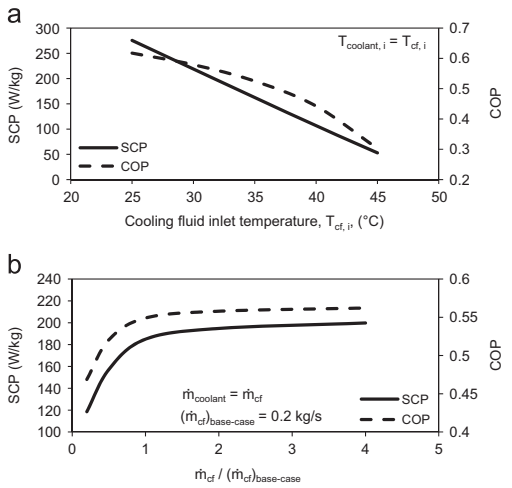

Fig. 7. Variation of SCP and COP as a function of (a) cooling fluid inlet temperature, and (b) normalized cooling fluid mass flow rate (other parameters are at the base-case operating conditions).

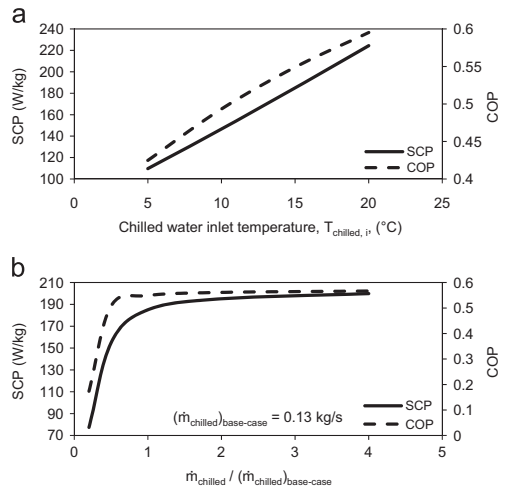

Fig. 9. Variation of SCP and COP as a function of (a) chilled water inlet temperature, and (b) normalized chilled water mass flow rate (other parameters are at the base-case operating conditions).

Fig. 6b shows the effects of normalized heating fluid mass flow rate on the performance of ACS. It can be seen in Fig. 6b that the SCP and COP do not vary significantly by normalized heating fluid mass flow rates greater than 0.75.

Fig. 7 displays the effects of cooling fluid inlet temperature and normalized mass flow rate on the SCP and COP. In a vehicle, the cooling fluid which flows through the adsorber bed and condenser during the adsorption and condensation processes, respectively, comes from an auxiliary radiator which is cooled down by the ambient air [26]. The auxiliary radiator is different from the engine radiator to prevent any interference with the engine cooling process. Therefore, in Fig. 7, it is assumed that the cooling fluid inlet temperature to the adsorber bed and coolant inlet temperature to the condenser have the same temperature and mass flow rate. As shown in Fig. 7a, the SCP linearly decreases from 275.7 to 52.9 W/kg (80%) and the COP reduces from 0.62 to 0.3 (50%) by increasing the cooling fluid inlet temperature from 25 to 45 °C. Comparing Figs. 7 and 6a indicates that for the designed silica gel–water ACS, the SCP and COP are more sensitive to the cooling fluid than the heating fluid inlet temperature. Fig. 7b shows that the SCP and COP remain constant for the normalized cooling fluid mass flow rates greater than one; the SCP and COP increases only 8% and 2.4% by increasing the normalized cooling fluid mass flow rate from 1 to 4.

The importance of sizing or rating of appropriate condensers and evaporators with proper overall heat transfer conductance is depicted in Fig. 8. As shown in Fig. 8a, by increasing the normalized condenser overall heat transfer conductance from 0.2 to 1, the SCP and COP increases by 72% and 38.6%, respectively. However, for the normalized condenser overall heat transfer conductance greater than 1, the SCP and COP do not change considerably.

Fig. 8b shows the effects of the normalized evaporator overall heat transfer conductance on the performance of ACS. It can be seen

in Fig. 8b that the SCP increases from 130 to 185 W/kg (42.6%) and the COP increases from 0.47 to 0.55 (17.8%) by increasing the normalized evaporator overall heat transfer conductance from 0.2 to 1. It should be noted that higher overall heat transfer conductance may result in adding weight to the ACS which should be included in the analysis. Fig. 8 indicates that having a well-designed adsorber bed with proper heat and mass transfer characteristics is not the sole factor in ACS to achieve high SCP and COP.

Fig. 9a demonstrates the effects of chilled water inlet temperature on the SCP and COP. As shown in Fig. 9a, increasing the chilled water inlet temperature from 5 to 20 °C increases the SCP and COP by 105% and 40%, respectively. The cabin temperature thermal comfort temperature range is about 20–23 °C [2]. As a result, the chilled water inlet temperature to the evaporator within the range of 15–20 °C results in achieving the SCP and COP of 185–224 W/kg and 0.55–0.6, respectively.

Fig. 9b depicts the effects of normalized chilled water mass flow rate on the SCP and COP. Fig. 9b indicates that the SCP and COP do not increase effectively for the normalized chilled water mass flow rates greater than one whereas the SCP and COP increases by 139% and 216% by increasing the normalized chilled water mass flow rate from 0.2 to 1.

According to the parametric study, important parameters in the sizing of ACS, which are fixed after building the ACS, are the adsorber bed, condenser and evaporator mass and overall heat transfer conductance (Figs. 5 and 8). Among these parameters, adsorber bed mass has the lowest and adsorber bed overall heat transfer conductance has the highest effects on the SCP. However, the adsorber bed mass should be minimized to reduce the dead mass in vehicles. The cycle time is the other parameter that should be calculated to maximize the SCP under specific operating conditions, see Fig. 4a. Other parameters are the heating and cooling fluids, and chilled water inlet temperatures and mass flow rates (Figs. 6, 7, and 9). According to Figs. 6, 7, and 9, the variable speed pumps are required to adjust the heating and cooling fluids, and chilled water mass flow rates. Although, these mass flow rates do not change the SCP and COP after specific values, their proper adjustments benefit to reach the acceptable SCP and COP with less feeding pump powers. The heating and cooling fluid inlet temperatures to the adsorber bed are fixed by the engine coolant and environment temperatures, respectively. Therefore, these parameters are not under the user control. The only parameter, that significantly changes the SCP and is under the user control, is the chilled water inlet temperature to the evaporator, see Fig. 9a. By adjusting the chilled water mass flow rate, the chilled water inlet temperature to the evaporator can be regulated.

Finally, the parametric study shows that under some operating conditions, the COP of ACS becomes less than 0.5 which indicates the engine coolant may not be sufficient for the regeneration of the adsorber bed during the desorption process. Therefore, depending upon the environmental conditions, a portion of the exhaust gas of the ICE can be used during the desorption process.

5. Conclusion

In this study, the performance of a 2 kW waste-heat driven ACS for light-duty vehicle A/C applications was studied through thermodynamic cycle modeling. The results showed that the SCP and COP of the ACS were maximized for the cycle times between 10 and 15 min and the ADTR of one. In addition, the results indicated that among the adsorber bed, condenser and evaporator, the adsorber bed overall heat transfer conductance and mass have the highest and the lowest effects on the SCP, respectively. Moreover, the results showed that the heating and cooling fluids, coolant and chilled water mass flow rates had not considerable effects on the SCP and COP after specific values. These mass flow rates had to be adjusted in order to reducing the feeding pump powers. Finally, the results showed that for the regeneration of the adsorber beds during the desorption process, the engine coolant was not sufficient and the exhaust gas of the ICE had also to be utilized to achieve the required cooling power under different operating conditions.

Acknowledgment

The authors gratefully acknowledge the financial support of the Natural Sciences and Engineering Research Council of Canada (NSERC) through the Automotive Partnership Canada Grant no. APCPJ 401826-10.

References

[1] Farrington R, Rugh J. Impact of vehicle air-conditioning on fuel economy, tailpipe emissions, and electric vehicle range. In: Proceeding of the earth technology forum. Washington, DC; 2000.
[2] De Boer R, Smeding SF. Thermally operated mobile air-conditioning system: development and test of a laboratory prototype. In: Proceeding of the international sorption heat pump conference. Seoul, Korea; 2008.
[3] Suzuki M. Application of adsorption cooling systems to automobiles. Heat Recover Syst CHP 1993;13:335–40.
[4] Abdullah MO, Tan IAW, Lim LS. Automobile adsorption air-conditioning system using oil palm biomass-based activated carbon: a review. Renew Sustain Energy Rev 2011;15:2061–72. http://dx.doi.org/10.1016/j.rser.2011.01.012.
[5] Demir H, Mobedi M, Ülkü S. A review on adsorption heat pump: problems and solutions. Renew Sustain Energy Rev 2008;12:2381–403. http://dx.doi.org/10.1016/j.rser.2007.06.005.
[6] Hulse GE. Freight car refrigeration by an adsorption system employing silica gel. Refrig Eng 1929;17:41–54.
[7] Aceves SM. An analytical comparison of adsorption and vapor compression air conditioners for electric vehicle applications. J Energy Resour Technol 1996;118:16–21.
[8] Hendricks TJ. Vehicle transient air conditioning analysis: model development and system optimization investigations. National Renewable Energy Laboratory, NREL/TP, 540-30715; 2001.
[9] Hendricks TJ. Optimization of vehicle air conditioning systems using transient air conditioning performance analysis. In: SAE conference proceedings; 2001.
[10] Hendricks TJ. Multi-variable optimization of electrically-driven vehicle air conditioning systems using transient performance analysis. In: Proceedings of the SAE vehicle thermal management system; 2003.
[11] Zhang LZ, Wang L. Performance estimation of an adsorption cooling system for automobile waste heat recovery. Appl Therm Eng 1997;17:1127–39.
[12] Zhang LZ, Wang L. Momentum and heat transfer in the adsorbent of a waste-heat adsorption cooling system. Energy 1999;24:605–24. http://dx.doi.org/10.1016/S0360-5442(99)00018-3.
[13] Zhang LZ, Wang L. Effects of coupled heat and mass transfers in adsorbent on the performance of a waste heat adsorption cooling unit. Appl Therm Eng 1999;19:195–215.
[14] Zhang LZ. Design and testing of an automobile waste heat adsorption cooling system. Appl Therm Eng 2000;20:103–14. http://dx.doi.org/10.1016/S1359-4311(99)00009-5.
[15] Zhang LZ. A three-dimensional non-equilibrium model for an intermittent adsorption cooling system. Sol Energy 2000;69:27–35. http://dx.doi.org/10.1016/S0038-092X(00)00010-4.
[16] Jiangzhou S, Wang RZ, Lu YZ, Xu YX, Wu JY. Experimental investigations on adsorption air-conditioner used in internal-combustion locomotive driver-cabin. Appl Therm Eng 2002;22:1153–62. http://dx.doi.org/10.1016/S1359-4311(02)00036-4.
[17] Lu YZ, Wang RZ, Jianzhou S, Zhang M, Xu Y, Wu J. Performance of a diesel locomotive waste-heat-powered adsorption air conditioning system. Adsorption 2004;10:57–68.
[18] Christy C, Toossi R. Adsorption air-conditioning for containerships and vehicles; 2004.
[19] Lambert MA, Jones BJ. Automotive adsorption air conditioner powered by exhaust heat. Part 1: conceptual and embodiment design. Proc Inst Mech Eng Part D J Automob Eng 2006;220:959–72. http://dx.doi.org/10.1243/09544070JAUTO221.
[20] Lambert MA, Jones BJ. Automotive adsorption air conditioner powered by exhaust heat. Part 2: detailed design and analysis. Proc Inst Mech Eng Part D J Automob Eng 2006;220:973–89. http://dx.doi.org/10.1243/09544070JAUTO222.
[21] Wang K, Wu JY, Wang RZ, Wang LW. Composite adsorbent of $CaCl_2$ and expanded graphite for adsorption ice maker on fishing boats. Int J Refrig 2006;29:199–210. http://dx.doi.org/10.1016/j.ijrefrig.2005.06.004.

[22] Wang LW, Wang RZ, Lu ZS, Xu YX, Wu JY. Split heat pipe type compound adsorption ice making test unit for fishing boats. Int J Refrig 2006;29:456–68. http://dx.doi.org/10.1016/j.ijrefrig.2005.08.007.
[23] Lu ZS, Wang RZ, Li TX, Wang LW, Chen CJ. Experimental investigation of a novel multifunction heat pipe solid sorption icemaker for fishing boats using $CaCl_2$/activated carbon compound – ammonia. Int J Refrig 2007;30:76–85. http://dx.doi.org/10.1016/j.ijrefrig.2006.07.001.
[24] Wang K, Wu JY, Xia ZZ, Li SL, Wang RZ. Design and performance prediction of a novel double heat pipes type adsorption chiller for fishing boats. Renew Energy 2008;33:780–90. http://dx.doi.org/10.1016/j.renene.2007.04.023.
[25] Wang LW, Wang RZ, Xia ZZ, Wu JY. Studies on heat pipe type adsorption ice maker for fishing boats. Int J Refrig 2008;31:989–97. http://dx.doi.org/10.1016/j.ijrefrig.2008.01.002.
[26] De Boer R, Smeding SF, Mola S. Silicagel–water adsorption cooling prototype system for mobile air conditioning. In: Proceedings of the heat powered cycles conference. Berlin, Germany; 2009.
[27] Narayanan S, Yang S, Kim H, Wang EN. Optimization of adsorption processes for climate control and thermal energy storage. Int J Heat Mass Transf 2014;77:288–300. http://dx.doi.org/10.1016/j.ijheatmasstransfer.2014.05.022.
[28] Narayanan S, Li X, Yang S, McKay I, Kim H, Wang EN. Design and optimization of high performance adsorption-based thermal battery. In: Proceedings of the ASME 2013 heat transfer summer conference. Minneapolis, MN, USA; 2013. p. 1–10.
[29] Sharafian A, Bahrami M. A quasi steady state model for adsorption cooling systems: Automotive applications. In: Proceedings of the ASME 2012 6th international conference on energy sustainability and 10th fuel cell science, engineering and technology conference. San Diego, CA, USA; 2012.
[30] Yong L, Sumathy K. Review of mathematical investigation on the closed adsorption heat pump and cooling systems. Renew Sustain Energy Rev 2002;6:305–38. http://dx.doi.org/10.1016/S1364-0321(02)00010-2.
[31] Miltkau T, Dawoud B. Dynamic modeling of the combined heat and mass transfer during the adsorption/desorption of water vapor into/from a zeolite layer of an adsorption heat pump. Int J Therm Sci 2002;41:753–62. http://dx.doi.org/10.1016/S1290-0729(02)01369-8.
[32] Marletta L, Maggio G, Freni A, Ingrasciotta M, Restuccia G. A non-uniform temperature non-uniform pressure dynamic model of heat and mass transfer in compact adsorbent beds. Int J Heat Mass Transf 2002;45:3321–30. http://dx.doi.org/10.1016/S0017-9310(02)00045-5.
[33] Leong KC, Liu Y. Numerical study of a combined heat and mass recovery adsorption cooling cycle. Int J Heat Mass Transf 2004;47:4761–70. http://dx.doi.org/10.1016/j.ijheatmasstransfer.2004.05.030.
[34] Leong KC, Liu Y. Numerical modeling of combined heat and mass transfer in the adsorbent bed of a zeolite/water cooling system. Appl Therm Eng 2004;24:2359–74. http://dx.doi.org/10.1016/j.applthermaleng.2004.02.014.
[35] Chua HT, Ng KC, Wang W, Yap C, Wang XL. Transient modeling of a two-bed silica gel–water adsorption chiller. Int J Heat Mass Transf 2004;47:659–69. http://dx.doi.org/10.1016/j.ijheatmasstransfer.2003.08.010.
[36] Maggio G, Freni A, Restuccia G. A dynamic model of heat and mass transfer in a double-bed adsorption machine with internal heat recovery. Int J Refrig 2006;29:589–600. http://dx.doi.org/10.1016/j.ijrefrig.2005.10.005.
[37] Liu Y, Leong KC. Numerical modeling of a zeolite/water adsorption cooling system with non-constant condensing pressure. Int Commun Heat Mass Transf 2008;35:618–22. http://dx.doi.org/10.1016/j.icheatmasstransfer.2007.12.004.
[38] Hu P, Yao J, Chen Z. Analysis for composite zeolite/foam aluminum–water mass recovery adsorption refrigeration system driven by engine exhaust heat. Energy Convers Manag 2009;50:255–61. http://dx.doi.org/10.1016/j.enconman.2008.09.022.
[39] Chen CJ, Wang RZ, Xia ZZ, Kiplagat JK. Study on a silica gel–water adsorption chiller integrated with a closed wet cooling tower. Int J Therm Sci 2010;49:611–20. http://dx.doi.org/10.1016/j.ijthermalsci.2009.09.009.
[40] Riffel DB, Wittstadt U, Schmidt FP, Núñez T, Belo Fa, Leite APF, et al. Transient modeling of an adsorber using finned-tube heat exchanger. Int J Heat Mass Transf 2010;53:1473–82. http://dx.doi.org/10.1016/j.ijheatmasstransfer.2009.12.001.
[41] Ge TS, Dai YJ, Wang RZ. Performance study of silica gel coated fin-tube heat exchanger cooling system based on a developed mathematical model. Energy Convers Manag 2011;52:2329–38. http://dx.doi.org/10.1016/j.enconman.2010.12.047.
[42] Solmuş İ, Rees DAS, Yamalı C, Baker D, Kaftanoğlu B. Numerical investigation of coupled heat and mass transfer inside the adsorbent bed of an adsorption cooling unit. Int J Refrig 2012;35:652–62. http://dx.doi.org/10.1016/j.ijrefrig.2011.12.006.
[43] Cacciola G, Restuccia G. Reversible adsorption heat pump: a thermodynamic model. Int J Refrig 1995;18:100–6. http://dx.doi.org/10.1016/0140-7007(94)00005-I.
[44] Hajji A, Khalloufi S. Theoretical and experimental investigation of a constant-pressure adsorption process. Int J Heat Mass Transf 1995;38:3349–58. http://dx.doi.org/10.1016/0017-9310(95)00102-F.
[45] Sokada A, Suzuki M. Fundamental study on solar powered adsorption. J Chem Eng Jpn 1984;17:52–7.
[46] Sakoda A, Suzuki M. Simultaneous transport of heat and adsorbate in closed type adsorption cooling system utilizing solar heat. J Sol Energy Eng 1986;108:239–45.
[47] Tiansuwan J, Hirunlabh J. Mathematical model of an activated carbon–ethanol refrigerator. Thammasat Int J Sci Technol 1998;3:66–71.
[48] Saha BB, Boelman EC, Kashiwagi T. Computational analysis of an advanced adsorption-refrigeration cycle. Energy 1995;20:983–94.
[49] Saha BB, Akisawa A, Kashiwagi T. Silica gel water advanced adsorption refrigeration cycle. Energy 1997;22:437–47.
[50] Wu JY, Wang RZ, Xu YX. Dynamic simulation and experiments of a heat regenerative adsorption heat pump. Energy Convers Manag 2000;41:1007–18. http://dx.doi.org/10.1016/S0196-8904(99)00161-2.
[51] Chua HT, Ng KC, Malek A, Kashiwagi T, Akisawa A, Saha BB. Modeling the performance of two-bed, silica gel–water adsorption chillers. Int J Refrig 1999;22:194–204.
[52] Wang DC, Xia ZZ, Wu JY, Wang RZ, Zhai H, Dou WD. Study of a novel silica gel–water adsorption chiller. Part I. Design and performance prediction. Int J Refrig 2005;28:1073–83. http://dx.doi.org/10.1016/j.ijrefrig.2005.03.001.
[53] Wang DC, Wu JY, Xia ZZ, Zhai H, Wang RZ, Dou WD. Study of a novel silica gel–water adsorption chiller. Part II. Experimental study. Int J Refrig 2005;28:1084–91. http://dx.doi.org/10.1016/j.ijrefrig.2005.03.002.
[54] Khan MZI, Alam KCa, Saha BB, Hamamoto Y. Akisawa a., Kashiwagi T. Parametric study of a two-stage adsorption chiller using re-heat—The effect of overall thermal conductance and adsorbent mass on system performance. Int J Therm Sci 2006;45:511–9. http://dx.doi.org/10.1016/j.ijthermalsci.2005.08.003.
[55] Wang X, Chua HT. Two bed silica gel–water adsorption chillers: an effectual lumped parameter model. Int J Refrig 2007;30:1417–26. http://dx.doi.org/10.1016/j.ijrefrig.2007.03.010.
[56] Wang X, Chua HT. A comparative evaluation of two different heat-recovery schemes as applied to a two-bed adsorption chiller. Int J Heat Mass Transf 2007;50:433–43. http://dx.doi.org/10.1016/j.ijheatmasstransfer.2006.08.003.
[57] Saha BB, Chakraborty A, Koyama S, Aristov YI. A new generation cooling device employing $CaCl_2$-in-silica gel–water system. Int J Heat Mass Transf 2009;52:516–24. http://dx.doi.org/10.1016/j.ijheatmasstransfer.2008.06.018.
[58] Miyazaki T, Akisawa A, Saha BB, El-Sharkawy II, Chakraborty A. A new cycle time allocation for enhancing the performance of two-bed adsorption chillers. Int J Refrig 2009;32:846–53. http://dx.doi.org/10.1016/j.ijrefrig.2008.12.002.
[59] Verde M, Cortés L, Corberán JM, Sapienza A, Vasta S, Restuccia G. Modelling of an adsorption system driven by engine waste heat for truck cabin A/C. Performance estimation for a standard driving cycle. Appl Therm Eng 2010;30:1511–22. http://dx.doi.org/10.1016/j.applthermaleng.2010.04.005.
[60] Verde M, Corberan JM, de Boer R, Smeding S. Modelling of a waste heat driven silica gel/water adsorption cooling system comparison with experimental results. In: Proceedings of the ISHPC conference. Padua, Italy; 2011. p. 7–8.
[61] Gong LX, Wang RZ, Xia ZZ, Chen CJ. Design and performance prediction of a new generation adsorption chiller using composite adsorbent. Energy Convers Manag 2011;52:2345–50. http://dx.doi.org/10.1016/j.enconman.2010.12.036.
[62] Rahman A, Ueda Y, Akisawa A, Miyazaki T, Saha B. Design and performance of an innovative four-bed, three-stage adsorption cycle. Energies 2013;6:1365–84. http://dx.doi.org/10.3390/en6031365.
[63] Restuccia G, Freni A, Vasta S, Aristov YI. Selective water sorbent for solid sorption chiller: experimental results and modelling. Int J Refrig 2004;27:284–93. http://dx.doi.org/10.1016/j.ijrefrig.2003.09.003.
[64] Saha BB, El-Sharkawy II, Chakraborty A, Koyama S. Study on an activated carbon fiber–ethanol adsorption chiller: Part I – system description and modelling. Int J Refrig 2007;30:86–95. http://dx.doi.org/10.1016/j.ijrefrig.2006.08.004.
[65] Chua HT, Ng KC, Chakraborty A, Oo NM, Othman MA. Adsorption characteristics of silica gel+water systems. J Chem Eng Data 2002;47:1177–81. http://dx.doi.org/10.1021/je0255067.
[66] Aristov YI, Tokarev MM, Cacciola G, Restuccia G. Selective water sorbents for multiple applications, 1. $CaCl_2$ confined in mesopores of silica gel: sorption properties. React Kinet Catal Lett 1996;59:325–33.
[67] Ruthven DM. Principles of adsorption and desorption processes. United States of America: John Wiley & Sons, Inc.; 1984.
[68] Karger J, Ruthven DM. Diffusion in zeolites and other microporous solids. United States of America: Wiley & Sons, Inc.; 1992.
[69] Glueckauf E. Theory of chromatography. Part 10 – formulæ for diffusion into spheres and their application to chromatography. Trans Faraday Soc 1955;51:1540–51.
[70] Kärger J, Pfeifer H, Rosemann M, Feokistova NN, Ž danov SP. Intracrystalline self-diffusion of water and short-chain-length paraffins in A-type zeolites. Zeolites 1989;9:247–9.
[71] Tatlıer M, Tantekin-Ersolmaz B, Erdem-Şenatalar A. A novel approach to enhance heat and mass transfer in adsorption heat pumps using the zeolite–water pair. Microporous Mesoporous Mater 1999;27:1–10. http://dx.doi.org/10.1016/S1387-1811(98)00174-7.
[72] Passos EF, Escobedo JF, Meunier F. Simulation of an intermittent adsorptive solar cooling system. Sol Energy 1989;42:103–11.
[73] Aristov YI, Glaznev IS, Freni A, Restuccia G. Kinetics of water sorption on SWS-1 L (calcium chloride confined to mesoporous silica gel): influence of grain size and temperature. Chem Eng Sci 2006;61:1453–8. http://dx.doi.org/10.1016/j.ces.2005.08.033.
[74] Cengel YA, Boles MA. Thermodynamcis: an engineering approach. New York: McGraw-Hill; 2006.
[75] Green DW, Perry RH. Perry's chemical engineers' handbook. 8th editionMc-Graw-Hill Professional; 2007.
[76] Zhao Y, Hu E, Blazewicz A. Dynamic modelling of an activated carbon–methanol adsorption refrigeration tube with considerations of interfacial convection and transient pressure process. Appl Energy 2012;95:276–84. http://dx.doi.org/10.1016/j.apenergy.2012.02.050.

[77] Grisel RJH, Smeding SF, de Boer R. Waste heat driven silica gel/water adsorption cooling in trigeneration. Appl Therm Eng 2010;30:1039–46. http://dx.doi.org/10.1016/j.applthermaleng.2010.01.020.
[78] Freni A, Sapienza A, Glaznev IS, Aristov YI, Restuccia G. Experimental testing of a lab-scale adsorption chiller using a novel selective water sorbent "silica modified by calcium nitrate". Int J Refrig 2012;35:518–24. http://dx.doi.org/10.1016/j.ijrefrig.2010.05.015.
[79] Mayer A. Number-based emission limits, VERT-DPF verification procedure and experience with 8000 retrofits. Switzerland; 2004.
[80] Sapienza A, Santamaria S, Frazzica A, Freni A. Influence of the management strategy and operating conditions on the performance of an adsorption chiller. Energy 2011;36:5532–8. http://dx.doi.org/10.1016/j.energy.2011.07.020.

Appendix G.

Performance analysis of a novel expansion valve and control valves designed for a waste heat-driven two-adsorber bed adsorption cooling system

(submitted to the Applied Thermal Engineering journal)

Performance analysis of a novel expansion valve and control valves designed for a waste heat-driven two-adsorber bed adsorption cooling system

Amir Sharafian, Patric Constantin Dan, Wendell Huttema, Majid Bahrami*

Laboratory for Alternative Energy Conversion (*LAEC*), School of Mechatronic Systems Engineering, Simon Fraser University, BC, Canada V3T 0A3

Abstract

Two new ideas for the expansion valve and control valves of an adsorption cooling system (ACS) for vehicle air conditioning applications are suggested to reduce the weight, parasitic power consumption, and control of the system. A check valve with cracking pressure of 3.5-7 kPa is proposed for the expansion valve and a combination of low cracking pressure check valves and solenoid valves with an innovative arrangement is proposed for the control valves to heat up and cool down the adsorber beds. These designs result in reducing the total mass of the ACS up to 10.5 kg and the parasitic power consumption of the control valves by 50%. These new designs are installed on a two-adsorber bed silica gel/$CaCl_2$-water ACS and tested under different operating conditions. The results show that the expansion valve and control valves operate effectively under the heating and cooling fluid inlet temperatures to the adsorber beds of 70-100°C and 30-40°C, respectively, the coolant water inlet temperature to the condenser of 30-40°C, and the chilled water inlet temperature to the evaporator of 15-20°C. Also, an ACS thermodynamic cycle model is developed and compared against the experimental data for

* Corresponding author: School of Mechatronic Systems Engineering, Simon Fraser University, # 4300, 250-13450 102nd Avenue, Surrey, BC, Canada V3T0A3.
Tel.: +1 (778) 782-8538; Fax: +1 (778) 782-7514.
E-mail addresses: asharafi@sfu.ca (A. Sharafian), mbahrami@sfu.ca (M. Bahrami).

prediction and further improvement of the ACS performance. The results of the numerical modeling show that by increasing the adsorber bed heat transfer coefficient and surface area, the specific cooling power of the system increases up to 6 times.

Keywords: Expansion valve, control valve, adsorption cooling system, silica gel/$CaCl_2$, vehicle air conditioning.

1. Introduction

Waste heat-driven driven adsorption cooling systems (ACS) are potential energy efficient replacements for vapor compression refrigeration cycles (VCRC) in vehicles' air conditioning (A/C) applications. An ACS utilizes a low grade thermal energy to generate cooling power required in a vehicle. Approximately 70% of the total fuel energy released in an internal combustion engine (ICE) is wasted as heat that is dissipated through the engine coolant and exhaust gas [1]. An ACS can use this wasted heat to provide cooling in vehicles and drastically reduce the vehicles' fuel consumption and carbon footprint.

An ACS uses an adsorbent-adsorbate working pair, where the adsorbate, such as water or methanol, is adsorbed and desorbed from the surface of the adsorbent, such as zeolite, silica gel, or activated carbon, in a waste heat-driven cycle. Most of these materials are non-toxic, non-corrosive, and inexpensive [2] making ACS a safe and environmentally friendly technology. An ACS operates more quietly than a VCRC and is easier to maintain because its only moving parts are valves [3]. However, current ACS are limited in their usefulness for commercial vehicle applications, specifically light-duty vehicles, because of their bulkiness and heavy weight which are due to the low thermal conductivity of adsorbent materials and the low mass diffusivity of adsorbent-adsorbate pairs. These properties result in a low coefficient of performance (COP =

cooling energy / input energy) and low specific cooling power (SCP = cooling energy / (adsorbent mass × cycle time)). In vehicle applications, the mass of auxiliary systems should be minimized. Therefore, the SCP becomes an important parameter in a vehicle ACS design [4].

Sharafian and Bahrami [5] conducted a comprehensive literature review on the feasibility of ACS installation in light-duty vehicles, different ACS thermodynamic cycle modeling, and practical examples of ACS installed in vehicles such as a refrigerated rail car with two-adsorber bed silica gel-sulphur dioxide ACS [6], a locomotive with waste heat-driven single-adsorber bed zeolite 13X-water ACS [7,8], and a fishing boat with waste heat-driven two-adsorber bed consolidated activated carbon/$CaCl_2$-ammonia ACS for ice production [9–13]. These examples were successful ACS installed in vehicle applications where the weight and footprint of the ACS were not problematic. For light-duty vehicle A/C applications, de Boer et al. [14–17] built and installed a two-adsorber bed silica gel-water ACS with 2-kW cooling power on a compact car, Fiat Grande Punto. In their setup, each adsorber bed was filled with 3 kg of silica gel with the adsorber bed to adsorbent mass ratio (AAMR) of 4.2 kg $_{\text{metal}}$/kg $_{\text{dry adsorbent}}$. The 86 kg total mass of their system exceeded the 35 kg limit set by the car manufacturer [14]. From the data reported in Refs. [14,15], one can conclude that the mass of the two adsorber beds loaded with adsorbent material was 31.2 kg (2 adsorber beds × (3 kg $_{\text{dry adsorbent}}$ + 4.2 kg $_{\text{metal}}$/kg $_{\text{dry adsorbent}}$ × 3 kg $_{\text{dry adsorbent}}$)) which made only 36% of the total mass of the system. The condenser, evaporator, expansion valve, piping and control valves contributed the remaining 64% of the ACS total mass. Therefore, minimizing the mass of all components not only adsorber beds became important for vehicle A/C applications. Table 1 shows the details of different waste heat-driven ACS including adsorber bed type, working pairs, and number and type of control valves.

Table 1. Performance analysis of different finned tube adsorber beds reported in the literature.

Ref. No.	Adsorber bed type	Working pairs	Control valves on Adsorber beds	Control valves on heating/cooling sys.
[18]	1 SS† 304 annulus tube HEX‡	Consolidated natural graphite+ zeolite 13X/ water	4 electrically actuated valves	4 electrically actuated valves
[19]	2 annulus tube HEX	Consolidated zeolite/ water	4 pneumatic vacuum valves	8 electrically actuated valves
[20–26]	2 plate-tube HEX	Act. carbon/ ammonia	4 check valve	12 valves
[27,28]	2 shell and tube HEX	Act. carbon/ methanol	4 magnetic vacuum valves	10 hand ball valves
[29]	4 shell and tube HEX	Act. carbon/ ammonia	14 valves	16 valves
[30–34]	SS simple tube	Consolidated act. carbon/ ammonia	No valve	No valve
[35–38]	Plate HEX	Consolidated act. carbon/ ammonia	4 check valves + 2 solenoid valves	4 three-way valves
[39]	4 plate HEX	Silica gel/ water	8 solenoid valves	20 solenoid valves
[40,41]	4 plate fin HEX	Silica gel/ water	10 pressure relief valves	16 valves
[42–44]	2 plate fin HEX	Silica gel/water	No valve	11 solenoid valves
[45]	2 plate fin HEX	Silica gel/ water	4 solenoid valves	Manual hand ball valves
[46]	1 flat-tube HEX with corrugated fins	Silica gel/ water	No valves	4 three-way valves
[47–49]	1 aluminum finned tube HEX	Consolidated activated carbon/ ammonia	4 check valves	10 shut-off valves
[50]	1 SS finned tube HEX	Silica gel/ methanol	2 hand ball valves	4 three-way valves
[51–53]	SS Cylindrical double finned tube HEX	Zeolite 13X/ water	3 manual vacuum valves	4 manual hand ball valves
[7,8]	1 finned tubes HEX	Zeolite 13X/ water	4 vacuum valves	3 check valves
[54]	1 SS finned tube HEX	silica gel + $CaCl_2$(SWS-1L)/ water	2 vacuum valves	2 three-way valves
[55]	2 Aluminum finned tube HEX	AQSOA FAM-Z02/ water	4 check valves + 1 hand ball valve	-
[56–58]	2 finned tube HEX	Silica gel/ water	1 solenoid vacuum valve	11 solenoid valves
[59]	1 SS finned tube HEX	Coated hydrophobic Y zeolite (CBV-901)/ methanol	2 vacuum valves	2 three-way valves
[60]	2 finned tube HEX	Silica gel/ water	1 solenoid vacuum valve	11 solenoid valves
[61–64]	2 finned tube HEX	Act. carbon+$CaCl_2$ (1:4)/ ammonia	4 hand ball valves	Hand ball valves
[65]	1 aluminum finned tube HEX	Silica gel + $CaCl_2$(SWS-1L)/ water	2 vacuum valves	2 three-way valves
[66]	Finned tube HEX	Silica gel + $CaCl_2$/ water	No valve	-
[14–17]	2 Aluminum finned tube HEX	Silica gel/ water	4 check valves	4 three-way valves
[67–69]	1 aluminum finned tube HEX	$LiNO_3$-Silica KSK/ water	2 vacuum valves	4 solenoid valve + 4 check valves
[70,71]	28 finned tube with 2.5 mm fin spacing	Silica gel + LiCl/ water	1 solenoid vacuum valve	11 solenoid valves
[72–74]	2 aluminum finned tube HEX	Silica gel + LiCl/ methanol Silica gel/water	1 solenoid vacuum valve	11 solenoid valves
[75]	2 aluminum finned tube HEX	AQSOA FAM-Z02/ water	4 electrically actuated valves	Solenoid valves
[76,77]	8 HEX with aluminum fins +steel pipes	Expanded graphite + $CaCl_2$/ ammonia Expanded graphite + $BaCl_2$/ ammonia	4 valves 1 solenoid vacuum valve	8 valves 11 solenoid valves
[78]	1 carbon steel finned tube HEX	Expanded graphite + NaBr/ ammonia	2 valves	4 valves
[79]	4 SS shell and aluminum finned tube HEX	Silica gel/ water	8 electrically actuated valves	16 electrically actuated valves
[80]	2 finned tube HEX	Expanded graphite +	No valve	3 three-way valves

[81]	2 copper finned tube HEX	$CaCl_2$/ ammonia Zeolite 13X + $CaCl_2$/ water	6 solenoid valves	10 solenoid valves

† SS: Stainless steel
‡ HEX: Heat exchanger

It can be seen in Table 1 that the best choice for the valves installed between the adsorber beds, and condenser and evaporator are check valves. These valves have no power consumption and operate by the pressure difference between the two sides of the valve. Also, Table 1indicates that electrically actuated ball valves and solenoid valves are installed on the most of ACS to control the heating and cooling systems automatically. Solenoid valves are lighter than electrically actuated ball valves and have faster response. However, they have higher electricity power consumption than electrically actuated ball valves. Our analysis showed that the power consumption and complexity of control valves have been overlooked in the literature and there is no information or strategy to minimize the parasitic power consumption of valves.

In the present study, two ideas are proposed for the expansion and control valves of an ACS for vehicle A/C applications to simplify the control system, and reduce the total mass of the ACS and the parasitic power consumption of the control valves. As a proof-of-concept demonstration, a two-adsorber bed silica gel/$CaCl_2$ ACS is designed and built to test these ideas. To evaluate the functionality of the expansion and control valves, parametric studies are performed under different operating conditions. An ACS thermodynamic cycle model is also developed and compared against the experimental data for prediction and further improvement of the ACS performance. Finally, additional modifications to improve the performance of the ACA are proposed.

2. ACS thermodynamic cycle

The thermodynamic cycle of an ACS is comprised of two main steps: heating-desorption-condensation and cooling-adsorption-evaporation. With a single adsorber bed, an ACS generates evaporative cooling power intermittently. To produce a continuous cooling power, one must use more than one adsorber bed. Figure 1a depicts a schematic of a typical two-adsorber bed ACS comprised of two adsorber beds, a condenser, an expansion valve, and an evaporator.

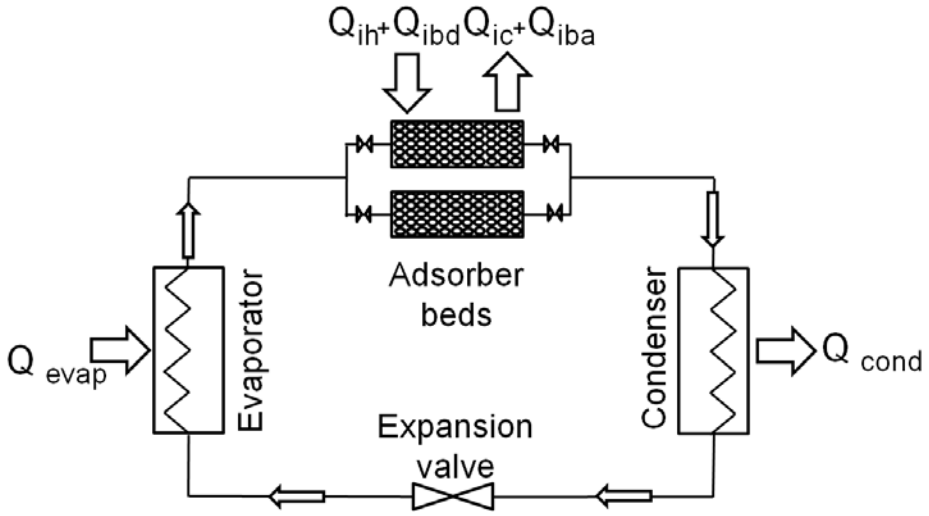

(a)

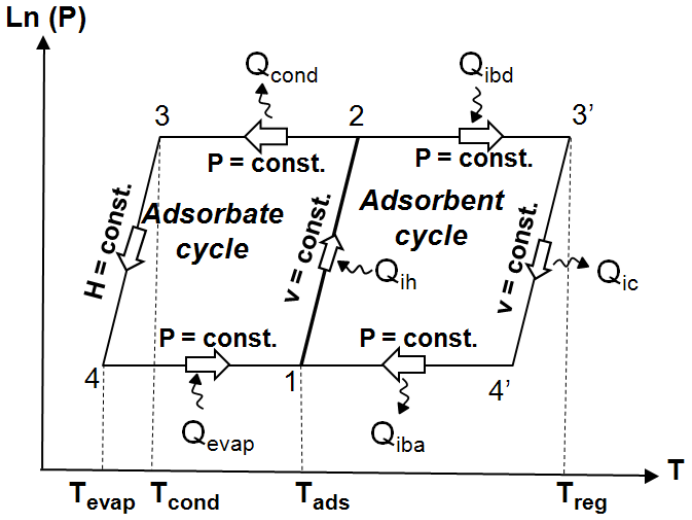

(b)

Figure 1. (a) Schematic and (b) thermodynamic cycle of a two-adsorber bed ACS [82].

Figure 1b shows the thermodynamic processes in an ACS which is divided into two subcycles: (i) an adsorbent cycle (on the right side), and (ii) an adsorbate cycle (on the left side). As shown in Figure 1b, the adsorbent cycle includes four steps: (1) isosteric heating (ih); process 1-2, (2) isobaric desorption (ibd); process 2-3', (3) isosteric cooling (ic); process 3'-4', and (4) isobaric adsorption (iba); process 4'-1. Isosteric processes occur at constant specific volume and isobaric processes occur at constant pressure. The adsorbate cycle shown in Figure 1b includes three steps: (1) isobaric condensation in the condenser; process 2-3, (2) isenthalpic process in the expansion valve; process 3-4, and (3) isobaric evaporation in the evaporator; process 4-1.

During step 1-2, the adsorbent-adsorbate pair absorbs heat of Q_{ih} from an external heat source in an isosteric process. In this step, temperature and pressure of the adsorber bed increase due to the adsorbate desorption from the adsorbent particles. This process is continued until the pressure of the adsorber bed reaches the pressure of the condenser and the inlet valve to the condenser is opened. In step 2-3', the external heat source continuously heats the adsorber bed (Q_{ibd}) during an isobaric desorption process, the adsorbate leaves the adsorber bed, and is condensed inside the condenser through an isobaric cooling process (step 2-3). Upon reaching the point 3', the maximum temperature of the cycle, the valve between the adsorber bed and the condenser is closed and during an isosteric cooling process (step 3'-4'), the temperature of the adsorbent is reduced by dissipating the heat of Q_{ic} through a heat sink. In step 3-4, the adsorbate inside the condenser passes through the expansion valve and enters to the evaporator. During step 4-1, the adsorbate absorbs the heat of Q_{evap} from the environment of interest and evaporates. At the same time, the valve between the evaporator and the adsorber bed is opened and the adsorbent adsorbs

the vaporous adsorbate through an isobaric adsorption process (step 4'-1) and releases heat of Q_{iba}.

3. Experimental study

An ACS with more than 60 different components was designed and built to test the proposed ideas. Figure 2a-c shows a schematic of the two-adsorber bed waste heat-driven ACS along with photos of the system components. The ACS equipped with four temperature control systems (TCS) to control the adsorption and desorption temperatures in the adsorber beds, and the condensation and evaporation temperatures in the condenser and evaporator, respectively. As shown in Figure 2a, valves V1-V4 are installed before and after the adsorber beds to control the adsorption and desorption processes, and eight valves (V5-V12) are installed on the TCSs (TCS_{HF} and TCS_{CF}) to intermittently heat up and cool down adsorber beds 1 and 2.

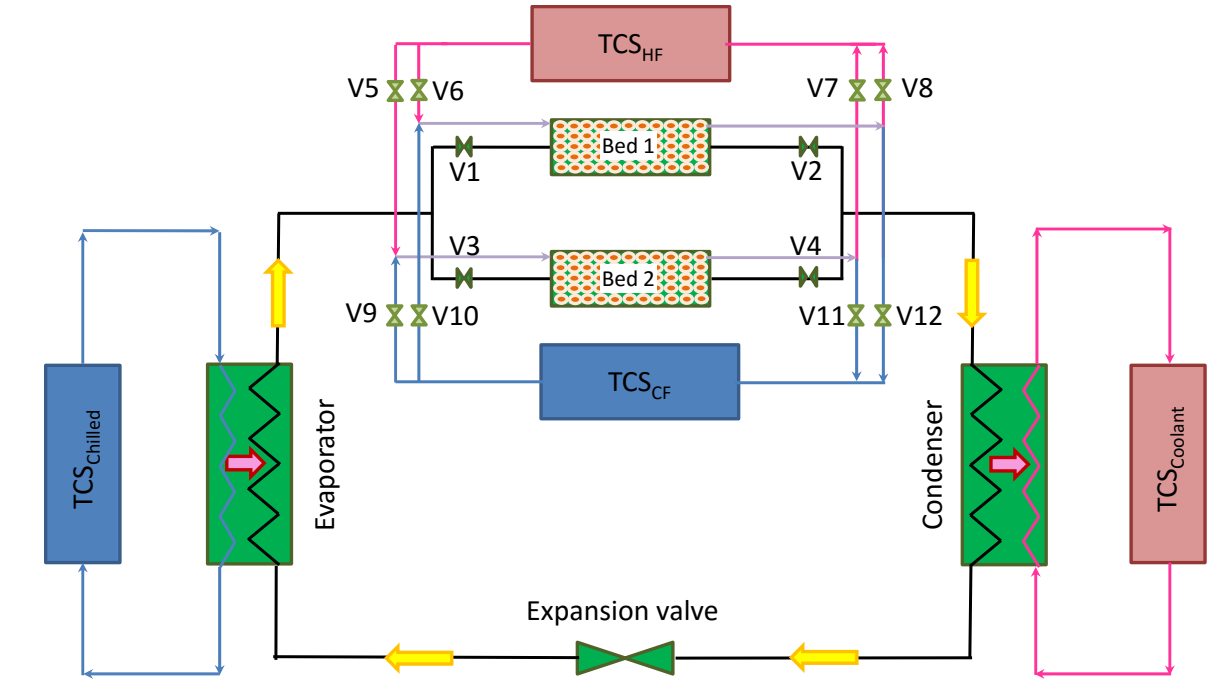

(a)

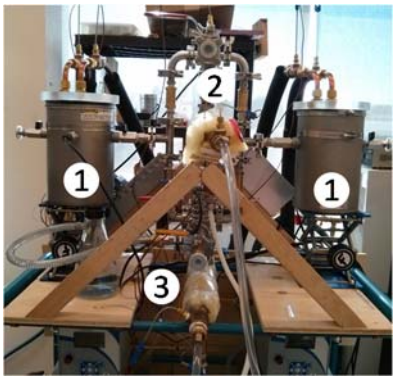

(b)

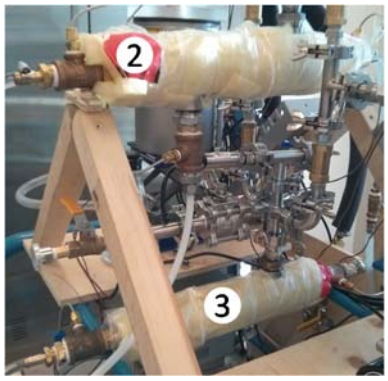

(c)

(d)

Figure 2. (a) Schematic of a two-adsorber bed ACS, (b)-(c) ACS components: 1- adsorber beds, 2-condenser, and 3-evaporator, and (d) custom-built heat exchanger located inside the adsorber beds.

Silica gel/$CaCl_2$ adsorbent material was prepared with combining chromatography-grade commercial silica gel with irregular-shaped grains (0.5–1.0 mm) and average pore diameter of 5.7 nm (SiliaFlash N60, Silicycle Inc.) with 30% wt. $CaCl_2$. Two heat exchangers, as shown in Figure 2d, were designed and built based on the results of Sharafian et al. [83] to be packed with

the silica gel/$CaCl_2$ composite adsorbent. Type T thermocouples (Omega, model #5SRTC-TT-T-36-36) with accuracy of 0.75% of reading and pressure transducers (Omega, model #PX309-005AI) with 0-34.5 kPa operating range and ±0.4 kPa accuracy were used to monitor and record the temperature and pressure variations in each component of the ACS over time.

Four check valves, V1-V4, were installed to reduce the weight and electrical power consumption of the ACS, and to simplify its control system. The check valves between the adsorber beds and the condenser, and the adsorber beds and the evaporator must have a low cracking pressure. An ACS which uses water as the refrigerant operates between 1 and 8 kPa, therefore any pressure drop between the adsorber beds and the condenser or the adsorber beds and the evaporator reduces the system performance. In this study, the check valves (Generant, model #DCV-375B-S) have a cracking pressure of less than 250 Pa, have no power consumption, and are durable and inexpensive.

To control the heating and cooling of the adsorber beds, eight solenoid valves, V5-V12, (StcValve, model #2W160-1/2-3-V with 14 W power consumption and #2WO160-1/2-3-V with 30 W power consumption) with a maximum operating temperature of 120°C and a total power consumption of 176 W were installed. The solenoid valve arrangements for the heat transfer fluid header and collector of the ACS are displayed in Figure 3.

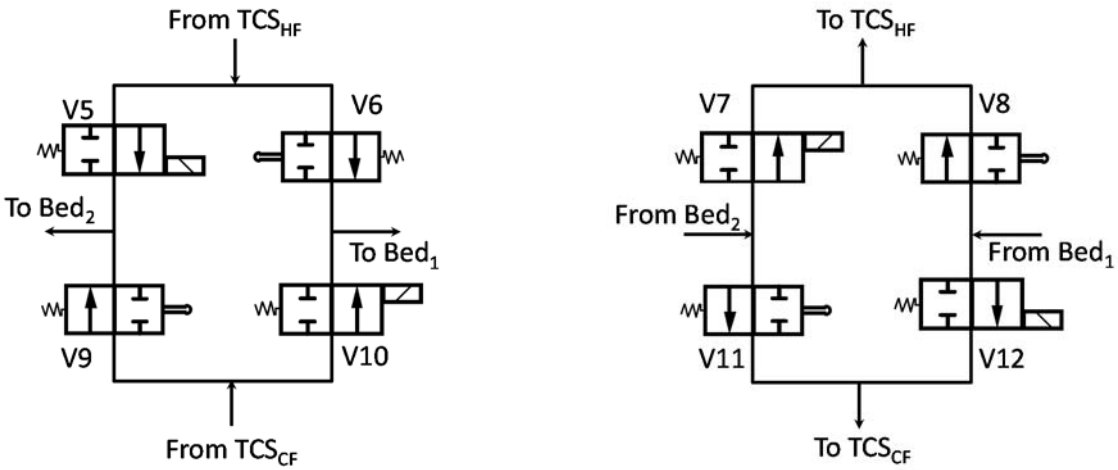

(a) (b)

Figure 3. Solenoid valve arrangements in (a) the header and (b) collector of the two-adsorber bed ACS. : normally opened, : normally closed.

As shown in Figure 3, solenoid valves V5, V7, V10, and V12 are normally closed and solenoid valves V6, V8, V9, and V11 are normally open. To desorb adsorber bed 1, heating fluid comes from TCS_{HF}, enters the header, passes through valve V6, and goes to adsorber bed 1, as shown in Figure 3a, and then returns from adsorber bed 1, passes through valve V8, and returns to TCS_{HF}, as shown in Figure 3b. For the adsorption process in adsorber bed 2, cooling fluid comes from TCS_{CF}, passes through valve V9, and enters adsorber bed 2. Then, it returns from adsorber bed 2, passes through valve V11, and returns to TCS_{CF}. When the solenoid valves are not energized, TCS_{HF} and TCS_{CF} are connected to adsorber beds 1 and 2, respectively. When the solenoid valves are energized, the flow directions of heating and cooling fluids are switched, and TCS_{HF} and TCS_{CF} are connected to adsorber bed 2 and 1, respectively.

With this design, valves V1-V8 are controlled with only a relay switch, which in turn is controlled automatically using a LabVIEW program, and the power consumption of valves V1-V8 for one cycle reduces by 50%. Also, check valves V1-V4 operate automatically, without power consumption, actuated by the pressure gradients between the adsorber beds, and the condenser and the evaporator. The total mass of the eight solenoid valves and four check valves is about 7 kg (8 × 0.815 kg + 4 × 0.115 kg). If electrically or pneumatically actuated ball valves were used, the total mass of eight valves and four check valves of the same size would be 17.5 kg (8 × 2.130 kg + 4 × 0.115 kg) which is 10.5 kg (2.5 times) heavier than the design in this study.

The expansion valve of a refrigeration system prevents the vaporous refrigerant in the condenser from flowing to the evaporator, and creates a pressure difference between the condenser and evaporator that is set by the refrigerant saturation pressure. Therefore, the expansion valve of an ACS that uses water as the refrigerant (adsorbate) differs from those of designed for conventional VCRCs that use commercial refrigerants such as chlorofluorocarbons (CFCs), hydrochlorofluorocarbons (HCFCs), and hydrofluorocarbons (HFCs). Among ACS experiments for stationary applications, a reverse U-bend tube was used as the expansion valve such as the one reported in Ref. [84]. The problem associated with a reverse U-bend tube in an ACS that uses water as the refrigerant is its fixed height. To create a pressure drop of 5 kPa between the condenser and evaporator, the height of such a reverse U-bend is about 50 cm which is not practical for light-duty vehicle A/C applications and limits the operating range of the ACS. In this study, to resolve the issue of U-bend tube for vehicle applications and design an expansion valve for a wide range of operating conditions, a check valve (Generant, model #CV-250B-S-1) with a cracking pressure of 3.4-6.9 kPa is proposed.

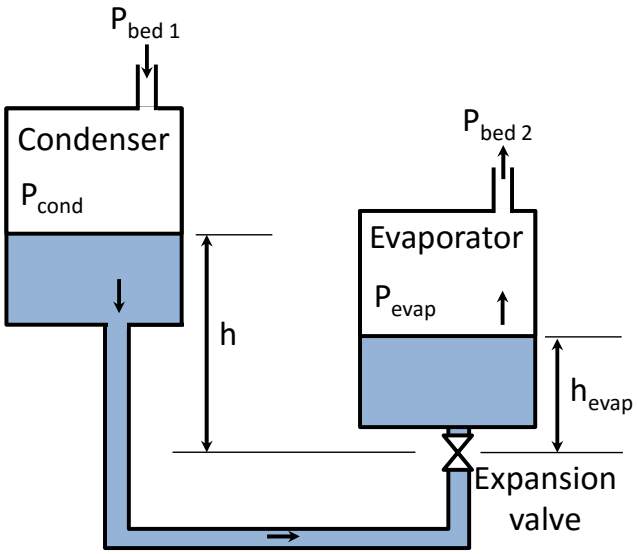

Figure 4. Schematic of the proposed expansion valve for a waste heat-driven ACS.

Figure 4 shows the positions of the condenser and evaporator, and the expansion valve located between them. The condensed refrigerant (adsorbate) is accumulated at the outlet of the condenser and before the expansion valve. As such, the hydrostatic pressure balance for the fluid between the condenser and evaporator is used to relate P_{cond} and P_{evap} to $P_{cracking}$ as follows:

$$P_{\text{cond}} - P_{\text{evap}} - \rho g h_{\text{evap}} + \rho g h > P_{\text{cracking}} \tag{1}$$

Equation (1) shows that the expansion valve connects the condenser to the evaporator only if the sum of the left-side terms become larger than the cracking pressure of the check valve, $P_{cracking}$. As such, the term ρgh in Eq. (1) created by the accumulation of liquid refrigerant (adsorbate) at the outlet of the condenser guarantees that no vaporous refrigerant passes through the expansion valve. Such a compact expansion valve can effectively operate in a vehicle where operating conditions vary significantly and vibrations are abundant. The other specifications of the designed ACS and the operating conditions are summarized in Table 2.

Table 2. Specifications and operating conditions of the ACS built in this study.

Parameter	Changed values
Working pairs	Silica gel/$CaCl_2$-water
Mass of adsorbent per adsorber bed (kg)	1.15
Metal mass of adsorber bed (kg)	2.8
Adsorber bed heat transfer surface area, A_{bed}, (m^2)	0.235
Adsorber bed heat transfer coefficient, U_{bed}, (W/m^2K)	20.0
Heating fluid mass flow rate to adsorber bed (kg/s)	0.058 (4.1 L/min of silicone oil)
Cooling fluid mass flow rate to adsorber bed (kg/s)	0.062 (4.1 L/min of silicone oil)
Heat capacity of silicone oil (kJ/kgK)	1.8
Metal mass of condenser (kg)	1.9
Condenser heat transfer surface area, A_{cond}, (m^2)	0.1444
Condenser heat transfer coefficient, U_{cond}, (W/m^2K)	250
Coolant water mass flow rate to condenser (kg/s)	0.036 (2.16 L/min of water)
Metal mass of evaporator (kg)	1.9
Evaporator heat transfer surface area, A_{evap}, (m^2)	0.072
Evaporator heat transfer coefficient, U_{evap}, (W/m^2K)	250
Chilled water mass flow rate to evaporator (kg/s)	0.02 (1.2 L/min of water)
Heating fluid inlet temperature (°C)	90
Cooling fluid inlet temperature (°C)	30
Coolant fluid inlet temperature (°C)	30
Chilled water inlet temperature (°C)	15

4. Numerical modeling

A dynamic lumped-body model was developed for the ACS thermodynamic cycle to predict the performance of the system and further improve the design. The energy balance on the adsorber bed during the isosteric heating (process 1-2 in Figure 1b) is expressed as follows:

$$m_{adsorbent}\left[c_{adsorbent}+c_{p,liq.adsorbate}\,\omega_{max}+c_{bed}\,\frac{m_{bed}}{m_{adsorbent}}\right]\frac{dT_{adsorbent}}{dt}=U_{bed}\,A_{bed}\,\Delta T_{LM,bed} \qquad (2)$$

where $m_{adsorbent}$ is the mass of dry adsorbent and $\frac{m_{bed}}{m_{adsorbent}}$ is the AAMR. In Eq. (2), $T_{adsorbent}$ is the adsorbent particles temperature and ω_{max} is the maximum adsorbate uptake at the adsorbent temperature and evaporator pressure, see Figure 1b. U_{bed} and A_{bed} are the overall heat transfer coefficient and heat transfer surface area of the adsorber bed, respectively. $\Delta T_{LM,bed}$ defines the adsorber bed log mean temperature difference (LMTD) between the adsorbent particles and heating fluid:

$$\Delta T_{LM,bed} = \frac{T_{hf,i} - T_{hf,o}}{\ln\left(\frac{T_{hf,i} - T_{adsorbent}}{T_{hf,o} - T_{adsorbent}}\right)} \tag{3}$$

where $T_{hf,i}$ and $T_{hf,o}$ are the heating fluid inlet and outlet temperatures. Equation (4) gives the heating fluid outlet temperature during the isosteric heating process:

$$\dot{m}_{hf} c_{p,hf} \left(T_{hf,i} - T_{hf,o}\right) = U_{bed} A_{bed} \Delta T_{LM,bed} \tag{4}$$

where $\dot{m}_{hf}$ is the heating fluid mass flow rate . During the isobaric desorption (process 2-3' in Figure 1b), the energy balance on the adsorber bed and the adsorbate uptake rate by the adsorbent particles are expressed as follows:

$$m_{adsorbent}\left[c_{adsorbent} + c_{p,liq.adsorbate}\,\omega + c_{bed}\frac{m_{bed}}{m_{adsorbent}}\right]\frac{dT_{adsorbent}}{dt} - m_{adsorbent}\frac{d\omega}{dt}\Delta h_{ads} = U_{bed} A_{bed} \Delta T_{LM,bed} \tag{5}$$

$$\frac{d\omega}{dt} = \frac{15 D_s}{R_p^2}\left(\omega_{eq} - \omega\right) \tag{6}$$

The first and second terms in the left-hand side of Eq. (5) represent the sensible and latent heats, respectively. Equation (6) gives the adsorbate uptake rate, $\frac{d\omega}{dt}$, which is a function of the solid-side mass diffusivity, D_s, the average radius of the adsorbent particles, R_p, and the equilibrium adsorbate uptake of the adsorbent particles, ω_{eq}. The solid-side mass diffusivity is expressed as $D_{s0}\exp\left(-E_a / R_u T_{adsorbent}\right)$, where D_{s0} is the pre-exponential constant, E_a is the activation energy, and R_u is the universal gas constant. In this study, the adsorbent material is silica gel/$CaCl_2$ and the constant values of D_{s0}, E_a, and R_p are 2.54×10^{-4} m^2/s, 42.0 kJ/mol, and 0.375×10^{-3} m, respectively [85,86]. Equation (7) gives the equilibrium water uptake by silica gel/$CaCl_2$ [85,86]:

$$\omega_{eq} = \frac{\omega_m K_0 \exp\left(\frac{\Delta h_{ads} M_{adsorbate}}{R_u T_{adsrobent}}\right) P}{\left[1+\left[K_0 \exp\left(\frac{\Delta h_{ads} M_{adsorbate}}{R_u T_{adsrobent}}\right) P\right]^n\right]^{1/n}} \tag{7}$$

where P, $M_{adsorbate}$ and Δh_{ads} are the operating pressure in mbar, the molar mass of adsorbate, and the enthalpy of adsorption, respectively. For silica gel/$CaCl_2$-water, Δh_{ads}, K_0, ω_m, and n are equal to 2760 kJ/kg, 2.0×10^{-10} $mbar^{-1}$, 0.8 kg/kg, and 1.1, respectively [85,86]. The energy balance on the condenser is expressed by Eqs. (8)-(10):

$$-m_{adsorbate}\frac{d\omega}{dt}\left[h_{fg,adsorbate@T_{cond}} + c_{p,vaporous\,adsorbate}\left(T_{adsorbent} - T_{cond}\right)\right] - U_{cond} A_{cond} \Delta T_{LM,cond} = m_{cond} c_{cond} \frac{dT_{cond}}{dt} \tag{8}$$

$$\Delta T_{LM,cond} = \frac{T_{coolant,i} - T_{coolant,o}}{\ln\left(\frac{T_{cond} - T_{coolant,o}}{T_{cond} - T_{coolant,i}}\right)} \tag{9}$$

$$\dot{m}_{coolant} c_{p,coolant} \left(T_{coolant,o} - T_{coolant,i}\right) = U_{cond} A_{cond} \Delta T_{LM,cond} \tag{10}$$

where $T_{coolant,i}$ and $T_{coolant,o}$ are the coolant fluid inlet and outlet temperatures to the condenser and h_{fg} is the enthalpy of vaporization during the condensation process. The set of Eqs. (3)-(10) should be solved simultaneously to find the adsorbent particles temperature, adsorbate uptake rate, heating fluid outlet temperature, and adsorber bed LMTD, as well as the condenser and coolant fluid outlet temperatures during the isobaric desorption and condensation processes. The amounts of heat transfer to the adsorber bed from the heat source during the isosteric heating and isobaric desorption processes, and the heat removal from the condenser during the condensation process are calculated as follows:

$$\dot{q}_{heating} = \dot{m}_{hf} c_{p,hf} \left(T_{hf,i} - T_{hf,o}\right) \tag{11}$$

$$\dot{q}_{cond} = \dot{m}_{coolant} c_{p,coolant} \left(T_{coolant,i} - T_{coolant,o}\right) \tag{12}$$

Equations (13)-(15) express the energy balance during the isosteric cooling (process 3'-4' in Figure 1b). This process is similar to the isosteric heating process except the cooling fluid replaces the heating fluid.

$$m_{adsorbent}\left[c_{adsorbent} + c_{p,liq.adsorbate}\,\omega_{min} + c_{bed}\frac{m_{bed}}{m_{adsorbent}}\right]\frac{dT_{adsorbent}}{dt} = U_{bed} A_{bed} \Delta T_{LM,bed} \tag{13}$$

$$\Delta T_{LM,bed} = \frac{T_{cf,i} - T_{cf,o}}{\ln\left(\frac{T_{cf,i} - T_{adsorbent}}{T_{cf,o} - T_{adsorbent}}\right)} \tag{14}$$

$$\dot{m}_{cf} c_{p,cf} \left(T_{cf,i} - T_{cf,o} \right) = U_{bed} A_{bed} \, \Delta T_{LM,bed} \tag{15}$$

where ω_{min} is the minimum equilibrium adsorbate uptake in the ACS thermodynamic cycle at the end of the isobaric desorption process and is calculated at the adsorber bed temperature and condenser pressure, see Figure 1b. The energy balance on the adsorber bed during the isobaric adsorption (process 4'-1 in Figure 1b) is expressed as follows:

$$\begin{aligned} m_{adsorbent} \left[c_{adsorbent} + c_{p,liq.adsorbate} \, \omega + c_{bed} \frac{m_{bed}}{m_{adsorbent}} \right] \frac{dT_{adsorbent}}{dt} - \\ m_{adsorbent} \frac{d\omega}{dt} \left[\Delta h_{ads} - c_{p,vaporous\,adsorbate} \left(T_{adsorbent} - T_{evap} \right) \right] = U_{bed} A_{bed} \, \Delta T_{LM,bed} \end{aligned} \tag{16}$$

The governing equations during the evaporation process are summarized in Eqs. (17)-(19):

$$\begin{aligned} -m_{adsorbate} \frac{d\omega}{dt} \left[h_{fg,adsorbate@T_{evap}} - c_{p,liq.adsorbate} \left(T_{cond} - T_{evap} \right) \right] \\ + U_{evap} A_{evap} \, \Delta T_{LM,evap} = m_{evap} \, c_{evap} \frac{dT_{evap}}{dt} \end{aligned} \tag{17}$$

$$\Delta T_{LM,evap} = \frac{T_{chilled,i} - T_{chilled,o}}{\ln \left(\dfrac{T_{chilled,i} - T_{evap}}{T_{chilled,o} - T_{evap}} \right)} \tag{18}$$

$$\dot{m}_{chilled} c_{p,chilled} \left(T_{chilled,i} - T_{chilled,o} \right) = U_{evap} A_{evap} \, \Delta T_{LM,evap} \tag{19}$$

Equations (6) and (14)-(19) should be solved simultaneously to find the adsorbent particles temperature and chilled water outlet temperature during the isobaric adsorption and evaporation processes, respectively. The heat removal from the adsorber bed during the isosteric cooling and isobaric adsorption processes as well as heat transfer to the evaporator during the evaporation process are calculated as follows:

$$\dot{q}_{cooling} = \dot{m}_{cf} c_{p,cf} \left(T_{cf,i} - T_{cf,o} \right) \tag{20}$$

$$\dot{q}_{evap} = \dot{m}_{chilled} c_{p,chilled} \left(T_{chilled,i} - T_{chilled,o} \right) \tag{21}$$

Equations (22)-(25) give the total amount of heat transfer to/removal from the adsorber beds, condenser and evaporator:

$$Q_{total\ heating} = \int_{steps\ (1-2)+(2-3')} \dot{q}_{heating}\ dt \qquad (J) \tag{22}$$

$$Q_{total\ cooling} = \int_{steps\ (3'-4')+(4'-1)} \dot{q}_{cooling}\ dt \qquad (J) \tag{23}$$

$$Q_{cond} = \int_{step\ (2-3)} \dot{q}_{cond}\ dt \qquad (J) \tag{24}$$

$$Q_{evap} = \int_{step\ (4-1)} \dot{q}_{evap}\ dt \qquad (J) \tag{25}$$

Accordingly, the COP and SCP of the ACS during one cycle are calculated:

$$COP = \frac{Q_{evap}}{Q_{total\ heating}} \tag{26}$$

$$SCP = \frac{Q_{evap}}{m_{adsorbent} \tau_{cycle}} \qquad (W/kg) \tag{27}$$

where τ_{cycle} in Eq. (27) is the cycle time.

To solve the set of differential equations simultaneously, the Runge–Kutta–Fehlberg method (RKF45) was adopted because the governing equations in the ACS thermodynamic modeling were only a function of time. In the in-house code, the marching time step was set at 0.1 s and the relative error difference between two consequent iterations at each time step was set at 10^{-9}. Also, the absolute error difference between the results at the end of two consequent cycles was set at 10^{-3}.

5. Results and discussion

5.1. Base-case operating condition

Figure 5 shows the performance of the ACS with a new expansion valve and control valves at the cycle time of 30 min and the base-case operating conditions summarized in Table 2. Figure 5a shows the inlet and outlet temperatures of the heating and cooling fluids before and after adsorber beds 1 and 2 as they are alternately heated and cooled for desorption and adsorption, respectively. Figure 5 shows that control valves V5-V12 can repetitively direct the heating and cooling fluids to the adsorber beds. The pressures of the adsorber beds, $P_{bed,1}$ and $P_{bed,2}$, corresponding to adsorption and desorption are shown in Figure 5b. It can be seen in Figure 5b that the pressures of the adsorber beds vary between the condenser and evaporator pressures, P_{cond} and P_{evap}, where condensation and evaporation processes occur. Also, Figure 5b indicates that whenever one of the adsorber beds undergoes the adsorption process, it is automatically connected to the evaporator via valves V1 or V3 and because of refrigerant evaporation in the evaporator, the chilled water outlet temperature, $T_{chilled,o}$, reduces. Figure 5b also indicates that the expansion valve can provide the required pressure drop between the condenser and evaporator under the base-case operating conditions.

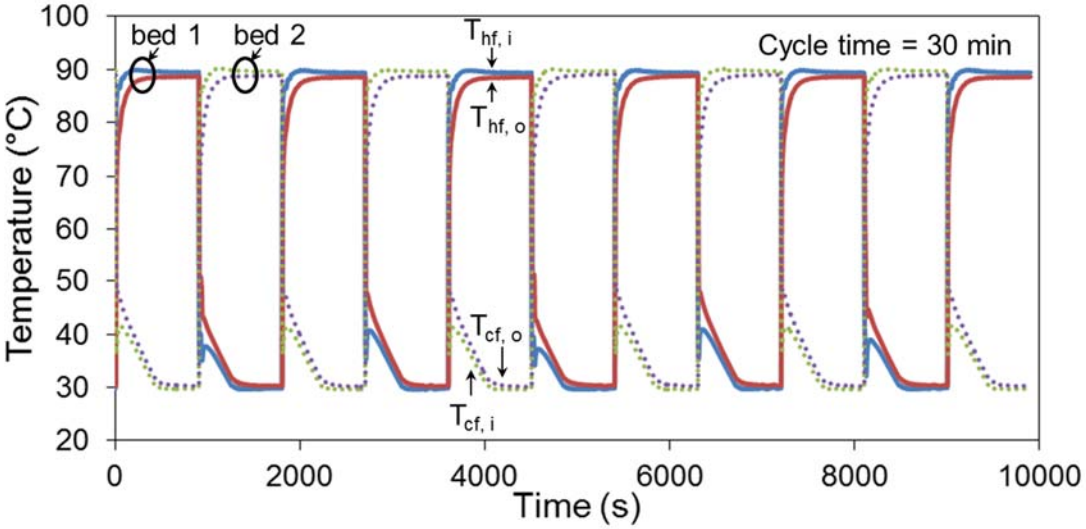

(a)

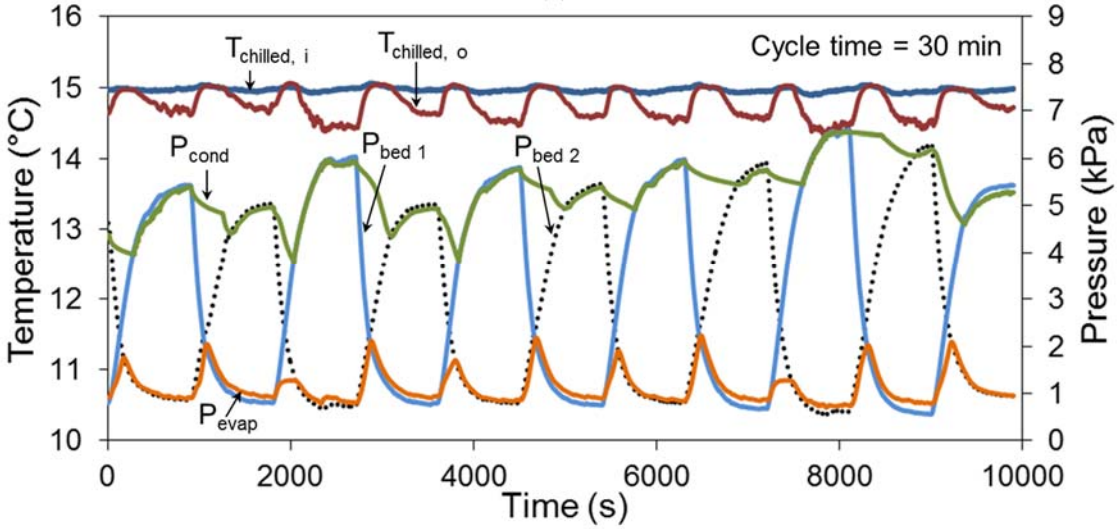

(b)

Figure 5. The ACS performance under the base-case operating conditions summarized in Table 2. (a) Inlet and outlet temperatures of heating and cooling fluids pumped to the adsorber beds, and (b) operating pressures of the adsorber beds, condenser and evaporator, and chilled water inlet and outlet temperatures in the evaporator.

5.2. Parametric study

In this section, the performance of the ACS is studied under different operating conditions. In order to verify the numerical modeling, the SCP of ACS calculated from the numerical modeling is compared against that of calculated from the experimental data. Figure 6 shows the effect of

cycle time on the SCP of the ACS. As shown in Figure 6, by increasing the cycle time from 20 to 30 min, the SCP increases by 177% from 3.3 to 9.15 W/kg. However, the SCP of ACS gradually reduces after the cycle time of 30 min because the adsorbate uptake capability of adsorbent particles reduces by increasing the cycle time. Figure 6 shows that the model is capable of predicting the SCP of ACS with a good agreement for cycle times less than 30 min which are of the interest of vehicle applications [87].

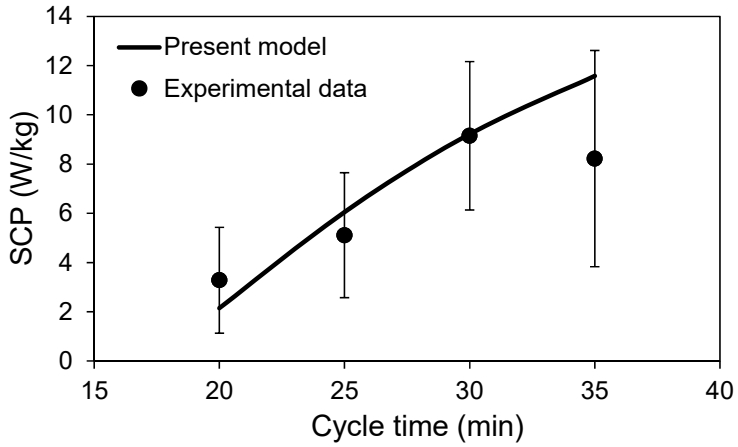

Figure 6. Effects of cycle time on the SCP of the ACS. The operating conditions are kept constant at the base-case operating conditions summarized in Table 2.

Figure 7 shows the effects of the heating and cooling fluid inlet temperatures on the SCP of the ACS. As shown in Figure 7a, increasing the heating fluid inlet temperature to the adsorber beds from 70 to 100°C increases the SCP from 0.7 to 14.8 W/kg. Increasing the temperature of the heating fluid to the adsorber beds during desorption causes faster heat transfer to the adsorbent material and, consequently, the rate of desorption of the adsorbate from the adsorbent material increases, and more adsorbate is desorbed. Accordingly, the drier adsorbent material adsorbs more adsorbate from the evaporator during the adsorption process. Therefore, higher cooling power (or SCP) is generated. In contrast, Figure 7b shows that by increasing the cooling fluid

inlet temperature from 30 to 40°C, the SCP of the ACS reduces from 9.2 to 4.0 W/kg because higher adsorbent temperature during the adsorption process reduces the adsorbate uptake capacity of the adsorbent. Figure 7 also depicts that the numerical modeling predicts the SCP of the ACS with good accuracy.

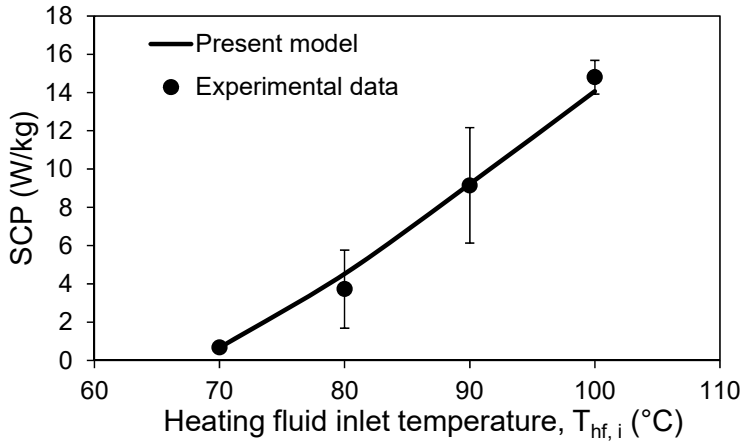

(a)

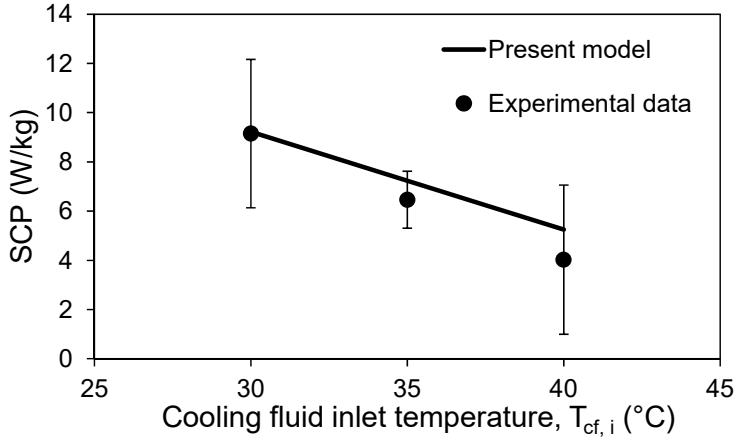

(b)

Figure 7. Effects of (a) heating fluid and (b) cooling fluid inlet temperatures to the adsorber beds on the SCP of the ACS. The other operating conditions are kept constant at the base-case operating conditions summarized in Table 2.

The effects of the coolant fluid inlet temperature circulated in the condenser on the SCP of ACS are shown in Figure 8a. The SCP of the ACS decreases when the coolant fluid inlet temperature

increases because of the increase in the condenser pressure and, as a result, lower amount of adsorbate condenses inside the condenser and adsorbent material dries less. Therefore, within a constant cycle time, lower adsorbate is desorbed from the adsorbent material and the adsorption capability of the adsorbent material during the adsorption process reduces. Figure 8b demonstrates the effects of the chilled water inlet temperature flowing through the evaporator on the SCP of the ACS. As shown in Figure 8b, by increasing the chilled water inlet temperature from 15 to 20°C, the SCP of the ACS increases from 9.2 to 14.2 W/kg, i.e., a 54% increase, because the adsorbate uptake capability of the adsorbent material increases with the increasing the evaporator pressure during the adsorption process. Figure 8 also displays that the numerical modeling is capable of predicting the SCP of the ACS with good accuracy.

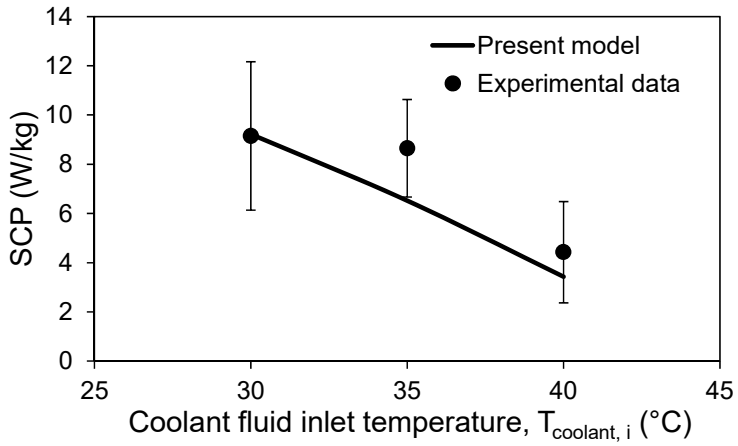

(a)

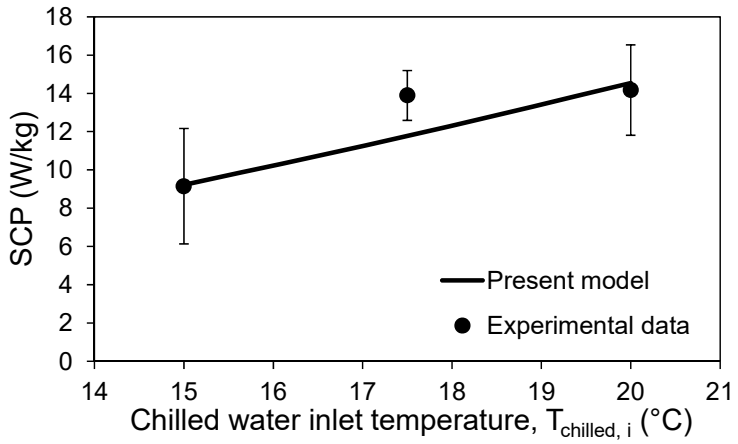

(b)

Figure 8. Effects of (a) coolant fluid and (b) chilled water inlet temperatures pumped to the condenser and evaporator, respectively, on the SCP of the ACS. The other operating conditions are kept constant at the base-case operating conditions summarized in Table 2.

5.3. Further improvement of the ACS

The parametric study indicates that the ideas proposed for the expansion and control valves of a waste heat-driven ACS can successfully operate under different operating conditions corresponding to what a light-duty vehicle A/C system experiences. However, the SCP of the designed ACS is not high enough because of low overall heat transfer conductance, $U_{bed}A_{bed}$, of the adsorber beds and, consequently, low heat transfer rate to the adsorbent material. Also, the

evaporator and condenser designs should be changed to increase the evaporation and condensation rate. Using the verified numerical modeling, as an example, one can study the effects of an adsorber bed with higher heat transfer rate. To this end, reducing the fin spacing of the adsorber bed to increase the overall heat transfer coefficient, U_{bed}, and increasing the adsorber bed heat transfer surface area, A_{bed}, are practical solutions. Figure 9 shows the SCP of the ACS with improved overall heat transfer conductance versus different cycle times. As shown in Figure 9, increasing U_{bed} from 20 to 70 W/m^{2}K, and A_{bed} from 0.235 to 2.8 m^2 result in the SCP of 83-96 W/kg within the cycle time 10-40 min.

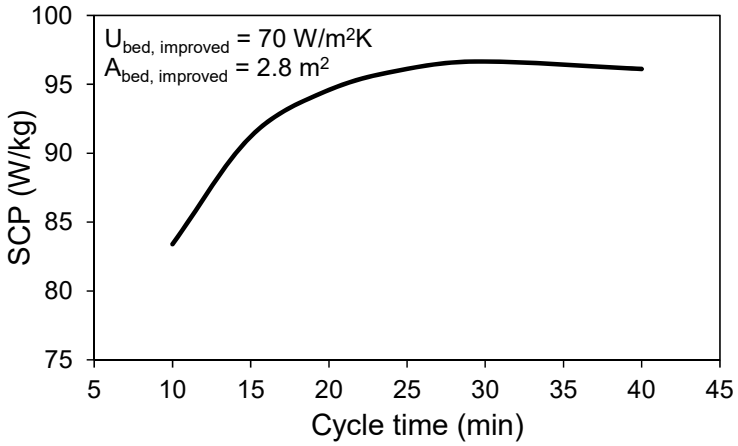

Figure 9. Effect of cycle time on the SCP of the ACS calculated by the numerical modeling for an adsorber bed with $U_{bed}A_{bed}$, of 196 W/K. The other operating conditions are kept constant at the base-case operating conditions summarized in Table 2.

6. Conclusion

In this study, new designs for the expansion valve and control valves of a waste heat-driven two-adsorber bed ACS were proposed and tested on a two-adsorber bed silica gel/$CaCl_2$-water ACS. The performance of the system was experimentally investigated under different operating

conditions. The results showed that the expansion valve and control valves operated effectively in the system while the mass of the system was reduced by 10.5 kg and electricity power consumption of control valves was reduced by 50%. Also, a numerical model was developed and compared against the experimental data. The numerical results showed a good agreement with the experimental results under a wide range of operating conditions. The validated numerical model showed that by increasing the adsorber bed overall heat transfer coefficient and heat transfer surface area, the SCP of the ACS could be improved up to 6 times.

Acknowledgment

The first author thanks to the LAEC members, Dr. Claire McCague, postdoctoral fellow, and Ms. Cecilia Berlanga, co-op student, for preparing silica gel/$CaCl_2$ required to run the experiments. Also, the authors gratefully acknowledge the financial support of the Natural Sciences and Engineering Research Council of Canada (NSERC) through the Automotive Partnership Canada Grant No. APCPJ 401826-10.

Nomenclature

A	heat transfer surface area (m^2)
A/C	air conditioning
ACS	adsorption cooling system
AAMR	adsorber bed to adsorbent mass ratio, ($kg_{metal}/kg_{dry\ adsorbent}$)
c	heat capacity of solid materials ($J/kg.K$)

c_p	heat capacity at constant pressure ($J/kg.K$)
COP	coefficient of performance
D_s	solid-side mass diffusivity (m^2/s)
D_{s0}	pre-exponential constant (m^2/s)
E_a	activation energy (J/mol)
Δh_{ads}	enthalpy of adsorption (J/kg)
ΔT_{LM}	log mean temperature difference (K)
h_{fg}	enthalpy of vaporization (J/kg)
ICE	internal combustion engine
M	molar mass (kg/mol)
m	mass (kg)
$\dot{m}$	mass flow rate (kg/s)
P	pressure ($mbar$)
Q_{total}	total heat transfer (J)
$\dot{q}$	heat transfer rate (W)
R_p	average radius of adsorbent particles (m)
R_u	universal gas constant ($J/mol.K$)

SCP	specific cooling power (*W/kg dry adsorbent*)
ω	adsorbate uptake (*kg/kg dry adsorbent*)
T	temperature (*K*)
t	time (*s*)
τ_{cycle}	cycle time (*s*)
U	overall heat transfer coefficient ($W/m^2.K$)
VCRC	vapor compression refrigeration cycle

Subscripts

adsorbate	adsorbate
adsorbent	adsorbent particles
bed	adsorber bed
chilled	chilled water
cf	cooling fluid
cond	condenser
coolant	coolant fluid
cooling	cooling process
eq	equilibrium state
evap	evaporator

heating	heating process
hf	heating fluid
i	in
liq.	liquid phase
max	maximum
min	minimum
o	out
sat	saturation
vaporous	vaporous phase

References

[1] Suzuki M. Application of adsorption cooling systems to automobiles. Heat Recover Syst CHP 1993;13:335–40.

[2] Abdullah MO, Tan IAW, Lim LS. Automobile adsorption air-conditioning system using oil palm biomass-based activated carbon: A review. Renew Sustain Energy Rev 2011;15:2061–72. doi:10.1016/j.rser.2011.01.012.

[3] Demir H, Mobedi M, Ülkü S. A review on adsorption heat pump: Problems and solutions. Renew Sustain Energy Rev 2008;12:2381–403. doi:10.1016/j.rser.2007.06.005.

[4] Sharafian A, Bahrami M. Assessment of adsorber bed designs in waste-heat driven adsorption cooling systems for vehicle air conditioning and refrigeration. Renew Sustain Energy Rev 2014;30:440–51. doi:10.1016/j.rser.2013.10.031.

[5] Sharafian A, Bahrami M. Critical analysis of thermodynamic cycle modeling of adsorption cooling systems for light-duty vehicle air conditioning applications. Renew Sustain Energy Rev 2015;48:857–69. doi:10.1016/j.rser.2015.04.055.

[6] Hulse GE. Freight car refrigeration by an adsorption system employing silica gel. Refrig Eng 1929;17:41–54.

[7] Jiangzhou S, Wang RZ, Lu YZ, Xu YX, Wu JY. Experimental investigations on adsorption air-conditioner used in internal-combustion locomotive driver-cabin. Appl Therm Eng 2002;22:1153–62. doi:10.1016/S1359-4311(02)00036-4.

[8] Lu YZ, Wang RZ, Jianzhou S, Zhang M, Xu Y, Wu J. Performance of a diesel locomotive waste-heat-powered adsorption air conditioning system. Adsorption 2004;10:57–68.

[9] Wang K, Wu JY, Wang RZ, Wang LW. Composite adsorbent of CaCl2 and expanded graphite for adsorption ice maker on fishing boats. Int J Refrig 2006;29:199–210. doi:10.1016/j.ijrefrig.2005.06.004.

[10] Wang LW, Wang RZ, Lu ZS, Xu YX, Wu JY. Split heat pipe type compound adsorption ice making test unit for fishing boats. Int J Refrig 2006;29:456–68. doi:10.1016/j.ijrefrig.2005.08.007.

[11] Lu ZS, Wang RZ, Li TX, Wang LW, Chen CJ. Experimental investigation of a novel multifunction heat pipe solid sorption icemaker for fishing boats using CaCl2/activated carbon compound–ammonia. Int J Refrig 2007;30:76–85. doi:10.1016/j.ijrefrig.2006.07.001.

[12] Wang K, Wu JY, Xia ZZ, Li SL, Wang RZ. Design and performance prediction of a novel double heat pipes type adsorption chiller for fishing boats. Renew Energy 2008;33:780–90. doi:10.1016/j.renene.2007.04.023.

[13] Wang LW, Wang RZ, Xia ZZ, Wu JY. Studies on heat pipe type adsorption ice maker for fishing boats. Int J Refrig 2008;31:989–97. doi:10.1016/j.ijrefrig.2008.01.002.

[14] De Boer R, Smeding SF. Thermally operated mobile air-conditioning system: Development and test of a laboratory prototype. Int. Sorption Heat Pump Conf., Seoul, Korea: 2008.

[15] De Boer R, Smeding SF, Mola S. Silicagel-water adsorption cooling prototype system for mobile air conditioning. Heat Powered Cycles Conf., Berlin, Germany: 2009.

[16] Verde M, Corberan JM, de Boer R, Smeding S. Modelling of a waste heat driven silica gel/water adsorption cooling system comparison with experimental results. Int. Sorption Heat Pump, Padua, Italy: 2011, p. 7–8.

[17] Sapienza A, Santamaria S, Frazzica A, Freni A. Influence of the management strategy and operating conditions on the performance of an adsorption chiller. Energy 2011;36:5532–8. doi:10.1016/j.energy.2011.07.020.

[18] Pons M, Laurent D, Meunier F. Experimental temperature fronts for adsorptive heat pump applications. Appl Therm Eng 1996;16.

[19] Poyelle F, Guilleminot JJ, Meunier F. Experimental tests and predictive model of an adsorptive air conditioning unit. Ind Eng Chem Res 1999;38:298–309. doi:10.1021/ie9802008.

[20] Wu JY, Wang RZ, Xu YX. Dynamic simulation and experiments of a heat regenerative adsorption heat pump. Energy Convers Manag 2000;41:1007–18. doi:10.1016/S0196-8904(99)00161-2.

[21] Wang RZ, Wu JY, Xu YX, Wang W. Performance researches and improvements on heat regenerative adsorption refrigerator and heat pump. Energy Convers Manag 2001;42:233–49. doi:10.1016/S0196-8904(99)00189-2.

[22] Wang RZ. Performance improvement of adsorption cooling by heat and mass recovery operation. Int J Refrig 2001;24:602–11.

[23] Wang RZ. Adsorption refrigeration research in Shanghai Jiao Tong University. Renew Sustain Energy Rev 2001;5:1–37.

[24] Qu TF, Wang RZ, Wang W. Study on heat and mass recovery in adsorption refrigeration cycles. Appl Therm Eng 2001;21:439–52. doi:10.1016/S1359-4311(00)00050-8.

[25] Wu JY, Wang RZ, Xu YX. Experimental results on operating parameters influence for an adsorption refrigerator. Int J Therm Sci 2002;41:137–45.

[26] Gui YB, Wang RZ, Wang W, Wu JY, Xu YX. Performance modeling and testing on a heat-regenerative adsorptive reversible heat pump. Appl Therm Eng 2002;22:309–20. doi:10.1016/S1359-4311(01)00082-5.

[27] Wang D, Wu J, Shan H, Wang R. Experimental study on the dynamic characteristics of adsorption heat pumps driven by intermittent heat source at heating mode. Appl Therm Eng 2005;25:927–40. doi:10.1016/j.applthermaleng.2004.07.013.

[28] Wang D, Wu J. Influence of intermittent heat source on adsorption ice maker using waste heat. Energy Convers Manag 2005;46:985–98. doi:10.1016/j.enconman.2004.06.002.

[29] Oliveira RG, Silveira V, Wang RZ. Experimental study of mass recovery adsorption cycles for ice making at low generation temperature. Appl Therm Eng 2006;26:303–11. doi:10.1016/j.applthermaleng.2005.04.021.

[30] Tamainot-Telto Z, Critoph RE. Monolithic carbon for sorption refrigeration and heat pump applications. Appl Therm Eng 2001;21:37–52. doi:10.1016/S1359-4311(00)00030-2.

[31] Critoph RE. Simulation of a continuous multiple-bed regenerative adsorption cycle. Int J Refrig 2001;24:428–37.

[32] Critoph RE. Multiple bed regenerative adsorption cycle using the monolithic carbon–ammonia pair. Appl Therm Eng 2002;22:667–77. doi:10.1016/S1359-4311(01)00118-1.

[33] Tamainot-Telto Z, Critoph RE. Advanced solid sorption air conditioning modules using monolithic carbon–ammonia pair. Appl Therm Eng 2003;23:659–74. doi:10.1016/S1359-4311(02)00238-7.

[34] Critoph RE. Adsorption Refrigeration Research at Warwick. 1st TECCS Meet., 2007.

[35] Critoph RE, Metcalf SJ. Specific cooling power intensification limits in ammonia–carbon adsorption refrigeration systems. Appl Therm Eng 2004;24:661–78. doi:10.1016/j.applthermaleng.2003.11.004.

[36] Critoph RE, Zhong Y. Review of trends in solid sorption refrigeration and heat pumping technology. Proc Inst Mech Eng Part E J Process Mech Eng 2005;219:285–300. doi:10.1243/095440805X6982.

[37] Tamainot-Telto Z, Metcalf SJ, Critoph RE. Novel compact sorption generators for car air conditioning. Int J Refrig 2009;32:727–33. doi:10.1016/j.ijrefrig.2008.11.010.

[38] Metcalf SJ, Tamainot-Telto Z, Critoph RE. Application of a compact sorption generator to solar refrigeration: Case study of Dakar (Senegal). Appl Therm Eng 2011;31:2197–204. doi:10.1016/j.applthermaleng.2010.11.001.

[39] Wang X, Chua HT, Ng KC. Experimental investigation of silica gel–water adsorption chillers with and without a passive heat recovery scheme. Int J Refrig 2005;28:756–65. doi:10.1016/j.ijrefrig.2004.11.011.

[40] Akahira A, Alam KCA, Hamamoto Y, Akisawa A, Kashiwagi T. Mass recovery four-bed adsorption refrigeration cycle with energy cascading. Appl Therm Eng 2005;25:1764–78. doi:10.1016/j.applthermaleng.2004.10.006.

[41] Alam KC a., Khan MZI, Uyun AS, Hamamoto Y, Akisawa A, Kashiwagi T. Experimental study of a low temperature heat driven re-heat two-stage adsorption chiller. Appl Therm Eng 2007;27:1686–92. doi:10.1016/j.applthermaleng.2006.07.006.

[42] Liu YL, Wang RZ, Xia ZZ. Experimental performance of a silica gel–water adsorption chiller. Appl Therm Eng 2005;25:359–75. doi:10.1016/j.applthermaleng.2004.06.012.

[43] Liu YL, Wang RZ, Xia ZZ. Experimental study on a continuous adsorption water chiller with novel design. Int J Refrig 2005;28:218–30. doi:10.1016/j.ijrefrig.2004.09.004.

[44] Wang DC, Xia ZZ, Wu JY. Design and performance prediction of a novel zeolite–water adsorption air conditioner. Energy Convers Manag 2006;47:590–610. doi:10.1016/j.enconman.2005.05.011.

[45] Akahira A, Alam KCA, Hamamoto Y, Akisawa A, Kashiwagi T. Experimental investigation of mass recovery adsorption refrigeration cycle. Int J Refrig 2005;28:565–72. doi:10.1016/j.ijrefrig.2004.10.001.

[46] Chang WS, Wang C-C, Shieh C-C. Experimental study of a solid adsorption cooling system using flat-tube heat exchangers as adsorption bed. Appl Therm Eng 2007;27:2195–9. doi:10.1016/j.applthermaleng.2005.07.022.

[47] Critoph RE. Towards a one tonne per day solar ice maker. Renew Energy 1996;9:626–31. doi:10.1016/0960-1481(96)88366-2.

[48] Tamainot-Telto Z, Critoph RE. Adsorption refrigerator using monolithic carbon-ammonia pair. Int J Refrig 1997;20:146–55.

[49] Critoph RE. Rapid cycling solar/biomass powered adsorption refrigeration system. Renew Energy 1999;16:673–8.

[50] Oertel K, Fischer M. Adsorption cooling system for cold storage using methanol/silicagel. Appl Therm Eng 1998;18:773–86. doi:10.1016/S1359-4311(97)00107-5.

[51] Zhang LZ, Wang L. Momentum and heat transfer in the adsorbent of a waste-heat adsorption cooling system. Energy 1999;24:605–24. doi:10.1016/S0360-5442(99)00018-3.

[52] Zhang LZ, Wang L. Effects of coupled heat and mass transfers in adsorbent on the performance of a waste heat adsorption cooling unit. Appl Therm Eng 1999;19:195–215.

[53] Zhang LZ. Design and testing of an automobile waste heat adsorption cooling system. Appl Therm Eng 2000;20:103–14. doi:10.1016/S1359-4311(99)00009-5.

[54] Restuccia G, Freni A, Vasta S, Aristov YI. Selective water sorbent for solid sorption chiller: experimental results and modelling. Int J Refrig 2004;27:284–93. doi:10.1016/j.ijrefrig.2003.09.003.

[55] Magnetto D. Thermally Operated Mobile Air Conditioning Systems. 2005.

[56] Wang DC, Xia ZZ, Wu JY, Wang RZ, Zhai H, Dou WD. Study of a novel silica gel–water adsorption chiller. Part I. Design and performance prediction. Int J Refrig 2005;28:1073–83. doi:10.1016/j.ijrefrig.2005.03.001.

[57] Wang DC, Wu JY, Xia ZZ, Zhai H, Wang RZ, Dou WD. Study of a novel silica gel–water adsorption chiller. Part II. Experimental study. Int J Refrig 2005;28:1084–91. doi:10.1016/j.ijrefrig.2005.03.002.

[58] Wang DC, Shi ZX, Yang QR, Tian XL, Zhang JC, Wu JY. Experimental research on novel adsorption chiller driven by low grade heat source. Energy Convers Manag 2007;48:2375–81. doi:10.1016/j.enconman.2007.03.001.

[59] Restuccia G, Freni A, Russo F, Vasta S. Experimental investigation of a solid adsorption chiller based on a heat exchanger coated with hydrophobic zeolite. Appl Therm Eng 2005;25:1419–28. doi:10.1016/j.applthermaleng.2004.09.012.

[60] Yang GZ, Xia ZZ, Wang RZ, Keletigui D, Wang DC, Dong ZH, et al. Research on a compact adsorption room air conditioner. Energy Convers Manag 2006;47:2167–77. doi:10.1016/j.enconman.2005.12.005.

[61] Wang LW, Wang RZ, Lu ZS, Chen CJ, Wu JY. Comparison of the adsorption performance of compound adsorbent in a refrigeration cycle with and without mass recovery. Chem Eng Sci 2006;61:3761–70. doi:10.1016/j.ces.2006.01.018.

[62] Lu ZS, Wang RZ, Wang LW, Chen CJ. Performance analysis of an adsorption refrigerator using activated carbon in a compound adsorbent. Carbon N Y 2006;44:747–52. doi:10.1016/j.carbon.2005.09.016.

[63] Wang LW, Wang RZ, Lu ZS, Chen CJ, Wang K, Wu JY. The performance of two adsorption ice making test units using activated carbon and a carbon composite as adsorbents. Carbon N Y 2006;44:2671–80. doi:10.1016/j.carbon.2006.04.013.

[64] Chen CJ, Wang RZ, Wang LW, Lu ZS. Studies on cycle characteristics and application of split heat pipe adsorption ice maker. Energy Convers Manag 2007;48:1106–12. doi:10.1016/j.enconman.2006.10.017.

[65] Freni A, Russo F, Vasta S, Tokarev M, Aristov YI, Restuccia G. An advanced solid sorption chiller using SWS-1L. Appl Therm Eng 2007;27:2200–4. doi:10.1016/j.applthermaleng.2005.07.023.

[66] Daou K, Wang RZ, Xia ZZ, Yang GZ. Experimental comparison of the sorption and refrigerating performances of a CaCl2 impregnated composite adsorbent and those of the host silica gel. Int J Refrig 2007;30:68–75. doi:10.1016/j.ijrefrig.2006.05.003.

[67] Aristov YI, Sapienza A, Ovoshchnikov DS, Freni A, Restuccia G. Reallocation of adsorption and desorption times for optimisation of cooling cycles. Int J Refrig 2012;35:525–31. doi:10.1016/j.ijrefrig.2010.07.019.

[68] Sapienza A, Glaznev IS, Santamaria S, Freni A, Aristov YI. Adsorption chilling driven by low temperature heat: New adsorbent and cycle optimization. Appl Therm Eng 2012;32:141–6. doi:10.1016/j.applthermaleng.2011.09.014.

[69] Freni A, Sapienza A, Glaznev IS, Aristov YI, Restuccia G. Experimental testing of a lab-scale adsorption chiller using a novel selective water sorbent “silica modified by calcium nitrate.” Int J Refrig 2012;35:518–24. doi:10.1016/j.ijrefrig.2010.05.015.

[70] Gong LX, Wang RZ, Xia ZZ, Chen CJ. Design and performance prediction of a new generation adsorption chiller using composite adsorbent. Energy Convers Manag 2011;52:2345–50. doi:10.1016/j.enconman.2010.12.036.

[71] Lu ZS, Wang RZ. Study of the new composite adsorbent of salt LiCl/silica gel–methanol used in an innovative adsorption cooling machine driven by low temperature heat source. Renew Energy 2014;63:445–51. doi:10.1016/j.renene.2013.10.010.

[72] Lu ZS, Wang RZ, Xia ZZ, Wu QB, Sun YM, Chen ZY. An analysis of the performance of a novel solar silica gel–water adsorption air conditioning. Appl Therm Eng 2011;31:3636–42. doi:10.1016/j.applthermaleng.2010.11.024.

[73] Lu Z, Wang R, Xia Z, Gong L. Experimental investigation adsorption chillers using micro-porous silica gel–water and compound adsorbent-methanol. Energy Convers Manag 2013;65:430–7. doi:10.1016/j.enconman.2012.09.018.

[74] Lu ZS, Wang RZ. Performance improvement and comparison of mass recovery in CaCl 2/activated carbon adsorption refrigerator and silica gel/LiCl adsorption chiller driven by low grade waste heat. Int J Refrig 2013;36:1504–11. doi:10.1016/j.ijrefrig.2013.03.008.

[75] Vasta S, Freni A, Sapienza A, Costa F, Restuccia G. Development and lab-test of a mobile adsorption air-conditioner. Int J Refrig 2012;35:701–8. doi:10.1016/j.ijrefrig.2011.03.013.

[76] Wang J, Wang LW, Luo WL, Wang RZ. Experimental study of a two-stage adsorption freezing machine driven by low temperature heat source. Int J Refrig 2013;36:1029–36. doi:10.1016/j.ijrefrig.2012.10.029.

[77] Song FP, Gong LX, Wang LW, Wang RZ. Study on gradient thermal driven adsorption cycle with freezing and cooling output for food storage. Appl Therm Eng 2014;70:231–9. doi:10.1016/j.applthermaleng.2014.04.066.

[78] Kiplagat JK, Wang RZ, Oliveira RG, Li TX, Liang M. Experimental study on the effects of the operation conditions on the performance of a chemisorption air conditioner powered by low grade heat. Appl Energy 2013;103:571–80. doi:10.1016/j.apenergy.2012.10.025.

[79] San J-Y, Tsai F-K. Testing of a lab-scale four-bed adsorption heat pump. Appl Therm Eng 2014;70:274–81. doi:10.1016/j.applthermaleng.2014.05.014.

[80] Pan QW, Wang RZ, Lu ZS, Wang LW. Experimental investigation of an adsorption refrigeration prototype with the working pair of composite adsorbent-ammonia. Appl Therm Eng 2014;72. doi:10.1016/j.applthermaleng.2014.06.054.

[81] Tso CY, Chan KC, Chao CYH, Wu CL. Experimental performance analysis on an adsorption cooling system using zeolite 13X/CaCl2 adsorbent with various operation sequences. Int J Heat Mass Transf 2015;85:343–55. doi:10.1016/j.ijheatmasstransfer.2015.02.005.

[82] Sharafian A, Bahrami M. A quasi steady state model for adsorption cooling systems: Automotive applications. ASME 2012 6th Int. Conf. Energy Sustain. 10th Fuel Cell Sci. Eng. Technol. Conf., San Diego, CA, USA: 2012.

[83] Sharafian A, McCague C, Bahrami M. Impact of fin spacing on temperature distribution in adsorption cooling system for vehicle A/C applications. Int J Refrig 2015;51:135–43.

[84] Grisel RJH, Smeding SF, de Boer R. Waste heat driven silica gel/water adsorption cooling in trigeneration. Appl Therm Eng 2010;30:1039–46. doi:10.1016/j.applthermaleng.2010.01.020.

[85] Aristov YI, Glaznev IS, Freni a., Restuccia G. Kinetics of water sorption on SWS-1L (calcium chloride confined to mesoporous silica gel): Influence of grain size and temperature. Chem Eng Sci 2006;61:1453–8. doi:10.1016/j.ces.2005.08.033.

[86] Saha BB, Chakraborty A, Koyama S, Aristov YI. A new generation cooling device employing CaCl2-in-silica gel–water system. Int J Heat Mass Transf 2009;52:516–24. doi:10.1016/j.ijheatmasstransfer.2008.06.018.

[87] Lambert MA, Jones BJ. Automotive adsorption air conditioner powered by exhaust heat. Part 1: Conceptual and embodiment Design. Proc Inst Mech Eng Part D J Automob Eng 2006;220:959–72. doi:10.1243/09544070JAUTO221.

Appendix H.

Effects of capillary-assisted tubes with different fin geometries on the performance of a low-operating pressure evaporator for adsorption cooling systems

(under review in the Applied Energy journal)

Effects of capillary-assisted tubes with different fin geometries on the performance of a low-operating pressure evaporator for adsorption cooling systems

Poovanna Cheppudira Thimmaiah[*], Amir Sharafian[*], Wendell Huttema, Majid Bahrami[†]

Laboratory for Alternative Energy Conversion (*LAEC*), School of Mechatronic Systems Engineering, Simon Fraser University, BC, Canada V3T 0A3

Abstract

In this study, the performance of a low-operating pressure evaporator using different enhanced tubes with application to adsorption cooling systems (ACS) is investigated. When using water as a refrigerant in an ACS, the operating pressure is quite low (<5 kPa) and the performance of the system is severely affected when using conventional evaporators. This problem can be addressed by using capillary-assisted evaporators. Five types of enhanced tubes with different fin geometries and a plain tube as a benchmark are tested under different chilled water inlet temperatures. The results showed that the enhanced tubes compared to the plain tube provide 1.65-2.23 times higher total evaporation heat transfer rate. Under equal inner and outer heat transfer surface area, the results also show that the enhanced tube with parallel continuous fins and higher fin height (Turbo Chil-26 FPI) provides 13% higher evaporator heat transfer

[*] Authors have contributed equally to the work.
[†] Corresponding author: School of Mechatronic Systems Engineering, Simon Fraser University, # 4300, 250-13450 102nd Avenue, Surrey, BC, Canada V3T0A3.
Tel.: +1 (778) 782-8538; Fax: +1 (778) 782-7514.
E-mail addresses: pthimmai@sfu.ca (P. Cheppudira Thimmaiah), asharafi@sfu.ca (A. Sharafian), mbahrami@sfu.ca (M. Bahrami).

coefficient than that with lower fin height (GEWA-KS-40 FPI). Furthermore, the effects of refrigerant height, dead volume inside the evaporator and chilled water mass flow rate on the performance of evaporator with Turbo Chil-40 FPI are studied. The parametric study show that the nominal total evaporation heat transfer rate reduces by 50% by increasing the water height to tube diameter ratio from one to 1.8. Also, increasing the chilled water mass flow rate from 2.5 to 15.3 kg/min (6.1 times) increases the total evaporation heat transfer rate and the evaporator heat transfer coefficient by 20% and 110%, respectively.

Keywords: capillary-assisted evaporation, enhanced tube, low-operating pressure, adsorption cooling system.

1. Introduction

Adsorption cooling systems (ACSs) can be a prominent replacement of vapor compression refrigeration cycles (VCRCs) where waste heat above 60°C is abundant. An internal combustion engine (ICE) of a light-duty vehicle wastes about 40% of fuel energy in the form of high temperature exhaust gas and dissipates about 30% of fuel energy from the engine coolant [1]. Therefore, a VCRC of a light-duty vehicle can be replaced by an ACS, and a portion of waste heat of ICE suffices to run the ACS and generate the cooling power required for vehicle air conditioning (A/C).

Instead of a compressor in a VCRC, ACS uses an adsorber bed in which a refrigerant (adsorbate), such as water or methanol, is adsorbed at the surface of an adsorbent, such as zeolite, silica gel, or activated carbon. Most of these materials are non-toxic, non-corrosive, and inexpensive [2] making ACS a safe and environmentally friendly technology. Among the existing refrigerants, water has the best thermo-physical properties of a good refrigerant, such as

the highest enthalpy of evaporation (latent heat). However, the saturation pressure of water at temperatures below 100°C, where the condenser and evaporator of an A/C system operate, is below the atmospheric pressure. For example, the saturation pressures of water corresponding to 15°C (evaporation temperature) and 30°C (condensation temperature) are 1.71 kPa and 4.25 kPa, respectively.

The condenser and evaporator of an ACS which uses water as the refrigerant are known as the low-operating pressure (LP) condenser and evaporator in which pressure drop significantly affects the overall performance of the ACS. For a LP condenser, one solution proposed in the literature is to use a shell-and-tube heat exchanger [3] in which the superheated water vapor flows in the shell-side of the heat exchanger and condenses on the outer surface of the tubes. At the end of the condensation process, the liquid water is accumulated at the outlet of the condenser. The design of a LP evaporator is different from that of a LP condenser. Accumulation of liquid water in a LP evaporator creates a water column which results in a static pressure difference between the liquid water-vapor interface and the bottom of the evaporator chamber. For example, having a liquid water column of 5 cm in a LP evaporator creates a static pressure difference of 490 Pa ($\rho_{lw} \times g \times h_{lw} = 1000\ kg/m^3 \times 9.81\ m/s^2 \times 0.05\ m$) from the liquid water-vapor interface to the bottom of the evaporator chamber. This static pressure changes the saturation temperature and pressure of water from 15°C and 1.71 kPa, as an example, to 19°C and 2.20 kPa (1.71 + 0.49 kPa), respectively. As a result of water saturation temperature variation in the LP evaporator, cooling power generation of ACS reduces drastically. To have a uniform water saturation temperature, the static pressure of water in a LP evaporator should be minimized. Two practical solutions to resolve this issue are: i) falling film evaporation, and ii) capillary-assisted evaporation.

There are several studies investigating the falling film evaporation from the plain and enhanced outside surface of horizontal tubes with the refrigeration applications. Ribatski and Jacobi [4] conducted a comprehensive literature review on the experimental and theoretical studies of falling film evaporation from the plain and enhanced surfaces of horizontal tubes. They concluded that enhanced tubes result in about 10 times higher evaporation heat transfer coefficient than plain tubes. Yang et al. [5] experimental studied the falling film heat transfer on the outer surface of horizontal tubes and investigated how the heat transfer coefficient was affected by flow density, evaporation temperatures, and temperature difference between the wall and saturated water. They showed that when the flow density was increased from 0.013 kg/ms to 0.062 kg/ms, the heat transfer coefficient was increased from 5,000 W/m^2K to 30,000 W/m^2K. Another experimental study was carried out by Li et al. [6] to investigate the characteristics of evaporative heat transfer on horizontal tube arrays of plain and enhanced tubes. The average heat transfer coefficients of water falling film on five types of enhanced tubes, with the plain tubes as a benchmark were investigated under vacuum. Their results showed that the tubes with both enhanced outer and inner surfaces were required to achieve high heat transfer rate. Li et al. [7] also conducted a set of experiments on a recently designed enhanced tube called Turbo CAB (19 and 26 FPI) which provided overall heat transfer coefficients of 3,000-4,000 W/m^2K at falling film flow rate of 1 m^3/h and temperature of 15°C. Their work again confirmed the importance of the tubes with enhanced inner surface which provided better heat transfer performance.

Abed et al. [8] reviewed the enhancement techniques with nanoparticles suspended with refrigerants in order to studying their function. The results from heat transfer showed that nanoparticles suspended in fluids were especially effective in enhancing the heat transfer and falling-film flow. However, the mechanisms involved were still unclear.

In conclusion, falling film evaporators succeed to avoid the influence of liquid column on the evaporation and provide high heat transfer coefficient specifically for large cooling capacities in a low footprint. However, equally distribution of refrigerant on horizontal tubes, parasitic power consumption (internal pump and circulator), and liquid spray equipment make the falling film evaporators impractical for an ACS installed in a light-duty vehicle A/C system. For low cooling capacities (less than 2 kW), in the contrary, capillary-assisted evaporators take advantage of uniform evaporation along the tubes, have no parasitic power consumption (no pump or circulator) with a lower weight and complexity.

There are few researches related to the capillary-assisted evaporation on the circumferential grooves. Capillary-assisted flow and evaporation inside a circumferential rectangular micro groove was studied by Xia et al. [9,10]. This capillary-assisted water evaporator was applied to a silica gel-water ACS. A heat transfer tube with outside circumferential micro-grooves was immersed into a pool of liquid. For the evaporation, the heating fluid flowing inside the tube heated up the thin liquid film located inside the micro-grooves. Due to the capillary action, the liquid water rose upwards along the micro-grooves and evaporated. Xia et al. [9,10] also investigated the factors influencing the capillary-assisted evaporation performance, such as the immersion depth, evaporation pressure, and superheating degree. Their experimental results showed that there was a positive correlation between the evaporation heat transfer coefficient and the evaporation pressure, and negative correlation for the superheating and immersion depth.

Wang et al. [11] developed a capillary-assisted evaporator for a silica gel-water ACS. The evaporators of two adsorption/desorption units were combined together by a heat-pipe heat exchanger. The exterior surface of the copper tubes in the upside of the heat exchanger was water-evaporating surface that was a porous medium to enhance the evaporating capability. They

concluded that the structure of the heat pipe evaporator was more complicated and heavier compared to the conventional evaporators. Chen et al. [12] used a capillary-assisted evaporator in the experimental study of a compact silica gel-water ACS. The evaporator consisted five trays and each tray contained nine copper tubes with outside micro-grooves. Capillary-assisted evaporation was employed in these evaporators based on Ref. [9,10]. They claimed they might achieve an evaporation heat transfer coefficient of about 5,000 W/m^2K.

Lanzerath et al. [13] studied the combination of finned tubes and thermal coating for capillary-assisted evaporation at low pressures. Their investigation showed a strong dependency of the evaporation heat transfer coefficient on the filling level. Their study also established that the combination of macroscopic fin structures and micro porous coatings led to further improvements and yielded evaporation heat transfer coefficient of 5,500 W/m^2K compared with ordinary plain tubes with the evaporation heat transfer coefficient of 500 W/m^2K.

High evaporation heat transfer coefficients (4,000-8,000 W/m^2K) can be achieved from capillary-assisted evaporation due to the water phase change on the outer surface of the tubes. To generate cooling, this heat has to be transferred from the chilled liquid water flowing inside the tube, to the tube wall, and finally, to the refrigerant. In this process, the main thermal resistance to heat transfer is due to the low chilled water heat transfer coefficient (compared with the evaporation heat transfer coefficient on the outer surface of the tube) because of no phase change. Since it is not possible to reach high heat transfer coefficient using a single-phase internal fluid, this study is focused on the overall heat transfer coefficient calculation of capillary-assisted evaporators. Five enhanced tubes with different fin geometries are tested under different operating temperatures and pressures to find the achievable cooling capacities and overall heat transfer coefficients, and to determine the most suitable tube for use in the LP

evaporator of an ACS. Also, a comprehensive parametric study is conducted on the selected tube under different refrigerant heights, dead volumes inside the evaporator, and chilled water flow rates.

2. Experimental details

The representation of capillary-assisted evaporation is shown in Figure 1. An evaporator tube with small fin spacing on its outside surface is in contact with a pool of liquid. Due to the capillary action, the liquid rises upward and covers the entire outside surface of the tube. Chilled liquid provided by a temperature control system (TCS) is circulated inside the tube and heat is transferred to the thin liquid film on the outside of the tube leading to evaporation.

(a) (b)

Figure 1. Capillary-assisted evaporation: (a) side view, and (b) cross-sectional view.

A capillary-assisted LP evaporator was designed and built in Laboratory for Alternative Energy Conversion (LAEC) as shown in Figure 2a. Evaporator tube consisted of a four-pass arrangement with a total length of 1.54 m. Capillary evaporation took place at the free surface of the tube helping to maintain the evaporation heat transfer rate as the water height decreases. The tube was placed horizontally at the bottom of the box to minimize the water height as shown in Figure 2b. Type T thermocouples (Omega, model #5SRTC-TT-T-36-36) with accuracy of 0.75% of reading, a pressure transducer with 0-34.5 kPa operating range (Omega, model #PX309-

005AI) and ±0.4 kPa accuracy and a positive displacement flow meter (FLOMEC, Model # OM015S001-222) with the accuracy of 0.5% of reading were used to monitor and record the temperature, pressure, and chilled water flow rate variations in the evaporator over time.

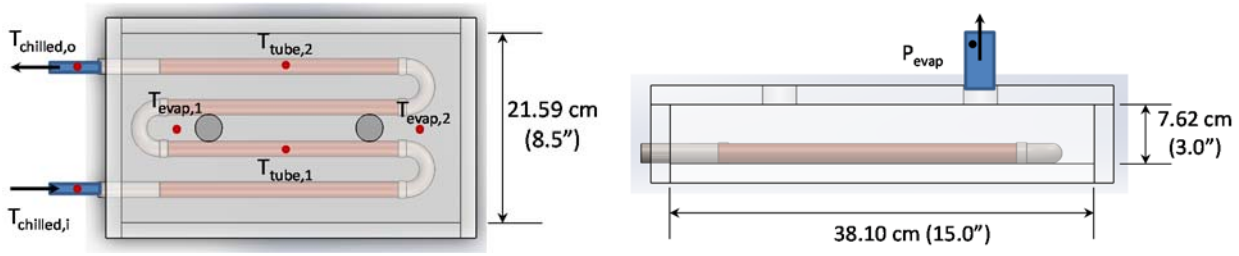

(a) (b)

Figure 2. Capillary-assisted evaporator built for testing different enhanced tubes: (a) top view, and (b) side view.

A schematic diagram of the experimental setup is shown in Figure 3a. The experimental test bed is designed to measure the cooling capacity and overall heat transfer coefficient of the evaporator. The setup consisted of a TCS and a variable speed pump to provide a constant temperature chilled water to the evaporator at different mass flow rates. Control valves are employed to regulate the pressure inside the evaporator. To protect the vacuum pump from the water vapor coming from the evaporator, a cold trap was installed before the vacuum pump to deposit (direct transition from gas to solid) water vapor. In the cold trap, a solution of dry ice and isopropyl alcohol (IPA) was used to produce cold temperature of -77°C. The vacuum pump and cold trap in this setup mimicked the adsorber bed of ACS. The actual test setup and custom-built heat exchanger with enhanced tube are shown in Figure 3b and c.

Once the evaporator was evacuated using the vacuum pump, the evaporator was filled with the makeup water (1,200 g) to immerse the evaporator tube in the water. When all the temperatures and pressure inside the evaporator became constant, the control valve was opened and adjusted

until the evaporator pressure reached the specific value given in Table 1. No water was added during the course of the experiment, so the water level dropped until all of the water in the chamber evaporated. The operating conditions during the experiments are summarized in Table 1.

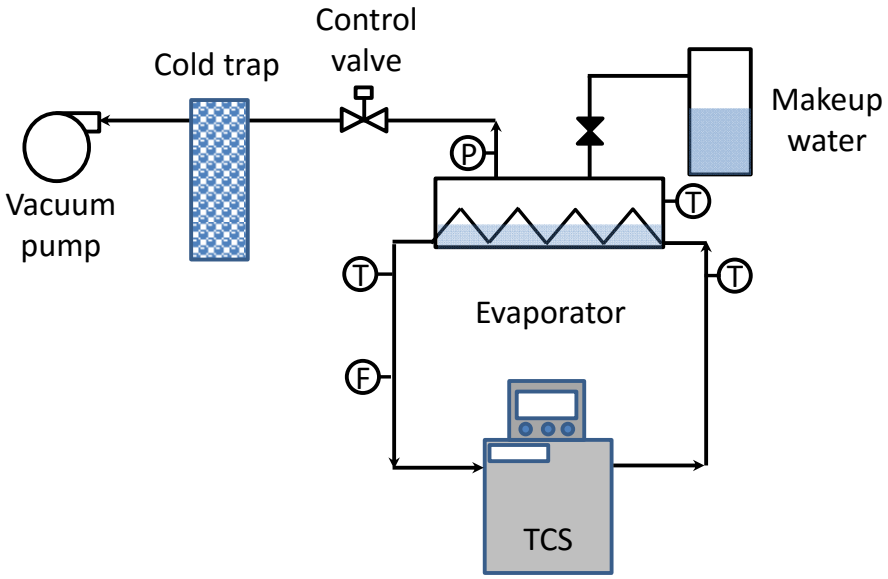

(a)

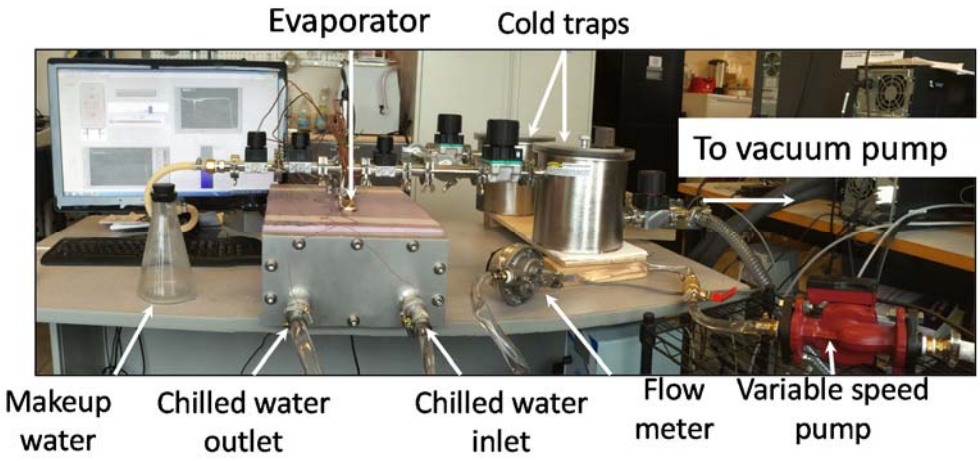

(b)

(c)

Figure 3. (a) Schematic of the LP evaporator experimental setup, (b) the actual experimental setup and the main components, and (c) custom-built heat exchangers prepared for the experiments.

Table 1. Base-case operating conditions for the experiments.

Parameter	Values
Chilled water inlet temperatures	10°C/ 15°C/ 20°C
Chilled water flow rate	2.4-2.7 kg/min
Evaporator pressure	0.5 kPa @ 10°C 0.6 kPa @ 15°C 0.8 kPa @ 20°C
Amount of water filled inside the evaporator for each experiment	1200 g

The tests are conducted for five types of enhanced heat transfer tubes with different fin structures and a plain tube as a benchmark as listed in Table 2.

Table 2. Geometric details of the enhanced tubes used for the experiments.

Tube name and details	Fin structure	5x zoom view
Turbo Chil-26 FPI (Wolverine Tube Inc.) Copper-Nickel Alloys OD: 3/4" (19.05 mm) Fin Height: 1.422 mm Min. wall under fins: 0.737 mm Inside surface area: 0.049 m^2/m Outside surface area: 0.193 m^2/m	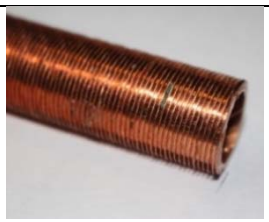	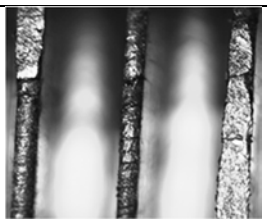
Turbo Chil-40 FPI (Wolverine Tube Inc.) Copper-Nickel Alloys OD: 3/4" (19.05 mm) Fin Height: 1.473 mm Min. wall under fins: 0.635 mm Inside surface area: 0.051 m^2/m Outside surface area: 0.263 m^2/m		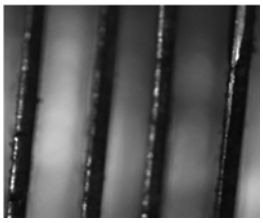
Turbo ELP (Wolverine Tube Inc.) Copper Alloys C12200 OD: 3/4" (19.05 mm) Min. wall under fins: 0.889 Inside surface area: 0.073 m^2/m Outside surface area: 194.8 m^2/m		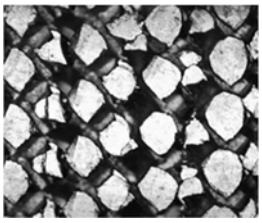
Turbo CLF-40 FPI (Wolverine Tube Inc.) Copper Alloys C12200 OD: 3/4" (19.05 mm) Fin Height: 0.965 mm Min. wall under fins: 0.787 mm Inside surface area: 0.0549 m^2/m Outside surface area: 0.2173 m^2/m		
GEWA-KS-40 FPI (Wieland Thermal Solutions) Copper Alloys C12200 OD: 3/4"(19.05 mm) Fin Height: 0.9 mm Min. wall under fins: 0.7 mm Inside surface area: 0.0489 m^2/m Outside surface area: 0.194 m^2/m		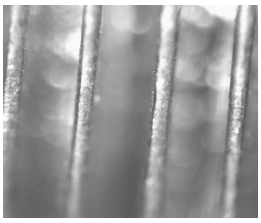
Plain Tube **Copper** OD: 3/4" (19.05 mm) Inside surface area: 0.0547 m^2/m Outside surface area: 0.0598 m^2/m	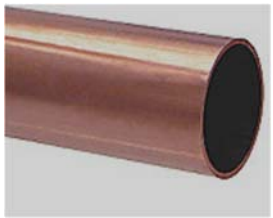	

3. Data analysis

The chilled water inlet and outlet temperatures, $T_{chilled,\,i}$ and $T_{chilled,\,o}$ as shown in Figure 2a, and mass flow rate as given in Table 1, are used to calculate the heat flow rate as follows:

$$\dot{q}_{evap}(W) = \dot{m}_{chilled}\, c_{p,cilled}\, (T_{chilled,i} - T_{chilled,o}) \tag{1}$$

The total evaporation rate is calculated by time averaging the heat flow rate given in Eq. (1):

$$\dot{Q}_{evap}(W) = \frac{\int_{t_1}^{t_2} \dot{q}_{evap}\, dt}{t_2 - t_1} \tag{2}$$

where t_1 and t_2 are the beginning and end of the time when the temperatures in the evaporator are constant. Finally, Eq. (3) gives the overall evaporator heat transfer conductance, $U_{evap} A_{evap}$:

$$U_{evap}\, A_{evap} = \frac{\dot{Q}_{evap}}{\Delta T_{LM,evap}} \tag{3}$$

where the logarithmic mean temperature difference between the chilled water circuit and the refrigerant is calculated by Eq. (4):

$$\Delta T_{LM,evap} = \frac{T_{chilled,i} - T_{chilled,o}}{\ln\left(\dfrac{T_{chilled,i} - T_{evap}}{T_{chilled,o} - T_{evap}}\right)} \tag{4}$$

where T_{evap} are the average evaporation temperatures of $T_{evap,1}$ and $T_{evap,2}$ as shown in Figure 2a. A_{evap} is chosen as the outside heat transfer surface area of the plain tube in order to having a reference (nominal) surface area for the calculation of U_{evap} for all tubes. The systematic uncertainty in the evaporator heat transfer rate calculation, Eq. (1), is:

$$\left(\frac{\delta \dot{q}_{evap}}{\dot{q}_{evap}}\right)_{systematic} = \sqrt{\left(\frac{\delta \dot{m}_{chilled}}{\dot{m}_{chilled}}\right)^2 + \left(\frac{\delta\left(T_{chilled,i} - T_{chilled,o}\right)}{T_{chilled,i} - T_{chilled,o}}\right)^2} \tag{5}$$

where,

$$\frac{\delta\left(T_{chilled,i} - T_{chilled,o}\right)}{T_{chilled,i} - T_{chilled,o}} = \sqrt{\left(\frac{\delta T_{chilled,i}}{T_{chilled,i}}\right)^2 + \left(\frac{\delta T_{chilled,o}}{T_{chilled,o}}\right)^2} = \sqrt{0.0075^2 + 0.0075^2} = 0.01 \tag{6}$$

Thus, the maximum systematic uncertainty in the calculation of evaporator heat transfer rate is:

$$\left(\frac{\delta \dot{q}_{evap}}{\dot{q}_{evap}}\right)_{systematic} \times 100 = \sqrt{0.005^2 + 0.01^2} = 1.1\% \tag{7}$$

Also, the standard deviation for $\dot{q}_{evap}$ due to the random uncertainty is 4.2%. Thus the maximum uncertainty of $\dot{q}_{evap}$ during the experiments is 5.3% (= 1.1% + 4.2%). Eq. (8) gives the systematic uncertainty of the evaporation heat transfer rate:

$$\left(\frac{\delta U_{evap}}{U_{evap}}\right)_{systematic} = \sqrt{\left(\frac{\delta \dot{Q}_{evap}}{\dot{Q}_{evap}}\right)_{systematic}^2 + \left(\frac{\delta \Delta T_{LM,evap}}{\Delta T_{LM,evap}}\right)^2} \tag{8}$$

where $\left(\frac{\delta \dot{Q}_{evap}}{\dot{Q}_{evap}}\right)_{systematic}$ and $\frac{\delta \Delta T_{LM,evap}}{\Delta T_{LM,evap}}$ are equal to 1.1% and 0.04%, respectively. Therefore, $\left(\frac{\delta U_{evap}}{U_{evap}}\right)_{systematic}$ is equal to 1.1% (≈ (1.1% + 0.04%). The random uncertainty in the measurement for U_{evap} over time is 7.4%. Thus, the maximum uncertainty in the calculation of evaporator heat transfer coefficient is 8.5% (= 1.1% + 7.4%).

4. Results and discussion

4.1. Base-case operating condition

Figure 4 shows the operating pressure and temperatures of evaporator with Turbo Chil-40 FPI at the constant chilled water inlet temperature of 15°C over time. In Figure 4a, it can be seen that the evaporator pressure reduces once the control valve is opened and remains constant until the evaporator runs out of water, at which time it drops to zero. The temperature data for the case of 15°C chilled water inlet are shown in Figure 4b. It can be seen in Figure 4b that all of the

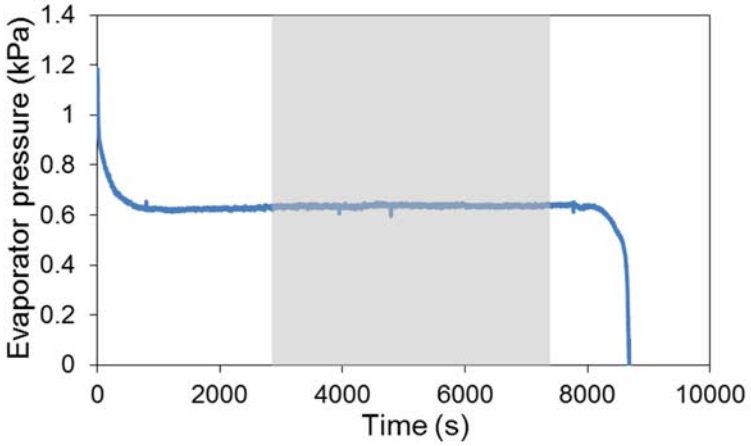

(a)

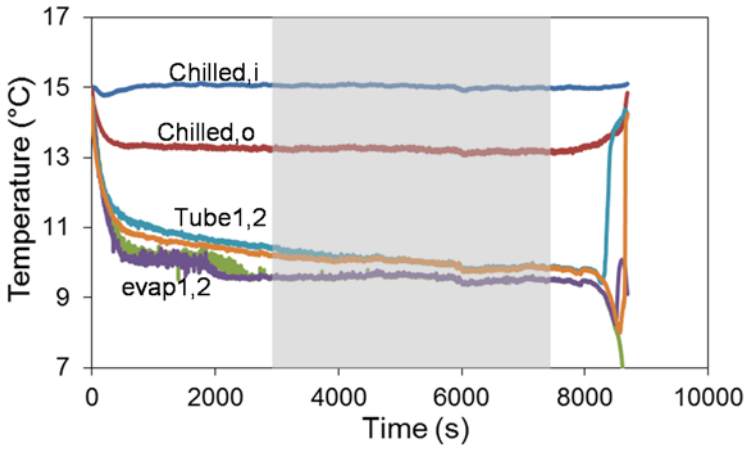

(b)

Figure 4. The behavior of evaporator with Turbo Chil-40 FPI at the chilled water inlet temperature of 15°C vs. time: (a) evaporator pressure and (b) temperature at different locations of evaporator.

thermocouples have the same reading at the beginning of the test (equilibrium state). After opening the control valve, the evaporation temperature is adjusted to the evaporation pressure. For calculation of the total evaporation heat transfer and the overall evaporator heat transfer coefficient, data are extracted from the steady state region demarcated in grey in Figure 4.

Figure 5 shows the effect of capillary phenomenon on the performance of an evaporator built with Turbo chil-40 FPI tube compared with the one built with the plain tube. As shown in Figure 5a and b, using Turbo chil-40 FPI tube results in an almost constant evaporation heat transfer rate and, consequently, constant evaporator heat transfer coefficient over time. Even as the height of the liquid water decreases, the capillary action covers the entire outside surface of the tube,

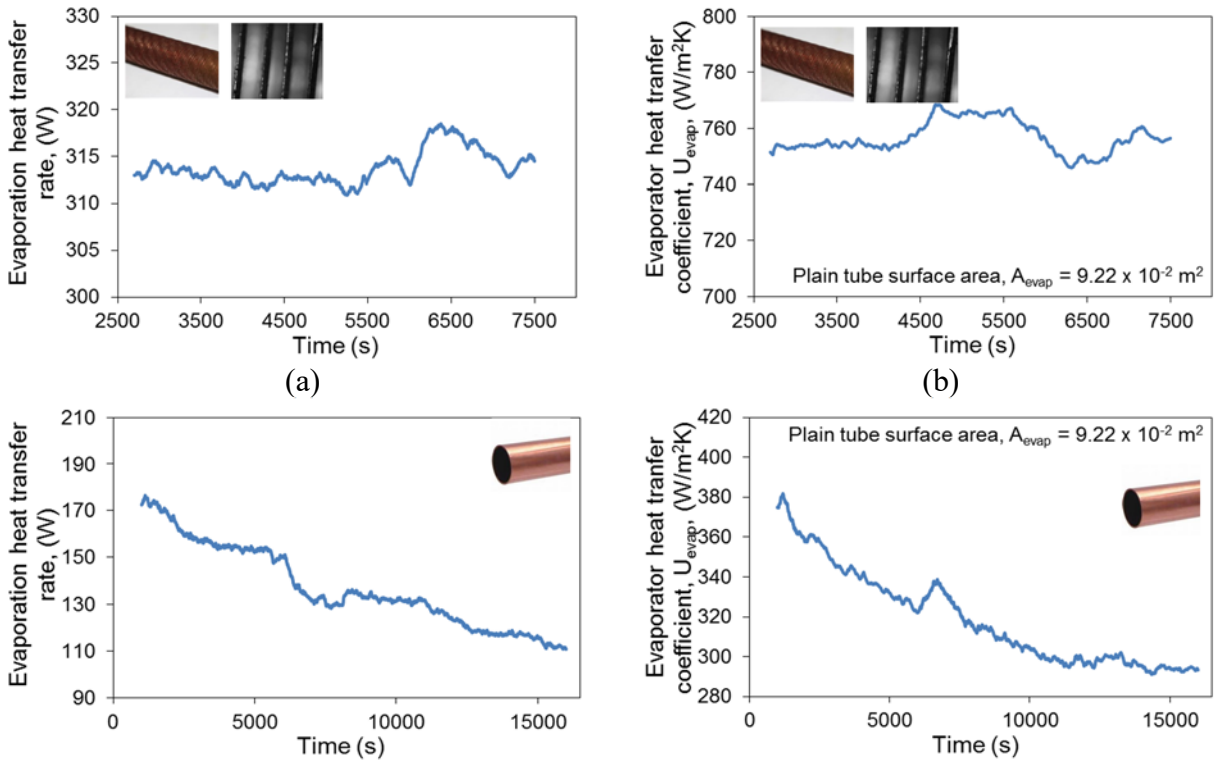

Figure 5. Effect of capillary phenomenon on the performance of the LP evaporator vs. time. Heat transfer rate and evaporator heat transfer coefficient achieved by using (a) and (b) Turbo chil-40 FPI tube, and (c) and (d) plain tube.

and the heat transfer rate and evaporator heat transfer coefficient are maintained. Figure 5c and d show that the plain tube fail to maintain the heat transfer rate and, consequently, the evaporator heat transfer coefficient drops as the height of the liquid water inside the evaporator drops.

To evaluate the performance of the tubes listed in Table 2, each tube was tested under the operating conditions summarized in Table 1. The performances of the enhanced tubes were compared to that of the plain tube at three different chilled water inlet temperatures of 10, 15, and 20°C. The chilled water mass flow rate was maintained constant at 2.4-2.7 kg/min. The total heat transfer rate and the overall evaporator heat transfer coefficient are shown in Figure 6. As shown in Figure 6a, the enhanced tubes result in an average heat transfer rate increase of 65%, 123%, and 96% compared to those of the plain tube at chilled water inlet temperatures of 10, 15, and 20°C, respectively. The Turbo Chil-40 FPI provides the highest total evaporation heat transfer rate of 422 W at the chilled water inlet temperature of 20°C, followed by Turbo Chil-26 FPI and Turbo ELP-42 FPI. To select the best enhanced tube, calculating the overall evaporator heat transfer coefficient is beneficial. Figure 6b depicts the overall evaporator heat transfer coefficient of the enhanced and plain tubes under different chilled water inlet temperatures. Figure 6b shows that the overall evaporator heat transfer coefficient as high as 596-888 W/m^2K can be achieved by using Turbo Chil-40 FPI under chilled water inlet temperatures of 10-20°C. While, for the plain tube, the overall evaporator heat transfer coefficient varies about 285-365 W/m^2K, which is 2-2.4 times lower than those of achieved by the Turbo Chil-40 FPI.

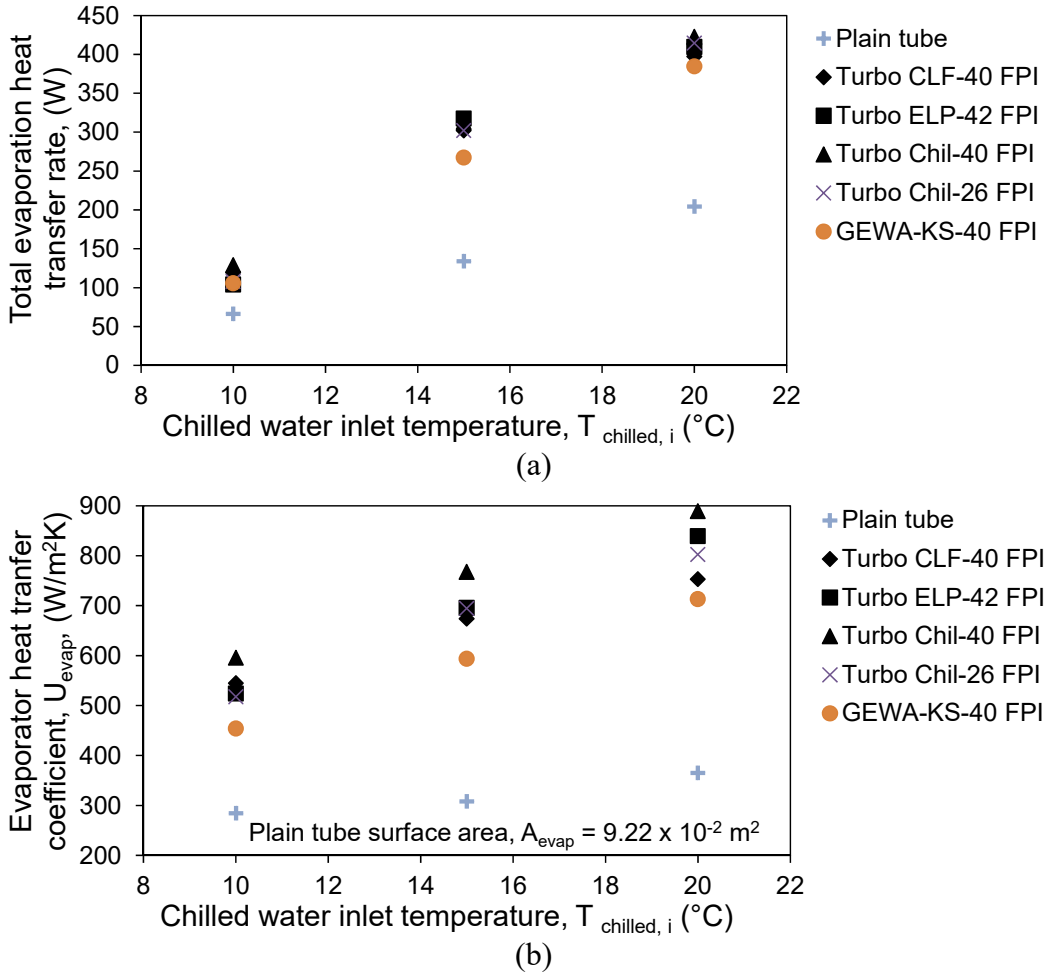

Figure 6. Effects of different enhanced tubes and a plain tube vs. different chilled water inlet temperatures on (a) the total evaporation heat transfer rate and (b) the evaporator heat transfer coefficient.

Comparing the evaporator heat transfer coefficients provided by the enhanced tubes, as shown in Figure 6b, and fin structures shown in Table 2 indicates that having continuous parallel fins, such as Turbo Chil-40 FPI and Turbo Chil-26 FPI, and high heat transfer surface area, such as Turbo ELP, are the two most important parameters in the design of capillary-assisted evaporators. Besides, comparing the results of Turbo Chil-26 FPI and GEWA-KS-40 FPI that have the same internal and external heat transfer surface area, and similar continuous parallel fins indicates that

Turbo Chil-26 FPI with lower fin density (26 to 40 FPI) has 13% higher evaporator heat transfer coefficient just because of having higher fin height (58%) as shown in Table 2. Thus, the main features of an enhanced tube designed for capillary-assisted evaporator are: i) continuous parallel fins, ii) high fin height, and iii) high heat transfer surface area. As a result, it can be concluded that the evaporator built with Turbo Chil-40 FPI for ACS provides the highest cooling power compared with the other enhanced tubes.

4.2. Parametric study

In this section, the effects of water height, dead volume inside the evaporator, and chilled water mass flow rate are studied on the performance of the evaporator built with Turbo Chil-40 FPI. Figure 7 shows the effect of water height on the performance of the evaporator. In this experiment, the evaporator was filled with exactly double the amount of water than the base-case condition (1,200 g) given in Table 1. Figure 7 shows the variations of evaporation heat transfer rate as a function of water height versus time at the chilled water inlet temperature and mass flow rate of 15°C and 2.53 kg/min, respectively. The evaporation heat transfer rate is divided into three regions: Region I (water height is higher than the tube diameter), Region II (transition region), and Region III (water height is lower than the tube diameter and the capillary evaporation is in effect). It can be seen in Figure 7 that when the water level is well above the height of the tube diameter (Region I), evaporation heat transfer rate is about 200 W. By evaporating the water inside the evaporator, the water level reduces until reaching the height of the tube diameter (Region II). In this region, the water level falls below the height of the tube diameter and evaporation heat transfer rate increases from 220 to 300 W/m^2K (36%) because of capillary evaporation. As the water level decreases the heat transfer rate remains high throughout Region III where the main portion of the evaporation is dominated by the capillary evaporation.

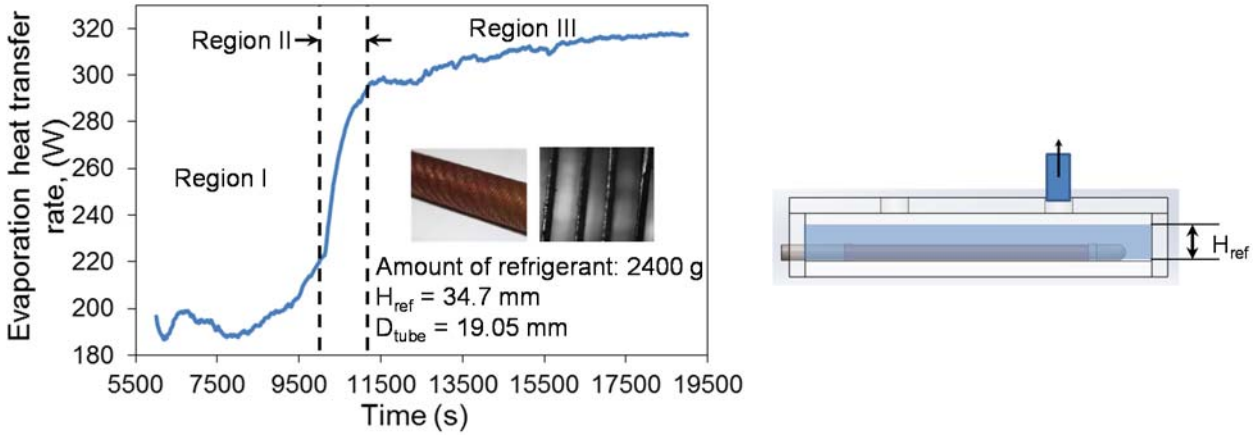

Figure 7. Effect of water height variation on the performance of capillary-assisted evaporator with Turbo Chil-40 FPI over time at chilled water inlet temperature and mass flow rate of 15°C and 2.53 kg/min. The other operating conditions are kept constant at the base-case operating conditions summarized in Table 1.

The effect of water non-dimensional height, H^*, inside the evaporator on the total evaporation heat transfer rate and evaporator heat transfer coefficient is shown in Figure 8. H^* represents the ratio of water (refrigerant) height to the tube diameter. Figure 8a shows that by increasing H^* from one to 1.8 (80%), the total evaporation heat transfer rate reduces by 25% from 313 W to 250 W. Accordingly, the evaporator heat transfer coefficient reduces by 33% as shown in Figure 8b.

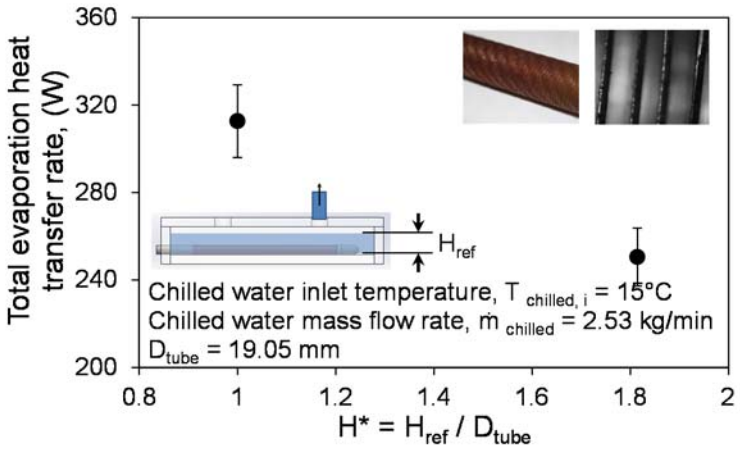

(a)

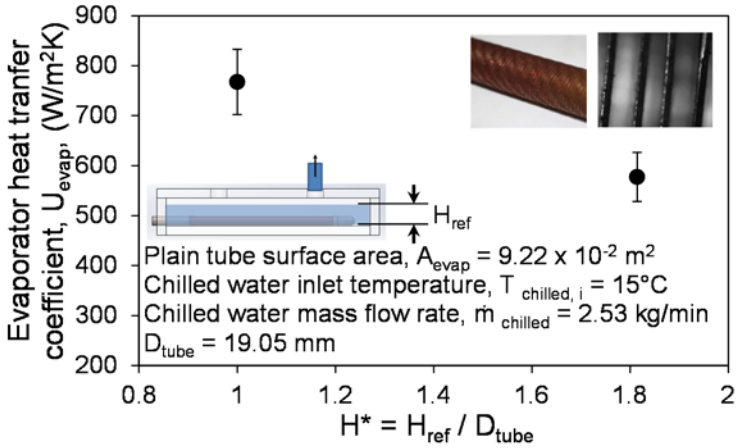

(b)

Figure 8. Effect of water non-dimensional height, H^*, on (a) total evaporation heat transfer rate and (b) evaporator heat transfer coefficient of capillary-assisted evaporator with Turbo Chil-40 FPI at chilled water inlet temperature and mass flow rate of 15°C and 2.53 kg/min. The other operating conditions are kept constant at the base-case operating conditions summarized in Table 1.

In order to estimate whether the dead volume inside the evaporator has any effect on the performance, the evaporator was tested by reducing the dead volume available above the enhanced tube. Figure 9 shows that by reducing the dead volume inside the evaporator up to 25%, the total evaporation heat transfer rate and evaporator heat transfer coefficient reduce by 2.3% and 10%, respectively, mainly because of increasing the mass transfer resistance in front of

water vapor leaving the evaporator. From this experiment, one can conclude that the dead volume available above the enhanced tube is not an important factor on the overall performance of the capillary-assisted evaporator.

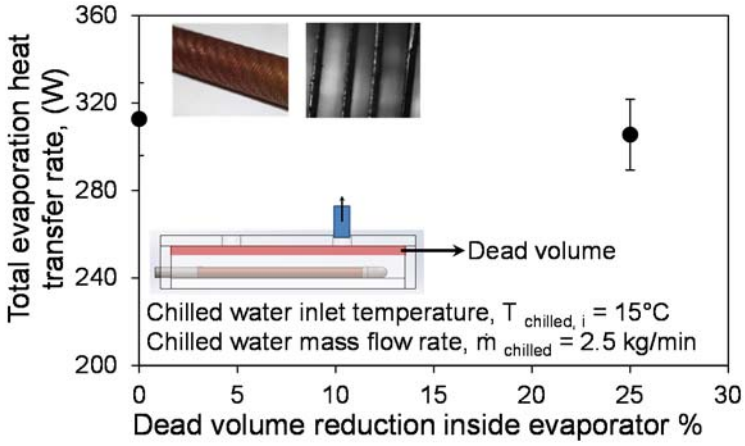

(a)

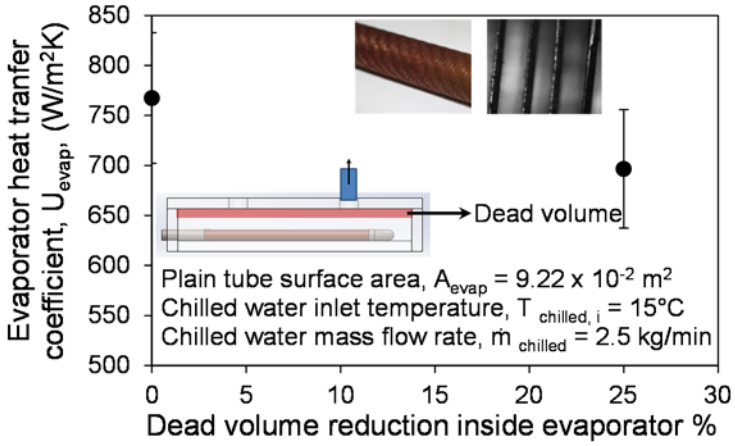

(b)

Figure 9. Effect of dead volume inside the evaporator on (a) total evaporation heat transfer rate and (b) evaporator heat transfer coefficient of capillary-assisted evaporator with Turbo Chil-40 FPI at chilled water inlet temperature and mass flow rate of 15°C and 2.5 kg/min. The other operating conditions are kept constant at the base-case operating conditions summarized in Table 1.

The heat transfer coefficient due to the capillary evaporation is about 4,000-8,000 W/m^{2}K [9,10]. However, transferring heat from the chilled water (single-phase heat transfer) inside the tube to

the refrigerant (heat transfer with phase-change) outside the tube is always limited by the heat transfer conductance of chilled water (UA). One way of increasing the evaporator heat transfer coefficient is to increase the chilled water flow rate inside the tube and, consequently, increase the heat transfer coefficient of chilled water. The effect of chilled water mass flow rate on the total evaporation heat transfer rate and evaporator heat transfer coefficient using the Turbo Chil-40 FPI tube is shown in Figure 10. It can be seen in Figure 10a that increasing the chilled water mass flow rate from 2.5 kg/min to 15.3 kg/min (6.1 times) increases the total evaporation heat transfer rate by 20% from 313 W to 373 W. Also, the evaporator heat transfer coefficient increases from 767 W/m^2K to 1,613 W/m^2K (2.1 times) by increasing the chilled water mass flow rate as shown in Figure 10b. However, higher chilled water mass flow rate causes higher water pump power consumption that should be considered in the design of capillary-assisted evaporators for an ACS installed in a vehicle A/C system.

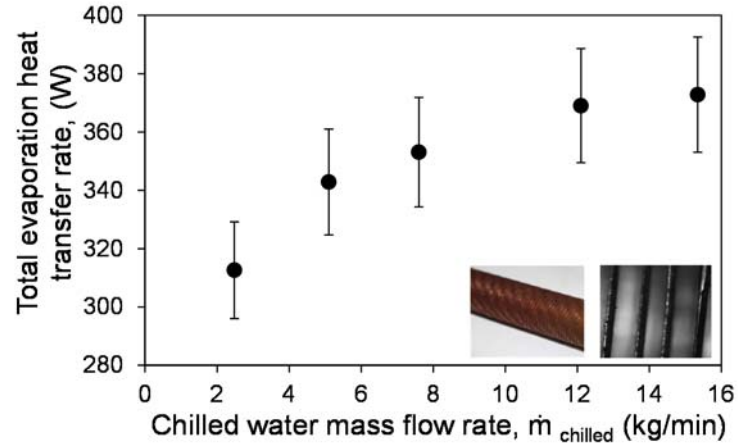

(a)

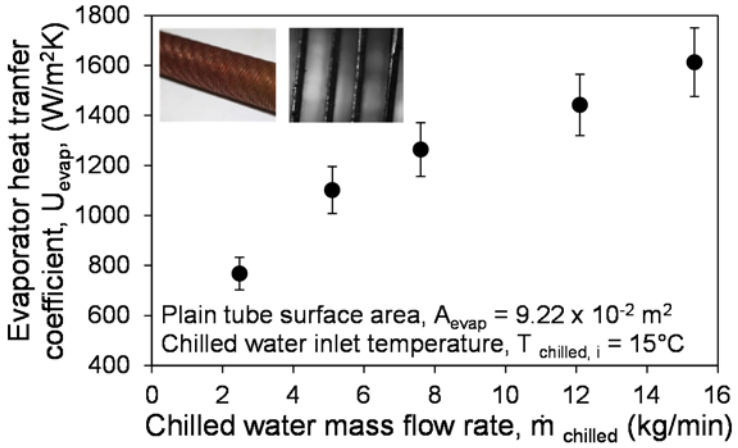

(b)

Figure 10. Effect of chilled water mass flow rate on (a) total evaporation heat transfer rate and (b) evaporator heat transfer coefficient of capillary-assisted evaporator with Turbo Chil-40 FPI at chilled water inlet temperature of 15°C. The other operating conditions are kept constant at the base-case operating conditions summarized in Table 1.

5. Conclusions

A flat LP evaporator with capillary-assisted tubes was proposed for the ACS with the applications to vehicle A/C system. The evaporator consisted of horizontal capillary-assisted tubes which were in contact with a pool of water while the pressure in the evaporator maintained between 0.5-0.8 kPa. In this study, the effects of five different enhanced tubes with various surface geometries and a plain tube on the total evaporation heat transfer rate and evaporator heat

transfer coefficient were experimentally investigated. The experimental results indicated that Turbo Chil-40 FPI took advantage of high capillary effect and, therefore, provided the highest evaporation heat transfer rate and evaporator heat transfer coefficient. The main findings of this study are summarized below:

- Turbo Chil-40 FPI showed the best performance under different operating conditions and was chosen for the evaporator of ACS.
- The main features of an enhanced tube designed for a capillary-assisted evaporator were continuous parallel fins, high fin height and high internal and external heat transfer surface area.
- Experimental data analyses indicated that the evaporator performance was limited by the heat transfer conductance of the chilled water flowing inside the tubes.
- Increasing the chilled water mass flow rate from 2.5 kg/min to 15.3 kg/min (6.1 times) increased the total evaporation heat transfer rate and evaporator heat transfer coefficient by 20% and 110%, respectively.
- Liquid water height in the evaporator had to be always less than the tube diameter.
- Dead volume available above the enhanced tubes was not an important factor on the overall performance of the capillary-assisted evaporator.

Acknowledgments

The authors gratefully acknowledge the financial support of the Natural Sciences and Engineering Research Council of Canada (NSERC) through the Automotive Partnership Canada Grant No. APCPJ 401826-10. Authors are thankful to Wolverine Tube Inc. and

Wieland Thermal Solutions for assisting our research by providing tube samples. Authors are also thankful to Mr. Ameer Ismail for his kind support in conducting the experiments in the laboratory.

Nomenclature

A	heat transfer surface area (m^2)
A/C	air conditioning
ACS	adsorption cooling system
c_p	heat capacity at constant pressure ($J/kg.K$)
ΔT_{LM}	log mean temperature difference (K)
FPI	fins per inch
ICE	internal combustion engine
$\dot{m}$	mass flow rate (kg/s)
P	pressure (Pa)
$\dot{Q}$	total heat transfer rate (W)
$\dot{q}$	heat transfer rate (W)
T	temperature ($°C$)
t	time (s)
U	overall heat transfer coefficient ($W/m^2.K$)
$VCRC$	vapor compression refrigeration cycle

Subscripts

chilled	chilled water
evap	evaporator
i	in
o	out

References

[1] Suzuki M. Application of adsorption cooling systems to automobiles. Heat Recover Syst CHP 1993;13:335–40.

[2] Abdullah MO, Tan IAW, Lim LS. Automobile adsorption air-conditioning system using oil palm biomass-based activated carbon: A review. Renew Sustain Energy Rev 2011;15:2061–72. doi:10.1016/j.rser.2011.01.012.

[3] Wang RZ, Wang L, Wu J. Adsorption Refrigeration Technology: Theory and Application. John Wiley & Sons; 2014.

[4] Ribatski G, Jacobi AM. Falling-film evaporation on horizontal tubes - A critical review. Int J Refrig 2005;28:635–53. doi:10.1016/j.ijrefrig.2004.12.002.

[5] Yang L, Shen S. Experimental study of falling film evaporation heat transfer outside horizontal tubes. Desalination 2008;220:654–60. doi:10.1016/j.desal.2007.02.046.

[6] Li W, Wu XY, Luo Z, Yao SC, Xu JL. Heat transfer characteristics of falling film evaporation on horizontal tube arrays. Int J Heat Mass Transf 2011;54:1986–93. doi:10.1016/j.ijheatmasstransfer.2010.12.031.

[7] Li W, Wu XY, Luo Z, Webb RL. Falling water film evaporation on newly-designed enhanced tube bundles. Int J Heat Mass Transf 2011;54:2990–7. doi:10.1016/j.ijheatmasstransfer.2011.02.052.

[8] Abed AM, Alghoul M a., Yazdi MH, Al-Shamani AN, Sopian K. The role of enhancement techniques on heat and mass transfer characteristics of shell and tube spray evaporator: a detailed review. Appl Therm Eng 2015;75:923–40. doi:10.1016/j.applthermaleng.2014.10.020.

[9] Xia ZZ, Yang GZ, Wang RZ. Experimental investigation of capillary-assisted evaporation on the outside surface of horizontal tubes. Int J Heat Mass Transf 2008;51:4047–54. doi:10.1016/j.ijheatmasstransfer.2007.11.042.

[10] Xia ZZ, Yang GZ, Wang RZ. Capillary-assisted flow and evaporation inside circumferential rectangular micro groove. Int J Heat Mass Transf 2009;52:952–61. doi:10.1016/j.ijheatmasstransfer.2008.05.041.

[11] Wang DC, Xia ZZ, Wu JY, Wang RZ, Zhai H, Dou WD. Study of a novel silica gel–water adsorption chiller. Part I. Design and performance prediction. Int J Refrig 2005;28:1073–83. doi:10.1016/j.ijrefrig.2005.03.001.

[12] Chen CJ, Wang RZ, Xia ZZ, Kiplagat JK, Lu ZS. Study on a compact silica gel–water adsorption chiller without vacuum valves: Design and experimental study. Appl Energy 2010;87:2673–81. doi:10.1016/j.apenergy.2010.03.022.

[13] Lanzerath F, Erdogan M, Schreiber H, Steinhilber M, Bardow A. Combination of finned tubes and thermal coating for high performance water evaporation in adsorption heat pumps. Int. Sorption Heat Pump, College Park, MD, USA: 2014, p. 1–10.

Appendix I.

Effects of adsorbent mass and number of adsorber beds on the performance of a waste-heat driven adsorption cooling system for vehicle air conditioning application

(submitted to the Energy journal)

Effects of adsorbent mass and number of adsorber beds on the performance of a waste heat-driven adsorption cooling system for vehicle air conditioning applications

Amir Sharafian, Seyyed Mahdi Nemati Mehr, Poovanna Cheppudira Thimmaiah, Wendell Huttema, Majid Bahrami*

Laboratory for Alternative Energy Conversion (*LAEC*), School of Mechatronic Systems Engineering, Simon Fraser University, BC, Canada V3T 0A3

Abstract

Waste heat-driven adsorption cooling systems (ACS) are potential replacements for vapor compression refrigeration cycles in vehicle air conditioning applications. However, the bulkiness and heavy weight of ACS are major challenges facing commercialization of these environmentally friendly systems. This study examines the importance of adsorbent mass and the number of adsorber beds on the specific cooling power (SCP) and coefficient of performance (COP) of a waste heat-driven FAM-Z02/water ACS under a variety of cycle times and operating conditions. The experimental results show that reducing the mass of FAM-Z02 from 1.9 to 0.5 kg in a one-adsorber bed ACS increases the SCP by 82% from 65.8 to 119.4 W/kg at cycle time of 20 min. However, the COP reduces by 37% because of the increase in the adsorber bed to adsorbent (dead to active) mass ratio. The results also show that the thermal mass of the evaporator limits the performance of the ACS, especially under short cycle times (8-20 min). To this end, a second adsorber bed is added to the one-adsorbed bed ACS testbed to generate continuous cooling in the evaporator. Comparing the performance of one- and two-adsorber bed

* Corresponding author: School of Mechatronic Systems Engineering, Simon Fraser University,
# 4300, 250-13450 102nd Avenue, Surrey, BC, Canada V3T0A3.
Tel.: +1 (778) 782-8538; Fax: +1 (778) 782-7514.
E-mail addresses: asharafi@sfu.ca (A. Sharafian), snematim@sfu.ca (S. Nemati Mehr), pthimmai@sfu.ca (P. Cheppudira Thimmaiah), wah@sfu.ca (W. Huttema), mbahrami@sfu.ca (M. Bahrami).

ACS packed with 0.5 kg of FAM-Z02 particles and cycle time of 20 min shows that the SCP and COP of the two-adsorber bed ACS increase by 28% and 47%, respectively.

Keywords: Adsorbent mass, FAM-Z02, adsorber bed, adsorption cooling system, vehicle air conditioning.

1. Introduction

Air conditioning and refrigeration (A/C-R) systems are responsible for using about 30% of the total worldwide energy produced [1]. In the automotive sector, A/C systems of light-duty vehicles consume about 40 billion liters of fuel per year in the U.S. alone [2]. A compressor of a vapor compression refrigeration cycle (VCRC) installed in a typical medium size sedan consumes up to 5-6 kW of the power generated by an internal combustion engine (ICE) to produce the required cooling. This power is sufficient for a 1200-kg sedan to cruise at 56 km/h [2]. Furthermore, about 70% of the total fuel energy released in an ICE is dissipated as a waste heat through the engine coolant and the exhaust gas [3]. Waste heat-driven adsorption cooling systems (ACS) are potential replacements for VCRCs that can significantly reduce fuel consumption and the environmental impacts of A/C systems where low-grade thermal energy is available.

A waste heat-driven ACS uses an adsorbate, such as water or methanol, which is adsorbed and desorbed from the surface of a porous adsorbent, such as zeolite, silica gel, or activated carbon. Most of these materials are non-toxic, non-corrosive, and inexpensive [4], making ACS a safe and environmentally friendly technology. An ACS operates more quietly than a VCRC and is easier to maintain because its only moving parts are valves [5]. However, current ACS have not been commercialized for light-duty vehicles due to their bulkiness and heavy weight. The main

challenges facing this technology are low specific cooling power (SCP = cooling energy / (adsorbent mass × cycle time)) and coefficient of performance (COP = cooling energy / input energy) that originate from the low thermal conductivity of adsorbent particles (~ 0.1 to 0.4 W/m.K) [6–9] and the low mass diffusivity of adsorbent-adsorbate pairs (~ 10^{-8} to 10^{-14} m^2/s) [7,10].

To overcome these obstacles, different composite adsorbent materials with high thermal conductivity and high adsorbate uptake capacity have been developed such as the ones reported in Refs. [11,12]. Besides using a proper adsorbent material, the designs of the adsorber beds, condenser, and evaporator (the main components of an ACS) can significantly affect the SCP and COP of the system. Sharafian and Bahrami [13] conducted a comprehensive literature review on the effects of nine different adsorber bed designs on the performance of an ACS designed for vehicle A/C applications. They identified the SCP, adsorber bed to adsorbent mass ratio (AAMR), and COP as the most influential parameters for evaluating the performance of an ACS. The COP was found to have a lower importance than the SCP and AAMR because the supplied waste heat for regeneration of the adsorber beds was abundant in a vehicle [13]. However, an ACS with a higher COP was preferred. The AAMR represents the dead to active mass ratio and should be minimized for vehicle A/C applications. Comparing more than 66 experiments with different adsorber bed designs reported in the literature showed that finned tube adsorber beds provided the best performance in comparison with other types of adsorber bed designs [13]. Table 1 provides further details on the performance of waste heat-driven ACS with different finned tube adsorber beds and working pairs.

Table 1. Performance analysis of different finned tube adsorber beds reported in the literature.

Ref. No.	Adsorber bed type and weight	Working pairs	COP	SCP (W/kg)	AAMR ($kg_{metal}/kg_{adsorbent}$)
[14–16]	Aluminum finned tube, 4.6 kg*	Consolidated activated carbon/ ammonia	0.06*	33*	5.75*
[17]	SS† finned tube	Silica gel/ methanol	-	30*	-
[18–20]	SS cylindrical double finned tube, 31 kg	Zeolite 13X/ water	0.38	22.8*	5
[21,22]	176-finned tubes, 260 kg	Zeolite 13X/ water	0.25	28.5	1.86
[23]	SS finned tube, 3.3 kg*	silica gel + $CaCl_2$(SWS-1L)/ water	0.43*	23.5*	3
[24]	2-bed Aluminum finned tube, 15 kg/bed	AQSOA FAM-Z02/ water	0.27*	131.5*	7.9
[25–27]	2-bed finned tube, 32.7 kg/bed	Silica gel/ water	0.43	48*	0.654
[28]	SS finned tube	Coated hydrophobic Y zeolite (CBV-901)/ methanol	0.11*	25*	3
[29]	2-bed finned tube	Silica gel/ water	0.29*	35*	-
[30–33]	2-bed finned tube	Act. carbon+$CaCl_2$ (1:4)/ ammonia	0.19*	70.8*	-
[34]	Aluminum finned tube, 6.08 kg	Silica gel + $CaCl_2$(SWS-1L)/ water	0.15	137*	3.47
[35]	Finned tube	Silica gel + $CaCl_2$/ water	0.23	43	-
[36,37]	2-bed Aluminum finned tube, 13.6 kg/bed*	Silica gel/ water	0.29	158*	4.53
[38–40]	Aluminum finned tube, 0.636 kg	$LiNO_3$-Silica KSK/ water	0.18*	318*	1.82
[41,42]	28 finned tube with 2.5 mm fin spacing	Silica gel + LiCl/ water	0.41	122	-
[43–45]	2-bed Aluminum finned tube	Silica gel + LiCl/ methanol	0.41	76.5	-
		Silica gel/water	0.42	122	
[46]	2-bed Aluminum finned tube, 3.22 kg/bed	AQSOA FAM-Z02/ water	0.45	330.2	1.4
[47,48]	8 tubes with Aluminum fins + steel pipes	Expanded graphite + $CaCl_2$/ ammonia	0.11	7.0	-
		Expanded graphite + $BaCl_2$/ ammonia			
[49]	Carbon steel finned tube, 115 kg	Expanded graphite + NaBr/ ammonia	0.35	296	20.9
[50]	4-bed SS shell and Aluminum finned tube	Silica gel/ water	0.31	46.5*	-
[51]	2-bed finned tube	Expanded graphite + $CaCl_2$/ ammonia	0.16	78.5	-
[52]	2-bed copper finned tube	Zeolite 13X + $CaCl_2$/ water	0.16	53	-

* These parameters are extracted based on the reported experimental data at $T_{hf,\,i}$ = 90°C, $T_{cf,\,i}$ = 30°C, $T_{coolant,\,i}$ = 30°C, and $T_{chilled,\,i}$ = 15°C. For zeolite 13X/water: $T_{hf,\,i}$ = 180°C.

† SS: Stainless steel

Of the studies cited in Table 1, those with finned tube adsorber beds packed or coated with composite salts in porous matrixes, such as expanded graphite + NaBr [49] and $LiNO_3$-Silica KSK [38–40], and those packed with silicoaluminophosphate AQSOA FAM-Z02 [46] had the highest SCP values. In a conceptual discussion on the optimal adsorbent for ACS applications, Aristov [12] highlighted the potential improvements in an ACS performance from using composite salts in porous matrixes, but leakage of salt solutions from the host matrixes during adsorption might cause corrosion of metal parts in an adsorber bed and, consequently, emission of non-condensable gases. Also, Okunev and Aristov [53] investigated the importance of adsorbent isobar shape on the SCP of an ACS. Their analysis indicated that with proper selection of an adsorbent material with respect to the operating conditions, the SCP could improve by a factor of 1.5 while other effective parameters, such as the adsorbent particle size, remained unchanged. AQSOA FAM-Z02 is one of the synthetic materials developed for A/C applications by Mitsubishi Chemical Ltd. [54]. It has an "S" shaped adsorption isotherm, as shown in Refs. [55–57], which provides quick water adsorption and desorption within a narrow pressure range. Also, FAM-Z02 showed high water vapor uptake capacity [55–58], low desorption temperature of 75-95°C, and high durability of 60,000 cycles [54] making it a good candidate for waste heat-driven ACS applications. Therefore, in this study, FAM-Z02 adsorbent is used to pack the adsorber beds.

Sharafian et al. [59] experimentally showed the effects of different finned tube adsorber bed designs packed with 2 mm FAM-Z02 particles with respect to their heat transfer surface area and fin spacing on in-situ water uptake rate measurements of FAM-Z02. The direct mass measurements showed that the adsorber bed with 2.8 m^2 heat transfer surface area and 2.5 mm fin spacing could increase the SCP and COP of the ACS by 3.1 and 2.9 times, respectively, in

comparison with the adsorber bed with 0.235 m^2 heat transfer surface area and 8.5 mm fin spacing. Following these results, in this study, the adsorber bed with high heat transfer surface area and small fin spacing was installed in our ACS testbed to study the effects of the amount of adsorbent material and the number of adsorber beds on the SCP and COP of ACS when the other components of the cycle, namely, the condenser, evaporator and expansion valve, remained unchanged. Also, detailed parametric study was performed to investigate the effects of cycle time and operating conditions on the SCP and COP of ACS.

2. ACS thermodynamic cycle

The thermodynamic cycle of an ACS is comprised of two main steps: heating-desorption-condensation and cooling-adsorption-evaporation. An ACS with one adsorber bed generates evaporative cooling power intermittently. To produce a continuous cooling power, two or more adsorber beds are required. Figure 1a depicts a schematic of a typical two-adsorber bed ACS comprised of two adsorber beds, a condenser, an expansion valve, and an evaporator.

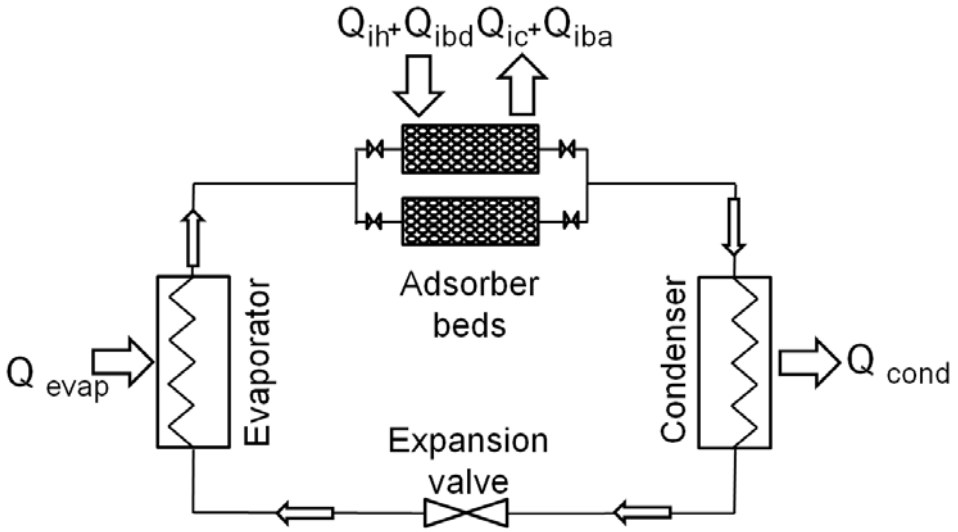

(a)

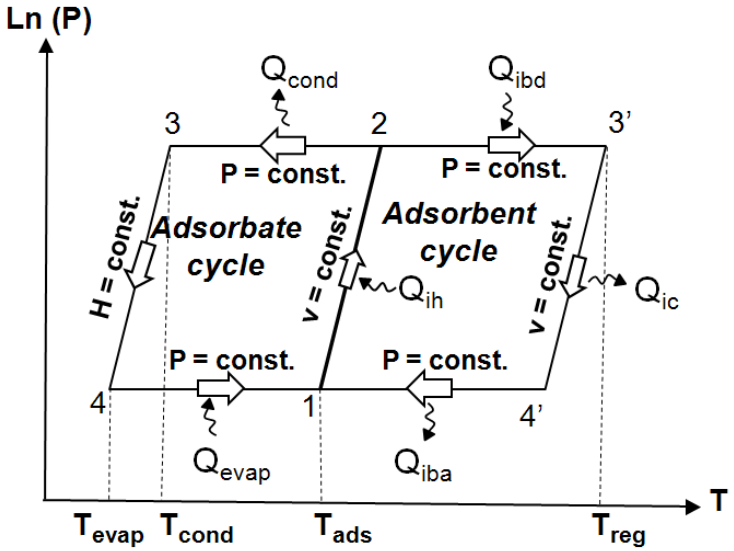

(b)

Figure 1. (a) Schematic and (b) thermodynamic cycle of a two-adsorber bed ACS [60].

Figure 1b shows the thermodynamic processes in an ACS which is divided into two subcycles: (i) an adsorbent cycle (on the right side), and (ii) an adsorbate cycle (on the left side). As shown in Figure 1b, the adsorbent cycle includes four steps: (1) isosteric heating (ih); process 1-2, (2) isobaric desorption (ibd); process 2-3', (3) isosteric cooling (ic); process 3'-4', and (4) isobaric adsorption (iba); process 4'-1. Isosteric processes occur at a constant specific volume and

isobaric processes occur at a constant pressure. The adsorbate cycle shown in Figure 1b includes three steps: (1) isobaric condensation in the condenser; process 2-3, (2) isenthalpic process in the expansion valve; process 3-4, and (3) isobaric evaporation in the evaporator; process 4-1.

During step 1-2, the adsorbent-adsorbate pair absorbs heat of Q_{ih} from an external heat source in an isosteric heating process. In this step, the pressure of the adsorber bed increases due to the adsorbate desorption from the adsorbent particles. This process is continued until the pressure of the adsorber bed reaches the pressure of the condenser and then the inlet valve to the condenser is opened. In step 2-3', the external heat source continuously heats the adsorber bed (Q_{ibd}) during an isobaric desorption process, the adsorbate leaves the adsorber bed, and is condensed inside the condenser through an isobaric condensation process (step 2-3). The total heat transfer to the adsorber bed, $Q_{total\,heating}$, during a desorption process is the sum of Q_{ih} and Q_{ibd}. Upon reaching point 3', the maximum temperature of the adsorber bed at the end of desorption time, the valve between the adsorber bed and the condenser is closed and during an isosteric cooling process (step 3'-4'), the temperature of the adsorbent is reduced by dissipating the heat of Q_{ic} to a heat sink. In step 3-4, the adsorbate inside the condenser passes through the expansion valve and enters to the evaporator. During step 4-1, the adsorbate absorbs the heat of Q_{evap} from the environment of interest and evaporates. At the same time, the valve between the evaporator and the adsorber bed is opened and the adsorbent adsorbs the vaporous adsorbate through an isobaric adsorption process (step 4'-1) and releases heat of Q_{iba}. This process continues until reaching the end of adsorption time. The total heat removed from the adsorber bed, $Q_{total\,cooling}$, during an adsorption process is the sum of Q_{ic} and Q_{iba}. The cycle time is the sum of desorption and adsorption times.

3. Experimental testbed

An ACS with one or two adsorber beds made up of more than sixty different components was built in the lab. Figure 2a shows a schematic of the two-adsorber bed ACS including heating and cooling circuits connected to the adsorber beds. The system was built modular to enable future modifications. The ACS was equipped with four temperature control systems (TCS) or thermal baths to control the adsorption and desorption temperatures in the adsorber beds, and the condensation and evaporation temperatures in the condenser and evaporator, respectively. Four check valves (V1-V4) with low cracking pressure were installed before and after the adsorber beds to control the adsorption and desorption processes, and eight two-way solenoid valves (V5-V12) were installed on the TCS_{HF} and TCS_{CF} to intermittently heat up and cool down adsorber beds 1 and 2 as shown in Figure 2a. Further information about the valves and their arrangement can be found in Ref. [61].

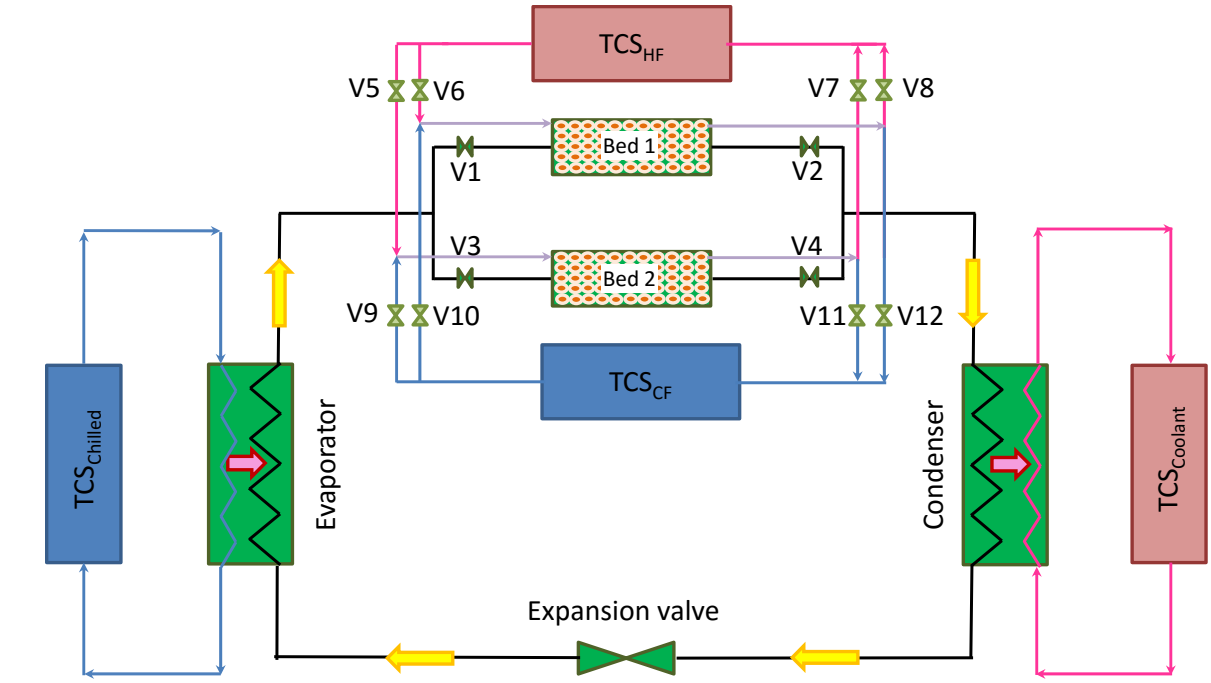

(a)

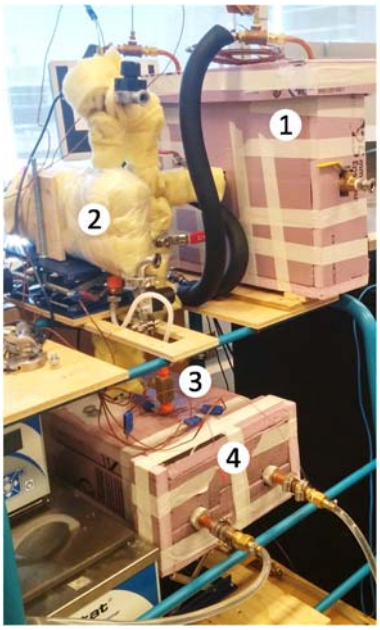

(b)

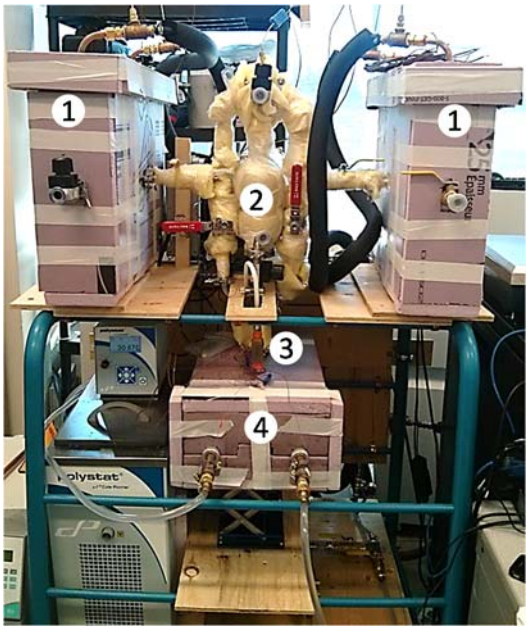

(c)

(d)

Figure 2. (a) Schematic of the two-adsorber bed ACS, (b) the one- and (c) two-adsorber bed ACS experimental testbeds, and (d) FAM-Z02 adsorbent particles packed between fins of the adsorber bed. Numbers in (b) and (c): 1- adsorber bed(s), 2-condenser, 3-expansion valve, and 4-evaporator.

Figure 2b and Figure 2c show the one- and two-adsorber bed ACS testbeds including the main components. A copper shell-and-tube heat exchanger with helical fins on the outer surface of the tubes was used as the condenser. A needle valve with high precision flow adjustment was used as the expansion valve and a low-operating pressure evaporator with capillary-assisted tubes was designed and installed on the cycle. Type T thermocouples (Omega, model #5SRTC-TT-T-36-36) with accuracy of 0.75% of reading and pressure transducers with 0-34.5 kPa operating range (Omega, model #PX309-005AI) and 0.4 kPa accuracy were installed to monitor and record the temperature and pressure variations in each component of the ACS over time. Positive displacement flow meters (FLOMEC, Model # OM015S001-222) with accuracy of 0.5% of reading were installed on the adsorber beds to measure the heating and cooling fluid flow rates. Similar flow meters were also installed on the condenser and evaporator to measure the coolant and chilled water flow rates, respectively. The heat transfer fluid used in the TCSs for heating and cooling of the adsorber beds was silicone oil (Julabo Inc., Thermal P60) that had a density change from 909 kg/m^3 at 30°C to 854 kg/m^3 at 90°C. Further details about the ACS testbed and operating conditions are summarized in Table 2.

Table 2. Specifications and operating conditions of the ACS built for this study.

Parameter	**One-bed ACS**	**Two-bed ACS**
Working pair	AQSOA FAM-Z02/water	
Adsorbent particles diameter (mm)	2	
Mass of adsorbent per adsorber bed (kg)	1.9/ 1.0/ 0.5	0.5
Adsorber bed heat transfer surface area, A_{bed}, (m^2)	2.80/ 1.47/ 0.74	0.74
Metal mass of adsorber bed (kg)	2.87	
Adsorber bed fin spacing (mm)	2.54	
Adsorber bed fin dimensions (cm)	43.18×30.48 (17"×12")	
Heating fluid mass flow rate to adsorber bed (kg/s)	0.058 (4.1 L/min of silicone oil)	
Cooling fluid mass flow rate to adsorber bed (kg/s)	0.062 (4.1 L/min of silicone oil)	
Heat capacity of heating and cooling fluids (kJ/kg.K)	1.8	
Condenser heat transfer surface area, A_{cond}, (m^2)	2.0	
Coolant water mass flow rate to condenser (kg/s)	0.052 (3.1 L/min)	
Evaporator heat transfer surface area, A_{evap}, (m^2)	0.405	
Chilled water mass flow rate to evaporator (kg/s)	0.037 (2.2 L/min)	
Heating fluid inlet temperature to adsorber bed (°C)	90	
Cooling fluid inlet temperature to adsorber bed (°C)	30	
Coolant water inlet temperature to condenser (°C)	30	
Chilled water inlet temperature to evaporator (°C)	15	
Cycle time (min)	20	

Water was used in the ACS as the refrigerant (adsorbate) and, as a result, the ACS operated under vacuum pressure. To produce enough cooling inside the evaporator, the design of evaporator was different from the conventional evaporator designs [62]. A capillary-assisted evaporator was designed and installed on the system [63], as shown in Figure 3. Further geometric details of the capillary-assisted evaporator are provided in Table 3.

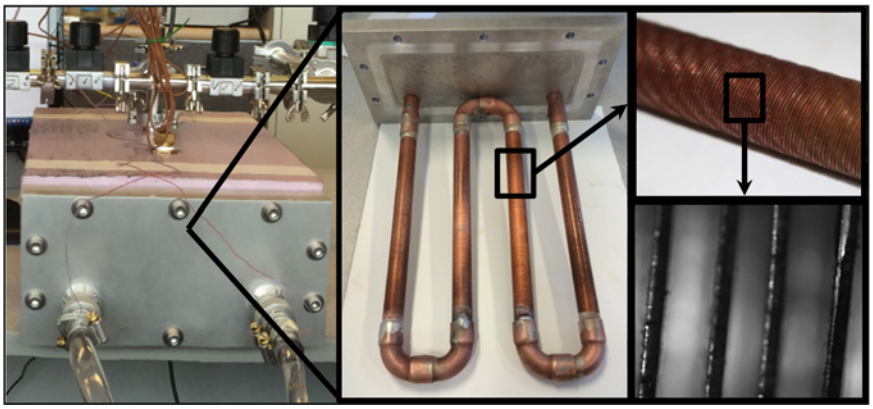

Figure 3. Capillary-assisted evaporator designed by Thimmaiah et al. [63].

Table 3. Geometric details of the capillary-assisted evaporator [63].

Parameter	**Value**
Tube model	Turbo Chil-40 FPI (Wolverine Tube Inc.)
Outer diameter (mm)	19.05 (3/4”)
Fin Height (mm)	1.473
Min. wall under fins (mm)	0.635
Inside surface area (m^2/m)	0.051
Outside surface area (m^2/m)	0.263
Tube length (m)	1.54

Before running the experiments, the adsorber beds packed with the FAM-Z02 were heated using a 90°C heating fluid for 8 hours and simultaneously evacuated to completely dry the FAM-Z02 out. The heating and cooling fluid inlet temperatures to the adsorber beds, and the coolant and chilled water inlet temperatures to the condenser and evaporator were set at temperatures given in Table 2. By setting the cycle time, water was adsorbed and desorbed by FAM-Z02 particles packed in the adsorber beds, and condensation and evaporation occurred inside the condenser and evaporator, respectively. An experiment at constant operating conditions was performed continuously until the dynamic behavior of the ACS became consistent. At this stage, the

thermodynamic cycle of ACS was repeated three more times to ensure the reproducibility of the collected data.

4. Data Analysis

To evaluate the performance of an ACS, the COP and SCP of the system should be calculated. Equation (1) gives the total evaporative cooling energy during an adsorption process:

$$Q_{evap}(J) = \int_{adsorption} \dot{m}_{chilled} c_{p,chilled} \left(T_{chilled,i} - T_{chilled,o}\right) dt \tag{1}$$

where $\dot{m}_{chilled}$ and $c_{p,chilled}$ are the chilled water mass flow rate and heat capacity, and $T_{chilled,i} - T_{chilled,o}$ is the temperature difference between the chilled water inlet and outlet temperatures. The total condensation energy is calculated as follows:

$$Q_{cond}(J) = \int_{desorption} \dot{m}_{coolant} c_{p,coolant} \left(T_{coolant,i} - T_{coolant,o}\right) dt \tag{2}$$

where $\dot{m}_{coolant}$ is the coolant water mass flow rate and $T_{coolant,i} - T_{coolant,o}$ is the temperature difference between the coolant water inlet and outlet temperatures. The total heat transfers to the adsorber beds during an adsorption or desorption process are calculated by:

$$Q_{total\ cooling}(J) = \int_{adsorption} \dot{m}_{cf} c_{p,cf} \left(T_{cf,i} - T_{cf,o}\right) dt \tag{3}$$

$$Q_{total\ heating}(J) = \int_{desorption} \dot{m}_{hf} c_{p,hf} \left(T_{hf,i} - T_{hf,o}\right) dt \tag{4}$$

where $\dot{m}_{cf}$ and $\dot{m}_{hf}$ are the cooling and heating fluid mass flow rates, and $T_{cf,i} - T_{cf,o}$ and $T_{hf,i}$ - $T_{hf,o}$ are the temperature differences between the cooling and heating fluid inlet and outlet

temperatures, respectively. Using Eqs. (1) and (4), the COP and SCP of an ACS during one cycle are determined by:

$$COP = \frac{Q_{evap}}{Q_{total\ heating}} \tag{5}$$

$$SCP\,(W/kg) = \frac{Q_{evap}}{m_{adsorbent}\,\tau_{cycle}} \tag{6}$$

where $m_{adsorbent}$ in Eq. (6) is the mass of dry adsorbent packed inside an adsorber bed and τ_{cycle} is the cycle time (sum of adsorption and desorption times). The maximum uncertainties in the calculations of COP and SCP were 13% and 11%, respectively (see the Appendix).

5. Results and discussion

5.1. Effects of adsorbent mass on the performance of a one-adsorber bed ACS

The one-adsorber bed ACS was packed with three different amounts of FAM-Z02 (1.9, 1.0, and 0.5 kg). The adsorber bed packed with more adsorbent mass creates higher suction and discharge pressures during adsorption and desorption, respectively. However, the evaporator and condenser should be able to supply sufficient evaporation and condensation rates, respectively. In the case of a mismatch between these components, the overall performance of ACS is affected.

Figure 4 shows the temperature and pressure variations inside the one-adsorber bed ACS packed with 1.0 kg of FAM-Z02 at cycle time of 20 min. It can be seen that the dynamic behavior of ACS is consistent for three continuous cycles and, as a result, the performance of the system is reproducible. During adsorption, uptake of the vapor by the adsorbent material lowers the adsorber bed pressure, P_{bed}, to less than the evaporator pressure, $P_{evap.}$ During this process,

marked “Ads.” in Figure 4, the adsorber bed temperature is maintained by the cooling fluid that dissipates the heat of adsorption. Due to the suction pressure created by the adsorber bed, evaporation happens inside the evaporator, heat is transferred from the chilled water to the adsorbate, and the chilled water temperature reduces at the outlet of the evaporator, $T_{chilled,\,o}$, as shown in Figure 4a. In a desorption process, the adsorber bed is heated, as shown in the region demarcated “Des.” in Figure 4, and the adsorber bed pressure, P_{bed}, increases, as shown in Figure 4b. Due to the pressure gradient between the adsorber bed and the condenser, the adsorbate desorbed from the FAM-Z02 flows to the condenser. Condensation happens inside the condenser and heat of condensation is transferred from the adsorbate to the coolant water. Therefore, the coolant water outlet temperature, $T_{coolant,\,o}$, increases as shown in Figure 4a.

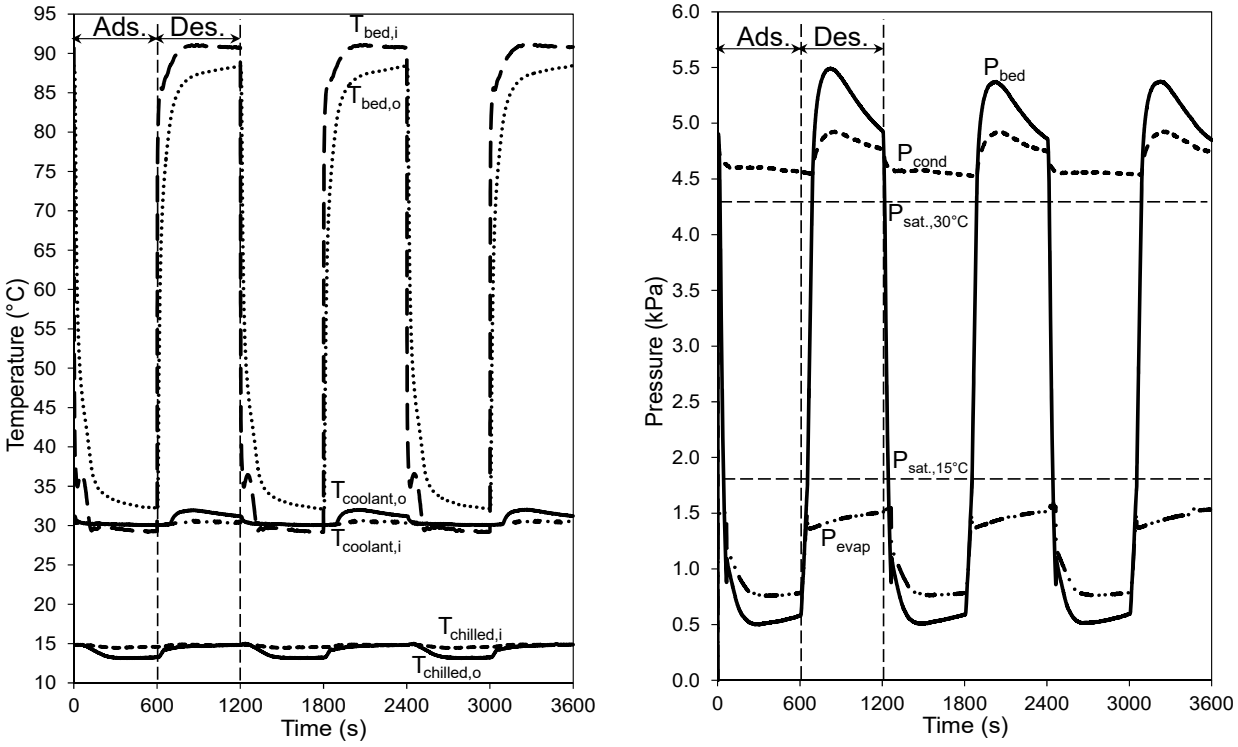

(a) (b)

Figure 4. Temperature and pressure variations in different components of the ACS for 1.0 kg of FAM-Z02 and cycle time of 20 min (other operating conditions are as given in Table 2).

The 206-260 Pa pressure difference between the adsorber bed and the evaporator during adsorption shown in Figure 4b indicates that the adsorbate evaporation rate in the evaporator is not sufficient to supply enough water vapor to the FAM-Z02 packed in the adsorber bed. The mismatch between the water uptake rate of FAM-Z02 and the water evaporation rate inside the evaporator significantly affect the SCP and COP of the system. Figure 5 shows the effects of different adsorber bed loads of FAM-Z02 (0.5, 1.0, 1.9 kg) on the SCP and COP of the one-adsorber bed ACS under different cycle times. It can be seen in Figure 5 that lowering the amount of FAM-Z02 increases the SCP of the system, while it lowers the COP. Increasing the SCP of the ACS by decreasing the mass of the FAM-Z02 from 1.9 to 0.5 kg under a constant cycle time indicates the enough vaporous adsorbate supply to the FAM-Z02 during adsorption. However, the COP of ACS decreases by decreasing the mass of FAM-Z02 under a constant cycle time because the AAMR increases from 1.5 to 5.7 kg $_{\text{metal}}$ / kg $_{\text{dry adsorbent}}$.

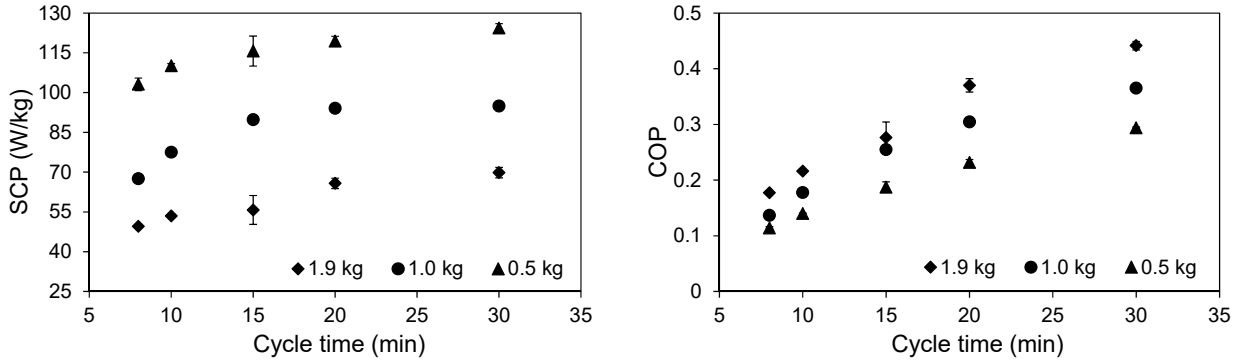

(a) (b)

Figure 5. Variations in SCP and COP of the one-adsorber bed ACS packed with different amounts of FAM-Z02 vs. cycle time (Other operating conditions are as given in Table 2).

Lambert and Jones [64] reported that the total daily commute time in the U.S. was about 40 min, ≈ 20 min to work and ≈ 20 min returning home. Therefore, the cycle time of 20 min was selected

for further analysis of the performance of the one-adsorber bed ACS. Effects of heating and cooling fluid inlet temperatures to the adsorbed bed on the SCP and COP of ACS are shown in Figure 6. It can be seen in Figure 6a and Figure 6b that by increasing the heating fluid inlet temperature from 70 to 90°C, the SCP and COP of the system increase. As shown in Figure 6a, at a heating fluid inlet temperature of 70°C, the adsorber bed with 1.9 kg of FAM-Z02 provides the SCP of 38.7 W/kg which is 45% higher than that with 0.5 kg of FAM-Z02. At the heating inlet temperatures of 80 and 90°C, however, the SCPs of ACS with 0.5 kg of FAM-Z02 are 78.8 and 119 W/kg which are 15% and 82% higher than those packed with 1.9 kg of FAM-Z02,

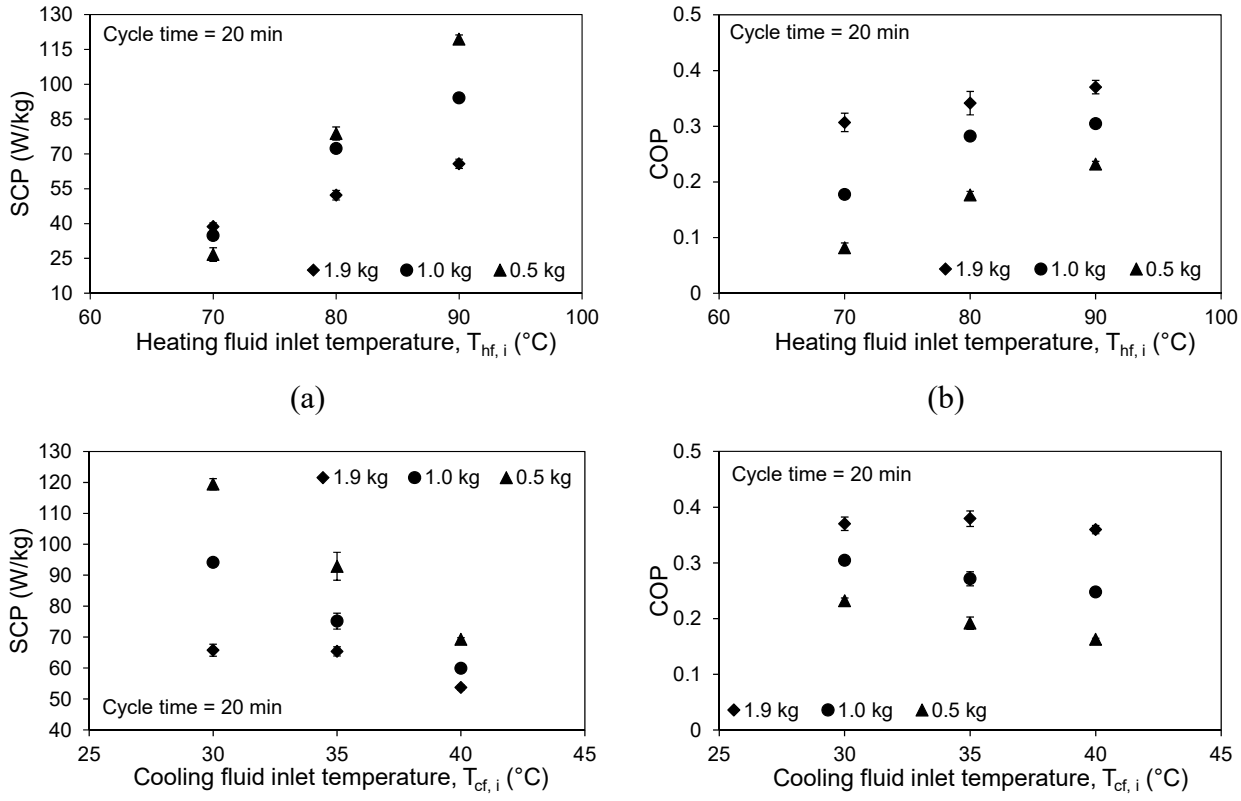

Figure 6. Variations in SCP and COP of the one-adsorber bed ACS packed with different amounts of FAM-Z02 vs. heating and cooling fluid inlet temperatures entering to the adsorber bed (Other operating conditions are as given in Table 2).

respectively. Such a behavior is not observed in the COP of the ACS, as shown in Figure 6b. At a constant heating fluid inlet temperature, the COP decreases by decreasing the mass of FAM-Z02 from 1.9 to 0.5 kg because of the increase in the AAMR.

Increasing the cooling fluid inlet temperature to the adsorber bed reduces the SCP and COP of the ACS for all three masses of FAM-Z02 as shown in Figure 6c and Figure 6d. The results also show that at a specific cooling fluid inlet temperature, increasing the mass of FAM-Z02 decreases the SCP and increases the COP of ACS. Finally, Figure 6 indicates that the performance of ACS packed with FAM-Z02 is more sensitive to the heating fluid inlet temperature (desorption temperature) rather than the cooling fluid inlet temperature (adsorption temperature).

Increasing the coolant water inlet temperature to the condenser decreases the rate of adsorbate condensation inside the condenser and therefore reduces the SCP and COP of the system as shown in Figure 7a and Figure 7b. The FAM-Z02 is only partially dried out under these cycle conditions. Increasing the mass of FAM-Z02 at a constant coolant water inlet temperature causes the SCP to decrease and the COP to increase.

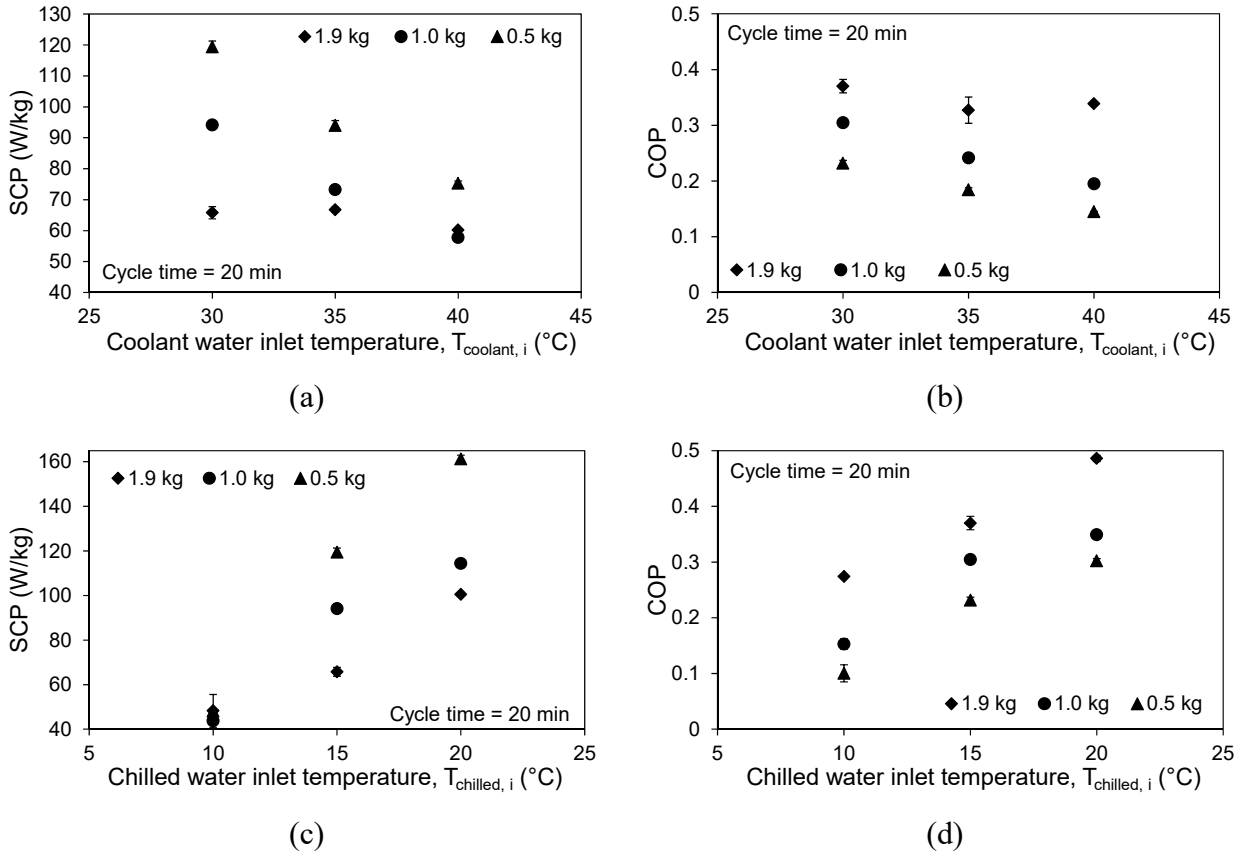

Figure 7. Variations in SCP and COP of the one-adsorber bed ACS packed with different amounts of FAM-Z02 vs. coolant and chilled water inlet temperatures entering to the condenser and evaporator (Other operating conditions are as given in Table 2).

Increasing the chilled water inlet temperature to the evaporator increases the water evaporation rate and the evaporator pressure, and consequently, more adsorbate is supplied to the FAM-Z02 within a constant adsorption time. As shown in Figure 7c and Figure 7d, increasing the chilled water inlet temperature increases the SCP and COP of ACS. Further, the SCP of the ACS increases and the COP decreases when the mass of FAM-Z02 reduces from 1.9 to 0.5 kg. As discussed in Section 1, the SCP of an ACS designed for vehicle A/C applications is more important than the COP as the waste heat available from an ICE is abundant. As a result, the adsorber bed packed with 0.5 kg of FAM-Z02 is considered for the next set of experiments.

5.2. Effects of the number of adsorber beds on the performance of an ACS

One of the limitations of the one-adsorber bed ACS was intermittent cooling power generation in the evaporator, especially for short cycle times, when the thermal mass of the evaporator became important. The thermal mass of the evaporator in an ACS postpones the heat transfer from the chilled water to the adsorbate inside the evaporator. Multi-adsorber bed systems produce continuous cooling in the evaporator. However, increasing the number of adsorber beds adds to the overall mass and complexity of the ACS. Knowing these limitations, a second adsorber bed was added to the one-adsorber bed ACS and its performance was studied and compared against that of the one-adsorber bed ACS.

The coolant and chilled water temperature variations in the one- and two-adsorber bed ACS packed with 0.5 kg of FAM-Z02 and cycle time of 20 min are shown in Figure 8. The regions demarcated on the chilled water temperatures in Figure 8 indicate that the chilled water outlet temperature in the two-adsorber bed ACS is more uniform than that in the one-adsorber bed ACS and does not reach to the chilled water inlet temperature because of continuous evaporation inside the evaporator. Therefore, the effect of thermal mass of the evaporator becomes less important to the performance of ACS especially for short cycle times.

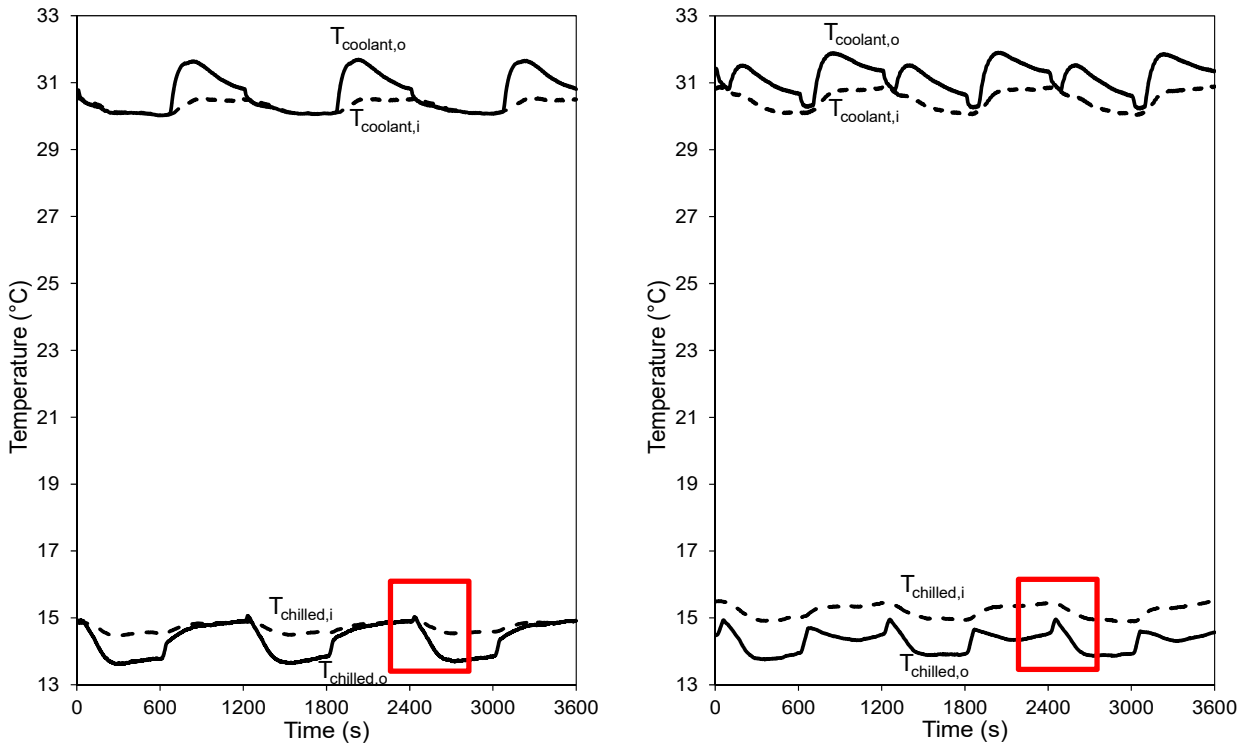

Figure 8. Coolant and chilled water inlet and outlet temperature variations in (a) the one-adsorber bed ACS and (b) the two-adsorber bed ACS packed with 0.5 kg of FAM-Z02 and cycle time of 20 min (Other operating conditions are as given in Table 2).

The effects of one- and two-adsorber bed ACS on the SCP under different cycle times are shown in Figure 9a. The SCP of one-adsorber bed ACS increases continuously as the cycle time increases from 8 to 30 min. However, the SCP of two-adsorber bed ACS peaks at 152.5 W/kg for a cycle time of 20 min before decreasing to 132.0 W/kg for a cycle time of 30 min. Figure 9a indicates that the two-adsorber bed ACS resulted in higher SCPs under short cycle times (8-20 min). By increasing the cycle time from 20 to 30 min, the effect of thermal mass of evaporator becomes less important and the SCP of two-adsorber bed ACS drops.

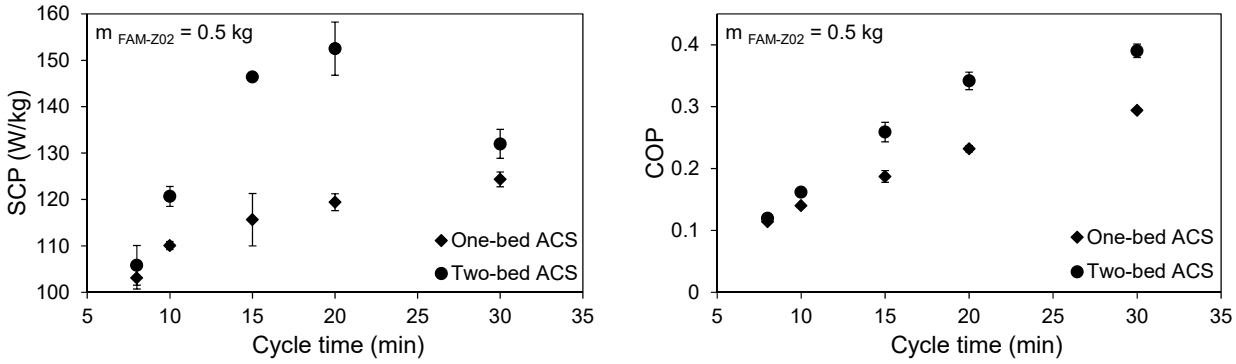

(a) (b)

Figure 9. Variations in SCP and COP of the one- and two-adsorber bed ACS packed with 0.5 kg of FAM-Z02 vs. cycle time (Other operating conditions are as given in Table 2).

The COP of the two-adsorber bed ACS is higher than that of one-adsorber bed ACS as shown in Figure 9b. At a cycle time of 8 min, the COPs of one- and two-adsorber bed ACS are 0.11 and 0.12, respectively. At a cycle time of 20 min, the COP of two-adsorber bed ACS in comparison with that of one-adsorber bed ACS increases by 47% from 0.23 to 0.34. The highest COP, 0.39, is observed for the two-adsorber bed ACS operated with the 30 min cycle time. However, considering both the SCP and COP, the two-adsorber bed ACS has the best performance at cycle time of 20 min.

Figure 10 shows the effects of heating and cooling fluid inlet temperatures to the adsorber beds on the performance of the one- and two-adsorber bed ACS packed with 0.5 kg of FAM-Z02 and operated with a 20 min cycle time. Figure 10 shows that, at constant heating and cooling fluid inlet temperatures, the SCP and COP increase by replacing the one-adsorber bed ACS with the two-adsorber bed ACS. At heating fluid inlet temperature of 70°C, shown in Figure 10a and Figure 10b, the SCP and COP of two-adsorber bed ACS are equal to 52.6 W/kg and 0.17 which are 98% and 105% higher than those of the one-adsorber bed ACS. Similarly, Figure 10c and

Figure 10d show that at cooling fluid inlet temperature of 40°C, the SCP and COP of two-adsorber bed ACS are 51% and 47% higher than those of one-adsorber bed ACS. For vehicle A/C applications, Figure 10 indicates that the two-adsorber bed ACS has better performance than the one-adsorber bed ACS specifically at low heating fluid inlet temperatures (70°C) and high cooling fluid inlet temperatures (40°C).

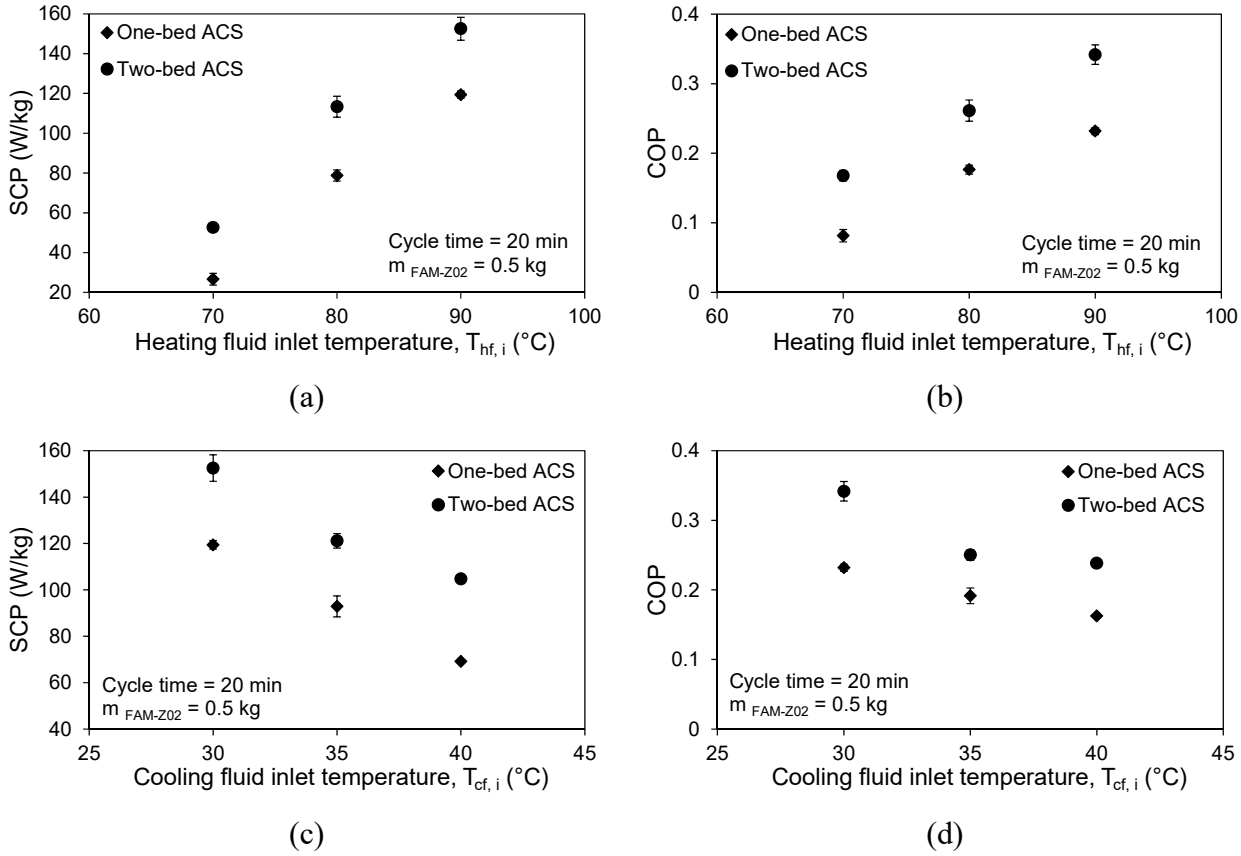

Figure 10. Variations in SCP and COP of the one- and two-adsorber bed ACS packed with 0.5 kg of FAM-Z02 vs. (a, b) heating and (c, d) cooling fluid inlet temperatures entering to the adsorber beds (Other operating conditions are as given in Table 2).

The effects of coolant and chilled water inlet temperatures to the condenser and evaporator on the SCP and COP of one- and two-adsorber bed ACS are shown in Figure 11. It can be seen in Figure 11a and Figure 11b that increasing the coolant water inlet temperature from 30 to 40°C,

decreases the SCP and COP of ACS because of the reduce in the adsorbate condensation rate during desorption. Also, Figure 11a and Figure 11b display that the SCP and COP of two-adsorber bed ACS is always higher than those of one-adsorber bed ACS under different coolant water inlet temperatures to the condenser.

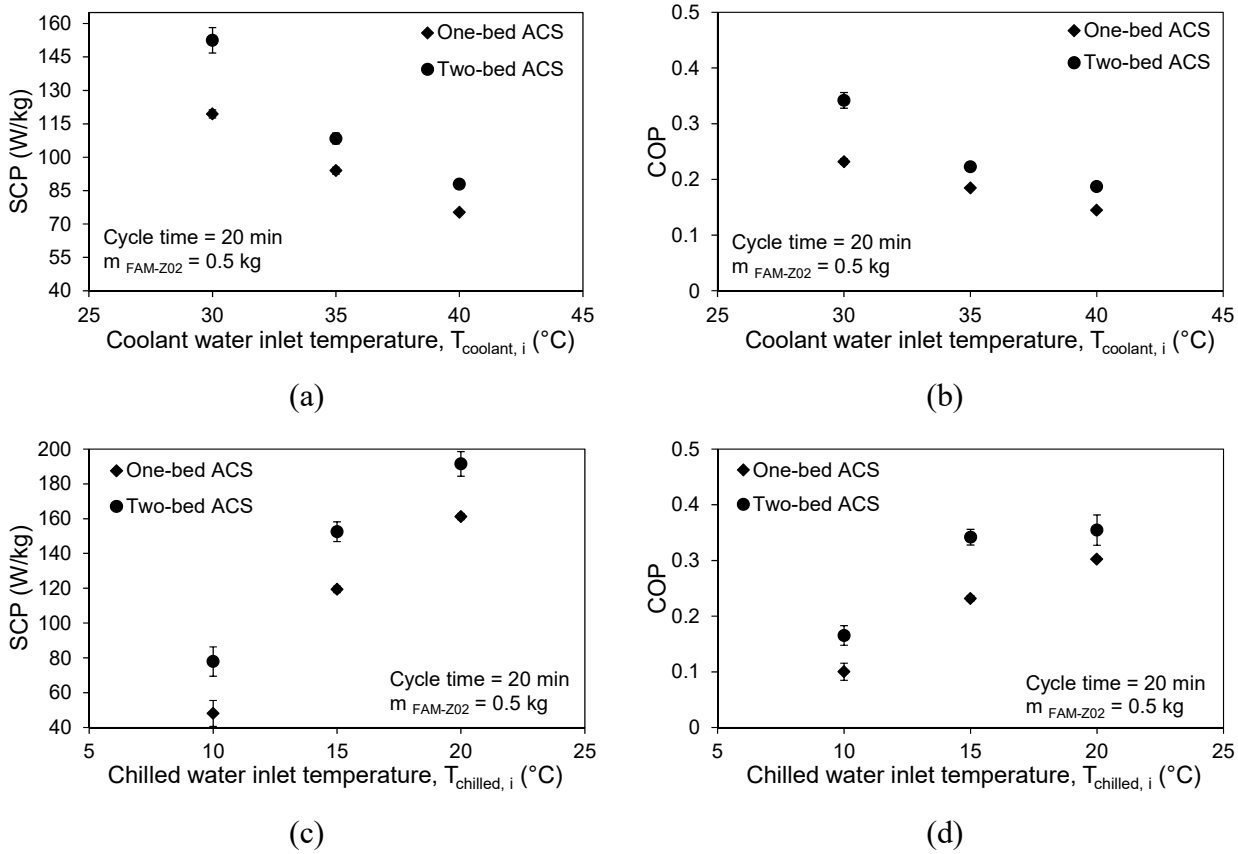

Figure 11. Variations in SCP and COP of the one- and two-adsorber bed ACS packed with 0.5 kg of FAM-Z02 vs. (a, b) coolant and (c, d) chilled water inlet temperatures entering to the condenser and evaporator (Other operating conditions are as given in Table 2).

Figure 11c and Figure 11d show that the SCP and COP of ACS increase with increasing the chilled water inlet temperature to the evaporator. The SCP and COP of two-adsorber bed ACS increase from 78 W/kg and 0.17 at 10°C to 191.5 W/kg and 0.35 at 20°C. Similar to previous

cases, the SCP and COP of the two-adsorber bed ACS are always higher than those of one-adsorber bed ACS.

6. Conclusion

In this study, the effects of adsorbent mass and the number of adsorber beds on the SCP and COP of ACS were investigated. A comprehensive parametric study was performed to investigate the variations of SCP and COP of ACS under different cycle times and operating conditions. Three different amounts of FAM-Z02 were packed in the one-adsorber bed ACS. The results showed that reducing the mass of FAM-Z02 from 1.9 to 0.5 kg increased the SCP of the ACS while the COP decreased due to the increase in the AAMR. Also, the results showed that the thermal mass of the evaporator reduced the SCP and COP of ACS under short cycle times (8-20 min). Addition of the second adsorber bed to the one-adsorber bed ACS indicated that the SCP and COP increased by 28% and 47% at cycle time of 20 min. Also, the results showed that the SCP and COP of the two-adsorber bed ACS were always higher than those of the one-adsorber bed ACS due to the reduction in the effects of the thermal mass of the evaporator especially at short cycle times. Finally, from this study, it could be concluded that for vehicle A/C applications, the mass of adsorbent should be optimized to reach the highest performance of the ACS and reduce the overall of mass of the system.

Acknowledgment

The authors gratefully acknowledge the financial support of the Natural Sciences and Engineering Research Council of Canada (NSERC) through the Automotive Partnership Canada Grant No. APCPJ 401826-10.

Appendix

The systematic uncertainty in the evaporative cooling energy calculations, Eq. (1), is:

$$\left(\frac{\delta Q_{evap}}{Q_{evap}}\right)_{systematic} = \sqrt{\left(\frac{\delta \dot{m}_{chilled}}{\dot{m}_{chilled}}\right)^2 + \left(\frac{\delta\left(T_{chilled,i} - T_{chilled,o}\right)}{T_{chilled,i} - T_{chilled,o}}\right)^2} \tag{7}$$

where,

$$\frac{\delta\left(T_{chilled,i} - T_{chilled,o}\right)}{T_{chilled,i} - T_{chilled,o}} = \sqrt{\left(\frac{\delta T_{chilled,i}}{T_{chilled,i}}\right)^2 + \left(\frac{\delta T_{chilled,o}}{T_{chilled,o}}\right)^2} = \sqrt{0.0075^2 + 0.0075^2} = 0.01 \tag{8}$$

Therefore, the maximum systematic uncertainty in the calculation of evaporative cooling energy is:

$$\left(\frac{\delta Q_{evap}}{Q_{evap}}\right)_{systematic} \times 100 = \sqrt{0.005^2 + 0.01^2} \times 100 = 1\% \tag{9}$$

Also, the maximum standard deviation for Q_{evap} due to the random uncertainties in the experiments was 10%. As a result, the maximum uncertainty in the calculation of Q_{evap} during the experiments was 11% (1% + 10%). Similarly, the maximum uncertainty in the calculation of $Q_{total\ heating}$ was 7% (= 1% + 6%). Therefore, the maximum uncertainties in the calculations of COP and SCP were as follows:

$$\frac{\delta COP}{COP} \times 100 = \sqrt{\left(\frac{\delta Q_{evap}}{Q_{evap}}\right)^2 + \left(\frac{\delta Q_{total\ heating}}{Q_{total\ heating}}\right)^2} \times 100 = \sqrt{0.11^2 + 0.07^2} \times 100 = 13\% \tag{10}$$

$$\frac{\delta SCP}{SCP}\times 100 = \sqrt{\left(\frac{\delta Q_{evap}}{Q_{evap}}\right)^2 + \left(\frac{\delta m_{adsorbent}}{m_{adsorbent}}\right)^2 + \left(\frac{\delta \tau_{cycle}}{\tau_{cycle}}\right)^2}\times 100$$
$$= \sqrt{0.11^2 + \left(\frac{1}{500}\right)^2 + \left(\frac{1}{1800}\right)^2}\times 100 = 11\% \quad (11)$$

Nomenclature

A	heat transfer surface area (m^2)
AAMR	adsorber bed to adsorbent mass ratio ($kg_{\ metal}$ / $kg_{\ dry\ adsorbent}$)
Ads.	adsorption
c_p	heat capacity at constant pressure ($J/kg.K$)
COP	coefficient of performance
Des.	desorption
m	mass (kg)
$\dot{m}$	mass flow rate (kg/s)
P	pressure (kPa)
Q	heat transfer (J)
SCP	specific cooling power ($W/kg_{\ dry\ adsorbent}$)
T	temperature (K)
t	time (s)
τ_{cycle}	cycle time (s)

Subscripts

adsorbate	adsorbate
adsorbent	adsorbent particles
bed	adsorber bed
cf	cooling fluid
chilled	chilled water
cond	condenser
coolant	coolant water
evap	evaporator
hf	heating fluid
i	in
o	out
sat.	saturation

References

[1] Buzelin LOS, Amico SC, Vargas JVC, Parise JAR. Experimental development of an intelligent refrigeration system. Int J Refrig 2005;28:165–75. doi:10.1016/j.ijrefrig.2004.08.013.

[2] Farrington R, Rugh J. Impact of vehicle air-conditioning on fuel economy, tailpipe emissions, and electric vehicle range. Proceeding Earth Technol. Forum, Washington, D.C.: 2000.

[3] Suzuki M. Application of adsorption cooling systems to automobiles. Heat Recover Syst CHP 1993;13:335–40.

[4] Abdullah MO, Tan IAW, Lim LS. Automobile adsorption air-conditioning system using oil palm biomass-based activated carbon: A review. Renew Sustain Energy Rev 2011;15:2061–72. doi:10.1016/j.rser.2011.01.012.

[5] Demir H, Mobedi M, Ülkü S. A review on adsorption heat pump: Problems and solutions. Renew Sustain Energy Rev 2008;12:2381–403. doi:10.1016/j.rser.2007.06.005.

[6] Poyelle F, Guilleminot JJ, Meunier F. Experimental tests and predictive model of an adsorptive air conditioning unit. Ind Eng Chem Res 1999;38:298–309. doi:10.1021/ie9802008.

[7] Tamainot-Telto Z, Critoph RE. Monolithic carbon for sorption refrigeration and heat pump applications. Appl Therm Eng 2001;21:37–52. doi:10.1016/S1359-4311(00)00030-2.

[8] Freni A, Tokarev MM, Restuccia G, Okunev AG, Aristov YI. Thermal conductivity of selective water sorbents under the working conditions of a sorption chiller. Appl Therm Eng 2002;22:1631–42. doi:10.1016/S1359-4311(02)00076-5.

[9] Sharafian A, Fayazmanesh K, McCague C, Bahrami M. Thermal conductivity and contact resistance of mesoporous silica gel adsorbents bound with polyvinylpyrrolidone in contact with a metallic substrate for adsorption cooling system applications. Int J Heat Mass Transf 2014;79:64–71. doi:10.1016/j.ijheatmasstransfer.2014.07.086.

[10] Sharafian A, Bahrami M. Adsorbate uptake and mass diffusivity of working pairs in adsorption cooling systems. Int J Heat Mass Transf 2013;59:262–71. doi:10.1016/j.ijheatmasstransfer.2012.12.019.

[11] Askalany AA, Salem M, Ismael IM, Ali AHH, Morsy MG, Saha BB. An overview on adsorption pairs for cooling. Renew Sustain Energy Rev 2013;19:565–72. doi:10.1016/j.rser.2012.11.037.

[12] Aristov Y. Concept of adsorbent optimal for adsorptive cooling/heating. Appl Therm Eng 2014;72:166–75. doi:10.1016/j.applthermaleng.2014.04.077.

[13] Sharafian A, Bahrami M. Assessment of adsorber bed designs in waste-heat driven adsorption cooling systems for vehicle air conditioning and refrigeration. Renew Sustain Energy Rev 2014;30:440–51. doi:10.1016/j.rser.2013.10.031.

[14] Critoph RE. Towards a one tonne per day solar ice maker. Renew Energy 1996;9:626–31. doi:10.1016/0960-1481(96)88366-2.

[15] Tamainot-Telto Z, Critoph RE. Adsorption refrigerator using monolithic carbon-ammonia pair. Int J Refrig 1997;20:146–55.

[16] Critoph RE. Rapid cycling solar/biomass powered adsorption refrigeration system. Renew Energy 1999;16:673–8.

[17] Oertel K, Fischer M. Adsorption cooling system for cold storage using methanol/silicagel. Appl Therm Eng 1998;18:773–86. doi:10.1016/S1359-4311(97)00107-5.

[18] Zhang LZ, Wang L. Momentum and heat transfer in the adsorbent of a waste-heat adsorption cooling system. Energy 1999;24:605–24. doi:10.1016/S0360-5442(99)00018-3.

[19] Zhang LZ, Wang L. Effects of coupled heat and mass transfers in adsorbent on the performance of a waste heat adsorption cooling unit. Appl Therm Eng 1999;19:195–215.

[20] Zhang LZ. Design and testing of an automobile waste heat adsorption cooling system. Appl Therm Eng 2000;20:103–14. doi:10.1016/S1359-4311(99)00009-5.

[21] Jiangzhou S, Wang RZ, Lu YZ, Xu YX, Wu JY. Experimental investigations on adsorption air-conditioner used in internal-combustion locomotive driver-cabin. Appl Therm Eng 2002;22:1153–62. doi:10.1016/S1359-4311(02)00036-4.

[22] Lu YZ, Wang RZ, Jianzhou S, Zhang M, Xu Y, Wu J. Performance of a diesel locomotive waste-heat-powered adsorption air conditioning system. Adsorption 2004;10:57–68.

[23] Restuccia G, Freni A, Vasta S, Aristov YI. Selective water sorbent for solid sorption chiller: experimental results and modelling. Int J Refrig 2004;27:284–93. doi:10.1016/j.ijrefrig.2003.09.003.

[24] Magnetto D. Thermally Operated Mobile Air Conditioning Systems. 2005.

[25] Wang DC, Xia ZZ, Wu JY, Wang RZ, Zhai H, Dou WD. Study of a novel silica gel–water adsorption chiller. Part I. Design and performance prediction. Int J Refrig 2005;28:1073–83. doi:10.1016/j.ijrefrig.2005.03.001.

[26] Wang DC, Wu JY, Xia ZZ, Zhai H, Wang RZ, Dou WD. Study of a novel silica gel–water adsorption chiller. Part II. Experimental study. Int J Refrig 2005;28:1084–91. doi:10.1016/j.ijrefrig.2005.03.002.

[27] Wang DC, Shi ZX, Yang QR, Tian XL, Zhang JC, Wu JY. Experimental research on novel adsorption chiller driven by low grade heat source. Energy Convers Manag 2007;48:2375–81. doi:10.1016/j.enconman.2007.03.001.

[28] Restuccia G, Freni A, Russo F, Vasta S. Experimental investigation of a solid adsorption chiller based on a heat exchanger coated with hydrophobic zeolite. Appl Therm Eng 2005;25:1419–28. doi:10.1016/j.applthermaleng.2004.09.012.

[29] Yang GZ, Xia ZZ, Wang RZ, Keletigui D, Wang DC, Dong ZH, et al. Research on a compact adsorption room air conditioner. Energy Convers Manag 2006;47:2167–77. doi:10.1016/j.enconman.2005.12.005.

[30] Wang LW, Wang RZ, Lu ZS, Chen CJ, Wu JY. Comparison of the adsorption performance of compound adsorbent in a refrigeration cycle with and without mass recovery. Chem Eng Sci 2006;61:3761–70. doi:10.1016/j.ces.2006.01.018.

[31] Lu ZS, Wang RZ, Wang LW, Chen CJ. Performance analysis of an adsorption refrigerator using activated carbon in a compound adsorbent. Carbon N Y 2006;44:747–52. doi:10.1016/j.carbon.2005.09.016.

[32] Wang LW, Wang RZ, Lu ZS, Chen CJ, Wang K, Wu JY. The performance of two adsorption ice making test units using activated carbon and a carbon composite as adsorbents. Carbon N Y 2006;44:2671–80. doi:10.1016/j.carbon.2006.04.013.

[33] Chen CJ, Wang RZ, Wang LW, Lu ZS. Studies on cycle characteristics and application of split heat pipe adsorption ice maker. Energy Convers Manag 2007;48:1106–12. doi:10.1016/j.enconman.2006.10.017.

[34] Freni A, Russo F, Vasta S, Tokarev M, Aristov YI, Restuccia G. An advanced solid sorption chiller using SWS-1L. Appl Therm Eng 2007;27:2200–4. doi:10.1016/j.applthermaleng.2005.07.023.

[35] Daou K, Wang RZ, Xia ZZ, Yang GZ. Experimental comparison of the sorption and refrigerating performances of a CaCl2 impregnated composite adsorbent and those of the host silica gel. Int J Refrig 2007;30:68–75. doi:10.1016/j.ijrefrig.2006.05.003.

[36] Verde M, Corberan JM, de Boer R, Smeding S. Modelling of a waste heat driven silica gel/water adsorption cooling system comparison with experimental results. Int. Sorption Heat Pump, Padua, Italy: 2011, p. 7–8.

[37] Sapienza A, Santamaria S, Frazzica A, Freni A. Influence of the management strategy and operating conditions on the performance of an adsorption chiller. Energy 2011;36:5532–8. doi:10.1016/j.energy.2011.07.020.

[38] Aristov YI, Sapienza A, Ovoshchnikov DS, Freni A, Restuccia G. Reallocation of adsorption and desorption times for optimisation of cooling cycles. Int J Refrig 2012;35:525–31. doi:10.1016/j.ijrefrig.2010.07.019.

[39] Sapienza A, Glaznev IS, Santamaria S, Freni A, Aristov YI. Adsorption chilling driven by low temperature heat: New adsorbent and cycle optimization. Appl Therm Eng 2012;32:141–6. doi:10.1016/j.applthermaleng.2011.09.014.

[40] Freni A, Sapienza A, Glaznev IS, Aristov YI, Restuccia G. Experimental testing of a lab-scale adsorption chiller using a novel selective water sorbent "silica modified by calcium nitrate." Int J Refrig 2012;35:518–24. doi:10.1016/j.ijrefrig.2010.05.015.

[41] Gong LX, Wang RZ, Xia ZZ, Chen CJ. Design and performance prediction of a new generation adsorption chiller using composite adsorbent. Energy Convers Manag 2011;52:2345–50. doi:10.1016/j.enconman.2010.12.036.

[42] Lu ZS, Wang RZ. Study of the new composite adsorbent of salt LiCl/silica gel–methanol used in an innovative adsorption cooling machine driven by low temperature heat source. Renew Energy 2014;63:445–51. doi:10.1016/j.renene.2013.10.010.

[43] Lu ZS, Wang RZ, Xia ZZ, Wu QB, Sun YM, Chen ZY. An analysis of the performance of a novel solar silica gel–water adsorption air conditioning. Appl Therm Eng 2011;31:3636–42. doi:10.1016/j.applthermaleng.2010.11.024.

[44] Lu Z, Wang R, Xia Z, Gong L. Experimental investigation adsorption chillers using micro-porous silica gel–water and compound adsorbent-methanol. Energy Convers Manag 2013;65:430–7. doi:10.1016/j.enconman.2012.09.018.

[45] Lu ZS, Wang RZ. Performance improvement and comparison of mass recovery in CaCl 2/activated carbon adsorption refrigerator and silica gel/LiCl adsorption chiller driven by low grade waste heat. Int J Refrig 2013;36:1504–11. doi:10.1016/j.ijrefrig.2013.03.008.

[46] Vasta S, Freni A, Sapienza A, Costa F, Restuccia G. Development and lab-test of a mobile adsorption air-conditioner. Int J Refrig 2012;35:701–8. doi:10.1016/j.ijrefrig.2011.03.013.

[47] Wang J, Wang LW, Luo WL, Wang RZ. Experimental study of a two-stage adsorption freezing machine driven by low temperature heat source. Int J Refrig 2013;36:1029–36. doi:10.1016/j.ijrefrig.2012.10.029.

[48] Song FP, Gong LX, Wang LW, Wang RZ. Study on gradient thermal driven adsorption cycle with freezing and cooling output for food storage. Appl Therm Eng 2014;70:231–9. doi:10.1016/j.applthermaleng.2014.04.066.

[49] Kiplagat JK, Wang RZ, Oliveira RG, Li TX, Liang M. Experimental study on the effects of the operation conditions on the performance of a chemisorption air conditioner powered by low grade heat. Appl Energy 2013;103:571–80. doi:10.1016/j.apenergy.2012.10.025.

[50] San J-Y, Tsai F-K. Testing of a lab-scale four-bed adsorption heat pump. Appl Therm Eng 2014;70:274–81. doi:10.1016/j.applthermaleng.2014.05.014.

[51] Pan QW, Wang RZ, Lu ZS, Wang LW. Experimental investigation of an adsorption refrigeration prototype with the working pair of composite adsorbent-ammonia. Appl Therm Eng 2014;72. doi:10.1016/j.applthermaleng.2014.06.054.

[52] Tso CY, Chan KC, Chao CYH, Wu CL. Experimental performance analysis on an adsorption cooling system using zeolite 13X/CaCl2 adsorbent with various operation sequences. Int J Heat Mass Transf 2015;85:343–55. doi:10.1016/j.ijheatmasstransfer.2015.02.005.

[53] Okunev BN, Aristov YI. Making adsorptive chillers faster by a proper choice of adsorption isobar shape: Comparison of optimal and real adsorbents. Energy 2014;76:400–5. doi:10.1016/j.energy.2014.08.031.

[54] Himooka SS, Shima KO. The evaluation of direct cooling and heating desiccant device coated with FAM. J Chem Eng Japan 2007;40:1330–4.

[55] Henninger SK, Schmidt FP, Henning HM. Water adsorption characteristics of novel materials for heat transformation applications. Appl Therm Eng 2010;30:1692–702. doi:10.1016/j.applthermaleng.2010.03.028.

[56] Okamoto K, Teduka M, Nakano T, Kubokawa S, Kakiuchi H. The development of AQSOA water vapor adsorbent and AQSOA coated heat exchanger. Int. Symp. Innov. Mater. Process. Energy Syst., Singapor: 2010.

[57] Goldsworthy MJ. Measurements of water vapour sorption isotherms for RD silica gel, AQSOA-Z01, AQSOA-Z02, AQSOA-Z05 and CECA zeolite 3A. Microporous Mesoporous Mater 2014;196:59–67. doi:10.1016/j.micromeso.2014.04.046.

[58] Dawoud B. On the Effect of Grain Size on the Kinetics of Water Vapor Adsorption and Desorption into/from Loose Pellets of FAM-Z02 under a Typical Operating Condition of Adsorption Heat Pumps. J Chem Eng Japan 2007;40:1298–306. doi:10.1252/jcej.07WE163.

[59] Sharafian A, Nemati Mehr SM, Huttema W, Bahrami M. Effects of different adsorber bed designs on in-situ water uptake rate measurements of AQSOA FAM-Z02 for vehicle air conditioning applications. Appl Therm Eng 2015:under review.

[60] Sharafian A, Bahrami M. A quasi steady state model for adsorption cooling systems: Automotive applications. ASME 2012 6th Int. Conf. Energy Sustain. 10th Fuel Cell Sci. Eng. Technol. Conf., San Diego, CA, USA: 2012.

[61] Sharafian A, Dan PC, Huttema W, Bahrami M. Performance analysis of a novel expansion valve and control valves designed for a waste heat-driven two-adsorber bed adsorption cooling system. Int J Refrig 2015:under review.

[62] Wang RZ, Wang L, Wu J. Adsorption Refrigeration Technology: Theory and Application. John Wiley & Sons; 2014.

[63] Cheppudira Thimmaiah P, Sharafian A, Huttema W, Bahrami M. Effects of capillary-assisted tubes with different fin geometries on the performance of a low-operating pressure evaporator for adsorption cooling systems. Appl Energy 2015:under review.

[64] Lambert MA, Jones BJ. Automotive adsorption air conditioner powered by exhaust heat. Part 1: Conceptual and embodiment Design. Proc Inst Mech Eng Part D J Automob Eng 2006;220:959–72. doi:10.1243/09544070JAUTO221.

Appendix J.

Practical design considerations in adsorption cooling systems packed with composite adsorbents

Progress in building of ACS testbed

During the course of this Ph.D. research project, four ACS testbeds were developed. Building an ACS for the first time was challenging and was accomplished using the information collected from the literature, experimental and thermodynamic cycle models developed in the lab, and with the technical assistance of LAEC group members with backgrounds in physics, chemistry, electrical engineering, and mechanical engineering. The first one-adsorber bed activated carbon-ethanol ACS was built in collaboration with students from Engineering Without Borders (EWB) Canada-Surrey chapter, as shown in Figure J1-a and b. According to the World Health Organization (WHO), nearly half of the vaccines in rural African regions go to waste every year due to improper storage and heat spoilage. This project focused on a simple, inexpensive ACS design for vaccine protection in off-grid regions of Africa. In principle, the adsorber bed could be regenerated during the day using solar energy and vaporous adsorbate left the adsorber bed condensed in the condenser. During the night, the adsorber bed is cooled down by the ambient. When the evaporator is connected to the adsorber bed, adsorption process happens and the cooling power is generated inside the evaporator box.

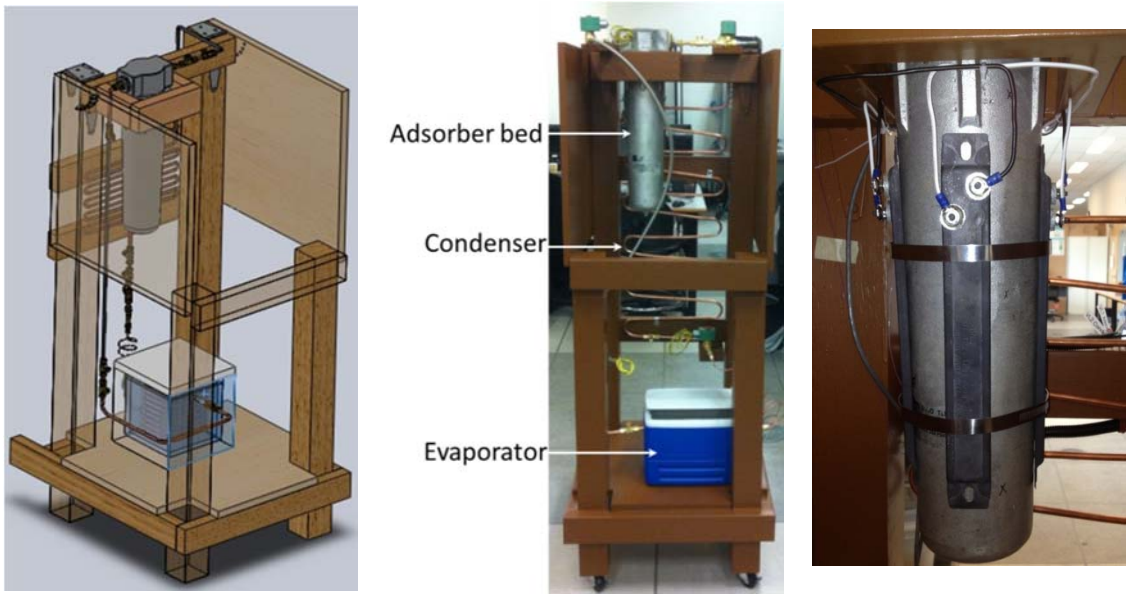

(a) (b) (c)

Figure J1. (a) Schematic and (b) prototype of solar thermal-driven activated carbon-ethanol ACS, and (c) location of heaters on the adsorber bed.

The system was tried to be built by natural materials available in Africa. The adsorbent was coconut shell activated carbon and adsorbate was ethanol. To simulate solar thermal regeneration, four 250 W heaters were installed on the adsorber bed, as shown in Figure J1-c. Also, two solenoid valves were installed to connect the adsorber bed to the condenser and evaporator automatically. To control the adsorption and desorption processes, a LabVIEW program was developed to automatically operate the heaters and solenoid valves. However, the solenoid valves could not isolate the adsorber bed from the condenser and evaporator because solenoid valves are designed for zero pressure gradients between two sides of the valves. The adsorber bed was heated and cooled only from the exterior surface and the low heat transfer rate to the adsorbent particles caused inefficient adsorption and desorption processes. Also, the piping between the components was long and resulted in high pressure drop. These design issues greatly impaired the performance of the test system. Therefore, the second ACS setup was built to test corrections to the design of the system.

Figure J2 shows the second ACS. It can be seen in Figure J2-a that the piping between the adsorber bed and condenser/evaporator container is short. Also, a vacuum rated manual ball valve was used between the adsorber bed and the condenser/evaporator container to perfectly isolate the two components from each other. To increase the heat transfer rate to the adsorber bed, a custom-built heat exchangerwas built in the LAEC, as shown in Figure J2-b. The adsorbent-adsorbate pair in the ACS was blue-indicating silica gel and water, as shown in Figure J2-c. Hot water at 88-93°C and cold water at 28-33°C were used for heating and cooling of the adsorber bed. Further information and results measured using the second ACS setup is reported in Appendix D. However, in this setup, there was no control on the temperature of condenser/evaporator container and continuous cooling power could not be extracted from the system.

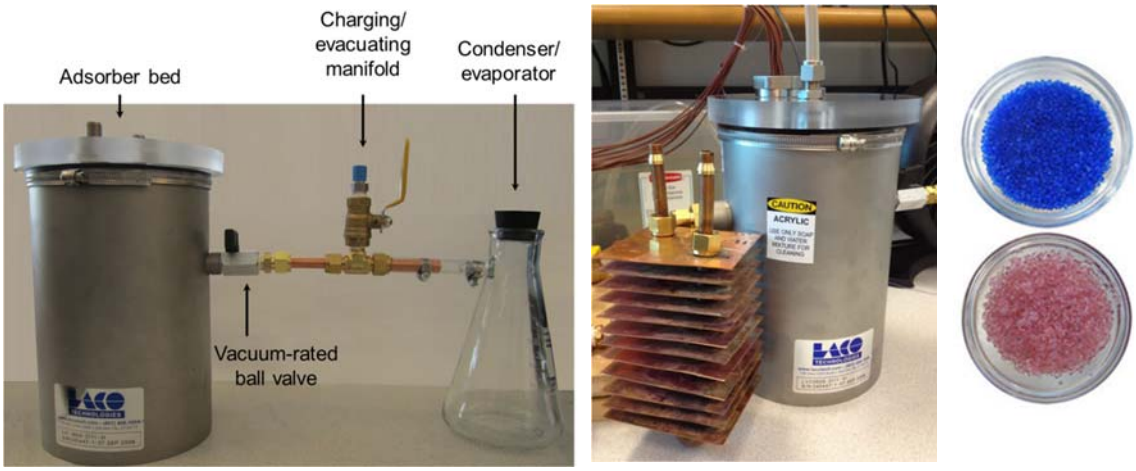

(a) (b) (c)

Figure J2. (a) Waste heat-driven silica gel-water ACS, (b) custom-built heat exchanger located inside the adsorber bed, and (c) blue-indicating silica gel used as the adsorbent.

The expansion valve is one of the main components in any refrigeration cycle. To study the behavior of the expansion valve, the second one-adsorber bed ACS had to be modified. Figure J3 shows the modified one-adsorber bed silica gel-water ACS and external heat sources/sinks to control the temperature of different components of the ACS. The specifications of each component and operating conditions are included in Figure J3.

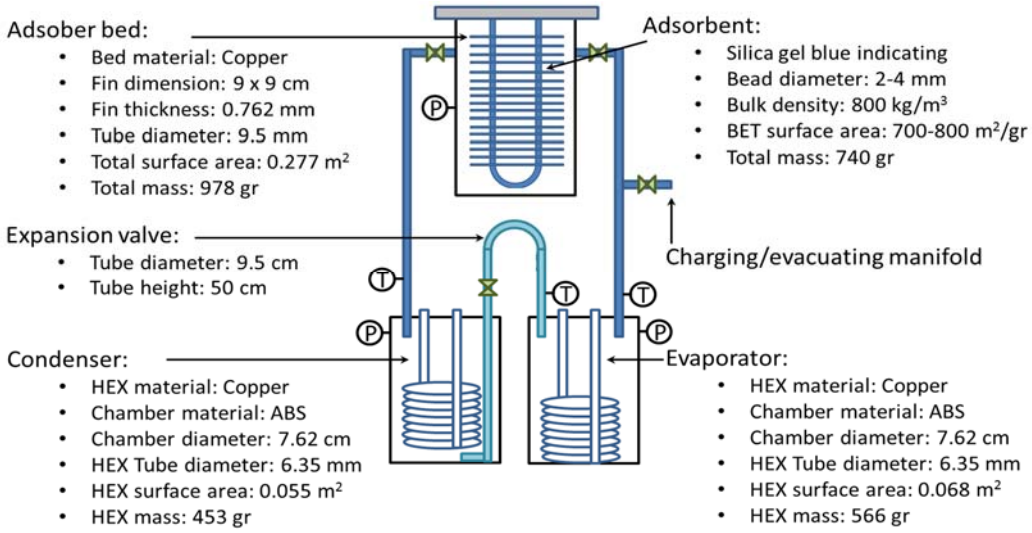

(a)

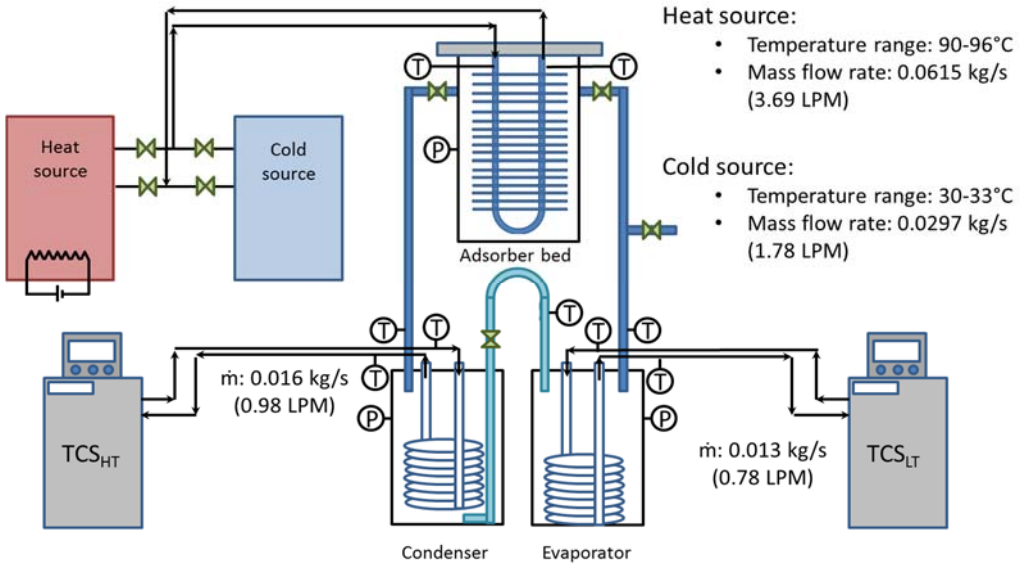

(b)

Figure J3. (a) Modified silica gel-water ACS and (b) heat sources/sinks to control the operating temperatures of different components.

In an ACS, which works with water, ethanol or methanol, a U-bend tube is often used as the expansion valve in stationary ACS applications. To test this design, the one-adsorber bed ACS was equipped with a U-bend tube, as shown in Figure J4.

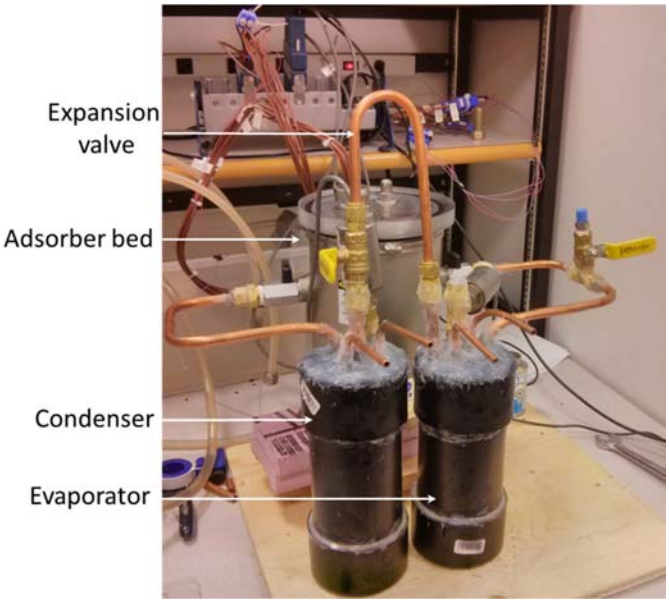

Figure J4. (a) Modified ACS to test a U-bend tubing expansion valve.

The height of designed expansion valve was 50 cm to create the pressure difference of about 5 kPa between the condenser and evaporator. This type of expansion valve only worked within specific range of condensation and evaporation pressures such as condensation and evaporation pressures of 5.6 and 2 kPa corresponding to the saturation pressures of water at 35 and 20°C, respectively. The U-bend tube only created a constant pressure difference between the condenser and evaporator and could not properly work if the operating conditions exceeded the design point. To fix this issue, a check valve with cracking pressure of 3.5-7 kPa was proposed to be used as the expansion valve.

Further information about the next systems with details of each component is provided in Appendix G and I.

In-situ water uptake rate measurements of composite adsorbents and their effects on metallic adsorber beds

In-situ water uptake rate measurements of different adsorbent materials packed inside an adsorber bed is the best method to find the maximum achievable SCP and COP of an ACS before installation of the adsorber bed on the ACS testbed. Silica gel-$CaCl_2$ is a composite adsorbent synthesized in the LAEC with high water uptake rate and its behavior was studied by using a TGA. To find the water uptake rate of silica gel-$CaCl_2$ packed in a finned tube adsorber bed, several experimental testbeds were designed. Figure J5-a shows the schematic of the first experimental setup. The setup included an adsorber bed connected to a temperature control system (TCS), which supplied a 30°C cooling fluid to the adsorber bed, and a glassware condenser/evaporator container. In this experiment,

there was no control on the temperature of the condenser/evaporator container, and as a result, the ambient temperature dictated the adsorber bed and condensation/ evaporation container pressure, as shown in Figure J5-b. Therefore, the water uptake rate of silica gel-$CaCl_2$ was affected, as shown in Figure J5-c.

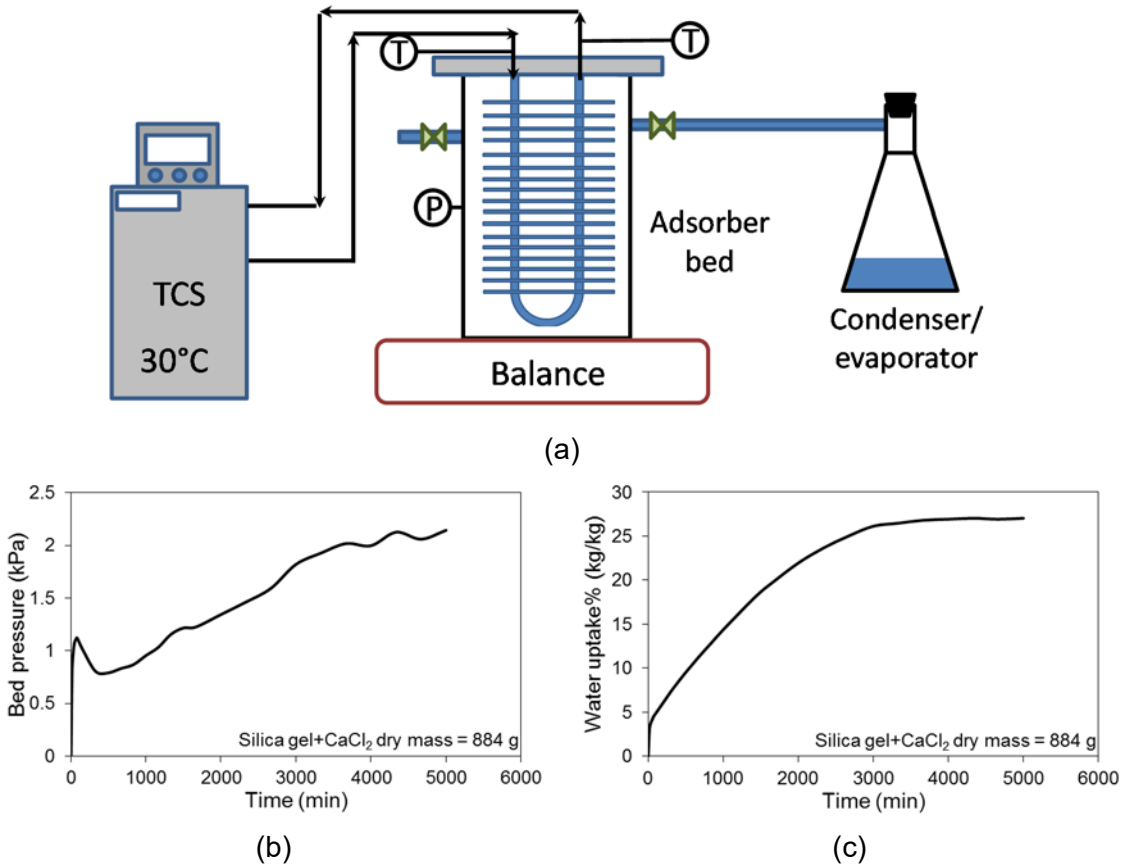

Figure J5. (a) Schematic of the first experimental setup for in-situ water uptake rate measurements of silica gel-$CaCl_2$, (b) adsorber bed pressure variations and, (c) water uptake rate variations during adsorption vs. time.

To increase the accuracy of the water uptake rate measurements, the experimental setup was modified by controlling the temperature of the condenser/evaporator container, as shown in Figure J6-a. In the second testbed, the condenser/evaporator container temperature was maintained constant at 20°C and the cooling fluid inlet temperature to the adsorber bed was set at 30°C. Figure J6-b and c show that the variations of adsorber bed pressure and water uptake rate improved. However, the adsorber bed pressure increased linearly with time. This trend was due to the lack of enough vapor supply from the condenser/evaporator container to the adsorber bed.

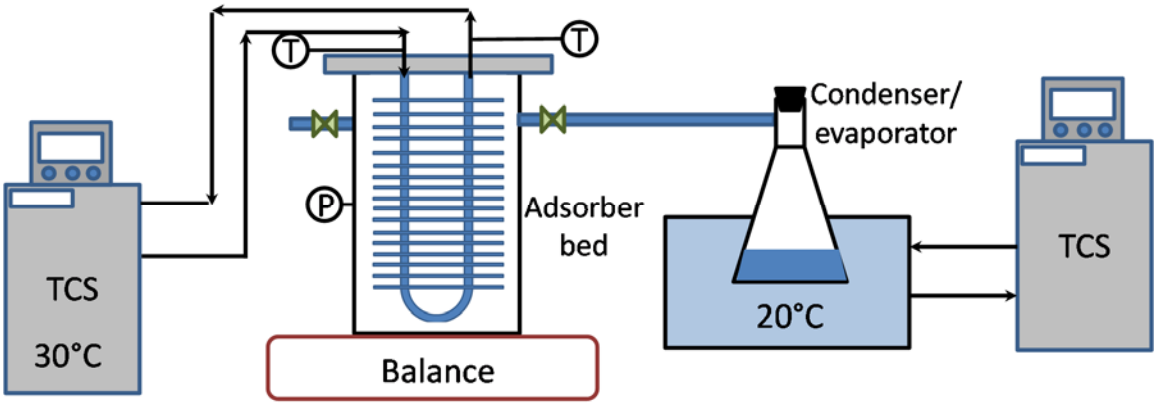

(a)

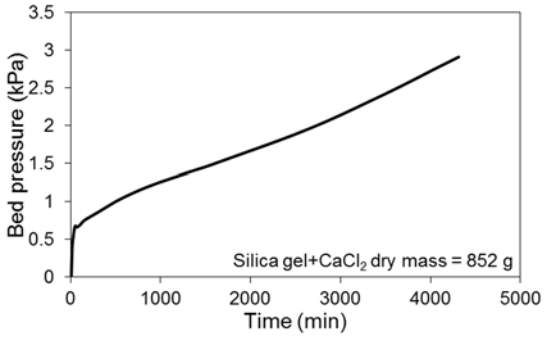

(b)

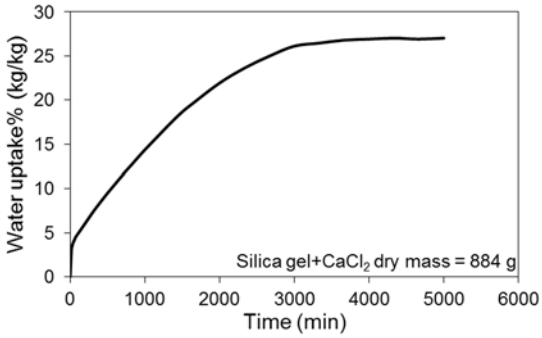

(c)

Figure J6. (a) Schematic of the second experimental setup for in-situ water uptake rate measurements of silica gel-$CaCl_2$, (b) adsorber bed pressure variations and, (c) water uptake rate variations during adsorption vs. time.

In the third attempt, the glassware condenser/evaporator was replaced with a metallic container, as shown in Figure J7-a. By this modification, the pressure of adsorber bed increased quickly from vacuum condition and reached the saturation pressure of water vapor coming from the condenser/evaporator container, as shown in Figure J7-b. As a result of proper vapor supply to the adsorber bed, the water uptake rate of silica gel-$CaCl_2$ improved significantly. At this stage, the water adsorption and desorption rates of silica gel-$CaCl_2$ could be studied.

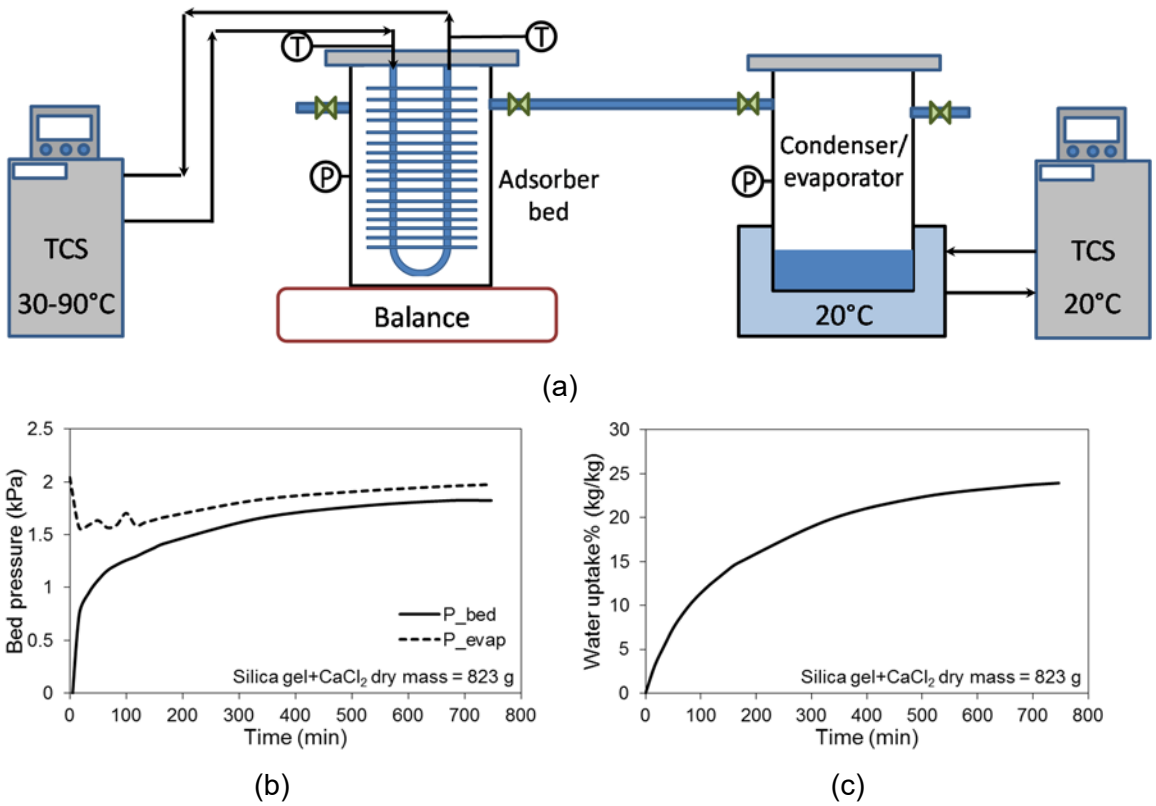

Figure J7. **(a) Schematic of the third experimental setup for in-situ water uptake rate measurements of silica gel-$CaCl_2$, (b) adsorber bed pressure variations and, (c) water uptake rate variations during adsorption vs. time.**

To run a set of adsorption and desorption processes, the heating and cooling fluids inlet temperatures to the adsorber bed were set at 90 and 30°C, and the condenser/evaporator temperature was maintained at 20°C. Adsorption and desorption of the adsorber bed were repeated and the water uptake rate of silica gel-$CaCl_2$ decreased for each adsorption and desorption cycles, as shown in Figure J8. It can be seen in the demarcated region in Figure J8-a that the minimum pressure of the adsorber bed at the end of desorption increased. The water uptake rate of silica gel-$CaCl_2$ was reduced due to the increase in the pressure of the adsorber bed, as shown in Figure J8-b. To resolve the issue, the silica gel-$CaCl_2$ particles were dried out by heating and the experiments were repeated. The same results were achieved.

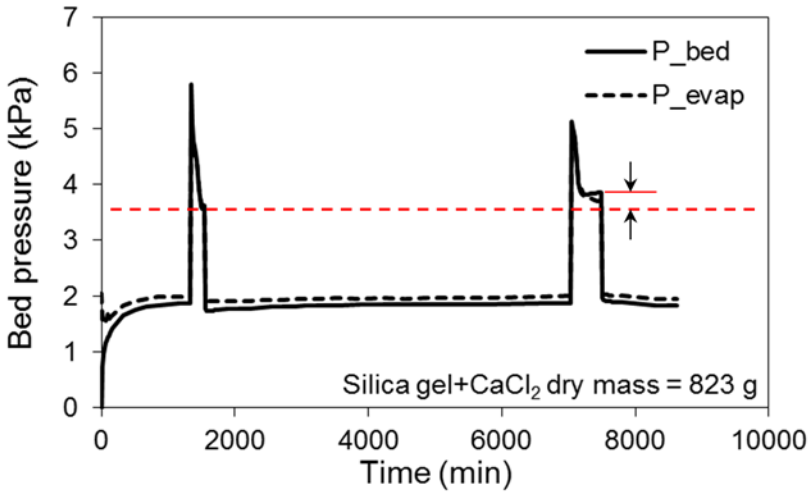

(a)

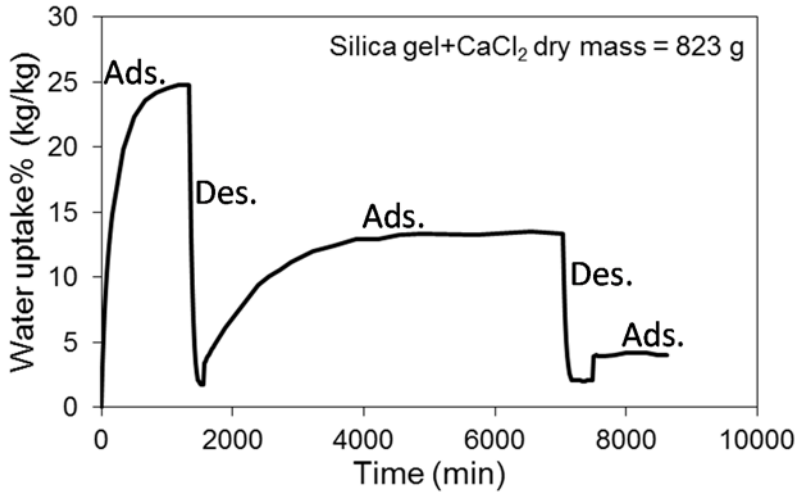

(b)

Figure J8. (a) Adsorber bed pressure variations and (b) water uptake rate of silica gel-$CaCl_2$ during adsorption and desorption in the third experimental setup. The heating and cooling fluids inlet temperatures to the adsorber beds were 90 and 30°C, and the condenser/evaporator temperature was set at 20°C.

Figure J9-a shows the copper heat exchanger before packing with the silica gel-$CaCl_2$. After running the adsorption and desorption tests, the adsorber bed was cleaned from the silica gel-$CaCl_2$. It was obvious that the copper heat exchanger was corroded, as shown in Figure J9-b. Also, Figure J9-c shows that the silica gel-$CaCl_2$ particles were clumped together due to the $CaCl_2$ leakage to the surface of the silica gel particles. Our further investigations indicated that galvanic corrosion was also happened inside the adsorber bed made by copper and aluminum at the presence of water. Also, $CaCl_2$ accelerated the corrosion rate. Corrosion of copper at the presence of water generated a background gas inside the adsorber bed and reduced the water uptake rate of silica gel-$CaCl_2$.

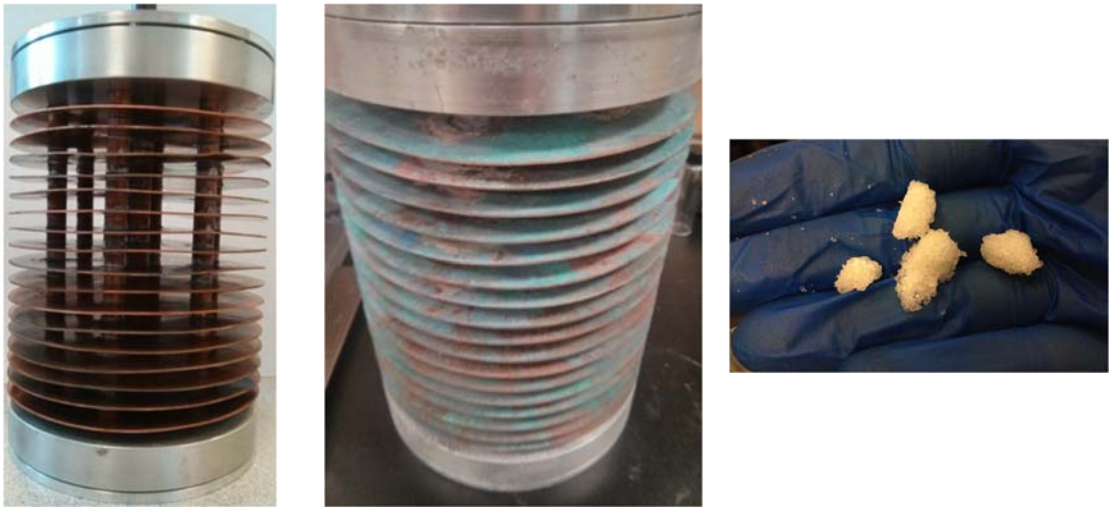

(a) (b) (c)

Figure J9. (a) Adsorber bed before packing with silica gel-$CaCl_2$, (b) corrosion of copper heat exchanger by galvanic corrosion and $CaCl_2$, and (c) silica gel-$CaCl_2$ particles were clumped together due to $CaCl_2$ leakage to the surface of silica gel.

To resolve this issue, AQSOA FAM-Z02 was replaced the silica gel-$CaCl_2$ and the same set of experiments were repeated. It can be seen in Figure J10 that the adsorber bed pressure and water uptake rate of AQSOA FAM-Z02 were reproducible.

Further information about the in-situ water uptake rate measurements of AQSOA FAM-Z02 is provided in Appendix E.

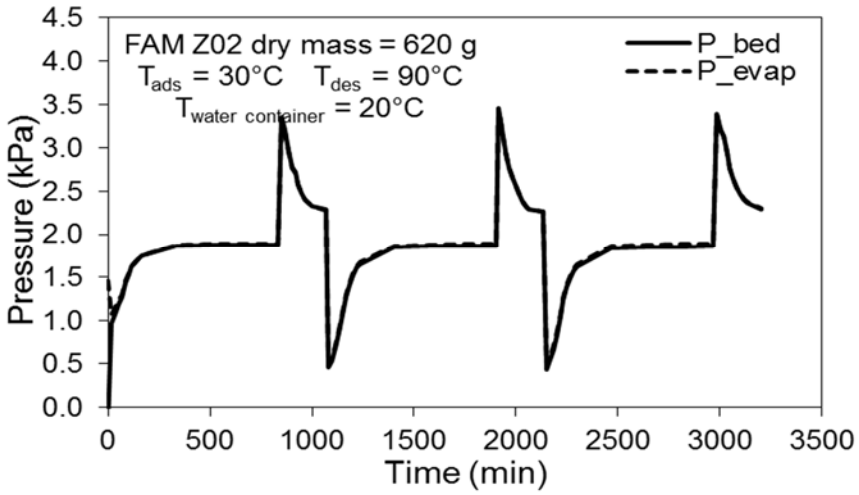

(a)

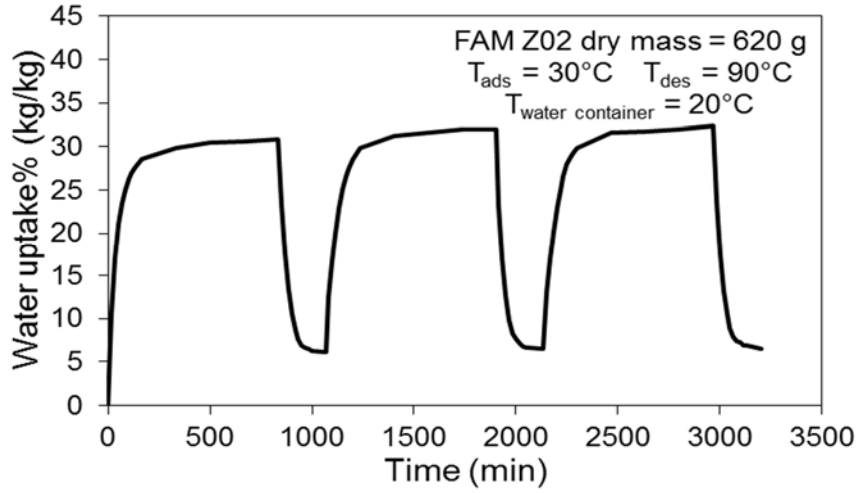

(b)

Figure J10. (a) Adsorber bed pressure variations and (b) water uptake rate of AQSOA FAM-Z02 during adsorption and desorption in the third experimental setup. The heating and cooling inlet temperatures to the adsorber beds were 90 and 30°C, and the condenser/evaporator temperature was set at 20°C.

List of materials used for building an ACS

Table J1 provides the list of equipment and fittings used to build the ACS testbeds.

Table J1. Equipment and fittings to build the ACS testbeds.

No.	Part Name	Part Number	Quantity	Supplier
1	Adsorber bed (vacuum chamber)	LVC0810-3111-VI	2	http://www.lacotech.com
2	Adsorber bed (engine oil cooler)	1268	2	www.haydenauto.com
3	Condenser and evaporator	BT-ST-55-1	2	http://www.brazetek.com
4	NW 16 Tee	NW16-075-T	3	http://www.ldsvacuumshopper.com/
5	NW 16 90 Elbow	NW16-075-E90	4	http://www.ldsvacuumshopper.com/
6	NW16 Cross, 5-Way	NW16-075-5X	1	http://www.ldsvacuumshopper.com/
7	NW16 Cross, 6-Way	NW16-075-6X	1	http://www.ldsvacuumshopper.com/
8	NW16 to 3/8" NPT (Male) SS	NW16x38NPT	8	http://www.ldsvacuumshopper.com/
9	NW16 to 1/2" NPT (Male)	NW16x50NPT	2	http://www.ldsvacuumshopper.com/
10	NW16 to 1/4" NPT (Male)	NW16x25NPT	2	http://www.ldsvacuumshopper.com/
11	NW16 To 1/4" NPT (Female)	NW16-075-SP25	4	http://www.ldsvacuumshopper.com/
12	NW16 Centering Ring Stainless	NW16-075-SR-S	24	http://www.ldsvacuumshopper.com/
13	Aluminum Wing Clamp NW16	NW16-075-CW	24	http://www.ldsvacuumshopper.com/
14	NW16 to 3/4" NPT (Male)	NW16x75NPT	2	http://www.ldsvacuumshopper.com/
15	NW16 Manual Ball Valve	LDS-KMBV-1075-NW16	2	http://www.ldsvacuumshopper.com/
16	NW40 hose adapter	NW40-150-SH	2	http://www.ldsvacuumshopper.com/
17	NW40 to NW16 Conical Reducer	NW40x16-CR	1	http://www.ldsvacuumshopper.com/
18	Aluminum Wing Clamp NW40	NW40-150-CW	3	http://www.ldsvacuumshopper.com/
19	NW40 Centering Ring SS Silicone	NW40-150-SR-S	3	http://www.ldsvacuumshopper.com/
20	Disc check valve	DCV-375B-S	4	http://www.generant.com/DCV.shtml
21	check valve	CV-250B-S-1	0	http://www.generant.com/cv.shtml
22	Adapter for 3/8" Tube OD x 3/4 NPT Male	5182K913	2	http://www.mcmaster.com
23	Stainless Steel Threaded Pipe Fitting 3/4	4464K52	1	http://www.mcmaster.com
24	High-Pressure/Vacuum Polyethylene Tubing 3/8	50375K47	5	http://www.mcmaster.com
25	SS Hex Nipple 3/4	51205K203	1	http://www.mcmaster.com
26	Vacuum-Rated 3-A Sanitary Clear PVC Tubing	5393K48	8	http://www.mcmaster.com
27	Worm-Drive Hose Clamp	5388K28	10	http://www.mcmaster.com
28	Tube Support for 3/8" Tube	5533K344	1	http://www.mcmaster.com
29	1 Male x 3/4 Female, Hex Reducing Bushing	4464K276	2	http://www.mcmaster.com
30	Brass Ball Valve 3/4 NPT Male x Female	47865K44	1	http://www.mcmaster.com
31	Brass Check Valve 3/4 NPT Male x Female	7768K43	1	http://www.mcmaster.com
32	1/8" Tube OD, x 1/4 NPT Male adaptor	5272K291	4	http://www.mcmaster.com

Table J2 provides the list of equipment and fittings to build the heating and cooling circuits connected to the adsorber beds for adsorption and desorption.

Table J2. Equipment and fittings for building the heating and cooling circuits.

No.	Part Name	Part Number	Quantity	Supplier
1	3/8" Hose ID x 1/2" NPT Female Pipe adaptor	5346K56	1	http://www.mcmaster.com
2	High-Temperature Viton Rubber Tubing, 3/8" ID, 1/2" OD	5119K45	30	http://www.mcmaster.com
3	3/8" Hose ID x 1/2" NPT Male Pipe adaptor	5346K21	40	http://www.mcmaster.com
4	Tee fitting, male	9171K158	4	http://www.mcmaster.com
5	1/2 Pipe Size, Female x Female x Male Tee	4429K326	8	http://www.mcmaster.com
6	1/2 x 1/4 x 1/2 Pipe Size, Inline Reducing Tee	4429K226	8	http://www.mcmaster.com
7	1/2" Tube OD x 1/2 NPT Male adaptor	5272K199	4	http://www.mcmaster.com
8	Bulkhead fitting for the beds	5272K233	4	http://www.mcmaster.com
9	3/4 x 1/2 Pipe Size, Hex Reducing Nipple	5485K34	2	http://www.mcmaster.com
10	1/2 Pipe Size Female Tee	4429K253	6	http://www.mcmaster.com
11	1 Male x 1/2 Female, Hex Reducing Bushing	4429K424	2	http://www.mcmaster.com
12	Brass Ball Valve, 1/2" NPT Connection, Female x Male	47865K43	10	http://www.mcmaster.com
13	Pipe Thread Sealant	8149K22	1	http://www.mcmaster.com
14	Worm-Drive Hose Clamp	5415K11	5	http://www.mcmaster.com
15	1/8" Tube OD, x 1/4 NPT Male adaptor (thermocouples)	5272K291	9	http://www.mcmaster.com
16	3/4 x 1/4 x 3/4 Pipe Size, Inline Reducing Tee (for condenser)	4429K229	3	http://www.mcmaster.com
17	Brass Hex Nipple 3/4	5485K25	5	http://www.mcmaster.com
18	1/2 Nipple	5485K24	4	http://www.mcmaster.com
19	Multipurpose Copper Tubing 1/2 OD	8967K94	1	http://www.mcmaster.com
20	Multipurpose Copper (Alloy 110)	8963K254	2	http://www.mcmaster.com
21	Multipurpose Copper Tubing 3/8 OD	8967K89	2	http://www.mcmaster.com
22	6061 Aluminum 5"dia x 1" thick	1610T25	4	http://www.mcmaster.com
23	Solder Aluminuim Kit	UNIW-4300	1	http://www.kmstools.com
24	M16x1 to 1/2" NPT Adapter (pair)	8890008	2	http://www.julabo.com
25	M16x1 Nipple	8970443	2	http://www.julabo.com
26	Quick Disconnect Thermocouples	CP-SS-18-G-12	13	http://www.omega.com
27	High Performance Pressure Transducer	PX309-005AI	4	http://www.omega.com
28	Solenoid Valve 1/2 FNPT normally closed	2W160-1/2-3-V	4	http://www.stcvalve.com
29	Solenoid Valve 1/2 FNPT normally open	2WO160-1/2-3-V	4	http://www.stcvalve.com

Sensors used for the measurements

Table J3 provides the list of sensors installed on the ACS testbeds for the measurements.

Table J3. Sensors installed on the experimental setups for the measurements.

No.	Part Name	Part Number	Supplier
1	Feedthrough thermocouple	CPSS-18G-12	http://www.omega.com
2	Insulated thermocouple	5SRTC-TT-T-36-36	http://www.omega.com
3	Pressure transducer	PX309-005AI	http://www.omega.com
4	Flow meter	OM015S001-222	http://www.flomec.com.au/
5	Scale for mass measurements	Supper II	http://scales.setra.com/

Appendix K.

Experimental data

The experimental data measured in different experiments are provided in this appendix.

Table K1. Evaporator temperature at the end of adsorption process vs. cycle time (Reported in Appendix D, Figure 5).

Fin spacing [mm]	9.53
ADTR	1
Cycle time [s]	**T_{evap} [°C]**
Day 1	
400	29.4
600	28.3
1000	22.7
1400	17.5
1800	16.2
Day 2	
600	27.74
900	24
1400	18.42

Table K2. Temperature differences between thermocouples TC1 andTC2 at the end of adsorption and desorption processes for adsorber beds with 6.35 mm and 9.5 mm fin spacing under different cycle times and ADTRs (Reported in Appendix D, Figure 6 and Figure 7).

Fin spacing [mm]	6.35				
		TC1-TC2 [°C]	**TC1-TC2 [°C]**	**TC6-TC7 [°C]**	**TC6-TC7 [°C]**
Cycle time [s]	**ADTR**	**Adsorption**	**Desorption**	**Adsorption**	**Desorption**
600	1	0.9	3.1	2.6	0.7
900	1	0.3	2.7	1.1	0.0
1400	1	0.2	2.5	0.8	0.0
600	2	0.3	3.8	1.1	2.8
900	2	0.0	3.0	0.5	1.0
1400	2	0.1	2.8	0.3	0.6
600	3	0.0	4.4	0.7	4.4
900	3	0.0	3.7	0.4	2.2
1400	3	0.1	3.1	0.2	0.9

Table K3. Temperature differences between thermocouples TC6 andTC7 at the end of adsorption and desorption processes for adsorber beds with 6.35 mm and 9.5 mm fin spacing under different cycle times and ADTRs(Reported in Appendix D, Figure 6 and Figure 7).

Fin spacing [mm]	9.53				
		TC1-TC2 [°C]	TC1-TC2 [°C]	TC6-TC7 [°C]	TC6-TC7 [°C]
Cycle time [s]	ADTR	Adsorption	Desorption	Adsorption	Desorption
600	1	4.1	7.7	0.7	5.6
900	1	3.2	6.7	0.7	5.6
1400	1	2.3	5.9	0.7	5.5
600	2	2.5	9.5	0.4	5.7
900	2	1.7	8.5	0.2	5.9
1400	2	0.9	7.1	0.1	5.6
600	3	1.7	10.9	0.0	5.7
900	3	1.2	9.9	0.1	6.0
1400	3	0.5	8.1	0.0	5.8

Table K4. Effects of fin spacing on the evaporator temperature under different cycle times and ADTRs (Reported in Appendix D, Figure 8).

		Fin spacing [mm]			
		6.35		9.53	
Cycle time [s]	ADTR	T_{evap} [°C]	T_{cond} [°C]	T_{evap} [°C]	T_{cond} [°C]
600	1	25.04	26.93	27.74	31.19
900	1	21.34	25.83	24	31.22
1400	1	16.67	25.62	18.42	29.4
600	2	21.31	23.82	23.78	27.68
900	2	17.42	22.21	20.43	28.15
1400	2	14.14	22.68	15.18	27.03
600	3	19.8	22.57	22.31	26.44
900	3	16.34	20.87	19.83	27.68
1400	3	14.04	22.54	14.87	26.02

Table K5. FAM-Z02 water uptake difference between adsorption and desorption processes, SCP_{ideal} and COP_{ideal} in Designs I and II vs. different cycle times (Reported in Appendix E, Figure 6).

Cycle time [s]	Cycle time [min]	COP	SCP [W/kg]	Δω%
Design I				
3600	60	0.216	23.82	3.49
5400	90	0.316	28.82	6.34
7200	120	0.356	29.31	8.60
10800	180	0.401	27.11	11.93
Design II				
480	8	0.34	110.41	2.16
600	10	0.40	112.86	2.76
900	15	0.45	98.75	3.62
1200	20	0.49	91.32	4.47
1800	30	0.54	82.09	6.02
3600	60	0.62	73.76	10.82
5400	90	0.65	65.83	14.49
7200	120	0.67	63.15	18.53

Table K6. Effects of cycle time on the SCP of the ACS (Reported in Appendix G, Figure 6).

Cycle time [s]	Cycle time [min]	SCP [W/kg]
1200	20	3.28
1500	25	5.11
1800	30	9.15
2100	35	8.22

Table K7. Effects of heating and cooling fluid inlet temperatures to the adsorber beds on the SCP of the ACS (Reported in Appendix G, Figure 7).

$T_{hf,\,i}$ [°C]	SCP [W/kg]	$T_{cf,\,i}$ [°C]	SCP [W/kg]
70	0.69	30	9.15
80	3.73	35	6.46
90	9.15	40	4.02
100	14.80		

Table K8. Effects of coolant and chilled water inlet temperatures pumped to the condenser and evaporator, respectively, on the SCP of the ACS (Reported in Appendix G, Figure 8).

$T_{coolant,\,i}$ [°C]	SCP [W/kg]	$T_{chilled,\,i}$ [°C]	SCP [W/kg]
30	9.15	15	9.15
35	8.65	17.5	13.89
40	4.43	20	14.17

Table K9. Effects of different enhanced tubes and a plain tube vs. different chilled water inlet temperatures on the total evaporation heat transfer rate and the evaporator heat transfer coefficient (Reported in Appendix H, Figure 6).

Tube type	Plain tube		Turbo CLF-40FPI		Turbo ELP-40 FPI	
$T_{chilled,\,i}$ [°C]	U [W/m^{2}K]	$\dot{Q}$ [W]	U [W/m^{2}K]	$\dot{Q}$ [W]	U [W/m^{2}K]	$\dot{Q}$ [W]
10	284.57	65.96	544.70	118.72	524.21	103.94
15	308.04	133.70	673.76	301.55	695.31	317.58
20	365.11	204.21	752.91	396.89	839.27	409.64
Tube type	**Turbo Chil-40 FPI**		**Turbo Chil-26 FPI**		**GEWA-KS-40 FPI**	
$T_{chilled,\,i}$ [°C]	U [W/m^{2}K]	$\dot{Q}$ [W]	U [W/m^{2}K]	$\dot{Q}$ [W]	U [W/m^{2}K]	$\dot{Q}$ [W]
10	595.79	128.51	517.60	107.42	453.91	105.65
15	767.46	312.62	694.42	301.67	593.66	267.17
20	888.72	422.00	802.32	413.95	713.19	384.68

Table K10. Effect of water non-dimensional height, H^*, on (a) total evaporation heat transfer rate and (b) evaporator heat transfer coefficient of capillary-assisted evaporator with Turbo Chil-40 FPI at chilled water inlet temperature and mass flow rate of 15°C and 2.53 kg/min (Reported in Appendix H, Figure 8).

$H^* = H_{ref}/D_{tube}$	U [W/m^{2}K]	$\dot{Q}$ [W]
1	767.46	312.62
1.81	577.54	250.51

Table K11. Effect of dead volume reduction inside the evaporator on total evaporation heat transfer rate and evaporator heat transfer coefficient of capillary-assisted evaporator with Turbo Chil-40 FPI at chilled water inlet temperature and mass flow rate of 15°C and 2.5 kg/min (Reported in Appendix H, Figure 9).

Dead volume reduction%	U [W/m^{2}K]	$\dot{Q}$ [W]
0	767.46	312.62
25	696.63	305.48

Table K12. Effect of chilled water mass flow rate on total evaporation heat transfer rate and evaporator heat transfer coefficient of capillary-assisted evaporator with Turbo Chil-40 FPI at chilled water inlet temperature of 15°C (Reported in Appendix H, Figure 10).

$\dot{m}_{chilled}$ [kg/min]	U [W/m^{2}K]	$\dot{Q}$ [W]
2.5	767.46	312.62
5.1	1101.77	342.83
7.6	1263.47	353.10
12.1	1442.27	369.02
15.3	1612.77	372.79

Table K13. Variations of SCP and COP of the one-adsorber bed ACS packed with different amounts of FAM-Z02 vs. cycle time (Reported in Appendix I, Figure 5).

$M_{FAM\ Z02}$ [kg]	1.9		1.0		0.5	
Cycle time [min]	COP	SCP [W/kg]	COP	SCP [W/kg]	COP	SCP [W/kg]
8	0.18	49.56	0.14	67.52	0.11	103.12
10	0.22	53.46	0.18	77.50	0.14	110.10
15	0.28	55.73	0.25	89.81	0.19	115.66
20	0.37	65.77	0.30	94.11	0.23	119.41
30	0.44	69.83	0.37	94.94	0.29	124.34

Table K14. Variations of SCP and COP of the one-adsorber bed ACS packed with different amounts of FAM-Z02 vs. heating and cooling fluid inlet temperatures entering to the adsorber bed (Reported in Appendix I, Figure 6).

$M_{FAM\ Z02}$ [kg]		1.9		1.0		0.5
$T_{hf,\ i}$ [°C]	COP	SCP [W/kg]	COP	SCP [W/kg]	COP	SCP [W/kg]
70	0.31	38.67	0.18	34.78	0.08	26.63
80	0.34	52.22	0.28	72.33	0.18	78.77
90	0.37	65.77	0.30	94.11	0.23	119.41
$T_{cf,\ i}$ [°C]	COP	SCP [W/kg]	COP	SCP [W/kg]	COP	SCP [W/kg]
30	0.37	65.77	0.30	94.11	0.23	119.41
35	0.38	65.40	0.27	75.17	0.19	92.88
40	0.36	53.72	0.25	59.94	0.16	69.24

Table K15. Variations of SCP and COP of the one-adsorber bed ACS packed with different amounts of FAM-Z02 vs. coolant and chilled water inlet temperatures entering to the condenser and evaporator (Reported in Appendix I, Figure 7).

$M_{FAM\ Z02}$ [kg]		1.9		1.0		0.5
$T_{coolant,\ i}$ [°C]	COP	SCP [W/kg]	COP	SCP [W/kg]	COP	SCP [W/kg]
30	0.37	65.77	0.30	94.11	0.23	119.41
35	0.33	66.74	0.24	73.22	0.18	93.98
40	0.34	60.21	0.20	57.78	0.14	75.30
$T_{chilled,\ i}$ [°C]	COP	SCP [W/kg]	COP	SCP [W/kg]	COP	SCP [W/kg]
10	0.27	48.28	0.15	43.78	0.10	48.12
15	0.37	65.77	0.30	94.11	0.23	119.41
20	0.49	100.47	0.35	114.41	0.30	161.22

Table K16. Variations of SCP and COP of the one- and two-adsorber bed ACS packed with 0.5 kg of FAM-Z02 vs. cycle time (Reported in Appendix I, Figure 9).

	One-bed ACS		Two-bed ACS	
Cycle time [min]	COP	SCP [W/kg]	COP	SCP [W/kg]
8	0.11	103.12	0.12	105.83
10	0.14	110.10	0.16	120.69
15	0.19	115.66	0.26	146.39
20	0.23	119.41	0.34	152.50
30	0.29	124.34	0.39	131.99

Table K17. Variations of SCP and COP of the one- and two-adsorber bed ACS packed with 0.5 kg of FAM-Z02 vs. heating and cooling fluid inlet temperatures entering to the adsorber beds (Reported in Appendix I, Figure 10).

	One-bed ACS		Two-bed ACS	
$T_{hf,\,i}$ [°C]	COP	SCP [W/kg]	COP	SCP [W/kg]
70	0.08	26.63	0.17	52.61
80	0.18	78.77	0.26	113.29
90	0.23	119.41	0.34	152.50
$T_{cf,\,i}$ [°C]	COP	SCP [W/kg]	COP	SCP [W/kg]
30	0.23	119.41	0.34	152.50
35	0.19	92.88	0.25	121.11
40	0.16	69.24	0.24	104.73

Table K18. Variations of SCP and COP of the one- and two-adsorber bed ACS packed with 0.5 kg of FAM-Z02 vs. coolant and chilled water inlet temperatures entering to the condenser and evaporator (Reported in Appendix I, Figure 11).

	One-bed ACS		Two-bed ACS	
$T_{coolant,\,i}$ [°C]	COP	SCP [W/kg]	COP	SCP [W/kg]
30	0.23	119.41	0.34	152.50
35	0.18	93.98	0.22	108.36
40	0.14	75.30	0.19	87.88
$T_{chilled,\,i}$ [°C]	COP	SCP [W/kg]	COP	SCP [W/kg]
10	0.10	48.12	0.17	77.96
15	0.23	119.41	0.34	152.50
20	0.30	161.22	0.35	191.47